AUTOMATIC IMAGE-BASED SBFE APPROACH FOR MULTIPHASE-MATERIALS TOPOLOGY OPTIMIZATION UNDER DYNAMIC LOADING

Mr. Rut Su

จุฬาลงกรณ์มหาวิทยาลัย
CHULALONGKORN UNIVERSITY

A Dissertation Submitted in Partial Fulfillment of the Requirements

for the Degree of Doctor of Philosophy in Civil Engineering

Department of Civil Engineering

FACULTY OF ENGINEERING

Chulalongkorn University

Academic Year 2022

Copyright of Chulalongkorn University

ระเบียบวิธีสเกลบาวน์ดารีไฟไนต์เอลิเมนต์โดยรูปภาพอัตโนมัติสำหรับการออกแบบโทโพโลยีแบบหลายเฟสวัสดุที่เหมาะสมที่สุดภายใต้แรงกระทำจลน์

นายรัฐ ซู

จุฬาลงกรณ์มหาวิทยาลัย
CHULALONGKORN UNIVERSITY

วิทยานิพนธ์นี้เป็นส่วนหนึ่งของการศึกษาตามหลักสูตรปริญญาวิศวกรรมศาสตรดุษฎีบัณฑิต
สาขาวิชาวิศวกรรมโยธา ภาควิชาวิศวกรรมโยธา
คณะวิศวกรรมศาสตร์ จุฬาลงกรณ์มหาวิทยาลัย
ปีการศึกษา 2565
ลิขสิทธิ์ของจุฬาลงกรณ์มหาวิทยาลัย

Thesis Title	AUTOMATIC IMAGE-BASED SBFE APPROACH FOR MULTIPHASE-MATERIALS TOPOLOGY OPTIMIZATION UNDER DYNAMIC LOADING
By	Mr. Rut Su
Field of Study	Civil Engineering
Thesis Advisor	Associate Professor SAWEKCHAI TANGARAMVONG, Ph.D.
Thesis Co Advisor	Professor Chongmin Song, Ph.D.

Accepted by the FACULTY OF ENGINEERING, Chulalongkorn University in Partial Fulfillment of the Requirement for the Doctor of Philosophy

..... Dean of the FACULTY OF ENGINEERING

(Professor SUPOT TEACHAVORASINSKUN, D.Eng.)

DISSERTATION COMMITTEE

..... Chairman

(Professor Suchart Limkatanyu, Ph.D.)

..... Thesis Advisor

(Associate Professor SAWEKCHAI TANGARAMVONG, Ph.D.)

..... Thesis Co-Advisor

(Professor Chongmin Song, Ph.D.)

..... Examiner

(Professor Jaroon Rungamornrat, Ph.D.)

..... Examiner

(Professor TEERAPONG SENJUNTICHAI, Ph.D.)

..... Examiner

(Associate Professor WATANACHAI SMITTAKORN, Ph.D.)

จุฬาลงกรณ์มหาวิทยาลัย
Chulalongkorn University

รัฐ ซู : ระเบียบวิธีสเกลบาวน์ดารีไฟไนต์เอลิเมนต์โดยรูปภาพอัตโนมัติสำหรับการออกแบบโทโพโลยีแบบหลายเฟสวัสดุที่เหมาะสมที่สุดภายใต้แรงกระทำจลน์. (AUTOMATIC IMAGE-BASED SBFE APPROACH FOR MULTIPHASE-MATERIALS TOPOLOGY OPTIMIZATION UNDER DYNAMIC LOADING) อ.ที่ปรึกษาหลัก : รศ. ดร.เสวกชัย ตั้งอร่ามวงศ์, อ.ที่ปรึกษาร่วม : ศ. ดร.ชองมิน ซอง

วิทยานิพนธ์ระดับดุษฎีบัณฑิตฉบับนี้นำเสนอวิธีการออกแบบโทโพโลยีภายใต้ระเบียบวิธีสเกลบาวน์ดารีไฟไนต์เอลิเมนต์ (SBFE) โดยวิธีนี้สามารถสร้างแบบจำลองที่มีลักษณะไม่ต่อเนื่องของโครงสร้างที่ประกอบด้วยรูปทรงโค้งซึ่งอยู่ในระนาบ 2 หรือ 3 มิติ และเมื่อรวมเข้ากับการปรับแต่งตาข่ายควอดทรี (ใน 2 มิติ) และออกทรี (3 มิติ) โครงร่างตาข่ายแบบปรับตัวอัตโนมัติที่ทำงานภายในเอลิเมนต์รูปหลายเหลี่ยมพบว่า SBFE มอบการสร้างแบบจำลองที่คุ้มค่าซึ่งช่วยแก้ไขปัญหาความไม่ต่อเนื่องของโหนดได้ คุณลักษณะที่โดดเด่นเหล่านี้นำไปสู่การพัฒนา SBFE ซึ่งเหมาะแก่การเป็นกรอบการสร้างแบบจำลองพื้นฐานสำหรับการเพิ่มประสิทธิภาพการออกแบบโทโพโลยีของของแข็ง โดยที่กระบวนการเพิ่มประสิทธิภาพโครงสร้างเชิงวิวัฒนาการแบบสองทิศทาง (BESO) ถูกรวมเข้ากับกระบวนการที่ใช้ภาพดิจิทัล ซึ่งเทคนิคการกรองแบบบิดเบี้ยวแบบใหม่จะปรับแต่งความเข้มระหว่างพื้นที่ทึบและพื้นที่ว่างเปล่าของวัสดุ สิ่งนี้นำไปสู่การบรรจบกันอย่างรวดเร็วภายใต้จัดวางที่เหมาะสมที่สุด (การกระจายวัสดุ) ของการออกแบบโครงสร้าง นอกจากนี้การประยุกต์ใช้วิธี BESO และ SBFE ที่รวมกันนั้นแสดงให้เห็นว่าการออกแบบโทโพโลยีที่เหมาะสมที่สุดของโครงสร้างนั้นไม่อยู่ภายใต้ข้อจำกัดของแรงกระทำแบบคงที่ (ไม่ขึ้นกับเวลา) แต่ยังรวมถึงแรงกระทำแบบไดนามิก (ขึ้นอยู่กับเวลา)ด้วย ซึ่งเทคนิคหลังนี้ใช้วิธีรวมเวลาลำดับสูง (ขั้นตอนเดียว) ที่ประมาณการตอบสนองไดนามิกของโครงสร้างการออกแบบได้อย่างแม่นยำ ยิ่งไปกว่านั้นคือการขยายวิธีการวิเคราะห์ไปสู่การออกแบบโทโพโลยีที่เหมาะสมที่สุดของโครงสร้างภายใต้ความถี่ธรรมชาติที่จำกัด ประกอบกับการใช้เทคนิคการแก้ไขวัสดุที่สร้างขึ้นจากการประสานงานระหว่าง BESO และ SBFE ช่วยให้สามารถขยายแอปพลิเคชันข้างต้นไปสู่ปัญหาการออกแบบที่ท้าทายด้วยเงื่อนไขวัสดุหลายเฟสได้ในท้ายที่สุด

จุฬาลงกรณ์มหาวิทยาลัย
CHULALONGKORN UNIVERSITY

สาขาวิชา	วิศวกรรมโยธา	ลายมือชื่อนิสิต .....
ปีการศึกษา	2565	ลายมือชื่อ อ.ที่ปรึกษาหลัก .....
		ลายมือชื่อ อ.ที่ปรึกษาร่วม .....

6278307021 : MAJOR CIVIL ENGINEERING

KEYWORD: Image-based mesh, Quadtree, Octree, Scaled Boundary Finite Element Method, Topology optimization, Bi-directional evolutionary structural optimization (BESO), Implicit time integration

Rut Su : AUTOMATIC IMAGE-BASED SBFE APPROACH FOR MULTIPHASE-MATERIALS TOPOLOGY OPTIMIZATION UNDER DYNAMIC LOADING. Advisor: Assoc. Prof. SAWEKCHAI TANGARAMVONG, Ph.D. Co-advisor: Prof. Chongmin Song, Ph.D.

This thesis presents the efficient topology optimization methods constructed within the state-of-the-art polygon scaled boundary finite element (SBFE) framework. The SBFE approach enables the discrete model construction of structures comprising of arbitrary curve geometry lying in 2D and/or 3D spaces. More explicitly, incorporated with quadtree (in 2D) and octree (3D) mesh refinements the automatic adaptive mesh scheme run within the polygon SBFE framework provides the cost-effective model generation allowing hanging nodes. These distinctive features present the developed SBFE approach well suiting as an underlying modeling framework for the topology design optimization of solids. The bi-directional evolutionary structural optimization (BESO) algorithm is integrated with the digital image-based processes, where a novel convolution-filtered technique refines the intensity between solid and void areas. This leads to the fast convergence of accurate optimal layout (distribution of materials) of the design structures. The applications of the combined BESO and SBFE method are illustrated though the optimal topology designs of structures under not only statically (time-independent) but also dynamically (time-dependent) applied load regimes. The latter applies a (single-step) high-order time integration technique that accurately approximates the dynamic responses of design structures. What is more is its nontrivial extension to the optimal topology design of structures under limited natural frequencies. Finally, the use of material interpolation techniques built on an unified BESO and SBFE framework allows the extension of the above applications to the challenging design problems with multi-phase material conditions.

จุฬาลงกรณ์มหาวิทยาลัย
CHULALONGKORN UNIVERSITY

Field of Study:	Civil Engineering	Student's Signature .....
Academic Year:	2022	Advisor's Signature .....
		Co-advisor's Signature .....

ACKNOWLEDGEMENTS

The process of undertaking research for a doctorate has been humbling, exposing the shallowness of my own knowledge in my professed field of expertise. It is really impossible to imagine dealing through this journey alone, and I would like to acknowledge everyone who has supported me along the path.

First and foremost, My deepest gratitude goes to Assoc. Prof. Dr. Sawekchai Tangaramvong, my primary supervisor, for his academic guidance and encouragement of my work throughout this process. Without his consistent advice and assistance, this Ph.D. program would not have been fulfilled. He provided excellent advice and insights, understanding when to challenge and when to support in the appropriate balance. His structural optimization approaches and ideas for designing compliant systems have proven to be extremely useful to me.

Next, I also want to express my sincere appreciation to my second supervisor, Professor Chongmin Song, for his invaluable supervision and support. He has always been patient and provided me with useful guidance.

Furthermore, I would like to thank other members of the Center of Excellence in Applied Mechanics and Structures. I frequently benefit from their recommendation, experience, and ideas. It has been an honor to spend time with such a talented group.

Last but not least, I want to express my gratitude to my family, particularly my parents, for their love, support, and patience. Their love and high expectations serve as a great source of encouragement and motivation for me to overcome the challenges of my research. Their ongoing support and encouragement have enabled me to successfully navigate the challenges of the Ph.D. program.

Rut Su

จุฬาลงกรณ์มหาวิทยาลัย
Chulalongkorn University

TABLE OF CONTENTS

Page

ABSTRACT (THAI) iii

ABSTRACT (ENGLISH) iv

ACKNOWLEDGEMENTS v

TABLE OF CONTENTS vi

CHAPTER 1 INTRODUCTION 1

1. Background and motivation 1

2. Aim and objectives of the research 6

3. Scope of research 6

4. Research Significance and Innovation 7

5. Layout of the dissertation 7

CHAPTER 2 LITERATURE REVIEW 9

1. Standard Finite Element Method 9

1.1 Introduction 9

1.2 Continuum Mechanics 9

1.2.1 State of stress at a point 9

1.2.2 State of strain and displacement at a point 10

1.2.3 Plane stress and plane strain problems 12

1.3 Potential Energy of Elastic Material 13

2. Scaled Boundary Finite Element Method. 16

2.1 Introduction 16

2.2 Concepts of Scaled Boundary Transformation of Geometry 17

จุฬาลงกรณ์มหาวิทยาลัย
CHULALONGKORN UNIVERSITY

2.3 Derivation of the SBFE equation using the virtual work principle.....24

2.4 Solving the SBFE equation by Eigenvalue Decomposition.....27

2.5 Solving the SBFE equation by Schur's decomposition 30

2.6 Features and Example Applications of SBFEM 34

3. Automatic Mesh Generation 36

3.1 Introduction.....36

3.2 Concept of Quadtree algorithm.....37

3.3 Concept of Octree algorithm.....40

3.4 Automatic Image-based mesh.....43

3.5 Quadtree/Octree Algorithm for SBFE Analysis 46

4. Topology Optimization 49

4.1 Introduction.....49

4.2 Topology Optimization Algorithms.....50

4.2.1 Homogenization 50

4.2.2 Solid Isotropic Microstructure with Penalization.....52

4.2.3 Evolutionary Structural Optimization 54

4.3 Bi–directional Evolutionary Structural optimization.....57

4.3.1 Early BESO method 57

4.3.2 Improvement in Computational Efficiency.....60

4.3.3 Sensitivity Filter Scheme.....60

4.3.4 Element Selection Process.....62

4.3.5 Stabilization Scheme of the Evolutionary Process.....63

4.3.6 Convergence Criterion.....64

4.3.7 Current BESO method.....65

จุฬาลงกรณ์มหาวิทยาลัย
CHULALONGKORN UNIVERSITY

4.4 BESO algorithm Procedure....68

5. Multimaterial Topology Optimization....70

5.1 Introduction....70

5.2 MMTO formulation....71

5.2.1 Problem statement....73

5.2.2 Sensitivity analysis....73

5.2.3 Filter Scheme....75

5.2.4 Variable updating....76

5.3 MMTO–BESO Procedure....76

CHAPTER 3 TOPOLOGY OPTIMIZATION FOR STATIC LOAD....79

1. Introduction....79

2. SMTO Research Procedure....81

2.1 The Quadtree/Octree Grid....81

2.2 Steps in Scaled Boundary Finite Element Analysis....82

2.3 Steps in the BESO-SBFEM algorithm....83

2.4 Benchmark problems for 2D uniform mesh SMTO with static load structures....87

2.4.1 SMTO of a short cantilever beam....87

2.4.2 SMTO of a Symmetric Beam....91

2.5 Benchmark problems for 3D uniform mesh SMTO with static load structures....94

2.5.1 SMTO of a 3D-MBB Cantilever Beam....94

3. Adaptive mesh refinement....97

3.1 Benchmark problems for 2D AM-SMTO with static load structures....99

3.1.1 AM-SMTO of a short cantilever beam....99

3.1.2 AM-SMTO of a symmetric beam....101

จุฬาลงกรณ์มหาวิทยาลัย
CHULALONGKORN UNIVERSITY

3.1.3 AM-SMTO of a Rectangular beam with two holes....103
3.1.4 AM-SMTO of a Circular domain with single hole 105
3.2 Benchmark problems for 3D AM-SMTO with static load structures....108
3.2.1 AM-SMTO of a 3D-MBB cantilever beam....108
3.2.2 AM-SMTO of a 3D Cantilever beam with uniform loaded 110
3.2.3 AM-SMTO of a 3D L-shaped structure 114
3.2.4 AM-SMTO of a 3D Strut and tie structure....117
4. MMTO Application and expected results 119
4.1 2D MMTO cantilever beam with static load structures 119
4.2 2D MMTO symmetric beam with static load structures....124
4.3 2D MMTO circular domain with static load structures 128
4.4 3D MMTO MBB cantilever beam with static load structures 131
4.5 3D MMTO cantilever beam with uniformly static load structures 140
4.6 3D L-shaped with static load structures....146
CHAPTER 4 TOPOLOGY OPTIMIZATION FOR DYNAMIC LOAD 152
1. Introduction. 152
2. Dynamic and Vibration Analysis....153
2.1 Equation of Motion 153
2.2 Time History Analysis Using the Newmark Method....155
2.3 High Order implicit time integration Method 157
2.3.1 Development of time integration method....158
2.3.2 Padé expansion of the matrix exponential function 160
2.3.3 Time-stepping scheme....161
2.4 Natural Frequencies and Mode Shapes....163

จุฬาลงกรณ์มหาวิทยาลัย
Chulalongkorn University

3. Dynamic Response Topology Optimization 165

3.1 Topology Optimization in the Time Domain.....166

3.1.1 Problem statement 167

3.1.2 The ESLSO Procedure 168

3.1.3 Numerical examples and expected results.....171

3.2 Topology Optimization in the Frequency Domain 183

3.2.1 Problem statement 183

3.2.2 MMTO and Compliance sensitivities.....184

3.2.3 Computational procedure 186

3.2.4 Numerical example and expected results 188

CHAPTER 5 CONCLUSIONS 195

Appendix A 198

Appendix B 202

REFERENCES 204

VITA 216

จุฬาลงกรณ์มหาวิทยาลัย
CHULALONGKORN UNIVERSITY

CHAPTER 1 INTRODUCTION

1. Background and motivation

A structure is defined in structural engineering as a collection of parts or materials designed to support a series of motions, forces, or energy. Furthermore, structural design is the process of selecting materials and parts, as well as their sizes and configurations, to provide adequate stability, strength, and rigidity for the structure. A good design achieves the numerous performance goals imposed by all stakeholders while conserving resources. It is necessary in structural design to investigate the most reliable and admissible solution to an engineering challenge. This is due to both commercial considerations and a government and social push for energy-efficient and low-carbon architecture. Due to limited material supplies, engineers are forced to design lightweight, low-cost, high-performance buildings.

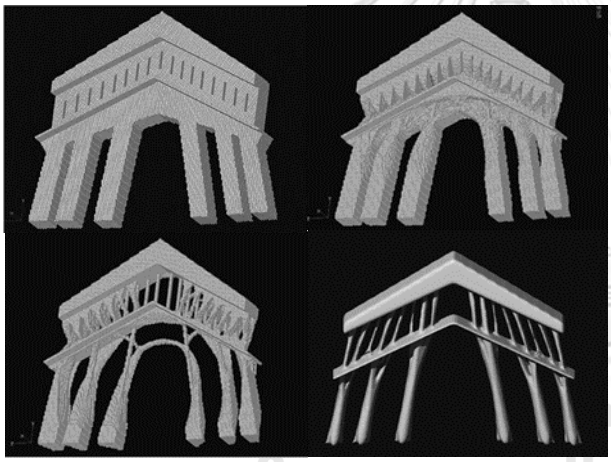

(a)

(b)

จุฬาลงกรณ์มหาวิทยาลัย
Chulalongkorn University

Figure 1.1 Passion Facade of Sagrada Familia church ((Burry, Felicetti, Tang, Burry, & Xie, 2005)): (a) Evolution of passion facade of Sagrada Familia church and (b) Real construction of the building.

Prior research into structural optimization dates back more than a century to Michell's (1904) theoretical studies in Melbourne, where the optimality criteria of the least-weight truss layout were derived. Historically, structural design was achieved through a series of trials and errors that gradually refined the design. However, early studies were primarily limited to the size and shape optimization of predetermined topologies, and topology optimization is a well-established method for structural optimization. Topology optimization in continuum mechanics can be expressed as a

discrete problem or as a binary design setting in which the structure only consists of solids or voids. The binary design for structural compliance, on the other hand, is ill-posed, as there exists a nonconvergent sequence of admissible designs with continuously refined geometrical details (Su, Van, & Tangaramvong[1], 2021). Given the emergence of various topology optimization methods, mathematical formulations have undergone continuous development. Bi-directional evolutionary structural optimization (BESO), a well-known technique for topology optimization proposed by Querin, Steven, and Xie (1998), uses intermediate density to overcome the binary design. When necessary, this method allows for the restoration of deleted items. Figure 1.1 depicts the use of the ESO/BESO methods in the construction of real buildings.

Topology optimization has been used to design single-phase and multiphase material structures. The first implementation of the BESO method in multiphase material distribution problems was published by Xiaodong Huang and Xie (2009). When compared to designing single-phase materials, designing multiphase structures can lead to a more effective and less expensive combined functional structure (see Figure 1.2). Furthermore, topology optimization design of multiphase materials has attracted the attention of researchers.

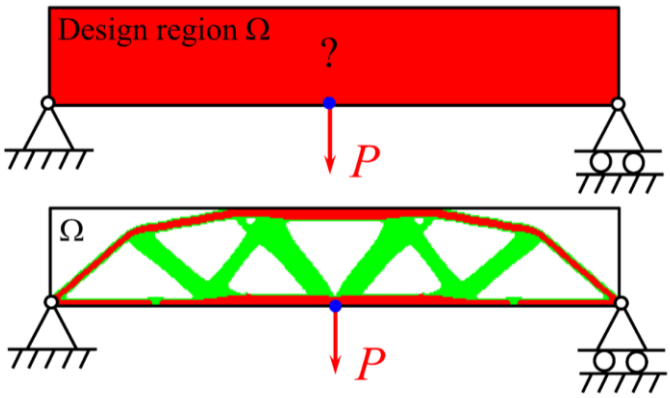

Figure 1.2 Combination design of three-material structures (two solid materials and a void).

Topology optimization can be used to determine the initial arrangement of a material or the reinforcing distribution of a structure. However, dynamic loads influence a real structure; thus, the structure should be optimized with dynamic characteristics. Dynamic topology optimization research has focused on the frequency and time domains, with frequency-domain problems

aiming to reduce vibration and noise and time-domain problems aiming to reduce weight or maximize structure stiffness.

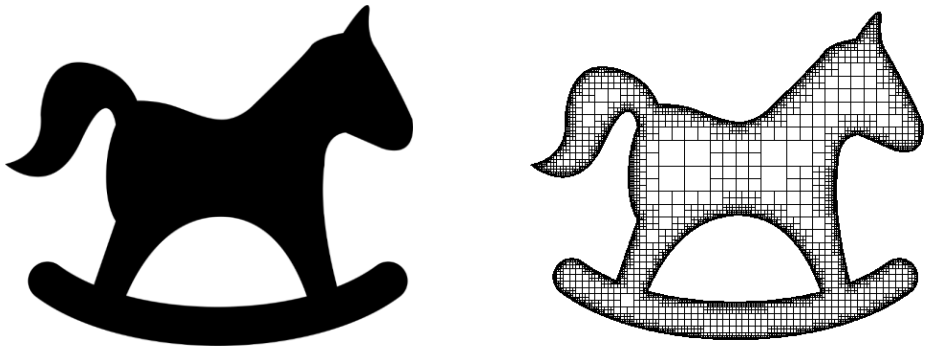

Figure 1.3 The rocking horse picture is decomposed by image-based Quadtree algorithm.

Tackling the structural optimization problem in the general concept of topology optimization implies configuring the design variables for the best performance, and the design variables of a structural optimization problem can be either continuous or discrete. The finite element mesh for the initial domain is discretized into subdomains called elements as a prerequisite for finite element analysis, so that each point in the domain is included within one of the elements. However, the primary disadvantage of this is that it takes a long time and is prone to errors when done manually. As a result, this dissertation encourages and employs automatic mesh generation. In structural continuum mechanics, several mesh generation techniques (for example, the contour-line method, Delaunay triangulation method, and advancing-front technique (AFT)) can be used. Yerry and Shephard (1983) proposed a well-known mesh generation technique called the Quadtree/Octree decomposition algorithm, which allows domain partition to be achieved automatically in accordance with the complexity of the problem. These hierarchical meshes have recently found application in image-based implementation, as illustrated in Figure 1.3, which shows the application of image-based Quadtree decomposition in finite element analysis.

จุฬาลงกรณ์มหาวิทยาลัย
Chulalongkorn University

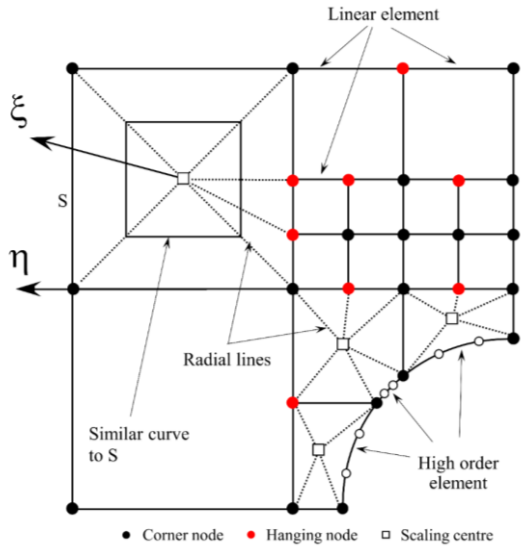

Figure 1.4 A quadtree mesh of S-elements.

As previously stated, the Quadtree/Octree decomposition algorithm appears to be an excellent method to use in conjunction with the finite element method. The primary limitation of applying standard finite elements to the Quadtree/Octree algorithm is dealing with discontinuities in displacement fields, i.e., hanging nodes. To overcome this drawback, the scaled boundary finite element (SBFE) is an appropriate method for numerical analysis when applied to the Quadtree/Octree algorithm (Man, Song, Natarajan, Ooi, & Birk, 2014). Figure 1.4 demonstrates an SBFE mesh produced by the Quadtree algorithm. An S-element is a type of element used in finite element analysis (FEA) to represent a region or volume in a finite element model. One of the key benefits of using S-elements is that the boundary of an S-element can be divided into an arbitrary number of smaller line elements, which allows for greater flexibility and accuracy in the model. When using S-elements, a common edge between cells at different levels (i.e., cells that are part of different levels of mesh refinement) is represented by multiple line elements. This helps to ensure that displacement compatibility is automatically satisfied, which means that the displacement of nodes on the common edge between cells at different levels is consistent and does not introduce any errors or discontinuities in the model. Additionally, using S-elements helps to eliminate the need for hanging nodes, which are nodes that are not connected to any other elements and can cause problems in the FEA model. Finally, a boundary-trimmed cell (i.e., a cell that has one or more of its edges removed) can also be directly modeled as an S-element, which allows for more accurate and efficient representation of the model geometry.

จุฬาลงกรณ์มหาวิทยาลัย
CHULALONGKORN UNIVERSITY

The preceding remarks serve as motivation for the work presented here. In essence, this dissertation characterizes topology optimization using an automatic image-based mesh generation method using Quadtree/Octree decomposition. To obtain optimal designs for SBFE analysis, we used the multiphase materials topology optimization concept and the BESO algorithm. With the privileges of image-based application, automated image compression techniques are combined with the scaled boundary finite element method (SBFEM) to produce analysis-ready adaptive meshes at each iterative process. Various case problems were solved for this purpose, and some were compared to solutions from the literature.

จุฬาลงกรณ์มหาวิทยาลัย
CHULALONGKORN UNIVERSITY

2. Aim and objectives of the research

The goal of this dissertation is to extend a practical and trustworthy methodology for topology optimization of continuum structures. The limitations of existing topology optimization techniques in a conventional finite element method are not present in this algorithm. Adopting such an algorithm has the potential to combine another finite element method and the design of structural applications with the best possible configuration. This goal was accomplished by meeting the following objectives.

(1) Investigating the topology optimization techniques, namely, bi-directional evolutionary structural optimization (BESO), adopted using the SBFEM.

(2) Combining the automatic image-based mesh generation (namely, the Quadtree/Octree algorithm) with convolution-based filtering technique to perform topology optimization for structures with non-discrete elements.

(3) Adopting the concept of multiphase materials using the BESO algorithm for designing nonhomogeneous materials in optimal solutions.

(4) Performing topology optimization by considering dynamic load based on equivalent static load response and natural frequency response.

3. Scope of research

จุฬาลงกรณ์มหาวิทยาลัย
CHULALONGKORN UNIVERSITY

(1) The material properties of the design domain are considered as linearly elastic isotropic materials.

(2) Discretization of all initial design problems is automatically generated by Quadtree/Octree decomposition.

(3) Stress analyses are performed based on the SBFEM.

(4) Performing topology optimization using stress analysis which the problems are considered as a 2D/3D problems model.

(5) Topology optimization procedures are based on the BESO algorithm.

(6) Time history equivalent static load is computed by high-order implicit time integration scheme based on Padé expansions.

4. Research Significance and Innovation

The BESO technique, which was developed relatively recently, has proven to be highly effective in solving topology optimization problems in various structural engineering applications. Examples of these applications include minimizing structural volume subject to displacement or compliance constraints (X Huang & Xie, 2008; X. Huang & Y. Xie, 2010), optimizing the stiffness of structures made of multiple materials (Xiaodong Huang & Xie, 2009), designing periodic structures (Huang and Xie, 2008), optimizing the structural frequencies (X Huang, Zuo, & Xie, 2010), optimizing the topology of energy absorption structures (X Huang & Xie, 2007b), and addressing geometrical and material nonlinearity issues (X Huang & Xie, 2007a).

Topology optimization has traditionally been constructed as a material distribution problem in a finite element-based framework. The optimal topology optimization solutions represented by finite elements typically perform in a standard finite element method. This research is significant because it investigates a scaled boundary finite element method (SBFEM) for topology optimization of continuum structures, resulting in solutions that require the least amount of post-processing before manufacturing. The proposed method is computationally efficient and produces better computational accuracy, a more optimal solution, and significantly less computation time than traditional element-based optimization methods. It is also demonstrated, using recognized color-encoding regions, that the proposed method can be applied to multiple materials and nonuniform mesh problems. Therefore, this method helps engineers reduce the computational time and design cost of products.

To obtain topology solutions with high representation, this research proposes a novel evolutionary structural optimization method that combines SBFEM with adaptive polygon element distribution and uses automatic image-based mesh generation. Furthermore, adaptive mesh refinement is used to achieve the best solution in topology optimization of multiphase-material structures. Finally, the topological designs of continuum structures for dynamic responses are considered in the proposed concepts.

5. Layout of the dissertation

This dissertation totally comprises five chapters.

Chapter 1 of this dissertation presents the introduction, motivation, advantages, and application fields of compliant mechanisms. Furthermore, this dissertation contends to the research the objectives and scopes of this study. Following that, the research significance and innovation of this study are discussed. Finally, the dissertation overview is proposed.

Chapter 2 of this dissertation presents a review of the SBFEM, i.e., the concepts of SBFEM, derivation, solution procedures, and features of this method. The chapter then briefly introduces the idea of automatic mesh generation, specifically the Quadtree/Octree technique. Furthermore, previous and current research on designing compliant mechanisms using kinematic-based approaches as well as more recent structural performance tuning approaches such as homogenization, solid isotropic material with penalization (SIMP), the evolutionary structural optimization (ESO) method, and the BESO methods is reviewed. Finally, a framework for extending multiphase materials topology optimization (MMTO) is described.

Chapter 3 of this dissertation presents examples of topology optimization problems based on static load responses for the standard finite element method and SBFEM. Both approaches can be directly compared using different techniques, and this chapter focuses on uniform mesh in the initial design domain. Following that, several benchmark examples of two-dimensional (2D) and three-dimensional (3D) problems are completely solved using the finite element method (FEM) and their solutions are compared to those found in the literature. The image compression convolution filter supports automated adaptive analysis-ready meshes. Finally, MMTO in conjunction with SBFEM is proposed.

จุฬาลงกรณ์มหาวิทยาลัย
Chulalongkorn University

Chapter 4 of this dissertation mainly focuses the concept of topology optimization based on dynamic responses, and some literature research on dynamic topology optimization based on the frequency and time domains are briefly discussed. Subsequently, the problem statements with optimization procedures are explained. Finally, several benchmark examples of 2D problem models are presented.

Chapter 5 of this dissertation precisely discusses the concluding remarks. Some of the further researches are reported in this chapter. Finally, the post-processing topological results are displayed.

CHAPTER 2 LITERATURE REVIEW

1. Standard Finite Element Method

1.1 Introduction

The FEM is a numerical approach used in solid mechanics to solve engineering and mathematical physics problems. It is one of the most well-known and original numerical methods used in the field, and there are countless publications and articles on it. This section briefly explains the theory and concept of finite element formulation based on Timoshenko and Goodier (1971). The concept of FEM gives the approximate values of the unknown variables at points of the discrete model. Instead of analytically solving partial differential equations for the whole domain, FEM discretizes a problem into smaller domain so-called elements. Subsequently, the characteristic equations representing these elements are combined to form a global system of discrete equations that encompasses the entire domain. Recent development in computer science has boosted this method to become more efficient because of its total dependency.

1.2 Continuum Mechanics

1.2.1 State of stress at a point

Since stress is the primary variable in solid mechanics, the state of stress at a particular point can be represented by the stress tensor, as shown in Eq. (1.1a). This stress tensor can be written in a vector form, the Voigt notation, Eq. (1.2a), where σ and τ are normal stress and shear stress, respectively.

$$\sigma = \begin{bmatrix} \sigma_{xx} & \tau_{xy} & \tau_{xz} \\ \tau_{xy} & \sigma_{yy} & \tau_{yz} \\ \tau_{xz} & \tau_{yz} & \sigma_{zz} \end{bmatrix} \tag{1.1a}$$

$$\sigma = \{\sigma_{xx} \quad \sigma_{yy} \quad \sigma_{zz} \quad \tau_{xy} \quad \tau_{yz} \quad \tau_{xz}\}^{\mathrm{T}} \tag{1.2a}$$

It is necessary that the stress distribution in a solid be compatible with the global equilibrium of the body when a combination of loads is applied to it. Furthermore, the equilibrium condition must be satisfied throughout the entire system, and when an infinitesimal element from this body is considered and its equations are solved, the outcome is the equilibrium equations of elasticity denoted by Eq. (1.3a).

$$\frac{\partial \sigma_{xx}}{\partial x} + \frac{\partial \tau_{xy}}{\partial y} + \frac{\partial \tau_{xz}}{\partial z} + V_x = 0$$
$$\frac{\partial \tau_{xy}}{\partial x} + \frac{\partial \sigma_{yy}}{\partial y} + \frac{\partial \tau_{yz}}{\partial z} + V_y = 0 \quad (1.3a)$$
$$\frac{\partial \tau_{xz}}{\partial x} + \frac{\partial \tau_{yz}}{\partial y} + \frac{\partial \sigma_{zz}}{\partial z} + V_z = 0$$

Using the gradient function (∇) with the stress tensor and body force vector, the system of equilibrium equation (Eq. (1.3a)) is further reduced to

$$\nabla\sigma + \mathrm{V} = 0 \quad (1.4a)$$

1.2.2 State of strain and displacement at a point

In the small deformation theory, a normal strain (ε) is the change in the length of a line segment between two points divided by the initial length of the line segment. Meanwhile, a shearing strain (γ) is the angular change between two-line segments that were initially perpendicular. From this point, the relationship between strains and displacement can be stated by Eq. (1.5a).

$$\varepsilon_{xx} = \frac{\partial u}{\partial x}, \ \gamma_{xy} = \frac{\partial u}{\partial y} + \frac{\partial v}{\partial x}$$
$$\varepsilon_{yy} = \frac{\partial v}{\partial y}, \ \gamma_{yz} = \frac{\partial v}{\partial z} + \frac{\partial w}{\partial y} \quad (1.5a)$$
$$\varepsilon_{zz} = \frac{\partial w}{\partial y}, \ \gamma_{yz} = \frac{\partial w}{\partial x} + \frac{\partial u}{\partial z}$$

จุฬาลงกรณ์มหาวิทยาลัย
Chulalongkorn University

Here, u, v, and w are the respective displacements in the x, y, and z directions. Therefore, the strain tensor is symmetric.

$$\gamma_{xy} = \gamma_{yx}$$
$$\gamma_{yz} = \gamma_{zy} \quad (1.6a)$$
$$\gamma_{zx} = \gamma_{xz}$$

In solid continuum mechanics, the equations (1.5a) are referred to as the cartesian strain–displacement relationships because of the manner in which strain and displacement are related. It is possible to write them in the matrix form as follows.

$$\varepsilon = \mathbf{Bu} \quad (1.7a)$$

Here, $\mathbf{B}$ and $\mathbf{u}$ are the strain–displacement relationships and displacement vector, respectively

$$\mathbf{B}=\begin{bmatrix} \frac{\partial}{\partial x} & 0 & 0 & \frac{\partial}{\partial y} & 0 & \frac{\partial}{\partial z} \\ 0 & \frac{\partial}{\partial y} & 0 & \frac{\partial}{\partial x} & \frac{\partial}{\partial z} & 0 \\ 0 & 0 & \frac{\partial}{\partial z} & 0 & \frac{\partial}{\partial y} & \frac{\partial}{\partial x} \end{bmatrix}^{\mathbf{T}} \tag{1.8a}$$

$$\mathbf{u}=\begin{Bmatrix} u \\ v \\ w \end{Bmatrix} \tag{1.9a}$$

Since a tensor describes the state of stress at a point, the same happens with the strain in Eq. (1.10a) and in vector form, Eq. (1.11a).

$$\varepsilon=\begin{bmatrix} \varepsilon_{xx} & \gamma_{xy} & \gamma_{xz} \\ \gamma_{xy} & \varepsilon_{yy} & \gamma_{yz} \\ \gamma_{xz} & \gamma_{yz} & \varepsilon_{zz} \end{bmatrix} \tag{1.10a}$$

$$\varepsilon=\{\varepsilon_{xx} \quad \varepsilon_{yy} \quad \varepsilon_{zz} \quad \gamma_{xy} \quad \gamma_{yz} \quad \gamma_{xz}\}^{\mathrm{T}} \tag{1.11a}$$

The majority of the material used in the research was considered isotropic and homogeneous in the standard finite element model. The elastic properties are defined by the modulus of elasticity, E, and Poisson's ratio, v. Hooke's laws describe the stress-strain relationship as follows.

$$\sigma=\mathbf{D}\varepsilon \tag{1.12a}$$

Here, $\mathbf{D}$ is the material stiffness, which is an asymmetric nonsingular matrix, yielding

จุฬาลงกรณ์มหาวิทยาลัย
CHULALONGKORN UNIVERSITY

$$\varepsilon=\mathbf{C}\sigma \tag{1.13a}$$

where $\mathbf{D}=\mathbf{C}^{-1}$ is a symmetric matrix of material compliance, given by

$$\mathbf{C}=\frac{1}{E}\begin{bmatrix} 1 & -v & -v & 0 & 0 & 0 \\ -v & 1 & -v & 0 & 0 & 0 \\ -v & -v & 1 & 0 & 0 & 0 \\ 0 & 0 & 0 & 2(1+v) & 0 & 0 \\ 0 & 0 & 0 & 0 & 2(1+v) & 0 \\ 0 & 0 & 0 & 0 & 0 & 2(1+v) \end{bmatrix} \tag{1.14a}$$

1.2.3 Plane stress and plane strain problems

When analyzing 3D elastostatic problems in which a body is subjected to a force applied in a specific plane and its body has a thickness that is smaller than the other dimensions, we can refer to the problem as a plane stress problem. Figure 2.1 illustrates the plane stress problem with applied force in the xy plane and the thickness is totally smaller than the other dimensions. In this particular case, we have

$$\sigma_{zz} = \tau_{xz} = \tau_{zy} = 0 \tag{1.15a}$$

resulting in new stress and strain vectors.

$$\sigma = \{\sigma_{xx} \quad \sigma_{yy} \quad \tau_{xy}\}^{\mathrm{T}} \text{and } \varepsilon = \{\varepsilon_{xx} \quad \varepsilon_{yy} \quad \gamma_{xy}\}^{\mathrm{T}} \tag{1.16a}$$

The material stiffness matrix $\mathbf{D}$ becomes

$$\mathbf{D} = \frac{E}{1-v^2}\begin{bmatrix} 1 & v & 0 \\ v & 1 & 0 \\ 0 & 0 & \dfrac{(1-v)}{2} \end{bmatrix} \tag{1.17a}$$

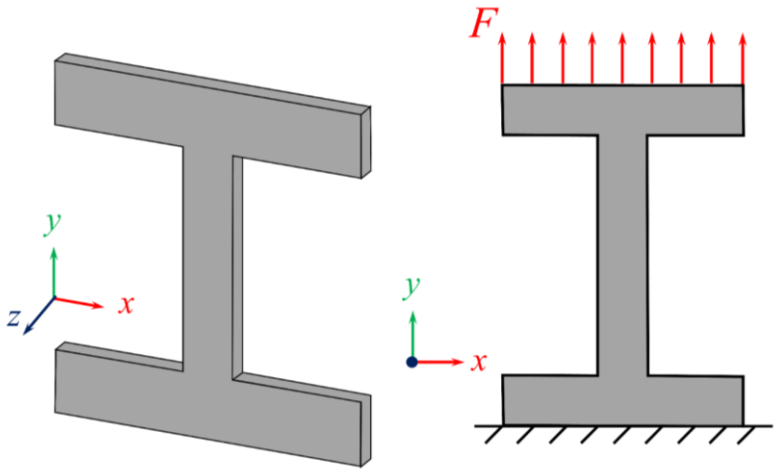

Figure 2.1 Plane stress.

In contrast, we have a plane strain problem when the thickness is no longer smaller than the other dimensions or the object has one of its dimensions larger than the others and the cross section does not vary in this direction, as shown in Figure 2.2. With the applied loads in the $x-y$ plane, the following equations can be reduced as follows:

$$w = 0 \text{ and } \frac{\partial}{\partial z} = 0 \tag{1.18a}$$

resulting in

$$\varepsilon_{xx} = \varepsilon_{yy} = \gamma_{xy} = 0 \tag{1.19a}$$

Subsequently, the material stiffness matrix $\mathbf{D}$ is reduced into

$$\mathbf{D} = \begin{bmatrix} \lambda + 2G & \lambda & 0 \\ \lambda & \lambda + 2G & 0 \\ 0 & 0 & G \end{bmatrix} \tag{1.20a}$$

where λ is the Lame coefficient and G is the modulus of rigidity. These constants are related to E and v by

$$G = \frac{E}{2(1+v)} \text{ and } \lambda = \frac{vE}{(1+v)(1-2v)} \tag{1.21a}$$

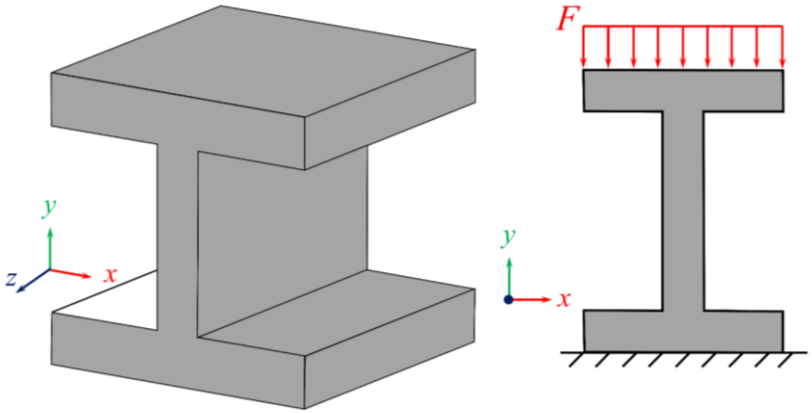

จุฬาลงกรณ์มหาวิทยาลัย
CHULALONGKORN UNIVERSITY

Figure 2.2 Plane strain.

1.3 Potential Energy of Elastic Material

For solid continuum mechanics, there are several categories of elements in the conventional FEM that can be used to perform the analysis. Each type of element has aspects that characterize its behavior: degrees of freedom, number of nodes, formulation, and integration. The rectangular element is one of the most commonly encountered types of elements. These elements are useful for modeling regular geometries because they are simple to handle with many problems. A four-term polynomial expression can be clearly defined in Appendix A as there are four nodes containing two degrees of freedom at each node.

Using the principle of minimum potential energy, the total potential energy can be written as

$$\Pi_p = U + W \tag{1.1b}$$

where the internal strain energy, U, is given by

$$U = \frac{1}{2}\int_V \{\varepsilon\}^T\{\sigma\}\,dV = \frac{1}{2}\int_V \{\varepsilon\}^T[D]\{\varepsilon\}\,dV \tag{1.2b}$$

The corresponding external work done on concentrated load is written as

$$W = -\{u\}^T\{P\} \tag{1.3b}$$

Here, $\{u\}$ represents the nodal displacement vector and $\{P\}$ represents the external forces.

Substituting internal term (Eq. (1.2b)) and external work (Eq. (1.3b)) into Eq. (1.1b), the total potential energy becomes

$$\Pi_p = \frac{1}{2}\int_V \{\varepsilon\}^T[D]\{\varepsilon\}\,dV - \{u\}^T\{P\} \tag{1.4b}$$

By writing Eq. (1.4b) in terms of displacement field, we obtain

$$\Pi_p = \frac{1}{2}\int_V \{u\}^T[B]^T[D][B]\{u\}\,dV - \{u\}^T\{P\} \tag{1.5b}$$

where $[B]$ is strain–displacement relationship matrix. Taking the derivative of Eq. (1.5b) with respect to nodal displacement results in

$$\frac{\partial \Pi_p}{\partial\{u\}} = \left[\int_V [B]^T[D][B]\,dV\right]\{u\} - \{P\} = 0 \tag{1.6b}$$

จุฬาลงกรณ์มหาวิทยาลัย
Chulalongkorn University

Rewriting Eq. (1.6b) as

$$\underbrace{\left[\int_V [B]^T[D][B]\,dV\right]}_{\mathbf{K}}\{u\} = \{P\} \tag{1.7b}$$

For a constant thickness, t, Eq. (1.7b) can be further written as

$$\mathbf{K}_e = \int_V [B]^T[D][B]\,dV = t\int_{\Omega_e} [B]^T[D][B]\,d\Omega \tag{1.8b}$$

In the isoparametric rectangular element, the elemental stiffness matrix is expanded as

$$\mathbf{K}_e = t \int_{\Omega_e} B^T(\xi,\eta)[D]B(\xi,\eta)\, d\Omega = t \int_{-1}^{1}\int_{-1}^{1} B^T(\xi,\eta)[D]B(\xi,\eta)\,|J| d\xi d\eta \qquad (1.9b)$$

where $B(\xi,\eta)$ is the derivative of shape function precisely described in Appendix A. $[D]$ is the material constitutive matrix, see Eq (1.17a) for plane stress and Eq. (1.20a) for plane strain.

The numerical integration by the summation of the Gauss points and weights achieved using the Gaussian Quadrature retains the commutativity of the integrals in the expected manner. The expression of the elemental stiffness matrix is evaluated using the N Gauss points for integration as

$$\mathbf{K}_e = \sum_{j=1}^{N}\sum_{k=1}^{N} W_j W_k\, B^T(\xi,\eta)[D]B(\xi,\eta)|J| \qquad (1.10b)$$

The global stiffness matrix (Figure 2.3) for all number of elements, N_{el}, is expressed as

$$\mathbf{K} = \sum_{e=1}^{N_{el}} \mathbf{K}_e \qquad (1.11b)$$

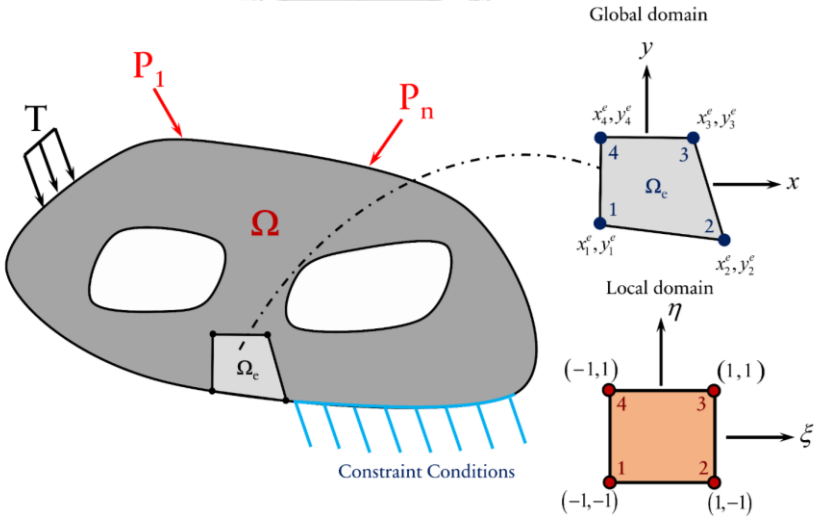

Figure 2.3 Schematic for continuum solid mechanics in global and local coordinates of a FE domain.

2. Scaled Boundary Finite Element Method.

2.1 Introduction

Many engineering and scientific issues are expressed mathematically in expressions of field variables such as forces and displacements. Mathematical models include governing differential equations that represent physical rules (e.g., equilibrium and compatibility in stress analysis), material constitutive models, and problem domain boundary conditions. Analytical solutions to the mathematical model are frequently used in traditional engineering analysis approaches. Analytical solutions are represented mathematically and may be assessed at any location of interest. Analytical solutions, on the other hand, are not accessible for complicated issues. To apply classical analytic methods to many engineering issues, significant simplifications must be made, which frequently results in overly cautious designs.

To solve complicated engineering challenges, numerical modeling approaches have been created. The mathematical model is solved by a numerical approach in numerical modeling of a field issue, and a common feature of the numerical methods is the use of mesh discretization to split a complicated problem domain into a set of discrete parts. C. Song and Wolf (1997), proposed one of the most prominent numerical approaches for the dynamic analysis of unbounded domains, known as the SBFEM, in which the rational boundary condition is defined at infinity (Bazyar & Song, 2008; Chen, Birk, & Song, 2015; C. Li, Man, Song, & Gao, 2013). The SBFEM employs a semi-analytical technique to generate an approximation solution in a subdomain, and only the subdomain border is discretized; the solution in the opposite direction is derived analytically. This differs from typical FEM, which needs the interpolation functions across the subdomain/element to be chosen a priori (Chongmin Song, 2018).

จุฬาลงกรณ์มหาวิทยาลัย
Chulalongkorn University

The next section will describe how the SBFEM method is derived using the concept of virtual work. The partial differential equations that govern the problem domain will be converted into ordinary differential equations with a radial coordinate serving as the independent variable. The finite element technique can be used to reduce a problem involving multiple dimensions (such as a three-dimensional model) to a problem in one spatial dimension by applying the technique

along the directions parallel to the boundary of the model. This results in a simplified representation of the problem, which can make it easier to analyze and solve. In the context of finite element analysis, this is often done by applying the technique along the circumferential direction, which refers to the direction around the circumference or perimeter of the model. By doing this, it is possible to represent the problem in a more straightforward and computationally efficient manner, while still capturing the essential features and behavior of the system being analyzed. In subsequent sections, the text will present several examples of how the SBFEM can be used for stress analysis and will discuss its various characteristics.

2.2 Concepts of Scaled Boundary Transformation of Geometry

C. M. Song and Wolf (2000) precisely outline the SBFEM idea, which aims to conduct geometry transformation. Figure 2.4a shows a two-dimensional linear elastic confined media with a comparable section is utilized to build the SBFEM, and the complete boundary must be visible when seen from a zone within the medium where the so-called scaling center, O, has been chosen. In the figure, the dashed lines represent the direct lines of sight from the scaling center (a reference point used to scale the model) to the corners of the domain (the area being analyzed). It is important to note that the border of the domain does not have to be convex (curved outward like the exterior of a circle or sphere) and the number of edges is not limited. This means that the domain can have any shape and can be divided into as many or as few edges as necessary. To achieve this flexibility, the overall domain can be subdivided into smaller subdomains (also known as S-domains), which can be treated as "super-elements" in their own right. This allows for more precise representation of the domain and can help to ensure that the model accurately reflects the behavior and characteristics of the system being analyzed. The displacements and tractions on S_u and S_t are applied to the medium's doubly curved border, S. Figure 2.4b, on the other hand, depicts an example of a domain that does not match the scaling condition. Three locations (A, B, and C) on the border, S, cannot be found in direct vision at the same time. This sort of domain must be divided into smaller ones that meet the scaling criteria for usage with the SBFEM.

จุฬาลงกรณ์มหาวิทยาลัย
Chulalongkorn University

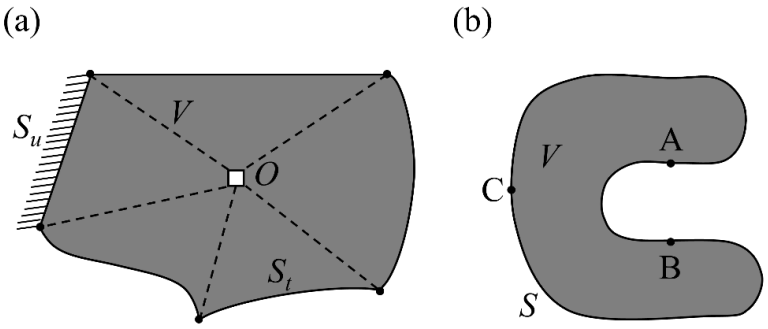

Figure 2.4 Illustration of the scaling requirement: (a) A bounded domain satisfies the scaling requirement. (b) A bounded domain does not satisfy the scaling requirement.

For a 3D case, a typical finite element with the surface, S^e, (superscript e for element) is illustrated in Figure 2.5, and two local curvilinear coordinates $(\eta, \zeta,)$ in the circumferential directions of the surface are defined (green line). This concept is reminiscent of the procedure applied in an isoparametric surface finite element. From Figure 2.5 and Figure 2.6, points from the scaling center, O, to a point on the boundary called the dimensionless radial coordinate, ξ, (red line), where $\xi = 0$ in O and $\xi = 1$ on the boundary, are selected. Connecting the edge of the surface finite element by straight lines (dash line) to the scaling center, O, forms the side-face, A^e, which regards to either $\eta = \pm 1$ or $\zeta = \pm 1$. The side-face, A^e, and the surface, S^e, interpret a pyramid with vertex, O, and volume, V^e.

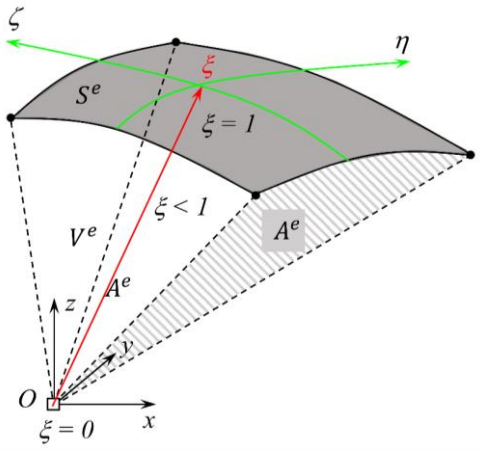

Figure 2.5 Transformation of the geometry surface finite element forming pyramid with volume based on scaled boundary finite element method

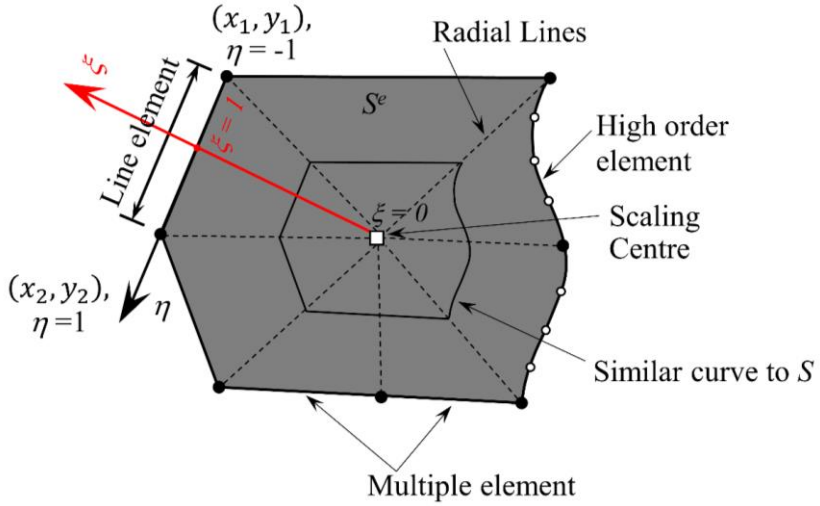

Figure 2.6 Schematic of scaled boundary polygonal element.

The standard 2D isoparametric with two-node element is addressed in Figure 2.7. The coordinates of a specific point along the line element are known as x, y. Two nodes with the coordinates (x_1, y_1) and (x_2, y_2) are arranged as

$$\{x\} = [x_1 \quad x_2]^T \tag{2.1a}$$

$$\{y\} = [y_1 \quad y_2]^T \tag{2.2a}$$

From Figure 2.7, the parent element in the natural coordinate, η, has a length of 2 units (ξ has been used for the radial coordinate). The linear interpolation of the x–coordinate on the two-node line element is expressed as

$$x(\eta) = a_0 + a_1 \eta \tag{2.3a}$$

Substitute natural coordinate, η, with interpolation constants, a_0 and a_1, are determined by formulating Eq. (2.3a) at the two nodes, resulting in

$$x_1 = x(-1) = a_0 + a_1 \times (-1) \tag{2.4a}$$

$$x_1 = x(+1) = a_0 + a_1 \times (+1) \tag{2.5a}$$

The solution of Eqs. (2.4a) and (2.5a) are expressed as

$$a_0 = \frac{1}{2}(x_1 + x_2) \tag{2.6a}$$

$$a_1 = \frac{1}{2}(x_2 - x_1) \tag{2.7a}$$

From Eqs. (2.6a) and (2.7a), the Eq. (2.3a) can be written as

จุฬาลงกรณ์มหาวิทยาลัย
Chulalongkorn University

$$x(\eta) = \frac{1}{2}(x_1 + x_2) + \frac{1}{2}(x_2 - x_1)\eta = \frac{1}{2}(1-\eta)x_1 + \frac{1}{2}(1+\eta)x_2 \quad (2.8a)$$

where the shape function, N, for standard isoparametric with two-node line element is expressed in matrix form as

$$[N(\eta)] = [N_1(\eta) \quad N_2(\eta)] = \left[\frac{1}{2}(1-\eta) \quad \frac{1}{2}(1+\eta)\right] \quad (2.9a)$$

The interpolation x in Eq. (2.8a) and, similarly, the interpolation of coordinate y are described as

$$x(\eta) = [N]\{x\} = \frac{1}{2}(1-\eta)x_1 + \frac{1}{2}(1+\eta)x_2 = \bar{x} + \frac{1}{2}\Delta_x\eta \quad (2.10a)$$

$$y(\eta) = [N]\{y\} = \frac{1}{2}(1-\eta)y_1 + \frac{1}{2}(1+\eta)y_2 = \bar{y} + \frac{1}{2}\Delta_y\eta \quad (2.11a)$$

with the abbreviations

$$\Delta_x = x_2 - x_1 \quad (2.12a)$$

$$\Delta_y = y_2 - y_1 \quad (2.13a)$$

and

$$\bar{x} = \frac{1}{2}(x_1 + x_2) \quad (2.14a)$$

$$\bar{y} = \frac{1}{2}(y_1 + y_2) \quad (2.15a)$$

For further use, differentiating Eqs. (2.10a) and (2.11a) results in

$$x(\eta)_{,\eta} = \frac{1}{2}\Delta_x \quad (2.16a)$$

$$y(\eta)_{,\eta} = \frac{1}{2}\Delta_y \quad (2.17a)$$

จุฬาลงกรณ์มหาวิทยาลัย
CHULALONGKORN UNIVERSITY

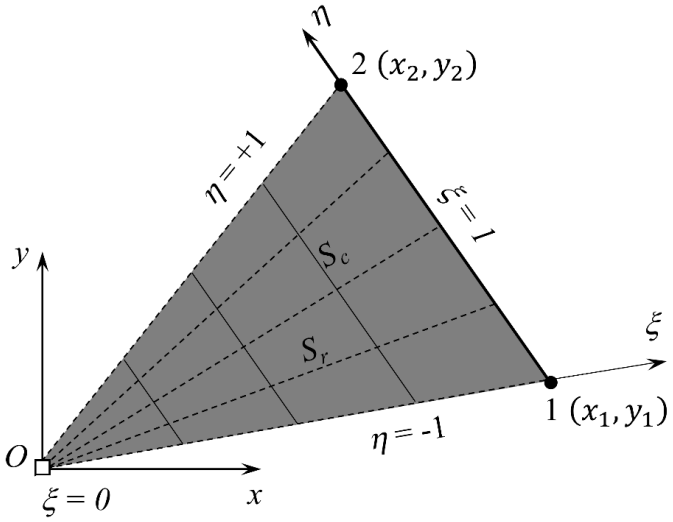

Figure 2.7 Scaled boundary transformation of geometry of simplest two-node line element.

The dimensionless radial coordinate, ξ, points ranging from O to a point on the boundary (with $\xi = 1$). The scaled boundary transformation between the Cartesian coordinates, x, y, and the scaled boundary coordinates, ξ, η, (as shown in Figure 2.7b) relates any point in the domain denoted as $\hat{x}$, $\hat{y}$ to the corresponding point on the line element as

$$\hat{x} = \xi x(\eta) = \xi\left(\bar{x} + \frac{1}{2}\Delta_x \eta\right) \tag{2.18a}$$

$$\hat{y} = \xi y(\eta) = \xi\left(\bar{y} + \frac{1}{2}\Delta_y \eta\right) \tag{2.19a}$$

The equation states that the coordinate curves labeled S_c, which have a constant value of ξ, are parallel to the line element. The coordinate curves labeled S_r, which have a constant value of η, are radial lines that connect the scaling center (labeled O) to the points on the line element. The partial derivatives of $\hat{x}$, $\hat{y}$ with respect to ξ, η can be found using equations (2.18a) and (2.19a).

$$\hat{x}_{,\xi} = x(\eta) = \left(\bar{x} + \frac{1}{2}\Delta_x \eta\right) \tag{2.20a}$$

$$\hat{y}_{,\xi} = y(\eta) = \left(\bar{y} + \frac{1}{2}\Delta_y \eta\right) \tag{2.21a}$$

$$\hat{x}_{,\eta} = \xi x(\eta)_{,\eta} = -\frac{1}{2}\Delta_x \xi \tag{2.22a}$$

$$\hat{y}_{,\eta} = \xi y(\eta)_{,\eta} = \frac{1}{2}\Delta_y \xi \tag{2.23a}$$

จุฬาลงกรณ์มหาวิทยาลัย
CHULALONGKORN UNIVERSITY

resulting in

$$\left[\hat{J}\right] = diag(1,\xi)\left[J(\eta)\right] = \begin{bmatrix} 1 & 0 \\ 0 & \xi \end{bmatrix}\left[J(\eta)\right] \tag{2.24a}$$

where the Jacobian matrix at the boundary is expressed as

$$\left[J(\eta)\right] = \begin{bmatrix} x(\eta) & y(\eta) \\ \xi x(\eta)_{,\eta} & \xi y(\eta)_{,\eta} \end{bmatrix} = \begin{bmatrix} \bar{x} + \frac{1}{2}\Delta_x \eta & \bar{y} + \frac{1}{2}\Delta_y \eta \\ \frac{1}{2}\Delta_x \xi & \frac{1}{2}\Delta_y \xi \end{bmatrix} \tag{2.25a}$$

The determinant of the Jacobian matrix on the boundary in Eq. (2.25a) is expressed as

$$\left|J(\eta)\right| = \frac{1}{2}\begin{vmatrix} \bar{x} & \bar{y} \\ \Delta_x & \Delta_y \end{vmatrix} = \frac{1}{2}\left(\bar{x}\Delta_y - \bar{y}\Delta_x\right) \tag{2.26a}$$

Using Equations from (2.12a) to (2.15a), Eq. (2.26a) simplified as

$$\left|J(\eta)\right| = \frac{1}{2}\begin{vmatrix} x_1 & y_1 \\ x_2 & y_2 \end{vmatrix} = \frac{1}{2}\left(x_1 y_2 - x_2 y_1\right) \tag{2.27a}$$

The inverse of the Jacobian matrix (Eq. (2.25a)) is expressed as

$$\left[J(\eta)\right]^{-1} = \frac{1}{\left|J(\eta)\right|}\begin{bmatrix} \frac{1}{2}\Delta_y & -\left(\bar{y} + \frac{1}{2}\Delta_y \eta\right) \\ \frac{1}{2}\Delta_x & \bar{x} + \frac{1}{2}\Delta_x \eta \end{bmatrix} \tag{2.28a}$$

It offers the converting of the scaled boundary coordinates to the partial derivatives in the Cartesian coordinates as

$$\begin{Bmatrix} \partial/\partial\hat{x} \\ \partial/\partial\hat{y} \end{Bmatrix} = \left[\hat{J}\right]^{-1}\begin{Bmatrix} \partial/\partial\xi \\ \partial/\partial\eta \end{Bmatrix} = \frac{1}{\left|J(\eta)\right|}\begin{bmatrix} y(\eta)_{,\eta} & -y(\eta) \\ -x(\eta)_{,\eta} & x(\eta) \end{bmatrix}\begin{Bmatrix} \partial/\partial\xi \\ 1/\xi \cdot \partial/\partial\eta \end{Bmatrix} \tag{2.29a}$$

This equation is obtained by substituting an expression into the differential operator for 2D elasticity and separating the terms according to their partial derivatives.

$$[L] = \begin{bmatrix} \partial/\partial\hat{x} & 0 \\ 0 & \partial/\partial\hat{y} \\ \partial/\partial\hat{y} & \partial/\partial\hat{x} \end{bmatrix} = [b_1]\frac{\partial}{\partial\xi} + \frac{1}{\xi}[b_2]\frac{\partial}{\partial\eta} \tag{2.30a}$$

where

$$[b_1] = \frac{1}{\left|J(\eta)\right|}\begin{bmatrix} y(\eta)_{,\eta} & 0 \\ 0 & -x(\eta)_{,\eta} \\ -x(\eta)_{,\eta} & y(\eta)_{,\eta} \end{bmatrix} \tag{2.31a}$$

$$[b_2] = \frac{1}{\left|J(\eta)\right|}\begin{bmatrix} -y(\eta) & 0 \\ 0 & x(\eta) \\ x(\eta) & -y(\eta) \end{bmatrix} \tag{2.32a}$$

For later use, the following identity between $[b_1]$ and $[b_2]$ exists

$$\left(\left|J(\eta)\right|[b_2]\right)_{,\eta} = -\left|J(\eta)\right|[b_1] \tag{2.33a}$$

The infinitesimal area, dV^e, of the domain is calculated as

$$dV^e = \left|\hat{J}\right| d\xi d\eta = \xi\left|J(\eta)\right| d\xi d\eta \tag{2.34a}$$

The infinitesimal length of a line, S^{ξ}, with constant, ξ, equals

จุฬาลงกรณ์มหาวิทยาลัย
Chulalongkorn University

$$dS^{\xi} = \sqrt{\left(\hat{x}_{,\eta}\right)^2 + \left(\hat{y}_{,\eta}\right)^2}\, d\eta = \frac{1}{2}\xi\sqrt{\Delta_x^2 + \Delta_y^2}\, d\eta \tag{2.35a}$$

The strain–displacement relationship is expressed concisely as

$$\{\varepsilon\} = [L]\{u\} \tag{2.36a}$$

Substituting Eq. (2.30a) into (2.36a), the strains are expressed in the scaled boundary coordinates as

$$\{\varepsilon\} = [b_1]\frac{\partial\{u\}}{\partial\xi} + \frac{1}{\xi}[b_2]\frac{\partial\{u\}}{\partial\eta} \tag{2.37a}$$

An approximate solution of displacement is sought in the form

$$\{u\} = \{u(\xi,\eta)\} = [N_u]\{u^e(\xi)\} \tag{2.38a}$$

where the superscript e denotes the functions of one element and the shape functions of the p^{th} order element (Figure 2.8) is expressed in matrix form as

$$[N_u] = \begin{bmatrix} N_1 & 0 & N_2 & 0 & \cdots & N_{p+1} & 0 \\ 0 & N_1 & 0 & N_2 & \cdots & 0 & N_{p+1} \end{bmatrix} \tag{2.39a}$$

Substituting the displacement field in Eq. (2.38a) into Eq. (2.37a), the strain field is expressed in the scale boundary coordinates as

$$\{\varepsilon\} = \{\varepsilon(\xi,\eta)\} = [b_1][N_u]\{u^e(\xi)\}_{,\xi} + \frac{1}{\xi}[b_2][N_u]_{,\eta}\{u^e(\xi)\} \tag{2.40a}$$

จุฬาลงกรณ์มหาวิทยาลัย
CHULALONGKORN UNIVERSITY

The strain–displacement matrices are introduced

$$[B_1] = [B_1(\eta)] = [b_1][N_u] \tag{2.41a}$$

$$[B_2] = [B_2(\eta)] = [b_2][N_u]_{,\eta} \tag{2.42a}$$

Now, the strain field in Eq. (2.40a) is rewritten as

$$\{\varepsilon\} = [B_1]\{u^e(\xi)\}_{,\xi} + \frac{1}{\xi}[B_2]\{u^e(\xi)\} \tag{2.43a}$$

The stress field is expressed in the scale boundary coordinates as

$$\{\sigma\} = \{\sigma(\xi,\eta)\} = [D]\left([B_1]\{u^e(\xi)\}_{,\xi} + \frac{1}{\xi}[B_2]\{u^e(\xi)\}\right) \tag{2.44a}$$

where $[D]$ is the elasticity matrix

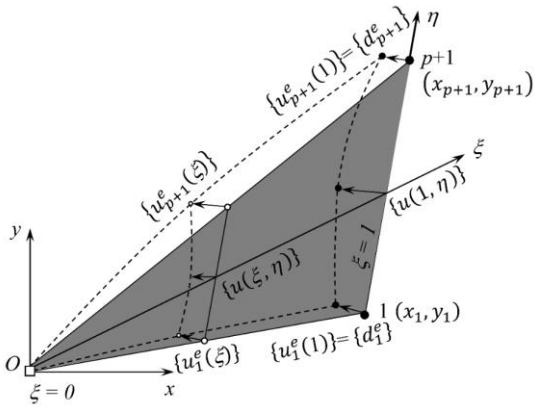

Figure 2.8 Representation of the displacement field in an S-element using independent interpolation of nodal displacement functions.

2.3 Derivation of the SBFE equation using the virtual work principle

The S-element boundary finite element (SBFE) equation is developed by taking the weak form of the governing partial differential equations in the circumferential direction only. This results in a system of ordinary differential equations with the radial coordinate as the independent variable. Two methods can be used to derive the SBFE equation: the Galerkin weighted residual approach (C. Song & Wolf, 1997) or the virtual work principle (Deeks & Wolf, 2002b). This section focuses on the derivation using the virtual work principle without considering body forces (for the derivation of the SBFE equation for a linear elastostatic problem with body forces, see C. M. Song and Wolf (1999)).

จุฬาลงกรณ์มหาวิทยาลัย
Chulalongkorn University

From Eq. (2.43a), using $\{\delta u(\xi = 1)\}$ to represent a fictitious displacement field as

$$\left\{\delta\varepsilon\left(\xi,\eta\right)\right\} = \left[B_1\left(\eta\right)\right]\left\{\delta u\left(\xi\right)\right\}_{,\xi} + \frac{1}{\xi}\left[B_2\left(\eta\right)\right]\left\{\delta u\left(\xi\right)\right\} \tag{2.1b}$$

To represent the corresponding virtual strains, the virtual work equation where there is no body load states that

$$\int_V \left\{\delta\varepsilon\left(\xi,\eta\right)\right\}^T \left\{\sigma\left(\xi,\eta\right)\right\} dV - \int_\eta \left\{\delta u\left(\eta\right)\right\}^T \left\{t\left(\eta\right)\right\} d\eta = 0 \tag{2.2b}$$

where the first term is internal virtual work and the second term is the external work performed by the boundary tractions $\{t(\eta)\}$, evaluated over the entire boundary.

Substituting Eq. (2.34a), (2.44a) and (2.1b) the internal work (first term) is expanded as

$$\begin{aligned}
&\int_V \{\delta\varepsilon(\xi,\eta)\}^T \{\sigma(\xi,\eta)\} dV \\
&= \int_V \left[[B_1(\eta)]\{\delta u(\xi)\}_{,\xi} + \frac{1}{\xi}[B_2(\eta)]\{\delta u(\xi)\} \right]^T \\
&\quad \times \left[[D][B_1(\eta)]\{u(\xi)\}_{,\xi} + \frac{1}{\xi}[D][B_2(\eta)]\{u(\xi)\} \right] dV \\
&= \int_\eta \int_0^1 \{\delta u(\xi)\}_{,\xi}^T [B_1(\eta)]^T [D][B_1(\eta)] \xi \{u(\xi)\}_{,\xi} |J| d\xi d\eta \\
&\quad + \int_\eta \int_0^1 \{\delta u(\xi)\}_{,\xi}^T [B_1(\eta)]^T [D][B_2(\eta)]\{u(\xi)\} |J| d\xi d\eta \\
&\quad + \int_\eta \int_0^1 \{\delta u(\xi)\}^T [B_2(\eta)]^T [D][B_1(\eta)]\{u(\xi)\}_{,\xi} |J| d\xi d\eta \\
&\quad + \int_\eta \int_0^1 \{\delta u(\xi)\}^T [B_2(\eta)]^T [D][B_2(\eta)] \frac{1}{\xi}\{u(\xi)\} |J| d\xi d\eta
\end{aligned} \tag{2.3b}$$

The area integral with $\{\delta u(\xi)\}_{,\xi}$ is integrated with respect to ξ using Green's Theorem (Integration by part), performing line integrals evaluated around the boundary as

$$\begin{aligned}
&\int_V \{\delta\varepsilon(\xi,\eta)\}^T \{\sigma(\xi,\eta)\} dV \\
&= \int_\eta \{\delta u(\xi)\}^T [B_1(\eta)]^T [D][B_1(\eta)] \xi \{u(\xi)\}_{,\xi} |J| d\eta \Big|_{\xi=1} \\
&\quad - \int_\eta \int_0^1 \{\delta u(\xi)\}^T [B_1(\eta)]^T [D][B_1(\eta)] \left\{ \{u(\xi)\}_{,\xi} + \xi \{u(\xi)\}_{,\xi\xi} \right\} |J| d\xi d\eta \\
&\quad + \int_\eta \{\delta u(\xi)\}^T [B_1(\eta)]^T [D][B_2(\eta)]\{u(\xi)\} |J| d\eta \Big|_{\xi=1} \\
&\quad - \int_\eta \int_0^1 \{\delta u(\xi)\}^T [B_1(\eta)]^T [D][B_2(\eta)]\{u(\xi)\}_{,\xi} |J| d\xi d\eta \\
&\quad + \int_\eta \int_0^1 \{\delta u(\xi)\}^T [B_2(\eta)]^T [D][B_1(\eta)]\{u(\xi)\}_{,\xi} |J| d\xi d\eta \\
&\quad + \int_\eta \int_0^1 \{\delta u(\xi)\}^T [B_2(\eta)]^T [D][B_2(\eta)] \frac{1}{\xi}\{u(\xi)\} |J| d\xi d\eta
\end{aligned} \tag{2.4b}$$

For convenience, the following coefficient matrices are introduced

$$[E_0]=\int_{\eta}\left[B_1(\eta)\right]^T[D]\left[B_1(\eta)\right]|J|d\eta \tag{2.5b}$$

$$[E_1]=\int_{\eta}\left[B_2(\eta)\right]^T[D]\left[B_1(\eta)\right]|J|d\eta \tag{2.6b}$$

$$[E_2]=\int_{\eta}\left[B_2(\eta)\right]^T[D]\left[B_2(\eta)\right]|J|d\eta \tag{2.7b}$$

Note that the coefficient matrices $[E_0]$, $[E_1]$, and $[E_2]$ of the S-element are obtained by combining them element-by-element based on how the elements are connected. These matrices are calculated on individual line elements at the boundary, and they are only influenced by the shape of the boundary as depicted by the line element. The integration process can be done numerically in a similar way to how the stiffness matrix of one-dimensional finite elements is calculated, and the same principles for selecting the integration quadrature order used in traditional FEM also apply.

Using $\{u_b\}$ to represent displacement field at the boundary $\{u(\xi=1)\}$ with Eqs. (2.5b), (2.6b) and (2.7b), Eq. (2.4b) is expressed succinctly as

$$\begin{aligned}&\int_V\left\{\delta\varepsilon(\xi,\eta)\right\}^T\left\{\sigma(\xi,\eta)\right\}dV\\&=\left\{\delta u\right\}^T\left\{[E_0]\{u_b\}_{,\xi}+[E_1]^T\{u_b\}\right\}-\int_0^1\left\{\delta u(\xi)\right\}^T\left\{[E_0]\xi\{u(\xi)\}_{,\xi\xi}\right.\\&\left.+\left[[E_0]+[E_1]^T-[E_1]\right]\{u(\xi)\}_{,\xi}-[E_2]\frac{1}{\xi}\{u(\xi)\}\right\}d\xi\end{aligned} \tag{2.8b}$$

By substituting virtual displacement field with the shape functions, $[N(\eta)]$, to interpolate between the nodes in the circumferential direction, Eq. (2.38a) becomes

$$\left\{\delta u(\xi,\eta)\right\}=\left[N(\eta)\right]\left\{\delta u(\xi)\right\} \tag{2.9b}$$

By substituting Eq. (2.9b), the external work (second term) in Eq. (2.2b) becomes

$$\int_{\eta}\left\{\delta u(\eta)\right\}^T\left\{t(\eta)\right\}d\eta=\left\{\delta u\right\}^T\underbrace{\int_{\eta}\left\{N(\eta)\right\}^T\left\{t(\eta)\right\}d\eta}_{\{F\}} \tag{2.10b}$$

จุฬาลงกรณ์มหาวิทยาลัย
CHULALONGKORN UNIVERSITY

The integral term on the right-hand side of Eq. (2.10b) can be identified as the equivalent nodal forces due to the boundary tractions, $\{F\}$. By substituting Eq. (2.8b) and (2.10b) back into Eq. (2.2b), the complete virtual work equation becomes

$$\{\delta u\}^T \left\{ [E_0]\{u_b\}_{,\xi} + [E_1]^T \{u_b\} \right\} - \{\delta u\}^T \{F\} - \int_0^1 \{\delta u(\xi)\}^T \left\{ [E_0]\xi \{u(\xi)\}_{,\xi\xi} + \left[[E_0] + [E_1]^T - [E_1] \right] \{u(\xi)\}_{,\xi} - [E_2] \frac{1}{\xi} \{u(\xi)\} \right\} d\xi = \{0\} \tag{2.11b}$$

Equation. (2.11b) needs to be satisfied for all $\{\delta u(\xi)\}$ (one is closely satisfied in the radial direction and the second is satisfied in the circumferential direction) the following conditions.

$$\{F\} = [E_0]\{u_b\}_{,\xi} + [E_1]^T \{u_b\} \tag{2.12b}$$

Equation (2.12b) is the nodal force functions at the boundary $\{F(\xi = 1)\}$ then

$$\{q(\xi)\} = [E_0]\xi \{u(\xi)\}_{,\xi} + [E_1]^T \{u(\xi)\} \tag{2.13b}$$

where $\{q(\xi)\}$ is the nodal force function in the domain $\{F(0 \le \xi < 1)\}$ and

$$[E_0]\xi^2 \{u(\xi)\}_{,\xi\xi} + \left[[E_0] + [E_1]^T - [E_1] \right] \xi \{u(\xi)\}_{,\xi} - [E_2]\{u(\xi)\} = \{0\} \tag{2.14b}$$

An equation system involving second-order differential equations with the dimensionless radial coordinate, ξ, as the independent variable is described in Equation (2.14b). This system was derived from the strong form of the governing partial differential equations of linear elasticity in the radial direction, while the circumferential direction was weakened in the FEM.

จุฬาลงกรณ์มหาวิทยาลัย
Chulalongkorn University

2.4 Solving the SBFE equation by Eigenvalue Decomposition

To convert the second-order differential equations in Eq. (2.14b) to first-order equations, we can use a straightforward solution strategy that is suitable for numerical computation. When the S-element is at the boundary of the plane, the number of degrees of freedom is equal to the number of equations in Eq. (2.14b), which is represented by the letter n. By reducing the order of the differential equations from two to one, the number of equations is doubled to $2n$. This can be useful for implementing the equations in a numerical computation.

To do this, equation (2.13b) is rewritten in displacement functions with respect to the radial coordinate, ξ, as

$$\xi\{u(\xi)\}_{,\xi} = [E_0]^{-1}\{q(\xi)\} - [E_0]^{-1}[E_1]^T\{u(\xi)\} \tag{2.1c}$$

Substituting into Eq. (2.14b) to eliminate $\xi\{u(\xi)\}_{,\xi}$ then rearrange the results in

$$\xi\{q(\xi)\}_{,\xi} - [E_1][E_0]^{-1}\{q(\xi)\} + [E_1][E_0]^{-1}[E_1]^T\{u(\xi)\} - [E_2]\{u(\xi)\} = 0 \tag{2.2c}$$

Introducing the variable $\{X(\xi)\}$ that comprises the n nodal displacement functions and the n force functions

$$\{X(\xi)\} = \begin{Bmatrix} \{u(\xi)\} \\ \{q(\xi)\} \end{Bmatrix} \tag{2.3c}$$

Now, equation (2.1c) and (2.2c) are reformulated as a system of $2n$ equations

$$\xi\{X(\xi)\}_{,\xi} = [Z_p]\{X(\xi)\} \tag{2.4c}$$

with Hamiltonian coefficient matrix

$$[Z_p] = \begin{bmatrix} -[E_0]^{-1}[E_1]^T & [E_0]^{-1} \\ [E_2] - [E_1][E_0]^{-1}[E_1]^T & [E_1][E_0]^{-1} \end{bmatrix} \tag{2.5c}$$

A well-known approach for solving Eq. (2.4c) is to postulate that its solution is of the form of a power function

$$\{X(\xi)\} = \xi^{\lambda}\{\phi\} \tag{2.6c}$$

Substituting this trial solution into Eq. (2.4c) yields

$$\lambda\xi^{\lambda}\{\phi\} = [Z_p]\xi^{\lambda}\{\phi\} \tag{2.7c}$$

Simplify as

$$[Z_p]\{\phi\} = \lambda\{\phi\} \tag{2.8c}$$

where exponents, λ_i, are the eigenvalue and corresponding eigenvector $\{\phi\}$, Eq. (2.8c) can be written as

$$\left([Z_p] - \lambda[I]_{2n}\right)\{\phi\} = 0 \tag{2.9c}$$

where $[I]_{2n}$ is an identity matrix of order $2n$. The eigenvalue decomposition is expressed in matrix form as

$$[Z_p][\Phi] = [\Phi]diag(\lambda) \tag{2.10c}$$

with the eigenvector matrix $[\Phi]$ containing $2n$ eigenvectors

$$[\Phi] = \begin{bmatrix} \{\phi_1\} & \{\phi_2\} & \cdots & \{\phi_i\} & \cdots & \{\phi_{2n}\} \end{bmatrix} \tag{2.11c}$$

จุฬาลงกรณ์มหาวิทยาลัย
Chulalongkorn University

The general solution to the homogeneous set of Euler-Cauchy differential equation represented by Eq. (2.4c) can be expressed as a linear combination of the trial solutions by $2n$ eigenvalues and eigenvectors as

$$\begin{aligned}\left\{X\left(\xi\right)\right\} &= \sum_{i=1}^{2n} c_i \xi^{\lambda_i} \left\{\phi_i\right\} \\ &= c_1\xi^{\lambda_1}\left\{\phi_1\right\} + c_2\xi^{\lambda_2}\left\{\phi_2\right\} + \cdots + c_i\xi^{\lambda_i}\left\{\phi_i\right\} + \cdots + c_{2n}\xi^{\lambda_{2n}}\left\{\phi_{2n}\right\}\end{aligned} \tag{2.12c}$$

where c_i are the integration constants dependent on the boundary conditions, exponents λ_i are the eigenvalue, and corresponding eigenvector $\left\{\phi_i\right\}$ can be interpreted as independent modes of deformation that closely satisfy internal equilibrium in the ξ direction.

Using Eqs. (2.3c) and (2.12c), an eigenvector $\left\{\phi_i\right\}$ can be partitioned into two subvectors $\left\{\phi_i^{(u)}\right\}$ and $\left\{\phi_i^{(q)}\right\}$ of the same size n

$$\left\{\phi_i\right\} = \begin{Bmatrix}\left\{\phi_i^{(u)}\right\} \\ \left\{\phi_i^{(q)}\right\}\end{Bmatrix} \tag{2.13c}$$

The solution for nodal displacement and force functions (bounded S-element) is written as

$$\begin{aligned}\left\{u\left(\xi\right)\right\} &= \sum_{i=1}^{n} c_i \xi^{\lambda_i} \left\{\phi_i^{(u)}\right\} \\ &= c_1\xi^{\lambda_1}\left\{\phi_1^{(u)}\right\} + c_2\xi^{\lambda_2}\left\{\phi_2^{(u)}\right\} + \cdots + c_i\xi^{\lambda_i}\left\{\phi_i^{(u)}\right\} + \cdots + c_n\xi^{\lambda_n}\left\{\phi_n^{(u)}\right\} \\ \left\{q\left(\xi\right)\right\} &= \sum_{i=1}^{n} c_i \xi^{\lambda_i} \left\{\phi_i^{(q)}\right\} \\ &= c_1\xi^{\lambda_1}\left\{\phi_1^{(q)}\right\} + c_2\xi^{\lambda_2}\left\{\phi_2^{(q)}\right\} + \cdots + c_i\xi^{\lambda_i}\left\{\phi_i^{(q)}\right\} + \cdots + c_n\xi^{\lambda_n}\left\{\phi_n^{(q)}\right\}\end{aligned} \tag{2.14c}$$

จุฬาลงกรณ์มหาวิทยาลัย
Chulalongkorn University

The remaining integral constants, c_i, are determined from the boundary condition at $\xi = 1$. Equation (2.14c) is written in matrix form as

$$\left\{u\left(\xi\right)\right\} = \left[\Phi_b^{(u)}\right]\xi^{\langle\lambda_b\rangle}\left\{c\right\} \tag{2.15c}$$

$$\left\{q\left(\xi\right)\right\} = \left[\Phi_b^{(q)}\right]\xi^{\langle\lambda_b\rangle}\left\{c\right\} \tag{2.16c}$$

where $\langle\lambda_b\rangle$ is the eigenvalue formed in diagonal matrix, vector $\{c\}$ is assembled the integration constants, and the eigenvector matrix $[\Phi_b]$ is constructed by combining the corresponding eigenvectors as columns.

$$\begin{bmatrix} \left[\Phi_b^{(u)}\right] \\ \left[\Phi_b^{(q)}\right] \end{bmatrix} = \begin{bmatrix} \left\{\phi_1^{(u)}\right\} & \left\{\phi_2^{(u)}\right\} & \cdots & \left\{\phi_i^{(u)}\right\} & \cdots & \left\{\phi_n^{(u)}\right\} \\ \left\{\phi_1^{(q)}\right\} & \left\{\phi_2^{(q)}\right\} & \cdots & \left\{\phi_i^{(q)}\right\} & \cdots & \left\{\phi_n^{(q)}\right\} \end{bmatrix} \tag{2.17c}$$

Eliminating the integration constants from Eq. (2.15c) and (2.16c) yields

$$\left\{q(\xi)\right\} = \left[\Phi_b^{(q)}\right]\left[\Phi_b^{(u)}\right]^{-1}\left\{u(\xi)\right\} \tag{2.18c}$$

Formulating Eq. (2.18c) at the boundary $(\xi = 1)$, the nodal force–displacement relationship of the S-element is expressed as

$$\left\{F\right\} = \left[K\right]\left\{u_b\right\} \tag{2.19c}$$

where the stiffness matrix of S-element of a bounded domain is equal to

$$\left[K\right] = \left[\Phi_b^{(q)}\right]\left[\Phi_b^{(u)}\right]^{-1} \tag{2.20c}$$

Eq. (2.15c) is stated at $\xi = 1$ to derive the integration parameters in the solution of the nodal displacement functions of the S-element.

$$\left\{u_b\right\} = \left\{u(\xi = 1)\right\} = \left[\Phi_b^{(u)}\right]\left\{c\right\} \tag{2.21c}$$

This leads to the integration constants $\{c\}$ as

$$\left\{c\right\} = \left[\Phi_b^{(u)}\right]^{-1}\left\{u_b\right\} \tag{2.22c}$$

The equations for the nodal displacement functions of the S-element, which describe the displacement along the lines connecting the scaling center and a node on the boundary, can be expressed in matrix form using either Eq. (2.14c) or Eq. (2.15c). These functions are used to calculate the displacements at each node on the boundary.

2.5 Solving the SBFE equation by Schur's decomposition

One way to solve a system of ordinary equations involving the S-element is to use eigenvalue decomposition. This involves using a dimensionless radial coordinate to create a power series representing the displacement field within the S-element and using eigenvectors to obtain the static stiffness matrix. However, if there are repeated eigenvalues with parallel eigenvectors, the eigenvalue decomposition process may not be possible and the solution may be lost, leading to a malfunction of the numerical method.

According to Deeks and Wolf (2002a), some elasticity theory problems include solutions that include power and logarithmic functions, which the eigenvalue decomposition method is unable to replicate. Under specific combinations of boundary conditions, material composition, and wedge opening angle, a logarithmic function may be seen. For the statics SBFE problem, Song suggested a Schur decomposition solution method in 2004.

In this section, the system of homogeneous first-order ordinary differential equations from Section 2.4 is solved using a method based on Schur decomposition (Laub, 1978) and the theory of matrices (Gantmacher, 1960). The first-order ordinary differential equations (Eq. (2.4c)) are conveniently simplified as follows.

$$\xi\left\{X\left(\xi\right)\right\}_{,\xi}=\left[Z_p\right]\left\{X\left(\xi\right)\right\} \tag{2.1d}$$

where the variable $\{X(\xi)\}$ comprises the n nodal displacement $\{u(\xi)\}$ and n force $\{q(\xi)\}$ functions

$$\left\{X\left(\xi\right)\right\}=\begin{Bmatrix}\left\{u\left(\xi\right)\right\}\\ \left\{q\left(\xi\right)\right\}\end{Bmatrix} \tag{2.2d}$$

The number of degrees of freedom in the vector of the unknown function $\{X(\xi)\}$ are $2n$. The constant matrix $\left[Z_p\right]$ (Eq. (2.5c)) is equal to

$$\left[Z_p\right]=\begin{bmatrix}-\left[E_0\right]^{-1}\left[E_1\right]^T & \left[E_0\right]^{-1}\\ \left[E_2\right]-\left[E_1\right]\left[E_0\right]^{-1}\left[E_1\right]^T & \left[E_1\right]\left[E_0\right]^{-1}\end{bmatrix} \tag{2.3d}$$

จุฬาลงกรณ์มหาวิทยาลัย
CHULALONGKORN UNIVERSITY

To decouple the system of $2n$ homogeneous ordinary differential equations in Eq. (2.1d), the Schur decomposition of the $2n \times 2n$ coefficient matrix $\left[Z_p\right]$ in Eq. (2.3d) is performed.

$$\left[S\right]=\left[V\right]^T\left[Z_p\right]\left[V\right] \tag{2.4d}$$

where $[S]$ denotes a real Schur form matrix. The real Schur form matrix $[S]$ is a quasi-upper triangular matrix. Its diagonal comprises 1 × 1 and 2 × 2 blocks. The real transformation matrix $[V]$ is an orthogonal matrix satisfying

$$\left[V\right]^T\left[V\right]=\left[I\right] \tag{2.5d}$$

where $[I]$ is an identity matrix.

The behavior of the solution is assessed based on the sign of the eigenvalues to analytically impose boundary conditions in the SBFE equation solution. The Hamiltonian matrix $[Z_p]$ has pairs of $(\lambda, -\lambda)$ eigenvalues. Two sets of eigenvalues in two dimensions that correspond to the two translational rigid body movements are equal to zero. The remaining eigenvalues may be split into two equal-sized groups, one of which includes eigenvalues with positive real parts and the other of which includes eigenvalues with negative real parts.

In order to satisfy the requirement of finiteness of displacement at the scaling center $\xi = 0$, equation (2.1d) is transformed into a form. The expression for the variable function $\{X(\xi)\}$ is

$$\{X(\xi)\} = [V]\{W(\xi)\} \tag{2.6d}$$

where the orthogonal transformation matrix $[V]$ in Eq. (2.4d) is the basis and $\{W(\xi)\}$ is the generalized-coordinate function. Substituting Eq. (2.6d) into Eq. (2.1d) yields

$$[V]\xi\{W(\xi)\}_{,\xi} = [Z_p][V]\{W(\xi)\} \tag{2.7d}$$

Premultiplying Eq. (2.7d) with $[V]^T$ and using Eqs. (2.4d) and (2.5d) results in a system of differential equations of the generalized coordinates $\{W(\xi)\}$

$$\xi\{W(\xi)\}_{,\xi} = [S]\{W(\xi)\} \tag{2.8d}$$

The real Schur form matrix $[S]$ of size $2n \times 2n$ is divided into four submatrices of size $(n \times n)$ to decouple the system of equations in order to meet the scaling center boundary condition.

จุฬาลงกรณ์มหาวิทยาลัย
Chulalongkorn University

$$[S] = \begin{bmatrix} [S_b] & * \\ 0 & [S_u] \end{bmatrix} \tag{2.9d}$$

where a nonzero real matrix is represented by the symbol "*". The solutions for the bounded domain (subscript b for bounded) defined by $0 \leq \xi \leq 1$ and the unbounded domain (subscript u for unbounded) defined by $\xi \geq 1$ are connected to $[S_b]$ and $[S_u]$ in Eq. (2.9d), as will be shown later. In Equation (2.5d), the orthogonal transformation matrix $[V]$ is divided into four submatrices of size $n \times n$.

$$[V] = \begin{bmatrix} \left[V_b^{(u)}\right] & \left[V_u^{(u)}\right] \\ \left[V_b^{(q)}\right] & \left[V_u^{(q)}\right] \end{bmatrix} \tag{2.10d}$$

Superscript u denotes the set of basis vectors for displacement, and the first-row block of $[V]$ in Eq. (2.10d) is treated as the solution of displacements, with the second-row block representing the nodal force functions (superscript q denoting the set of basis vectors of forces).

The generalized-coordinate functions $\{W(\xi)\}$ are also divided into two subsystems of the same size, n, as the system of $2n$ equations in Eq. (2.8d).

$$\{W(\xi)\} = \begin{Bmatrix} \{W_b(\xi)\} \\ \{W_u(\xi)\} \end{Bmatrix} \tag{2.11d}$$

Using Eqs. (2.2d) and (2.10d), Eq. (2.6d) is rewritten as two sets of equations that provide the solutions for the nodal displacement and force functions.

$$\{u(\xi)\} = \left(\left[V_b^{(u)} \right] \{W_b(\xi)\} + \left[V_u^{(u)} \right] \{W_u(\xi)\} \right) \tag{2.12d}$$

$$\{q(\xi)\} = \left(\left[V_b^{(q)} \right] \{W_b(\xi)\} + \left[V_u^{(q)} \right] \{W_u(\xi)\} \right) \tag{2.13d}$$

The solution of Eq. (2.1d) with a general coefficient matrix $[Z_p]$ becomes the solution of Eq. (2.8d) with a real Schur matrix $[S]$. Using Eqs. (2.9d) and (2.11d), Eq. (2.8d) is demonstrated as

$$\xi \frac{\mathrm{d}}{\mathrm{d}\xi} \begin{Bmatrix} \{W_b(\xi)\} \\ \{W_u(\xi)\} \end{Bmatrix} = \begin{bmatrix} [S_b] & * \\ 0 & [S_u] \end{bmatrix} \begin{Bmatrix} \{W_b(\xi)\} \\ \{W_u(\xi)\} \end{Bmatrix} \tag{2.14d}$$

At the scaling center $(\xi = 0)$, enforcing the condition of finiteness of solution will lead to

$$\{W_u(\xi)\} = 0 \tag{2.15d}$$

จุฬาลงกรณ์มหาวิทยาลัย
CHULALONGKORN UNIVERSITY

The proof of Eq. (2.15d) is precisely described in Chongmin Song (2018).

Substituting Eq. (2.15d) into Eq. (2.14d), the first set of Eq. (2.14d) is written as

$$\xi \{W_b(\xi)\}_{,\xi} = [S_b] \{W_b(\xi)\} \tag{2.16d}$$

The general solution of Eq. (2.16d) is expressed as

$$\{W_b(\xi)\} = \xi^{[S_b]} \{c_b\} \tag{2.17d}$$

where $\{c_b\}$ is the integration constant.

Substituting Eqs. (2.15d) and (2.17d) into Eqs. (2.12d) and (2.13d) yields the solutions for the nodal displacement and force functions

$$\{u(\xi)\} = \left[V_b^{(u)}\right] \xi^{[S_b]} \{c_b\} \tag{2.18d}$$

$$\{q(\xi)\} = \left[V_b^{(q)}\right] \xi^{[S_b]} \{c_b\} \tag{2.19d}$$

At the boundary $(\xi = 1)$, the static stiffness matrix of the S-element is equal to

$$[K] = \left[V_b^{(q)}\right]\left[V_b^{(u)}\right]^{-1} \tag{2.20d}$$

which is in the same form as Eq. (2.20c) obtained using the eigenvalue decomposition method. The solution of the displacement functions Eq. (2.18d) is formulated at $\xi = 1$, leading to

$$\{u_b\} = \{u(\xi = 1)\} = \left[V_b^{(u)}\right]\{c\} \tag{2.21d}$$

where $\xi^{[S_b]} = 1^{[S_b]} = [I]$ has been applied. The integration constants $\{c\}$ are obtained as

$$\{c\} = \left[V_b^{(u)}\right]^{-1} \{u_b\} \tag{2.22d}$$

The nodal displacement and force functions are solved by substituting Eq. (2.22d) into Eq. (2.18d).

2.6 Features and Example Applications of SBFEM

The scaled boundary finite element method (SBFEM) is a recently developed technique for analyzing stress in various engineering applications. It has been used to study linear elastic fracture mechanics in unbounded domains with arbitrary geometry (Bazyar & Song, 2008), multimaterial wedges (C. M. Song, Tin-Loi, & Gao, 2010), automatic crack propagation using polygon elements (Ooi, Song, Tin-Loi, & Yang, 2012), crack and notch problems in piezoelectric materials (C. Li et al., 2013), elastic wave propagation in layered media (Chen et al., 2015), and nonmatching mesh problems in domain decomposition and contact mechanics (Xing, Zhang, Song, & Tin-Loi, 2019). In addition, the SBFEM can be combined with an automatic mesh generation approach based on the Quadtree/Octree algorithm to conduct stress analysis (Hirshikesh et al., 2019). The SBFEM and the Quadtree algorithm are mathematical models that work well together, with the S-elements allowing for arbitrary division of line elements based on element size and the Quadtree/Octree algorithm providing a detailed approach for mesh generation in 2D and 3D problems. The edges of smaller cells in the SBFEM are represented by

จุฬาลงกรณ์มหาวิทยาลัย
Chulalongkorn University

multiple line elements, which show the edges of the S-domain at different refinement levels and also model shared edges between S-domains at different refinement levels.

จุฬาลงกรณ์มหาวิทยาลัย
Chulalongkorn University

3. Automatic Mesh Generation

3.1 Introduction

Numerous scientific and engineering fields now use numerical approaches, ranging from straightforward static, fluid, dynamic, heat transfer, instability and damage mechanics studies to more complex applications including adaptive refinement analysis, massive deformation nonlinear analysis, and fluid dynamic issues with shock lines (Frey & George, 2007). The FEM is one of the well-known methods. The entire system must be broken down into numerous distinct subsystems or components whose behavior is easily understood before an analysis is conducted. Additionally, the amount of nodes in the mesh where they were put and the geometry of the pieces created both affect how accurate a FEM solution is. Large-scale difficult engineering simulations and scientific calculations via FEM are now more accessible to ordinary design operations and research students because to recent increases in computer performance. Similar to this, mesh generation and its uses have establishing effective.

Sluiter (1982) originally devised the mesh generation method for automatically triangulating generic two-dimensional finite element domains. Nonuniform computational grids gained popularity over time for two reasons. First, they permitted the placement of points on the curved domain borders that had irregular shapes (Phai, 1982). Second, they facilitated the distribution of points with varied nodal spacing throughout the domain. In several literatures, a number of mesh generating strategies have been continually developed. Examples of successful methods for mesh generation using FEM include the Contour-line approach (S. Lo, 1991), Coring method (S. Lo & Lee, 1992), AFT (Zhu, Zienkiewicz, Hinton, & Wu, 1991), Delaunay triangulation (George & Hermeline, 1992), and Refinement by subdivision technique (Rivara, 1997).

จุฬาลงกรณ์มหาวิทยาลัย
Chulalongkorn University

One of the prominent algorithms developed for 2D-FE mesh creation by Yerry and Shephard (1983) is called a Quadtree decomposition algorithm. One year later, this algorithm was extended into 3D mesh generation by Yerry and Shephard (1984) and was called an Octree decomposition. Thereafter, several variants of the techniques have been developed by (Greaves & Borthwick, 1999; Jung & Lee, 1993; Weiler, Schindler, & Schneiders, 1996; Wille, 1992)). In 2002,

(Hjaltason & Samet)improved the speed of the Quadtree mesh construction using spatial indexes. An advantage of Quadtree/Octree mesh generation is that all the topological details can be memorized as a tree. Using this algorithm, assorted information such as level, neighbors, ancestors, and children of an element is easily obtained. In addition, this algorithm guarantees the construction of well-shaped elements with a reasonably tiny amount of computational time and memory storage.

In the next section, the Quadtree and Octree mesh generation with the main concepts underlying spatial decomposition approaches are briefly explained. The image-based mesh generation with hierarchical-tree algorithm is also presented. These processes drastically reduce the amount of DOFs, accelerating the solution of the problem by alleviating computational effort and memory requirements. Finally, some works of hierarchical-tree algorithm for the generation of SBFE meshes directly from geometric models are presented.

3.2 Concept of Quadtree algorithm

The square enclosing box of the problem domain is used to represent the root cell of the Quadtree technique. This root cell (bounding box) must be big enough to hold all the nodal points. Starting from the root cell and continuing until the stopping requirements are satisfied, an initial cell is divided recursively by bisecting the edges into Quadtree cells (elements) in accordance with the given element size. As seen in Figure 2.9, newly generated cells are referred to as their parent cells during subdivision.

จุฬาลงกรณ์มหาวิทยาลัย
Chulalongkorn University

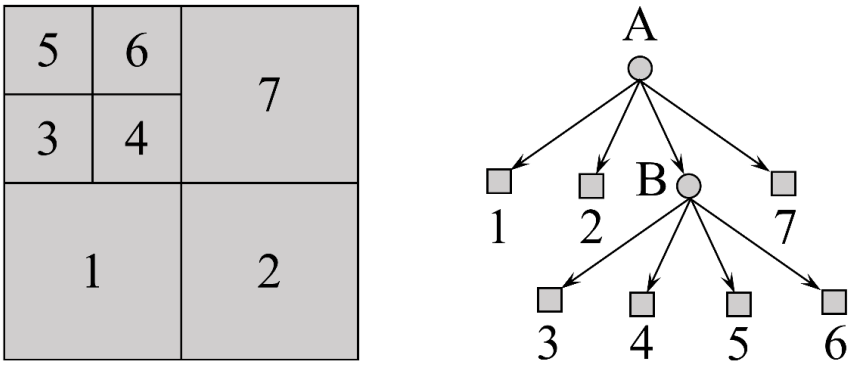

Figure 2.9 The block partitioning and tree structure of a simple Quadtree, where leaf blocks are labeled with numbers and non-leaf blocks with letters.

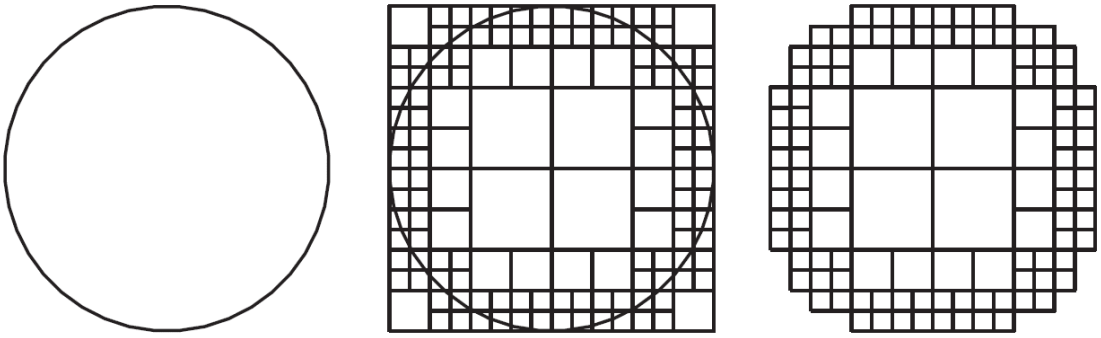

(a) (b) (c)

Figure 2.10 Creating a circular domain based on quadtree method involves three steps: (a) the problem domain; (b) a quadtree mesh covering the problem domain; and (c) a quadtree mesh that has been cleared of extraneous cells. (Man et al., 2014)

An example of meshing for circular domain based on quadtree approach is shown in Figure 2.10 The root cell is a square bounding box that encloses the circle completely. To more accurately represent the circle at each level, the cells that intersect with the domain are divided into four groups by cutting the sides in half. The recursive subdivision procedure (shown in Figure 2.11a) is used to discretize a square domain into Quadtree cells (elements) with the desired element size while adhering to the one-level limitation. The difference in division levels between any two neighboring cells during mesh formation must be kept to a single value to ensure accuracy in the analysis.

จุฬาลงกรณ์มหาวิทยาลัย
CHULALONGKORN UNIVERSITY

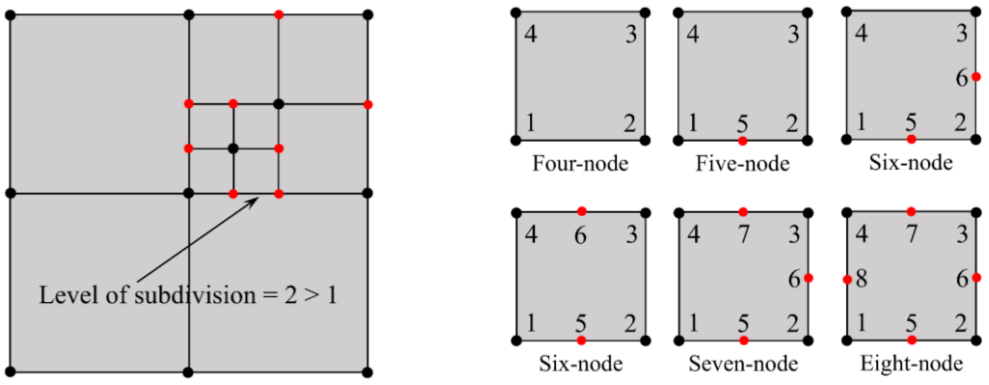

(a) (b)

Figure 2.11 Quadrilateral element: (a) Level of subdivision between neighboring cells; (b) Family of transition.

To employ the one-level Quadtree decomposition, first identify the types of quadrilaterals and their node-labeling scheme, as shown in Figure 2.11(b). In general, only six unique types of quadrilaterals in a transition square mesh fulfill the one-level refinement limitation (D. S. Lo, 2014), which states that once constructed, an eight-node element may be split into four four-node elements. A four-node quadrilateral can have four neighbors along its edges, according to the neighboring relationship of the transition FE mesh (1–2, 2–3, 3–4, and 4–1, respectively).

In accordance with the explanation of one-level limitation, Quadtree cells can be enforced by simply comparing the refinement level (RL) values of nearby cells. Each element in the first stage of a single Quadtree cell, a FE mesh of quadrilateral components, is assigned an RL value of zero. It is both essential and sufficient to examine the nearby RL values as the partition continues and when a cell is marked for refining. If the RL values of the surrounding cells are equal to or greater than the RL value of this cell, it can be split into smaller cells, and the RL value of the four subdivided cells is increased by one. The cell cannot be split until the cells around its are partitioned. A recursive algorithm can readily implement this basic yet effective RL-checking process.

จุฬาลงกรณ์มหาวิทยาลัย
Chulalongkorn University

The process of partitioning a rectangular area with a one-level mesh restriction is shown in Figure 2.12. At the beginning of the mesh, each element has a refinement level (RL) value of zero, as seen in Figure 2.12 (a). If element (1) needs to be divided to meet the element size requirement, the RL values of elements (2) and (3) nearby are checked to satisfy that the one-level mesh limitation is met As shown in Figure 2.12(b), when element (1) is divided, it creates four new elements with RL = 1. The RL values of element (5)'s neighbors (elements (1), (2), and (6)) are then checked to see if they need to be divided in the next phase. Since element (2) has a lower RL value than element (1), it is split first, as shown in Figure 2.12(c). The one-level restriction is satisfied for element (2) and it is refined by checking the RL values of element (2)'s neighbors. The process is repeated for the other elements, as shown in Figure 2.12(d). Both the analytical

function for element size distribution and the practical adaptive refinement analysis uses the recursive refinement technique to divide and refine the elements.

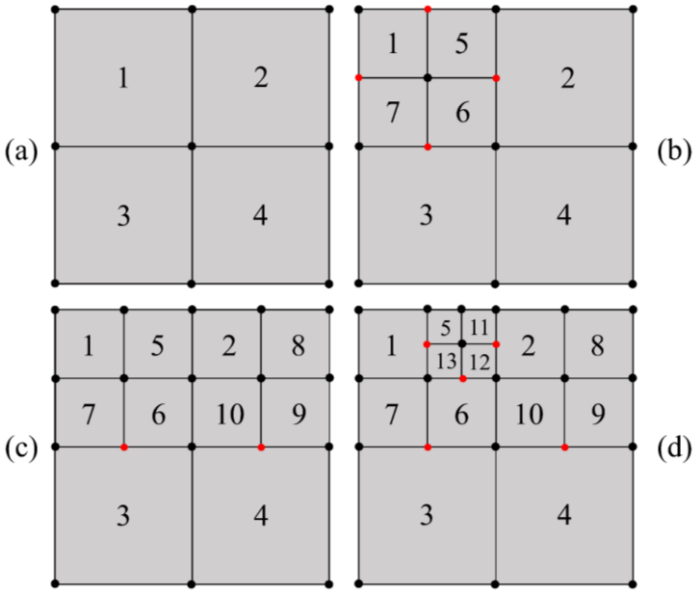

Figure 2.12 Refinement of the mesh with a level restriction: (a) Initial mesh, (b) first subdivision, (c) second subdivision, and (d) third subdivision are all examples of subdivisions.

3.3 Concept of Octree algorithm

Meagher (1982) pioneered Octree encoding in 3D mesh creation. The creation process begins with a cube, which is the initial cell of the Octree grid, also known as the grid's root. By bisecting the sides, the cubic root (elements) is segmented into eight (2^3) cells until the specific halting conditions are met. Figure 2.13 depicts a three-level Octree. The cell information is efficiently stored in a tree-type data structure, with the root cell at the top of the storage structure's hierarchy of levels.

จุฬาลงกรณ์มหาวิทยาลัย
Chulalongkorn University

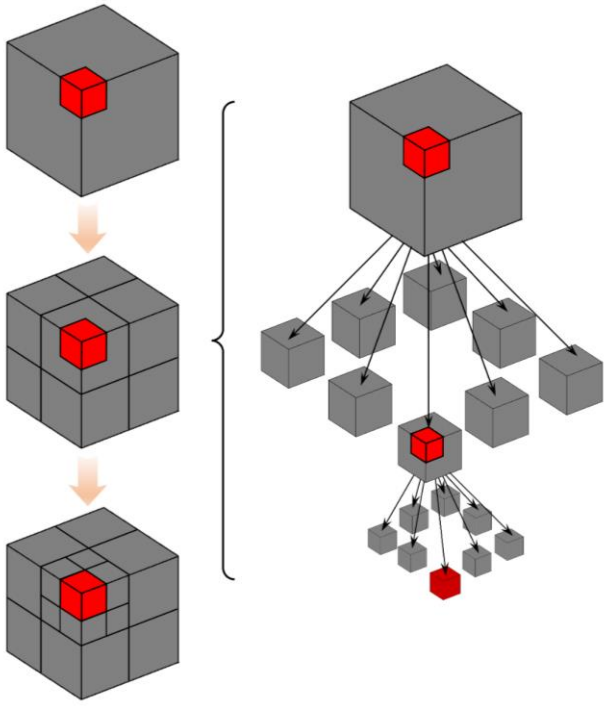

Figure 2.13 An example of Octree with three levels subdivision.

Figure 2.14 shows an illustration of an Octree mesh for a cylinder as a starting point for mesh production. The bounding box is partitioned into eight cells in the first phase (Figure 2.14(a)). To more accurately reflect the border, the cells are constantly split (Figure 2.14(b)). The 2:1 balancing restriction (Sundar, Sampath, & Biros, 2008) is imposed on the Octree grid once all subdivisions have been finished. Figure 2.14(C) shows how a balanced Octree turned out. The Octree mesh shown in Figure 2.14(d) is then created when the exterior cells (cells outside the issue domains) are eliminated.

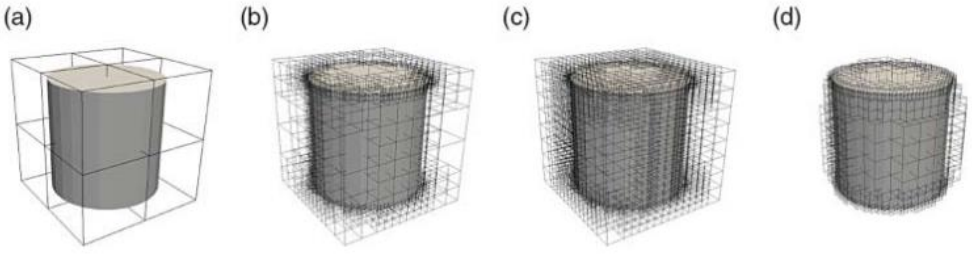

Figure 2.14 Creation of an Octree mesh for a cylinder (Y. Liu, Saputra, Wang, Tin-Loi, & Song, 2017): (A) The problem domain and the basic bounding box division. Cells are adjusted in (b) order to suit the border. Octree mesh that is balanced (2:1 rule). (d) Octree mesh with exterior cells removed.

When one or more hanging nodes occur on one face of an Octree cell, this face is dissected into a mix of triangular and quadrilateral parts. There are also six unique configurations of hanging nodes on a face of an Octree cell, and the surface discretization configurations are shown in Figure 2.15. Notably, in Types 1, 2, and 5, a node is added to the middle of the face. Because the discretization of the edges remains unchanged, no changes are necessary on the other faces of the cell as a result of this change. In comparison to the preceding rectangular elements, only isosceles triangular and rectangular elements appear on the faces of an Octree cell with the inclusion of the extra center node. When the usual 2D Gauss-Lobatto quadrature is used, these elements provide precise integration results (Saputra, Talebi, Tran, Birk, & Song, 2017).

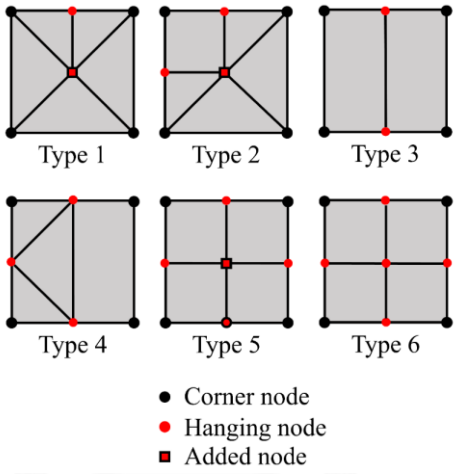

จุฬาลงกรณ์มหาวิทยาลัย
Chulalongkorn University

Figure 2.15 On one face of an Octree cell in a balanced Octree decomposition, there are six different forms of surface discretizations for potential hanging node configurations.

A mesh produced using the previously described surface discretization method is shown in Figure 2.16. In the center of the image are the octree cells with hanging nodes. The left side of the image displays faces S^1 and S^2, each of which is connected to two cells. Using triangular and quadrilateral components, the faces are discretized in the right-hand part of the diagram, where face S^1 is given a new node. The two cells that are closely related to that face are the only ones that are affected by the face discretization with hanging nodes. To control the hanging nodes, the graphic's right side additionally demonstrates the discretization of faces S^3 and S^4.

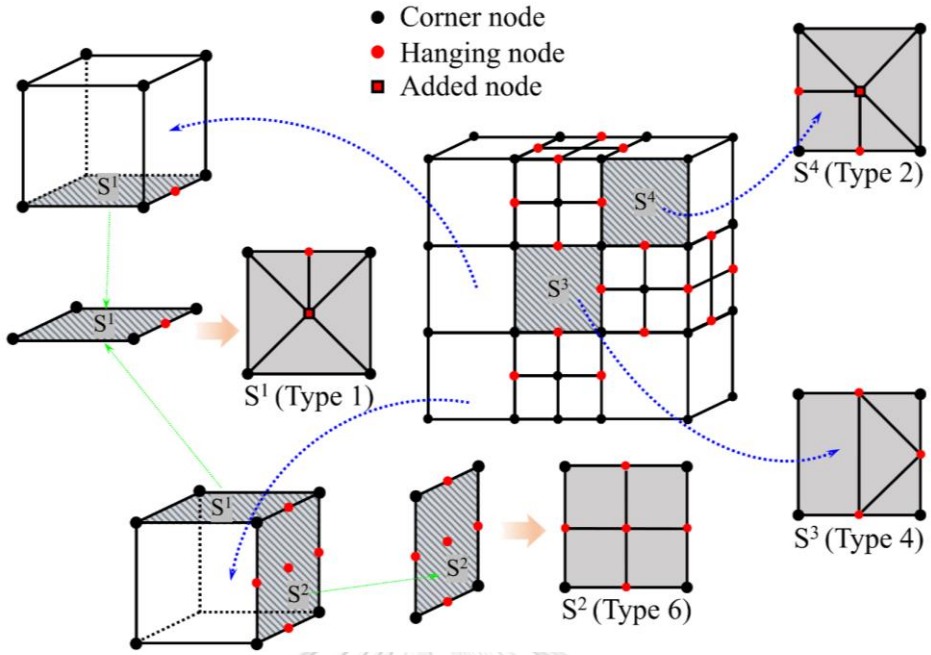

Figure 2.16 The surface discretization process of surfaces from S^1 to S^4 for a balanced Octree mesh with hanging nodes ((Saputra et al., 2017)).

3.4 Automatic Image-based mesh

Digital imaging techniques including X-ray computed tomography (X-ray CT) scans, electromagnetic resonance imaging, and ultrasound enable the noninvasive capturing of high-resolution images of an object's internal structure. Color intensity, for example, reveals characteristics about an object's shape and material distribution in digital photographs. As a consequence, this data may be converted into a useful mesh for use in a variety of computations. This technique, colloquially known as image-based analysis, has been studied in a variety of domains, including material characterization for finite element analysis (FEA) (Giraldi, Nouy, Legrain, & Cartraud, 2013; Terada, Miura, & Kikuchi, 1997); Legrain, Cartraud, Perreard, and Moës (2011) have discussed the extended finite element method (X-FEM) with level set computational approach for image-based analysis. The picture is presumed to have been split and saved in digital format.

จุฬาลงกรณ์มหาวิทยาลัย
Chulalongkorn University

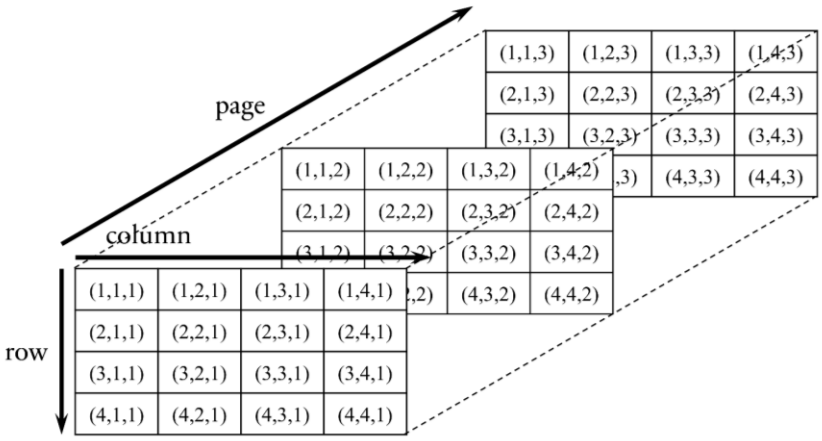

Figure 2.17 Multidimensional Arrays: Each element is defined by three subscripts; the row index, column index, and third dimension represent pages of elements.

After a 2D picture is inputted, each pixel is considered to represent a square domain of size $h \times h$, where h is the image sampling interval. An original image color matrix ($\mathbf{I}_{\text{ori}}$) stores all of the pixel's colors. In all arrays of matrix $\mathbf{I}_{\text{ori}}$, the color of each pixel is represented in the third dimension (page) by each array (Figure 2.17). The matrix's pages represented RGB triplets ranging from 0 to 255. (See Figure 2.18) This matrix, $\mathbf{I}_{\text{ori}}$, is padded with a backdrop color to create a square boundary matrix, $\mathbf{I}_{\text{bound}}$. The size of $\mathbf{I}_{\text{bound}}$ is an integer power of two, i.e., $2^n \times 2^n$, where n is a nonnegative integer. Any color can be used as the backdrop as long as it differs enough from every other hue in the original image.

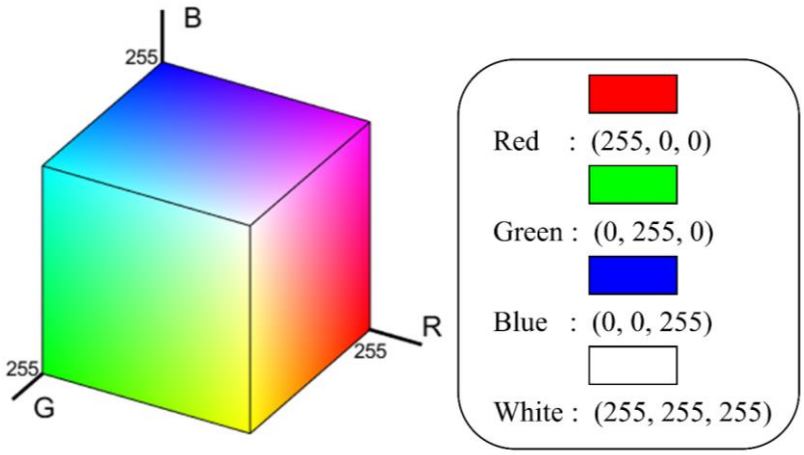

Figure 2.18 RGB color triplet cube for an image.

Figure 2.19a depicts a generic picture that will be discretized with a Quadtree mesh to demonstrate the Quadtree decomposition method. In this case, the standard for homogeneity is the tone of each cell. The picture in Figure 2.19a is split into four cells as a result of a preliminary application of the Quadtree decomposition (Figure 2.19b). The two bottom cells have now met the homogeneity requirement and will not undergo further partitioning. The two cells at the top are divided until the homogeneity condition is satisfied in all cells since they do not really fulfill it (Figure 2.19c).

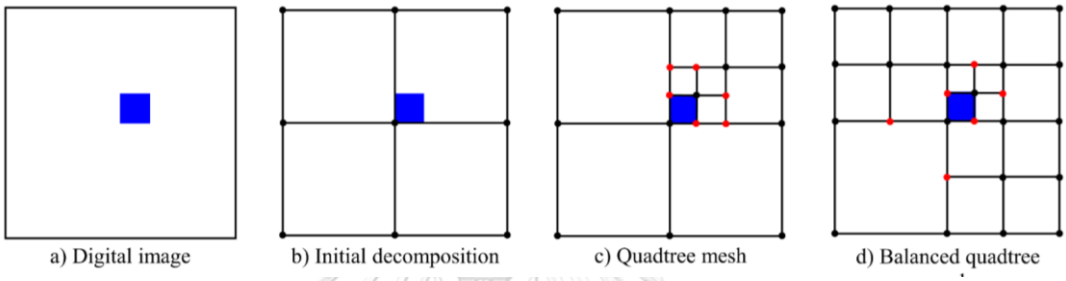

Figure 2.19 Balanced Quadtree mesh generation.

When a balanced Quadtree mesh is employed, the range of possible cell types is constrained to only those shown in Figure 2.20. This may be used to solve shifting boundary problems or large-scale computing problems efficiently. Only the cell type is required in a balanced Quadtree mesh, and this data may be precomputed, kept in CPU memory, and retrieved when necessary, during real calculations.

จุฬาลงกรณ์มหาวิทยาลัย
Chulalongkorn University

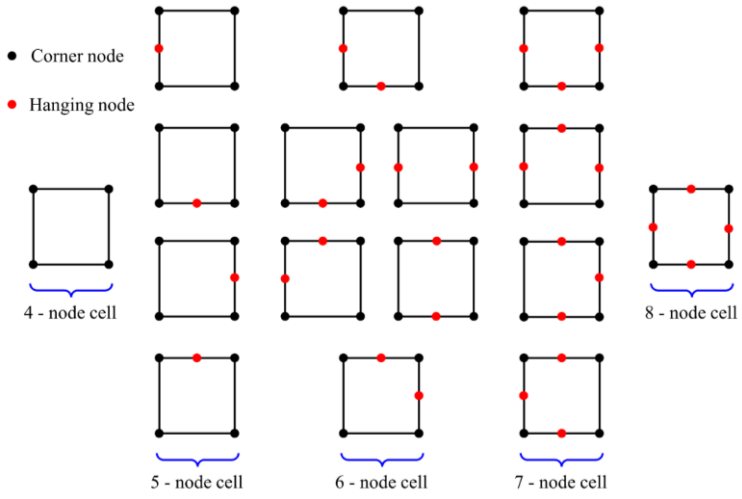

Figure 2.20 Specific quadtree cells based on a balanced Quadtree decomposition.

3.5 Quadtree/Octree Algorithm for SBFE Analysis

Automatic mesh generation was originally applied in SBFEM ((Ooi, Shi, Song, Tin-Loi, & Yang, 2013)) using the Delaunay triangulation algorithm with a polygon element. After a year, a modified SBFEM including the Quadtree mesh generation technique was proposed for stress analysis ((Man et al., 2014)). This approach of mesh creation using SBFEM overcomes two significant issues associated with conventional FEM. First, the use of hanging nodes is permitted in the absence of element subdivision. Because the edges of a quadtree cell can be subdivided into multiple line elements, it is possible to achieve displacement compatibility with the smaller cells adjacent to the larger cells. Each Quadtree cell is represented as a polygon element as illustrated in Figure 2.21. Second, curved boundaries are fitted accurately without excessive Quadtree mesh refinement using a high-order element. Recently, SBFEM with Quadtree algorithm has been extended to perform stress analysis in 3D complex geometry using the Octree algorithm ((Talebi, Saputra, & Song, 2016)). The study demonstrated that the Octree algorithm can successfully perform automatic mesh generation using SBFEM in a 3D domain. Additionally, Y. Liu et al. (2017) utilized polyhedral mesh creation using standard tessellation language (STL) models for SBFEM. This technique uses an STL model, which is straightforward but reliable for meshing a model with complicated surface geometry, to systematically trim a polyhedral mesh. With encouraging outcomes, a Quadtree mesh generation method has recently been applied in SBFEM for the simulation of mesoscale fractures in concrete (Guo et al., 2019). Digital pictures are automatically discretized using a balanced Quadtree decomposition and an image smoothing method in order to prepare them for analysis (Figure 2.22).

จุฬาลงกรณ์มหาวิทยาลัย
Chulalongkorn University

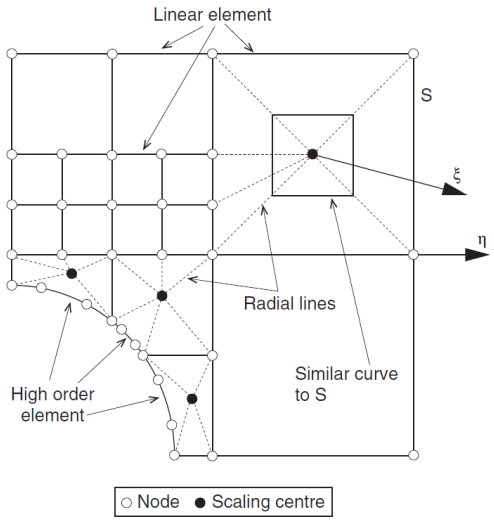

Figure 2.21 Scaled boundary representation of Quadtree cells. ((Man et al., 2014))

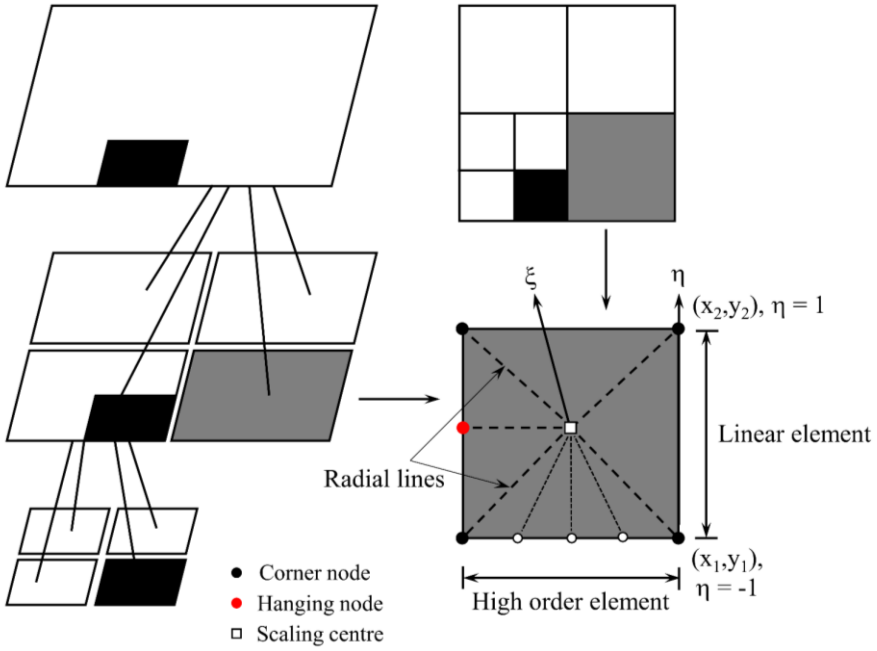

Figure 2.22 Example of image decomposition by Quadtree algorithm with sample SBFEM polygon element.

Each cubic cell is treated as a scaled boundary polyhedral element composed of surface components on the boundary to mitigate the aforementioned Octree decomposition. The issue area covered by the volume displayed in Figure 2.23 serves as an illustration of the salient aspects of an SBFEM. This volume covered the Octree cell's center, or the scaling center O. In terms of

local boundary coordinates (η, ζ), the surface elements along the border are specified. Therefore, a 2D interpolation shape function $[N(\eta, \zeta)]$ with natural coordinates $-1 \leq \eta \leq 1$ and $-1 \leq \zeta \leq 1$ may be used to represent each surface element. The reader can turn to these sources for further in-depth derivations and explanations: Saputra et al. (2017); Talebi et al. (2016)).

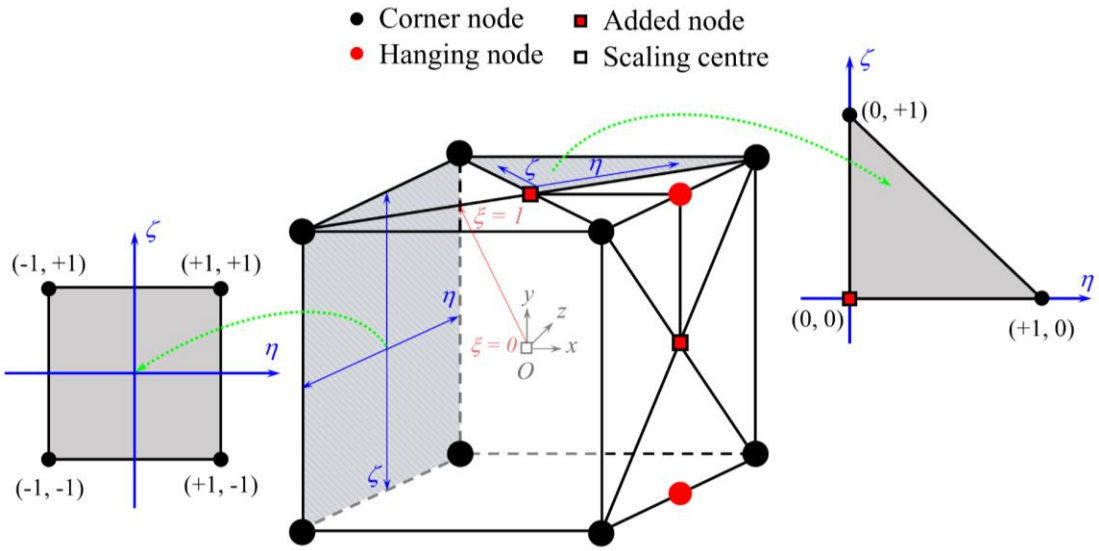

Figure 2.23 The surface formulation of the polyhedral elements using the isoparametric triangular and quadrilateral finite elements, with scaled boundary finite element local coordinates in an Octree cell.

จุฬาลงกรณ์มหาวิทยาลัย
CHULALONGKORN UNIVERSITY

4. Topology Optimization

4.1 Introduction

The goal of structural optimization is to meet certain limitations, such as using a certain quantity of material, but yet achieving the greatest mechanical performance for a structure. Because they may be utilized to characterize structural behavior during service, mechanical characteristics serve as the foundation for the formulation of structural optimization issues. The need for lightweight, affordable, high-performance structures has grown due to a lack of material resources, environmental effect, and technological rivalry. As a result, structural optimization design has gained importance and appeal among academics. Size, form, and topological optimizations are the three subcategories of structural optimization. The oldest and most straightforward method for improving structural performance is size optimization. The idea is to experiment with different size parameters, such as plate thicknesses and the cross-sectional sizes of trusses and frames, to discover the best design. In order to create the best designs, shape optimization is typically done on continuum structures by changing preset limits. For discrete structures like trusses and frames, topology optimization is utilized to find the best spatial arrangement and connection of the bars. The optimum placements and cavity geometries within the design domains are found via topology optimization of continuum structures (Figure 2.24) (X. Huang & M. Xie, 2010).

จุฬาลงกรณ์มหาวิทยาลัย

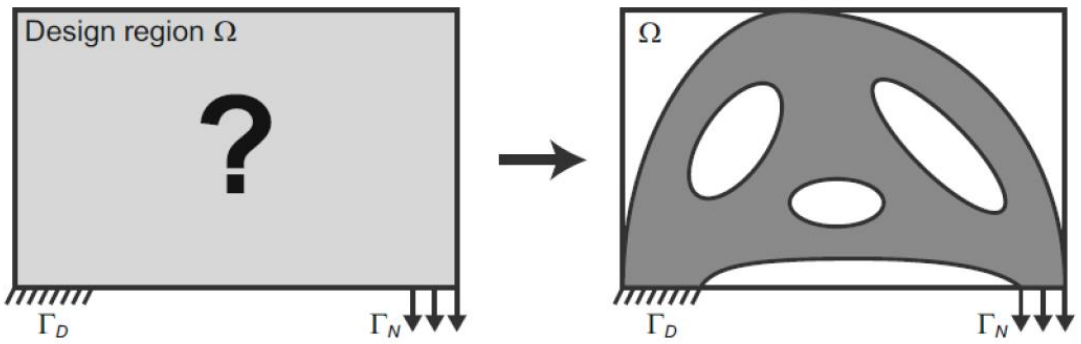

Figure 2.24 An example of conventional structural topology optimization (Xia, 2016).

The least-weight truss layout's optimality criteria were developed by Michell (1904), who also conducted the earliest topology optimization (TO) research. 70 years later, Rozvany and his team

expanded Mitchell's theory to account for the precise analytical optimum solutions of grid-type structures (W Prager & Rozvany, 1977; G. Rozvany, 1972a, 1972b). Numerous structural TO techniques have been created and improved over the years, primarily for the purpose of identifying the lightest, stiffest, and strongest structures. Examples include the homogenization method (Martin Philip Bendsøe & Kikuchi, 1988), SIMP (G. Rozvany & Zhou, 1991; Zhou & Rozvany, 1991), and ESO (Yi M Xie & Steven, 1993; Yi Min Xie & Steven, 1997). BESO is a well-known method that Huang and Xie have proposed (X Huang & Xie, 2007b; Xiaodong Huang & Xie, 2009). By using this technique, lost items can be recovered in close proximity to severely stressed locations. The sensitivity filter and stabilization techniques are included into the convergent and mesh independent BESO method utilizing some historical data.

In the next section, several concepts of TO algorithm are briefly explained. Notably, the TO algorithm can be readily used to achieve an optimal shape. However, the advantages and shortcomings of each algorithm differ. Finally, some literature reviews of BESO algorithm and procedures for obtaining an optimal solution are presented.

4.2 Topology Optimization Algorithms

4.2.1 Homogenization

Cheng and Olhoff (1981) originally suggested the mathematical formulation for the best plate design in the homogenization method, which was based on the thin plate principle. They came to the conclusion that neither the class of smooth functions nor the class of smooth functions with a finite number of discontinuities typically has a global optimum solution. Years later, a microstructure was used to address a number of research on optimum design issues. The idea of relaxing was developed by Kohn and Strang (1986a) for the variational issue of formulating for optimum design. By taking into account the useful qualities for porous finite elements in a domain, (Suzuki & Kikuchi, 1991) use the homogenization technique (HM) to TO. The HM was initially created by Anathasuresh et al. as a structural optimization method for the creation of compliant mechanisms (Ananthasuresh, 1994). Assuming that these porous patches had a rectangular shape (Figure 2.25), HM was able to conduct TO since the holes' length $\mu(x)$,

จุฬาลงกรณ์มหาวิทยาลัย
Chulalongkorn University

breadth $\gamma(x)$, and orientation $\theta(x)$ could all be mathematically described. One benefit of this approach is the creation of a porous optimum design with densities ρ ranging from zero to one, or $0 \leq \rho \leq 1$.

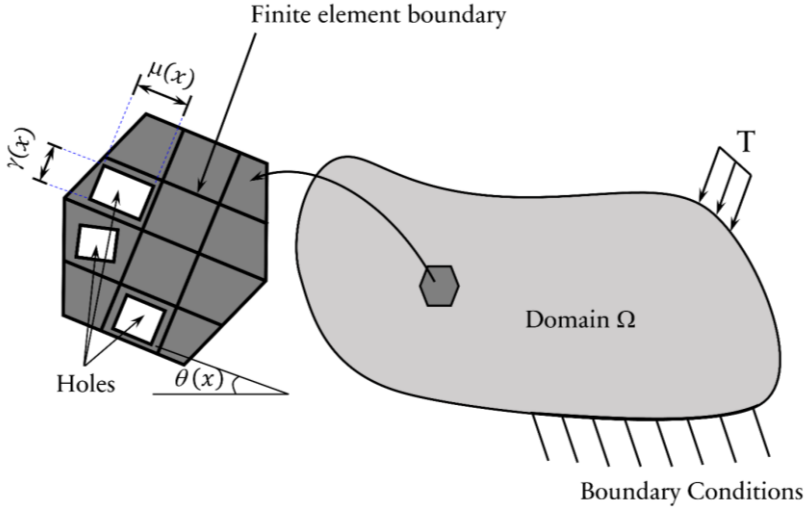

Figure 2.25 Rectangular hole in elements with various parameters i.e., $\mu(x)$, width, $\gamma(x)$, and orientation, $\theta(x)$.

The whole concept of HM ((Allaire, 1997)) obtained the optimum sizes and orientation of holes in each element with both ρ and the Stiffness tensor $\left(E_{ijkl}\right)$ of the domain related to $\mu(x)$, $\gamma(x)$, and $\theta(x)$.

$$\rho(x) = \rho\left(u(x), \gamma(x), \theta(x)\right), \qquad E_{ijkl} = \tilde{E}_{ijkl}\left(u(x), \gamma(x), \theta(x)\right) \tag{4.1}$$

Yuge, Iwai, and Kikuchi (1999) state that the following four stages should be followed in order to apply modeling holes in HM procedures: (1) Assuming initial parameter values for $\mu(x)$, $\gamma(x)$, and $\theta(x)$; (2) determining the rotated homogenized effective elasticity tensor; (3) using FEA to obtain displacement field; and (4) updating the values of the three design variables and their Lagrange multipliers and repeating this process until the optimality criteria is met (William Prager, 1968). The fact that the holes are rectangular assures that the whole spectrum of elemental porosities, from completely empty to fully solid, is acceptable. HM with quadrilateral meshes with rectangular-shaped holes, however, may be challenging to apply in a triangle mesh in 2D

จุฬาลงกรณ์มหาวิทยาลัย
CHULALONGKORN UNIVERSITY

FEA issues. Additionally, HM implementation necessitates a great deal of effort because each element requires a lot of variables.

Although the HM originally took use of TO compliant mechanisms and has significant implications for improving compliant mechanisms using continuum-based models, the HM will not be used in this dissertation to achieve the best possible design of compliant mechanisms. The goal of the research should be to find and create an optimization strategy that can result in final designs of compliant mechanisms that are stable and clear. The paper by Xia and Breitkopf (2017) explains additional efforts to apply HM.

4.2.2 Solid Isotropic Microstructure with Penalization

In order to address issues with compliant mechanism design, the SIMP technique has been investigated. The SIMP technique, which provided an artificial density (intermediate density) for forecasting the topology of a mechanical element, was initially studied by Martin P Bendsøe (1989). This density-based strategy for the ideal design of a compliant mechanism was recently proposed by Sigmund (1997). The SIMP method employs the material density to characterize each element, as opposed to the HM, which uses the sizes and orientation of the micro voids (Y. Li, 2014). As seen in Figure 2.26, the SIMP technique uses intermediate densities for each element. In structural optimization, the material density is punished to deter the development of intermediate densities.

จุฬาลงกรณ์มหาวิทยาลัย
CHULALONGKORN UNIVERSITY

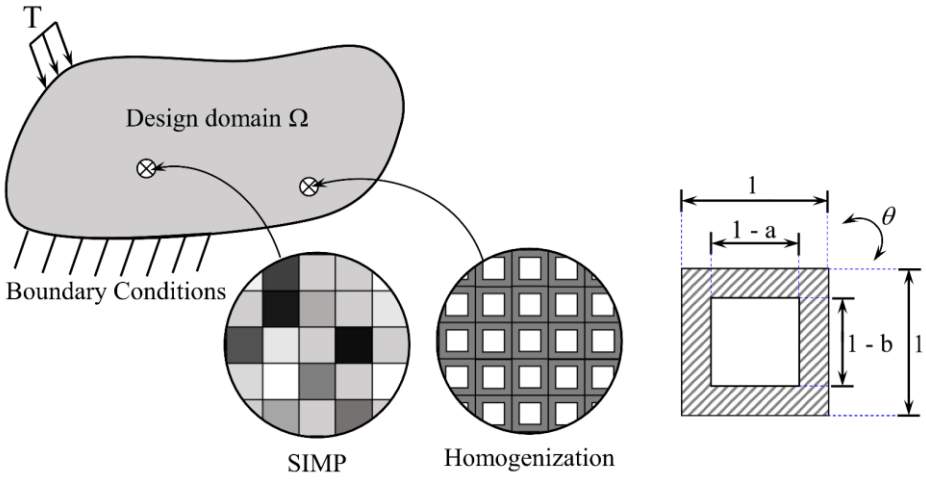

Figure 2.26 Comparison of SIMP and HM algorithms.

To get elemental densities to a precise specification of an optimal value, fictitious densities $(0 \leq \rho \leq 1)$ are subjected to a gradual penalization. By this, the Stiffness tensor $\left(E_{ijkl}\right)$ can be represented as a function of the density, $\rho(x)$, and it has the form (Martin P Bendsøe & Sigmund, 1999):

$$E_{ijkl}\left(x\right) = \rho\left(x\right)^{P} \bar{E}_{ijkl} \tag{4.2}$$

where p is the penalty factor, which is usually assumed to be greater than 1. The elastic tensor of the substance connected to domain is $\bar{E}_{ijkl}$. It was covered by Rietz (2001) that this penalty element can vary. The SIMP approach for standard problems was first given by Sigmund (2001) in MATLAB and involved 99 lines of code. Andreassen, Clausen, Schevenels, Lazarov, and Sigmund (2011) offered an improved version that required just 88 lines of code. Additionally, K. Liu and Tovar (2014) expanded the SIMP approach into a productive 3D MATLAB code. Figure 2.27 shows the process flow for these steps. At first, elemental densities were used to run the algorithm. The elemental elastic modulus, E_e, is calculated from Eq (3.2) using these densities. To prevent singularities in the design domain, a lower restriction on the modulus E_{min} must be introduced. Consequently, Eq. 3.2 becomes

$$E_e\left(\rho_e\right) = E_{\min} + \rho_e^P\left(\bar{E}_{ijkl} - E_{\min}\right) \tag{4.3}$$

The objective function for a task requiring the Compliance, C minimization can be written as

$$C = \sum_{e=1}^{N} E_e\left(\rho_e\right) u_e^T K_e u_e \tag{4.4}$$

จุฬาลงกรณ์มหาวิทยาลัย
Chulalongkorn University

where N represents the overall number of elements in the domain, u_e represents the elemental nodal displacement matrix produced from a FEA, and K_e represents the element stiffness. The elemental sensitivity number (α_e) is calculated using sensitivity analysis by differentiating equation 3.4 with regard to ρ_e. To avoid areas of deleted and undeleted elements grouped in a grid-like arrangement, filtered elemental densities are further calculated using these sensitivity numbers (checkerboard pattern). New elements densities are calculated using filtered elemental sensitivities after filtering, and the entire process is repeated until the convergence condition is met.

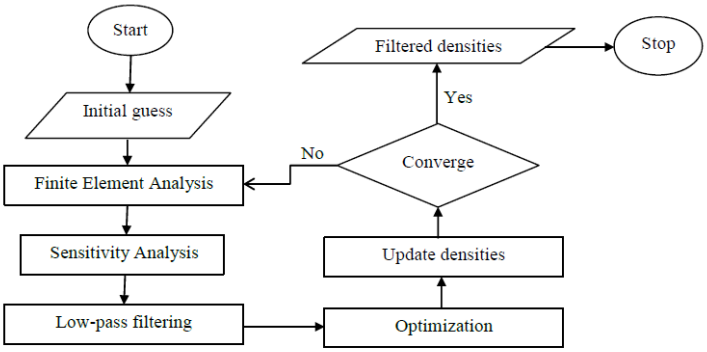

Figure 2.27 Flowchart of the SIMP algorithm (Aremu, 2013).

Continuous improvement has been made to the SIMP algorithm. The SIMP model and associated density-based approaches have been promoted and expanded to cope with the synthesis of large displacement compliant mechanisms (Y. Du, Chen, & Luo, 2008), capturing these techniques in geometrically nonlinear structures (Yoon & Kim, 2005). In 2010, Le, Norato, Bruns, Ha, and Tortorelli (2010) introduced stress-based TO issues with the SIMP method. Their research inspired the definition of stress to combat the stress singularity phenomena and the measurement of global and regional stress in conjunction with an adaptive normalization strategy to regulate local stress levels.

According to Montes, Ivvan, Pe, and Rionda (2016), this is a strong TO algorithm that has been developed extensively in a variety of applications. However, because the SIMP approach is used to inhibit the emergence of intermediate densities in a solution, ambiguous resultant topologies typically show up in earlier work.

จุฬาลงกรณ์มหาวิทยาลัย
CHULALONGKORN UNIVERSITY

4.2.3 Evolutionary Structural Optimization

Yi M Xie and Steven (1993) devised a technique known as ESO. It is based on the idea of gradually eliminating inefficient materials from the structure's finite element model so that the structure's topology gradually grows toward an ideal state. The approach was initially used to look for answers to completely stressed design issues. The ESO method was then constantly improved and used to a variety of TO designs, including stiffness limitations (Chu, Xie, Hira, & Steven, 1996) and frequency difficulties (Yi Min Xie & Steven, 1997) Since its first appearance, the treatment has become extremely popular and has been the focus of in-depth research because

to how straightforward it is. The stress criterion and sensitivity number were the two key element-removing criteria used in this method under the ESO technique.

Stress Criterion: Based on the amount of stress in the components, this idea was utilized to establish the rejection criterion. The degree of Von Mises stress in the structure's components, according to Hinton and Sienz (1995), was used as the criterion for determining which pieces should be removed. Small von Mises stresses were regarded as ineffective materials and eliminated. The Von Mises stress is expressed as follows in aircraft stress issues:

$$\sigma_e^{VM} = \sqrt{\sigma_{11}^2 + \sigma_{22}^2 - \sigma_{11}\sigma_{22} + 3\sigma_{12}^2} \tag{4.5}$$

where a FEA is used to determine the stress level in the elements. The elemental Von Mises stress in each element is compared to the maximum Von Mises stress of the structure σ_{max}^{VM} in each iteration of the ESO method. Elements that comply with the following requirement are entirely eliminated from the structure's finite element model at the conclusion of each FEA.

$$\frac{\sigma_e^{VM}}{\sigma_{\max}^{VM}} = RR^k \tag{4.6}$$

The rejection ratio at iteration k is represented here by RR^k. The "stationary state" occurs when no more elements can be removed from the structure, and the iteration process is then complete. All structural parts have a stress level greater than $\sigma_{max}^{VM} \times RR^i$ at steady state. The evolutionary rate (ER), which is referred to as an initial parameter in the ESO, is raised by the rejection ratio if it is essential at this point.

CHULALONGKORN UNIVERSITY

$$RR^{k+1} = RR^k + ER \tag{4.7}$$

The same procedure is then repeated until the new steady state is attained after this increment. When the structure reaches the target stress level (for example, when there are no longer any components with a stress level less than 20% of the maximum stress), the operation is finished. The only situations in which a fully strained structure may be achieved are a few rare ones, thus this idea might not be the greatest one overall.

Sensitivity Number: Sensitivity rankings may be used as one of the additional design domain element elimination criteria. The sensitivity number serves as a gauge for assessing how each factor affects the variance of the goal function or constraint for a given evolutionary process. To

push structures toward optimums, low sensitivity element numbers are eliminated from the FEA. Chu et al. (1996) modified the elements removal criterion in the original ESO for the compliance optimization by employing the elemental sensitivity number α_e as

$$\alpha_e = u_e^T K_e^0 u_e \tag{4.8}$$

where K_e^0 is the volume of each elemental stiffness matrix and u_e is the displacement vector of the e^{th} element resulting from the FEA of the structure. The optimization process adopted in the compliance-based procedure is basically the same as that used in the stress-based ESO procedure. The only necessary modifications are that α_{max} and α_e were replaced with σ_{max}^{VM} and σ_e^{VM}, respectively.

Overall, one of the suitable options for TO is the ESO algorithm. When the criteria are rigorously applied, this notion can yield the best result (G. I. Rozvany & Querin, 2002). To address 3D issues, the ESO method was improved. However, researchers pointed up a number of shortcomings. First, in certain circumstances, appropriate solutions cannot be achieved since the deleted parts could not be restored into the design domains. The rationale for this is that the material that was permanently eliminated in earlier iterations could now be required for the current iteration's best design (X. Huang & Y.-M. Xie, 2010). Second, in comparison to the ideal design from the previous iteration, the topology may alter significantly (Zhou & Rozvany, 2001). The conventional ESO approach failed to address significant numerical TO issues including checkerboard pattern and mesh dependence (X. Huang & M. Xie, 2010).

Currently, researchers have proposed a new advancement for ESO. The technique included an evolutionary strategy additive algorithm (X Huang & Xie, 2007b). In order to address the drawbacks of the ESO approach, an enhanced version of the technique known as BESO was developed (Querin et al., 1998; Querin, Steven, & Xie, 2000; Querin, Young, Steven, & Xie, 2000). The BESO approach and its modified version were used in this research to construct compliant systems. The next part will provide a detailed description and analysis of the BESO algorithm idea.

จุฬาลงกรณ์มหาวิทยาลัย
Chulalongkorn University

4.3 Bi–directional Evolutionary Structural optimization

The BESO concentrates on concurrently adding and removing elements from the FE model of the structure and has a search capacity that is superior to that of the original ESO. The ESO technique entirely eliminates the inefficient components from the design domain, therefore the implications of these components on the objective function in subsequent stages of optimization are unknown. The primary idea of BESO is to come up with a plan to replace the deleted elements, if necessary. Studies on the ESO have led to major developments, one of which being the BESO method (Radman, 2013).

4.3.1 Early BESO method

The early BESO approach, which is an enhanced variant of the ESO methodology, both eliminates inefficient components from structures and recovers the elements that have been removed. By using a stress-based optimality criteria, this BESO technique progresses from a minimal ground structure to a fully strained structure. The early version of the BESO approach is more reliable and effective in structural optimization when compared to the ESO method (Yang, Xie, Liu, Parks, & Clarkson, 2002).

Additionally, BESO was modified by Yang et al. (2002) to include perimeter control and a smoothing technique, respectively. Figure 2.28 shows the Messerschmitt-Bolkow-Blohm (MBB) beam in its ideal form. The end material volume, or objective volume, may be less than the initial design domain's volume. Additionally, this approach can enhance numerical stability and produce solutions independent of the mesh. X Huang and Xie (2007a) presented new work on the BESO approach in 2007. By expanding the linear BESO approach, a TO process for the stiffness design of structures with nonlinear material undergoing significant geometric deformations was provided. This improvement may have a big impact on local buckling issues. Furthermore, X Huang and Xie (2008) introduced the BESO algorithm of geometrically and materially nonlinear structures under displacement loading.

จุฬาลงกรณ์มหาวิทยาลัย
Chulalongkorn University

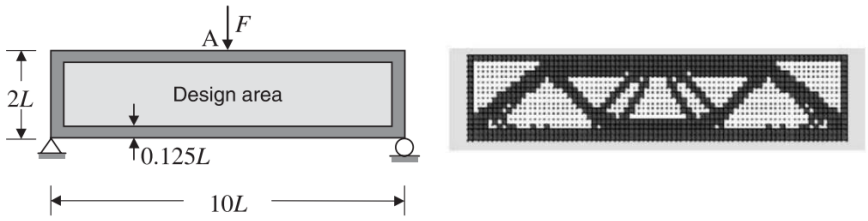

Figure 2.28 Design area and its optimal solution by the BESO algorithm (Yang et al., 2002).

However, the aforementioned version of BESO (especially the early BESO method) was not suitable for obtaining optimal solutions (G. I. Rozvany & Querin, 2002; Zhou & Rozvany, 2001). This dissertation emphasizes the following defects.

1. *Checkerboard pattern*: The sensitivity values may become discontinuous across element borders when a continuum structure is discretized using a low-order finite elements mesh. The generated topologies exhibit a checkerboard pattern of the continuum structure (Xuan, 2012). Figure 2.29 depicts a typical continuous structure from the ESO approach in the form of a checkerboard pattern. Structure design with checkerboard pattern is impractical. The element-scaled details are difficult to interpret and fabricating such a design is also impractical.

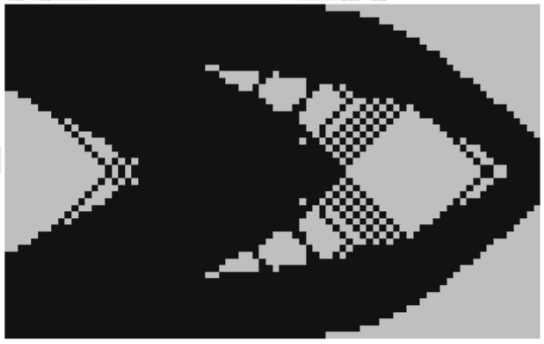

Figure 2.29 A typical checkerboard pattern.

2. *Mesh-dependency Problems*: These are the issues encountered while trying to use different FE meshes to achieve diverse solutions. The numerical process of structural optimization will result in a topology with more members of smaller sizes in the final design when a finer mesh is generated. Instead of producing a more intricate or qualitatively different structure, mesh refinement should ideally produce a better finite element modeling of the original

optimum structure and a better description of boundaries (Sigmund & Bondsgc, 2003). Figure 2.30 shows challenges with mesh independence.

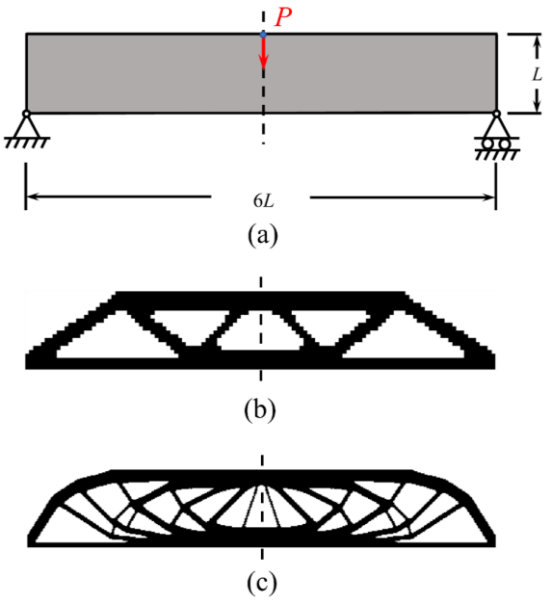

Figure 2.30 A simply supported beam with mesh-dependency problems; (a). Problem set; (b). design result with coarse mesh; (c). design result with fine mesh.

3. *Computational Efficiency*: The original BESO technique is considered a less efficient algorithm. Element addition and removal are carried out independently during the evolutionary process. As a result, multiple revisions are required to generate the final designs. Additionally, the algorithm is unable to ensure TO's correctness. The approach is unable to correctly estimate the change in the objective function because it is imprecise in estimating the sensitivity number of empty elements.

4. *Convergence*: The empirical premise is the basic underpinning of the element removal/addition technique. It is necessary to have a solid mathematical justification that guides the evolutionary process in the direction of the best design. Without mathematical explanation, chaotic convergence results in the historical outcome of the optimization process.

จุฬาลงกรณ์มหาวิทยาลัย
Chulalongkorn University

4.3.2 Improvement in Computational Efficiency

An enhanced BESO approach process has been offered as a novel BESO development (X Huang & Xie, 2007b). Discrete design variables are still utilized in this approach to overcome optimization issues. The optimization approach will use the approximate variation of the objective function to estimate the sensitivity numbers of the components after deleting individual ones. However, the method of optimization has been given a few innovative approaches. Every time the design domain is iterated, for instance, the elements might be concurrently removed and added. By applying the material interpolation approach, the erased elements (void elements) can be regarded as soft elements (Xiaodong Huang & Xie, 2009). Ferrari and Sigmund (2020) provide the condensed and effective MATLAB implementations of conformance TO for 99 lines in 2D and 125 in 3D continuum mechanics.

4.3.3 Sensitivity Filter Scheme

Additionally, by averaging the initial sensitivity values of nearby components, the filter scheme idea is used to increase each element's sensitivity number. The definition of *a filter* is a zone where all components have an impact on the center elements' sensitivity number (Figure 2.31).

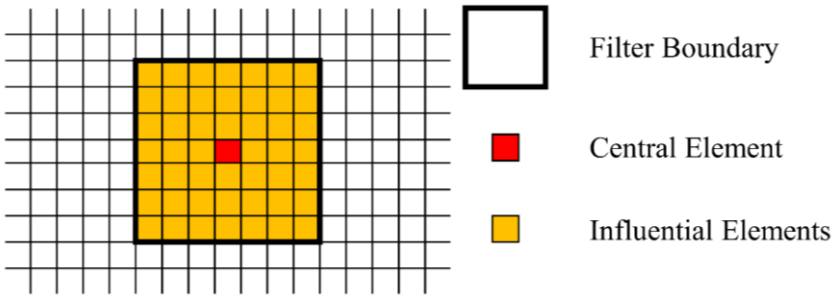

Figure 2.31 Illustration of Filter Scheme Concept.

The process of filter scheme formation comprises two steps. In the first step, sensitivity numbers are defined in the nodes and called *nodal sensitivity numbers*. These nodes are the interconnection points of elements (Xuan, 2012). By averaging the sensitivity numbers of all elements connected to a node, nodal sensitivity numbers are obtained. The typical expression is

$$\alpha_j^n = \sum_{e=1}^{M} w_e \alpha_e \tag{4.9}$$

where M is the total number of elements connected at j^{th} node and w_e is the weight factor of the e^{th} element which can be defined as

$$w_e = \frac{1}{M-1}\left(1-\frac{r_{ej}}{\sum_{e=1}^{M} r_{ej}}\right) \tag{4.10}$$

where r_{ej} is the central distance between the e^{th} element and j^{th} node and $\sum_{e=1}^{M} w_e = 1$.

However, this concept has no physical meaning; it was produced for the purpose of calculating sensitivity in each element.

The second step is to produce *elemental sensitivity numbers* by averaging *nodal sensitivity numbers* within a filter. Theoretically the filter can be any shape as long as it covers an adequate neighborhood to ensure the smoothness of resulted values. Circular filters are illustrated below for easy understanding.

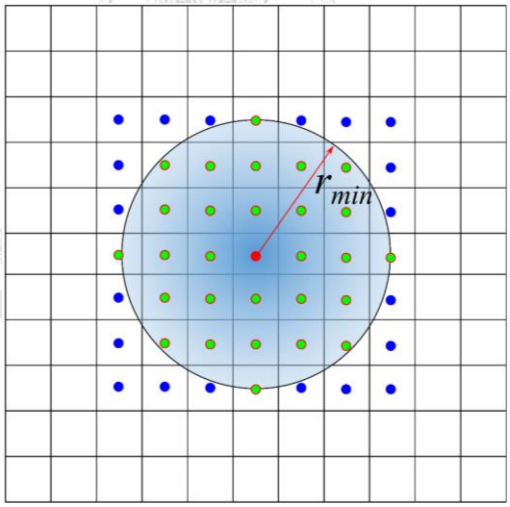

Figure 2.32 Diagram of sensitivity filter method; green dots and the red line represent the included nodes/elements; blue dots represent the nodes/elements that are not included.

As depicted in Figure 2.32, this scheme has a radius of filter, r_{min}, which does not change with mesh refinement. All nodes inside the filter domain will be identified as influential to the central element. Therefore, the elemental sensitivity number can be calculated using

$$\alpha_e = \frac{\sum_{j=1}^{K} w\left(r_{ej}\right)\alpha_j^n}{\sum_{j=1}^{K} w\left(r_{ej}\right)} \tag{4.11}$$

where K is the total number of nodes inside the filter domain and $w\left(r_{ej}\right)$ is the weight factor obtained by $w\left(r_{ej}\right) = r_{min} - r_{ej}$.

The sensitivity number of a void element is initially assigned as zero. According to FEA, displacement vectors for all DOFs are obtained. Initial sensitivity numbers can subsequently be calculated using Eq. (4.8). Based on initial sensitivity numbers, an improved value for both solid and void elements of the domain will be obtained with the filter scheme. The resulting sensitivity numbers are used in element selection for the topology design in the current iteration. By averaging, this filter scheme avoids a sudden change in sensitivity numbers around neighboring elements, and thus, the checkerboard pattern can be overcome. The filter size does not change with mesh refinement, so the problem of mesh-dependency no longer exists.

4.3.4 Element Selection Process

The ground domain elements are added and removed using the BESO algorithm to improve the structure. It applies two discrete values: x_{min} for void elements and 1 for solid elements. The discrete element x_{min}= 0 is used in the original BESO, also known as hard-kill BESO. The total elimination of a solid element from the design domain, however, can lead to theoretical issues with TO and numerical instability. It is also possible to "eliminating" an element by decreasing its elastic modulus or one of its defining characteristics, such thickness, to a very low number. This technique is known as soft-kill BESO. The solid and void elements' sensitivity numbers are written as

จุฬาลงกรณ์มหาวิทยาลัย
Chulalongkorn University

$$\alpha_e = \begin{cases} \frac{1}{2}\mathbf{u}_e^T \mathbf{K}_e^0 \mathbf{u}_e & \text{when } x_e = 1 \\ x_{\min}^{p-1}\left(\frac{1}{2}\mathbf{u}_e^T \mathbf{K}_e^0 \mathbf{u}_e\right) & \text{when } x_e = x_{\min} \end{cases} \tag{4.12}$$

The sensitivity numbers of solid elements are independent of the penalty exponent p, while those of the soft elements depend on the p value.

After improvements in elemental sensitivity numbers are determined from Eq. (4.11), the element selection process may commence. The initial volume in the design domain of a structure is assumed to be 1 or 100 %, i.e., all elements are solid. This total volume will be reduced step by step in iterations until the prescribed objective volume constraint V^* is reached. An *evolutionary rate ratio*, ER, is introduced to produce a volume constraint in iterations. For the iteration k, volume constraint V_k is obtained from

$$V_k = V_{k-1} \times (1 - ER) \geq V^* \tag{4.13}$$

The elemental sensitivity number with the largest values will appear as (1) until the solid elements amount to the volume V_k. The remaining elements with a volume of $(1 - V_k)$ and low sensitivity numbers will be selected as absent (0). Consequently, current elements form a structure topology as a design of iteration k.

4.3.5 Stabilization Scheme of the Evolutionary Process

As previously mentioned, one topology design is obtained in each iteration. This design is analyzed in the next iteration and further improved upon to generate a new design. By repeating this process, the evolutionary procedure continues until the optimal solution is obtained.

The goal function and associated topology, however, might not converge. Large oscillations in the objective function's development history are frequently seen in practice, slowing or preventing the convergence of the final design. The optimization procedure's reliance on discrete design variables of presence (1) and absence is the cause of this chaotic behavior (0). Averaging the sensitivity number with its historical data is a practical technique to address this issue, according to X Huang and Xie (2007b). The averaging method is described as

$$\alpha_i = \frac{\alpha_i^k + \alpha_i^{k-1}}{2} \tag{4.14}$$

where superscript k is the current iteration number and α represents the sensitivity number. Let $\alpha_i^k = \alpha_i$ in the current iteration for topology design and in the next iteration as historical information. The comparison experiment of the effectiveness in the stabilization process is depicted below.

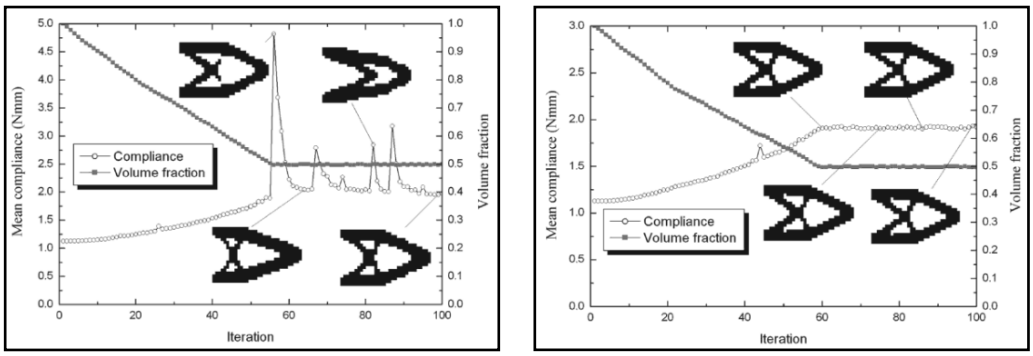

Figure 2.33 History of evolution for structural compliance: (a) with no stabilization strategy; (b) with a stabilization strategy (X Huang & Xie, 2007b).

As illustrated in Figure 2.33, fluctuations in the objective function of compliance occur during optimization without the stabilization scheme. When the averaging technique is applied, most of the oscillation is absent, and the process becomes very steady; the optimization result converges sooner than without averaging technique. The final topologies of the two processes are very similar, meaning this technique only influences the result of the evolutionary process to a small extent.

Consequently, it is a good practice to average the current improved sensitivity numbers with historical ones and to use the averaged values for element selection.

จุฬาลงกรณ์มหาวิทยาลัย
Chulalongkorn University

4.3.6 Convergence Criterion

The cycle of performing FEA and element removal/addition continues until an objective volume, V^*, is reached. Subsequently, the evolutionary process continues with the constant volume V^*. To confirm that an optimization has successfully obtained its final design, a convergence criterion must be satisfied as a stopping criterion of the evolutionary process.

$$error = \frac{\left| \sum_{i=1}^{N} C_{k-i+1} - \sum_{i=1}^{N} C_{k-N-i+1} \right|}{\sum_{i=1}^{N} C_{k-i+1}} \leq \tau \qquad (4.15)$$

This criterion implies that a design is considered to be convergent when the sum of objective functions from iteration $(k - 2N + 1)$ to iteration $(k - N)$ is adequately close to the sum of

that from iteration $(k - N + 1)$ to iteration (k). The tolerance τ can be determined as required by users.

Once the above criterion is satisfied, the entire optimization process is terminated and the final design is taken as the optimum design ((Tikenoğulları, 2015)).

4.3.7 Current BESO method

The BESO algorithm is a method that has been continually refined and improved since it was first introduced. In its current form, the BESO method incorporates a number of new techniques into its optimization procedure. One example of this is the use of material interpolation schemes with penalization, which allows the BESO method to be applied to multiple materials at once (as described in (Xiaodong Huang & Xie, 2009)). This mathematical interpolation technique is demonstrated in Figure 2.34, which shows an example of an optimal solution using the BESO method with multiple materials.

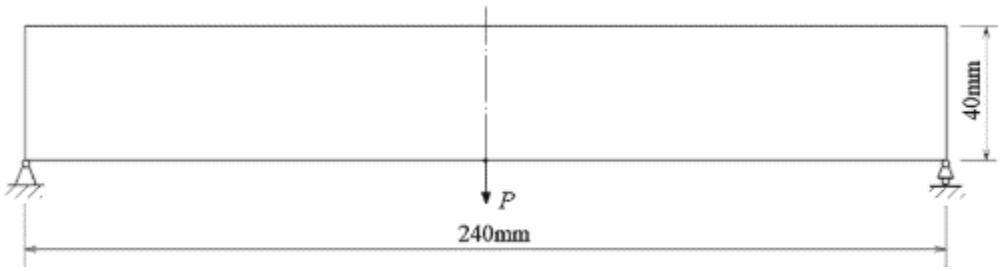

(a)

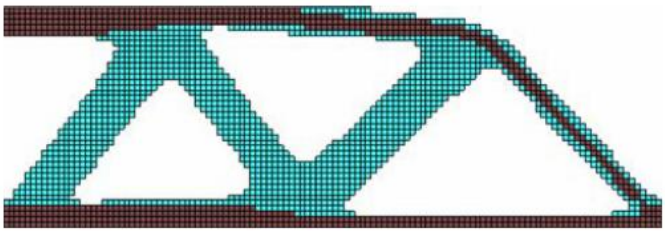

(b)

Figure 2.34 TO in multimaterials: (a) design domain and support conditions for a beam; and (b) BESO optimal design for a three-phase structure. ((Xiaodong Huang & Xie, 2009))

Moreover, an extended BESO method for stiffness optimization with a material volume or local displacement constraint has been introduced by X. Huang and Y. Xie (2010). The results of this work show the possibility of solving any TO problems with multiple constraints using the BESO technique. In the same year, X Huang et al. (2010) also performed TO using the BESO technique for the frequency optimization problems. Recently, a method of BESO was formulated for compliance minimization (stiffness optimization) and incorporated into X-FEM ((Abdi, 2015)). The optimal solution by X-FEM combined with BESO is illustrated in Figure 2.35. The result confirms a significant improvement in the boundary representation of the solutions.

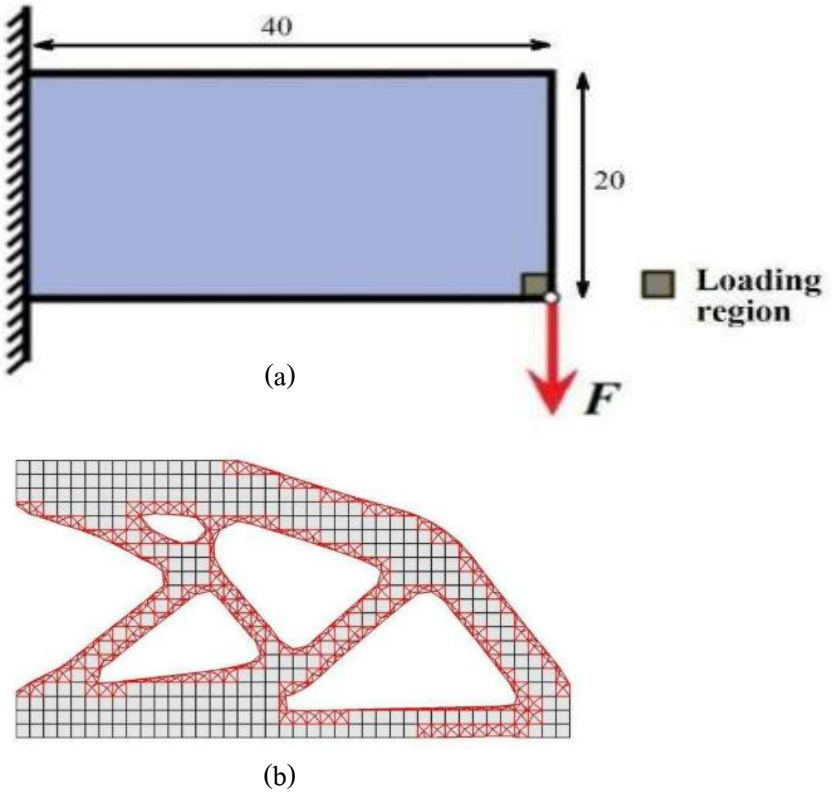

Figure 2.35 TO of continuum structures using X-FEM: (a) design domain and support conditions for a cantilever plate; (b) BESO optimal design of the 2D cantilever plate. (Abdi, 2015)

Furthermore, Xia, Zhang, Xia, and Shi (2018) have presented an evolutionary TO technique for stress minimization design utilizing the BESO method. Using the traditional p-norm global stress metric, the maximum stress is roughly estimated. In particular, the adjoint sensitivity of the global

stress measure is used to build a sensitivity number formulation that is computationally efficient. Figure 2.36 shows the stress minimization design for the TO method's optimal solution based on the BESO algorithm. Since the technique inherits the BESO method's advantage of being discrete, it automatically avoids the "singularity" issue in stress-based topology designs.

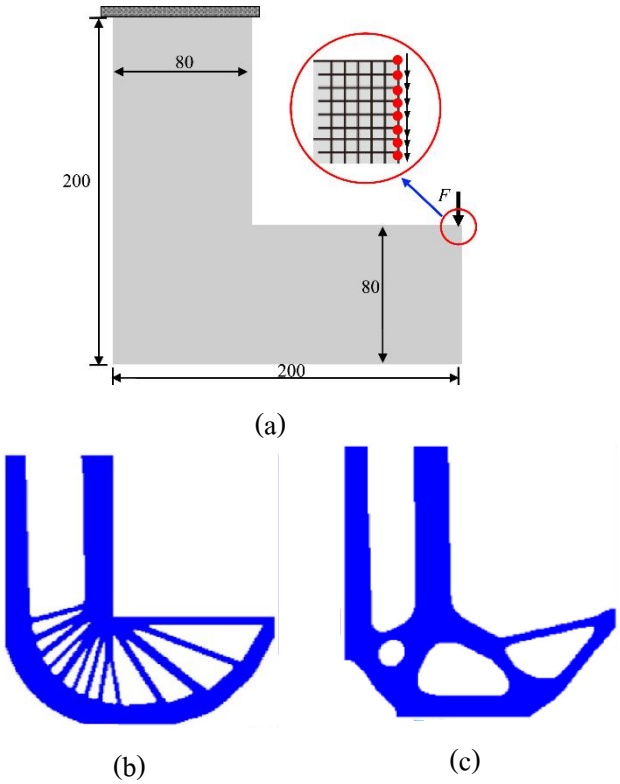

จุฬาลงกรณ์มหาวิทยาลัย
CHULALONGKORN UNIVERSITY

Figure 2.36 Illustration of the L-bracket benchmark problem: (a) load and boundary conditions; (b) linear stiffness design without stress constraint; and (c) optimum design with stress constraint. (Xia et al., 2018)

Finally, Han, Xu, and Liu (2021) suggested an expanded BESO approach for stress reduction TO of material nonlinear structures. Filtering topological variables and sensitivity values stabilized the optimization process for highly nonlinear stress behavior. Figure 2.37 shows the outcomes of the L-bracket utilizing the BESO technique for stress reduction and the elastic-plastic incremental stress-strain relationship. The suggested method's efficacy and applicability are well demonstrated by the optimal solutions to a number of 2D benchmark design challenges.

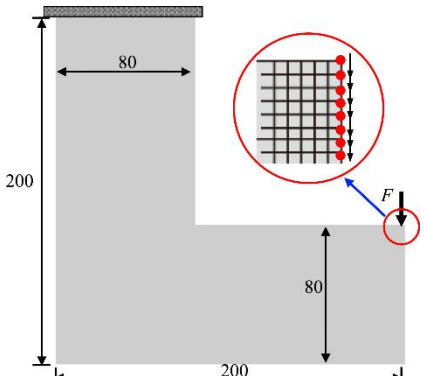

Problem statement with load and boundary conditions.

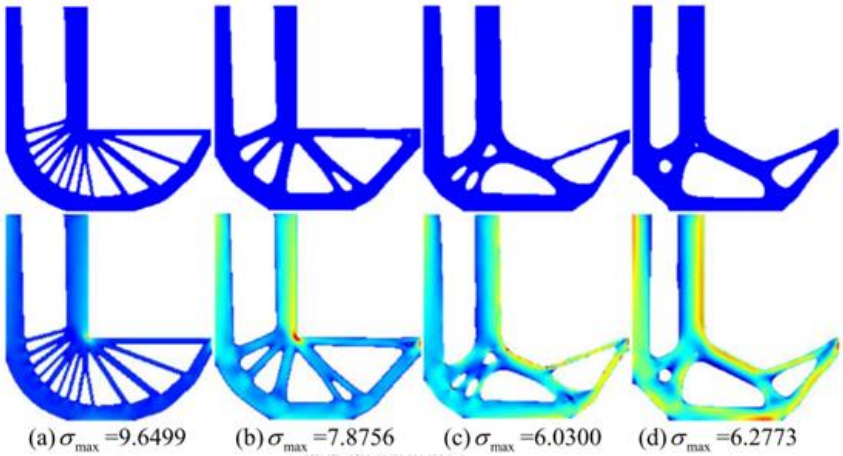

Figure 2.37 The L-bracket benchmark under various topological designs and von Mises stress distributions, including (a) a linear stiffness design, (b) a material nonlinear stiffness design, (c) a linear stress design, and (d) a material nonlinear stress design ((Xu et al., 2021))

จุฬาลงกรณ์มหาวิทยาลัย
Chulalongkorn University

4.4 BESO algorithm Procedure

The overall processes of evolutionary optimization for a single material can be outlined as follows.

Step 1: To create an initial design, the whole design domain is discretized using a finite element (FE) mesh with sufficient elements. Initial property values x_i (x_{min} or 1) are then assigned to the elements to construct the initial design. This process involves dividing the design domain into smaller elements in order to accurately represent the structure's geometry and material properties in the analysis. The initial property values assigned to the elements serve as a starting point for

the optimization process, and will be adjusted during the optimization to improve the performance of the structure.

Step 2: Define BESO parameters such as objective volume, V^*, evolutionary rate ratio ER, radius of filter r_{min}, and penalty exponent, p.

Step 3: Define the design domain, where the domain can be designable or limited.

Step 4: Perform FEA for the real and virtual structures (which undergo the dummy load) and subsequently calculate the elemental sensitivity numbers α_i.

Step 5: To determine the target volume for the next iteration of the design, the current volume of the design V_k need to be calculated. If this current volume exceeds the target or objective volume V^*, then using equation (Eq. 4.13) to calculate the target volume for the next design iteration. By using this equation, the target volume for the next design iteration is determined in order to more closely approach the desired objective volume.

Step 6: The elemental sensitivity number are filtered by Eq. (4.11) for the whole design domain.

Step 7: Reduce and add to the finite element model. For solid elements, the elemental density is changed from 1 to x_{min} if the following criterion is satisfied:

$$\alpha_e \leq \alpha_{th}$$

จุฬาลงกรณ์มหาวิทยาลัย
CHULALONGKORN UNIVERSITY

Conversely, the elemental density for a void element is changed from x_{min} to 1 if the following criterion is satisfied.

$$\alpha_e > \alpha_{th},$$

where α_{th} is the threshold of the sensitivity number, which was determined by the target material volume, $V_{(k+1)}$, and the relative ranking of the sensitivity numbers.

5. Multimaterial Topology Optimization

5.1 Introduction

The material is predetermined in single-material topology optimization (SMTO), and the structure is optimized with regard to it. Engineers have more design freedom to develop a range of high-performance inventive structures thanks to the SMTO design of the continuum structure, which optimizes size and shape. As a result, it is regarded as the most complicated area in structural optimization. The utilization of individual materials has advanced significantly thanks to this revolution, but the structural system as a whole is made up of a range of elements with unique features. Therefore, it is essential for the design and fabrication of the overall performance of the structure to optimize the topology of multiphase materials.

In contrast to SMTO, MMTO is a subject of ongoing study. A combined functional structure with improved performance and cheaper cost may be created via the design of multiphase materials. The MMTO is designed to concurrently seek the best structural shape and different material distributions. The inherent mathematical structure of the design space is mostly responsible for MMTO's difficulties. When dealing with a single material, the design variable is just the occupancy of that material. The corresponding design space is typically sufficiently regular and is simple to resolve, for example by applying the optimality criteria (Deng, Vulimiri, & To, 2021).

จุฬาลงกรณ์มหาวิทยาลัย
CHULALONGKORN UNIVERSITY

Since the introduction of MMTO, there has been constant progress employing different methods. One common SIMP material model in MMTO, for instance, takes into account three-phase materials, including two solids and one void (Bendsoe & Sigmund, 2003). Recently, Xiaodong Huang and Xie (2009) introduced the multimaterial BESO method. Ghabraie (2015) developed a more effective soft-kill BESO algorithm that can manage issues with both single- and multiple-material distribution. D. Li and Kim (2018); Sanders, Aguiló, and Paulino (2018) as well as D. Li and Kim (2018) provide detailed descriptions of the MMTO continuum based on several objective functions. For the local modal problem in the dynamic frequency problem, an improved multiphase material BESO is also put out (Gan & Wang, 2021).

5.2 MMTO formulation

The design area for the continuum structure will be divided into a few material parts for the TO design, and each of them will be given M topological design variables that each represent a variety of materials. Figure 2.38 depicts a MMTO design schematic. The topology design variables in the TO framework of the soft-kill BESO algorithm only accept the value of x_{min} or 1, without the intermediate density value. For numerous materials, the topological design variables x of the entire design domain may be written as

$$x_e^m = \begin{bmatrix} x_1^1 & \cdots & x_n^1 \\ \vdots & \ddots & \vdots \\ x_1^M & \cdots & x_n^M \end{bmatrix}, \tag{5.1}$$

where n is the overall number of elements in the design domain, M is the overall number of materials phases, and x_e^m is the design variable for elements with the m^{th} material.

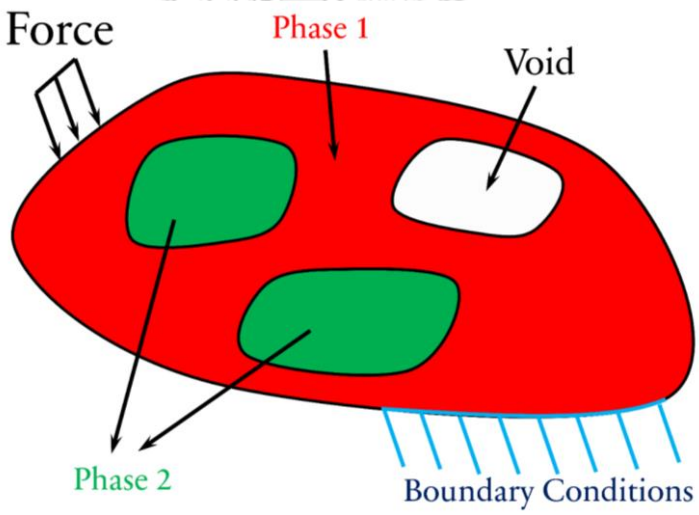

Figure 2.38 Schematic of the MMTO design.

In density techniques, "porous" material qualities are determined by design variables (so-called densities) using an interpolation function. A power function is utilized as the relationship in the well-known SIMP approach.

$$E^{(1,2)}(\varphi^1) = (\varphi^1)^p E^1 + (1 - (\varphi^1)^p) E^2, \tag{5.2}$$

where $E^{(m)}$ is the Elastic modulus of the m^{th} material and $\varphi^{(m)}$ is an artificial density of m^{th} material when $\varphi^{(m)} \in (0, 1]$. For three-phase materials, Eq. (4.17) can be extended as

$$E^{(1,2,3)}(\varphi^1,\varphi^2) = (\varphi^1,\varphi^2)^p E^1 + (\varphi^1)^p(1-(\varphi^2)^p)E^2 + (1-(\varphi^1)^p)E^3 \tag{5.3}$$

The M materials required by the SIMP method $(M-1)$ design variables (void is treated as a special material). From this point forward, the relative density and equivalent elastic modulus of multiphase materials may be represented as

$$E^{(1,\ldots,M)}(\varphi) = \sum_{m=1}^{M} w_m\, E^{(M-m+1)} \tag{5.4}$$

where

$$w_m = [1-(\varphi^m - \varphi^m \delta_{mM})^p] \prod_{j=1}^{m-1} (\varphi^j)^p \tag{5.5}$$

$$\delta_{mM} = \begin{cases} 1, m = M \\ 0, m \neq M \end{cases} \tag{5.6}$$

Figure 2.39(a) shows the interpolation of Young's modulus for three-phase SIMP material methods (two solids and one void). An important method for updating material characteristics is the multimaterial interpolation theory. But the BESO algorithm divides the design variable into two categories: black and white (without the intermediate density). Figure 2.39(b) shows the BESO material interpolation system, which is portrayed as linear. The objective, constraints, and sensitivities of MMTO issues may be calculated via material interpolation such that optimization algorithms can solve MMTO problems.

จุฬาลงกรณ์มหาวิทยาลัย
CHULALONGKORN UNIVERSITY

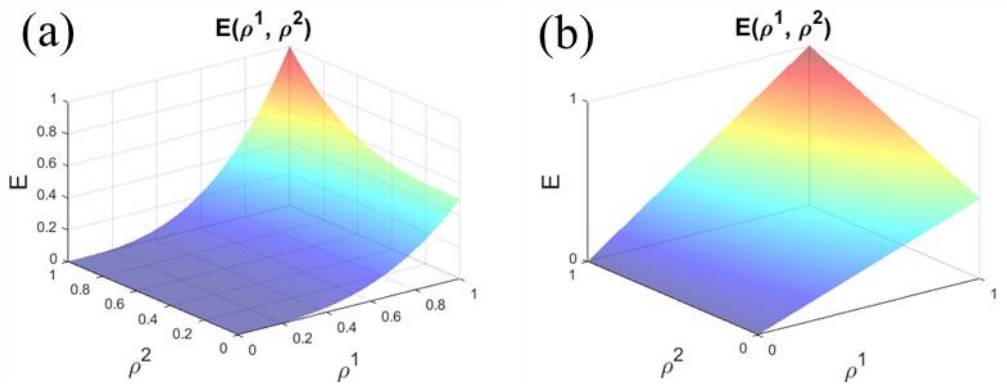

Figure 2.39 Plots and contours for elastic modulus of an element of the traditional MMTO: (a) material interpolation of elastic modulus for SIMP and (b) material interpolation for BESO.

5.2.1 Problem statement

The static features of the structure with MMTO will be taken into account in this challenge. The MMTO problem takes into account the maturity level challenge of increasing a structure's stiffness or compliance while keeping the amount of total mass under control. The compliance minimization issue for SMTO is represented as

$$\min C(x) = \sum_{e} \mathbf{u}_e^T \mathbf{K}_e \mathbf{u}_e = \frac{1}{2}\mathbf{F}^T\mathbf{u}$$

$$s.t.: \frac{\sum_e x_e^1 V_e}{\sum_e V_e} \leq V_1^* \tag{5.7}$$

$\mathbf{Ku} = \mathbf{F}$, for static problem

$x_e^1 = x_{min}\ or\ 1, e = 1, \dots, n$

For MMTO, the compliance minimization problem in Eq. (4.22) is extended as

$$\min C(x) = \sum_{e} \mathbf{u}_e^T \mathbf{K}_e \mathbf{u}_e = \frac{1}{2}\mathbf{F}^T\mathbf{u}$$

$$s.t.: \frac{\sum_e \left[V_e \prod_{m=1}^{j}(x_e^m)\right]}{\sum_e V_e} \leq V_j^*\ j = 1, \dots, M \tag{5.8}$$

$\mathbf{Ku} = \mathbf{F}$, for static problem

$x_e^m = x_{min}\ or\ 1, e = 1, \dots, n;\ m = 1, , \dots, M$

where C is the compliance, $\mathbf{F}$ is the external force vector, V_e is the volume of e^{th} element, V_j^* is a volume fraction limit, totally M constraints for M materials, and $\mathbf{K}$ is the global stiffness matrix.

จุฬาลงกรณ์มหาวิทยาลัย
Chulalongkorn University

5.2.2 Sensitivity analysis

To obtain elemental sensitivity in multimaterial interpolation, taking derivatives on both sides of the equilibrium equation with respect to the design variable x_e^m gives

$$\frac{\partial \mathbf{K}(x_e^m)}{\partial x_e^m}\mathbf{u}(x_e^m) + \mathbf{K}(x_e^m)\frac{\partial \mathbf{u}(x_e^m)}{\partial x_e^m} = 0 \tag{5.9}$$

with basic transformation, we have

$$\frac{\partial \mathbf{u}(x_e^m)}{\partial x_e^m} = -\mathbf{K^{-1}}(x_e^m)\frac{\partial \mathbf{K}(x_e^m)}{\partial x_e^m}\mathbf{u}(x_e^m) \tag{5.10}$$

From the compliance definition and equilibrium equation, the compliance of structure can be written as

$$C(x) = \sum_{\boldsymbol{e}} \mathbf{u}^{\boldsymbol{T}}(x_e^m)\mathbf{K}(x_e^m)\mathbf{u}(x_e^m) = \frac{1}{2}\mathbf{F}^{\boldsymbol{T}}\mathbf{u} \tag{5.11}$$

Any sensitivity in the multimaterial interpolation theory can be derived by differentiating Eq. (5.11) with respect to design variable x_e^m

$$\frac{\partial C(x)}{\partial x_e^m} = \frac{1}{2}\mathbf{F}^{\boldsymbol{T}}\frac{\partial \mathbf{u}}{\partial x_e^m} \tag{5.12}$$

Sensitivities of the objective with respect to design variable x_e^m can be expressed via the chain rule in an identical manner as single material case.

$$\frac{\partial C(x)}{\partial x_e^m} = \frac{\partial C(x)}{\partial \varphi_e^m}\frac{\partial \varphi_e^m}{\partial x_e^m} \tag{5.13}$$

The objective function can only compute the derivatives with regard to their internal parameters thanks to this division of the derivatives. These derivatives are suitable for volume restricted compliance minimization.

$$\frac{\partial C(x)}{\partial \varphi_e^m} = -\frac{1}{2}\mathbf{u}^{\boldsymbol{T}}\frac{\partial \mathbf{K}}{\partial \varphi_e^m}\mathbf{u} \tag{5.14}$$

For term $\frac{\partial \mathbf{K}}{\partial x_e^m}$ in material stiffness interpolation function, using the chain rule again, we separate the sensitivities of the design parameter as

$$\frac{\partial \mathbf{K}}{\partial \varphi_e^m} = \frac{\partial E}{\partial \varphi_e^m}\frac{\mathbf{K_e}}{E_e} \tag{5.15}$$

where $\mathbf{K_e}$ is the elemental stiffness matrix, $\frac{\partial \varphi_e^m}{\partial x_e^m}$ is the separate sensitivity number of each design variable. For BESO approach, this separate sensitivity function computes as

$$\frac{\partial \varphi_e^m}{\partial x_e^m} = (x_e^m)^{p-1} \tag{5.16}$$

จุฬาลงกรณ์มหาวิทยาลัย
Chulalongkorn University

The term $\frac{\partial E}{\partial \varphi_e^m}$, which is required by sensitivity analysis computation, can be obtained from the material interpolation equations. We differentiate the multimaterial interpolation equations (5.4) and (5.5).

$$\frac{\partial E^{(1,\ldots,M)}}{\partial \varphi_e^m} = \frac{\partial\left(\sum_{m=1}^{M} w_m E^{(M-m+1)}\right)}{\partial \varphi_e^m} = \sum_{m=1}^{M} \frac{\partial w_m}{\partial \varphi_e^m} E^{(M-m+1)} \tag{5.17}$$

where

$$w_m = [1 - (\varphi^m - \varphi^m \delta_{mM})^p] \prod_{j=1}^{m-1} (\varphi^j)^p \tag{5.18}$$

$$\delta_{mM} = \begin{cases} 1, m = M \\ 0, m \neq M \end{cases} \tag{5.19}$$

Using equilibrium equation and Eq. (5.10), the elemental sensitivity in multimaterial interpolation is further written as

$$\frac{\partial C(x)}{\partial x_e^m} = -\frac{1}{2}\mathbf{u}^{\boldsymbol{T}} \frac{\partial \mathbf{K}}{\partial x_e^m}\mathbf{u} = -\frac{1}{2}(x_e^m)^{p-1}\mathbf{u}_{\boldsymbol{e}}^{\boldsymbol{T}} \frac{\boldsymbol{K}_e}{E_e} \frac{\partial E}{\partial \varphi_e^m}\mathbf{u}_{\boldsymbol{e}} = -\alpha_e^m, \tag{5.20}$$

where the component-wise of α_e^m is the elemental sensitivity number for multimaterial element

$$\alpha_e^m = \frac{1}{2}(x_e^m)^{p-1}\mathbf{u}_{\boldsymbol{e}}^{\boldsymbol{T}} \frac{\boldsymbol{K}_e}{E_e} \frac{\partial E}{\partial \varphi_e^m}\mathbf{u}_{\boldsymbol{e}} \tag{5.21}$$

5.2.3 Filter Scheme

The elemental sensitivity number in the structural domain is averaged using the filter strategy in order to prevent frequent numerical instabilities including checkerboard pattern and mesh-dependency in TO. The filtered sensitivity number of multiphase materials can be extended from single material Eq. (4.11) as

$$\hat{\alpha}_e^m = \frac{\sum_{j=1}^{n} w(r_{ej})\alpha_e^m}{\sum_{j=1}^{n} w(r_{ej})} \tag{5.22}$$

$$w(r_{ej}) = \max(r_{min} - r_{ej}, 0), \tag{5.23}$$

where r_{min} is the filter radius, n is the total number of nodes inside filter domain, $\hat{\alpha}_e^m$ is the filtered sensitivity value of the e^{th} element in the m^{th} material, and r_{ej} denotes the distance between the center of elements e and j.

จุฬาลงกรณ์มหาวิทยาลัย
Chulalongkorn University

5.2.4 Variable updating

The sensitivity calculation method stated above offers a way to determine how the goal function changes over time. Elements with high sensitivity members are preferred kept in the design domain according to BESO's topological variable updating rule, whereas those with low sensitivity numbers are removed or allocated to weak-level structures. Notably, a multimaterial TO requires $M-1$ sets of sensitivity information rather than a single piece of sensitivity information for solid void design in order to update the design variables. As a result, the relationship between the number of material kinds and the quantity of sensitivity information is linear. For instance, in the three-phase materials design, the single material 1 is present in the design space at the first step of optimization. The stated volume-removal rate, RR, (also known as the evolutionary rate ratio, ER), for material 1 and the defined volume-addition rate, AR, for material 2, serve as the starting points for the optimization-process evolution. The following iteration's goal volume in the three-phase materials may be described as

$$\begin{aligned} V_1^{*(k+1)} &= \max\left(V_1^{*(k)}(1-ER), V_1^*\right) \\ V_2^{*(k+1)} &= \min\left(V_2^{*(k)}(1+AR), V_2^*\right) \\ V_3^{*(k+1)} &= 1 - V_1^{*(k+1)} - V_2^{*(k+1)}, \end{aligned} \tag{5.24}$$

where $V_m^{*(k)}$ is a representation of the material's current volume fraction of phase m at the k^{th} iteration. The volume of base material 2 is sustainably raised until the required volume of material 2 is satisfied, as shown from Eq. (4.34), as can be seen. The volume of base material 3 (the void element) then starts to rise as the volume of material 2 remains static and the volume of material 1 keeps shrinking. As was already established, the material interchanging only happens between two adjacent stages, and it ends when the volume restrictions of all the foundation materials are met.

จุฬาลงกรณ์มหาวิทยาลัย
CHULALONGKORN UNIVERSITY

5.3 MMTO–BESO Procedure

The entire MMTO–BESO-SBFEM procedure is simulated as in the SMTO algorithm described above. However, MMTO requires $M-1$ groups of sensitivity information to update the design

variables rather than a single sensitivity information for solid void design. From this point, the design variable for the MMTO must have an M set to perform a material interpolation scheme.

The flowchart of the MMTO scheme is shown in Figure 2.40 to help with understanding the reporting in the MMTO section. Notably, the MMTO-BESO (3-phase materials) method adds materials 2 and 3 without the intermediate element density and removes material 1 while progressively bringing the volume fraction closer to its volume constraint value. The optimization iteration procedure comes to a conclusion and the desired TO result is obtained when the volume of all materials is satisfied, and the minimal compliance of the objective function starts to converge.

จุฬาลงกรณ์มหาวิทยาลัย
CHULALONGKORN UNIVERSITY

Phase	MMTO-BESO-SBFEM steps	Equation
Pre-process	Define initial image and parameters $(V_j^*, RR, AR, r_{min}, p)$	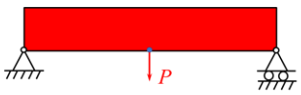
Process	While change in sensitivity value > tolerant	
	Input image and generate mesh	Chapter 3 section 2.1
	Identify material from colorized image	Chapter 2 section 3.4
	Apply load and boundary conditions	
	Generate design variable for M^{th} materials	(5.1)
	Match design variable for each material	
	Compute objective volume $V_j^{*(k+1)}$	(5.24)
	Perform SBFE analysis	Chapter 3 section 2.2
	Compute elemental sensitivity number α_e^m	(5.17 – 5.21)
	Average α_e^m by filter scheme	(5.22 – 5.23)
	Update design variables to match $V_j^{*(k+1)}$	(5.8)
	Perform material interpolation scheme	(5.4 – 5.6)
	Compute change in sensitivity value	(4.15)
Post-process	Optimal Topology	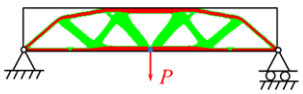

จุฬาลงกรณ์มหาวิทยาลัย
CHULALONGKORN UNIVERSITY

Figure 2.40 Flowchart of an MMTO–BESO with SBFEM analysis linked to corresponding equations.

CHAPTER 3 TOPOLOGY OPTIMIZATION FOR STATIC LOAD

1. Introduction

The soft-kill BESO (boundary element single objective) algorithm has become a popular method for solving topology optimization (TO) problems. The main goal of linear static response TO is to maximize stiffness, and there are two approaches to achieve this. One approach is to alter the material properties of a given structure configuration to optimize its stiffness, while the other approach involves fixing the material properties and choosing an arrangement that maximizes stiffness. TO typically focuses on the latter approach, which involves minimizing the compliance (the objective function) to maximize stiffness, subject to a specified volume constraint. Many researchers find it challenging to solve more complex TO problems, as illustrated in Figure 3.1. The standard finite element method (FEM) is often used to perform numerical analysis of optimal solutions for static responses obtained using the BESO technique, and an optimization methodology has been discussed in detail in previous sections.

The strong form boundary element method (SBFEM) was developed as an extension of the classical finite element method (FEM) in order to address some of the limitations and shortcomings of the FEM, such as its inability to handle complex geometries, nonmatching meshes, and hanging nodes in discretized domains. As briefly mentioned in Chapter 2, the SBFEM uses an image-based Quadtree/Octree approach to mesh initial continuum mechanic models, which effectively handles complex geometries. The use of S-elements in the SBFEM also allows for greater topological flexibility, eliminating the issue of hanging nodes. It is not necessary to further partition the Quadtree/Octree cells into finite elements with limited topological shapes, as the SBFEM can effectively handle a wide range of geometries. Overall, the combination of the SBFEM and the Quadtree/Octree approach allows for improved performance in structural analysis.

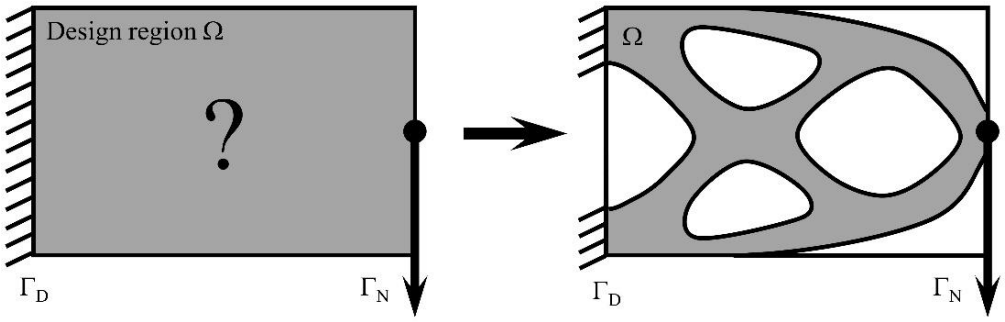

Figure 3.1 Illustration of typical structural topology optimization.

In this chapter, several benchmarks from the literature are selected to be solved using standard FEM with uniform meshes. Moreover, the optimal results from FEM are directly compared to the solutions from SBFEM intending to highlight the characteristics of the optimization and to validate the approaches that have been provided. The several examples is the short cantilever and symmetric half beam in 2D problems from the study by X Huang and Xie (2007b). Finally the 3D Messerschmitt–Bolkow–Blohm (MBB) beam optimization problem is solved and compared to the solution found in the study by X. Huang and M. Xie (2010). Subsequently, the convolution-filtered technique is applied to the benchmark problems, resulting in a flexible mesh with significantly fewer DOFs than conventional grid solutions. Finally, the MMTO is employed to achieve the optimal design with different materials.

จุฬาลงกรณ์มหาวิทยาลัย
CHULALONGKORN UNIVERSITY

2. SMTO Research Procedure.

2.1 The Quadtree/Octree Grid

Quadtree meshing is a process where a space is divided into four equal-sized quadrants, called "children," which can be further divided if a higher resolution is needed in a specific area. These quadrants are organized in a hierarchical tree structure, with the coarser "parent" at the top and the more refined regions towards the bottom according to predetermined rules. In MATLAB, the "qtdecomp" function can be used to divide image files into quadtrees based on the uniformity of color in each region, meaning that each quadrant can only contain one color. The creation of Octree meshes uses this idea in the same way. Additionally, MATLAB comes with a built-in feature called "otdecomp" that breaks down image files into an octree mesh. An image matrix model's bounding box is first identified as a square or cubic shape, and the user then specifies a maximum and minimum cell size. The border box is split into uniformly sized cells that do not exceed the permitted maximum cell size. Figure 3.2 shows examples of quadtree image-based implementation for concrete specimens subjected to uniaxial tensile strain at the top and bottom of the picture. In the illustration of Figure 3.3, the gray substance stands in for mortar, while the black substance represents aggregates. For both materials, Figure 3.3a for the aggregates and Figure 3.3b for the mortar, the results of the tensile primary stress are likewise displayed.

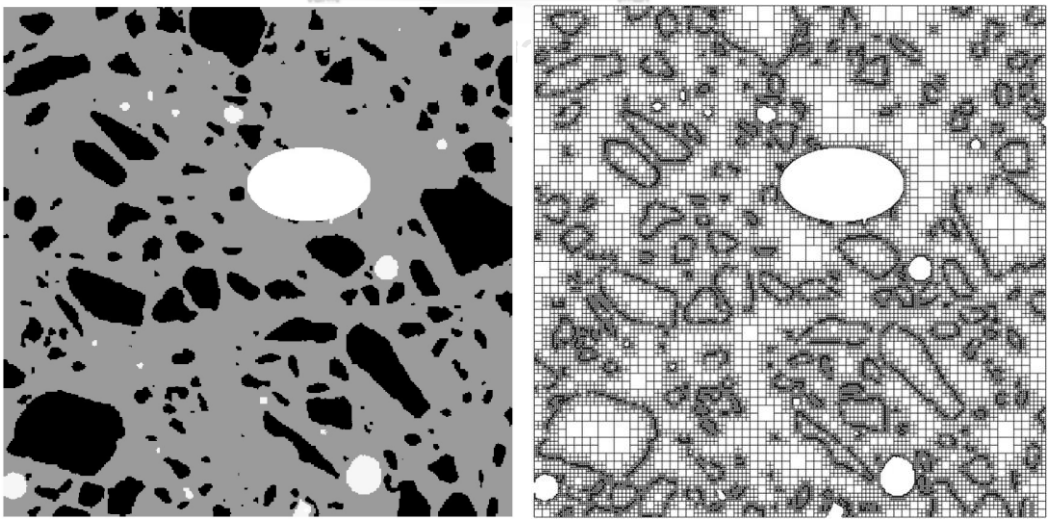

Figure 3.2 Mesh generation of concrete specimen by quadtree and an example of 2D concrete picture.

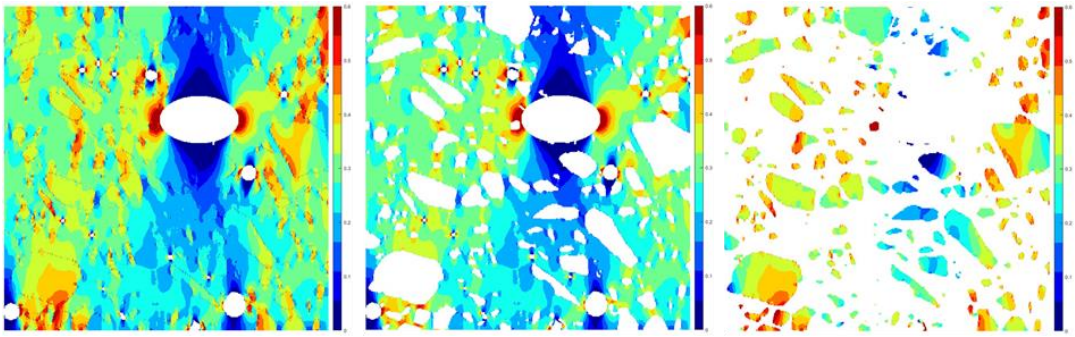

a) b) c)

Figure 3.3 The tensile principal stress in (a) both materials, (b) aggregates, and (c) mortar for 2D concrete.

2.2 Steps in Scaled Boundary Finite Element Analysis

The flowcharts in Figure 3.4 and Figure 3.5 have been included to help readers clearly understand the procedures, computational complexity, and effort needed for an SBFEM analysis because the whole process of TO is carried out using SBFEM. SBFEM investigations are best suited for domains with a low surface-to-volume ratio since constraining discretization along the border primarily compromises the resolution of an eigenproblem.

Phase	SBFEM steps	Equation
Pre-process	Input processing	
solution	For each sub-domain For each line element For each integration point	(2.41a-2.42a)
	evaluate coefficient matrices	(2.5b-2.7b)
	assemble coefficient matrices	
	form Hamiltonian	(2.5c)
	Eigen decomposition	(2.8c-2.10c)
	construct stiffness matrix	(2.20c)
	domain stiffness matrix	
	apply boundary condition	
	solve FEM equation	$\{u\} = [K]^{-1}\{F\}$
Post-process	back calculation	(2.22c) (2.15c) (2.43a) (2.44a)

Figure 3.4 SBFEM analysis flow chart with associated equations from Chapter 2.2.

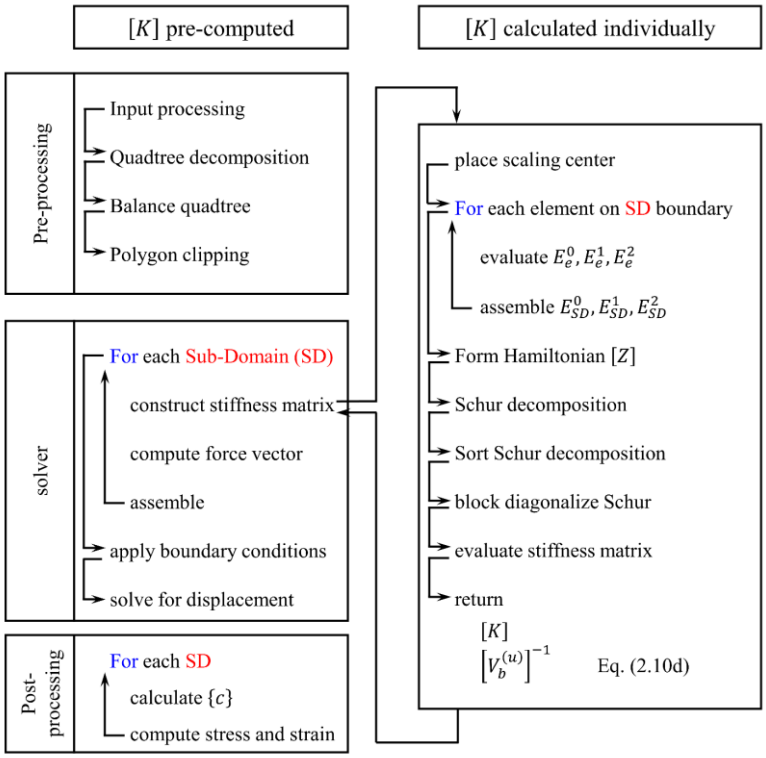

Figure 3.5 Steps comprising SBFEM analysis (Egger, 2019).

Each of the three coefficient matrices must be assessed and built separately for each of the three element-wise coefficient matrices using a standard numerical integration methodology, which is similar to the method used in traditional FE-based techniques. Contrary to the X-FEM, no extra enrichment words are required to be added. Consequently, it is not necessary to include the integration of singleton words. Many worries about the condition number of the stiffness matrix may be avoided with this technique since all the SBFEM components can be handled similarly. There is no need for any extra presumptions, such as those relating to the type of singularity to include in the enrichment of the crack tips.

2.3 Steps in the BESO-SBFEM algorithm

The entire BESO-SBFEM procedure for obtaining optimal solutions corresponding to the objective function comprises the following steps.

1. Precompute: For the 2D case, 16 possible Quadtree element realizations are precomputed with modulus of elasticity equal to one, and the steps differ slightly between 2D and 3D

since in 3D, the precomputation procedure employed for 2D results in 4096 unique Octree element realizations, whose construction requires building a substantial library and accompanying algorithmic logic. Instead, the unique element realizations for each 3D mesh are determined, and these are computed once and subsequently cloned for the remaining mesh.

2. Initialization: In this step, the dimensions of the design domain, an automatic image-based Quadtree/Octree mesh generation from previous sections, and the initial material distribution within the design domain are defined. By exploiting hierarchical image decomposition techniques, regions with homogeneous material properties are identified and represented by a single element. Boundary and loading conditions are prescribed and parameters of the optimization algorithm such as performance evolution rate ratio, ER, radius of filter, r_{min}, penalty exponent, p, and the final volume fraction, V^*, are defined.
3. Scaled Boundary Finite Element Analysis: After the design domain is automatically discretized by Quadtree/Octree decomposition, the SBFE analysis of the initial design domain is utilized. Numerical solutions such as the strain $\{\varepsilon\}$ and stress $\{\sigma\}$ field on the boundaries are obtained from Eqs. (2.43a) and (2.44a), respectively
4. Calculate the structural responses over the design domain (Sensitivity number α_i in each S-element).
5. To determine the target volume for the next iteration of the design process, the current volume, V_k, is compared to the objective volume, V^*. If the current volume is larger than the objective volume, the target volume for the next design can be calculated using Equation (4.13). This equation allows the optimization algorithm to adjust the target volume based on the current volume, ensuring that the final design meets the desired volume constraint.
6. Filter sensitivity numbers for each S-element in the entire design domain using Eq. (4.11) to avoid the checkerboard pattern and mesh-independent issues.
7. To achieve the convergent without large oscillations, the current sensitivity numbers of the current step are averaged with the previous step using Eq. (4.15)

จุฬาลงกรณ์มหาวิทยาลัย
Chulalongkorn University

8. The threshold sensitivity, α_{th} is chosen so that the number of elements with sensitivities lower than α_{th} is equal to the number of void elements. This is done by ranking all elemental sensitivity numbers.
9. To reset the design variables of all elements, the sensitivity of each element is compared to a threshold value, α_{th} If the sensitivity is less than the threshold, the minimum density, x_{min}, is assigned to the element; otherwise, a density of 1 is assigned to the element. This process allows the optimization algorithm to identify elements that do not significantly contribute to the performance of the structure and assign them a minimum density, reducing the weight of the structure.
10. Repeat 2–9 until the prescribed volume is achieved and the convergent criterion from Eq. (4.15) is satisfied.

The process of generating the mesh for the structure is simple and automatic, requiring only a minimal number of mesh control parameters from the user. Figure 3.6 shows the flow chart of the overall process, where S_{max} is the maximum cell size allowed in the Quadtree/Octree algorithm, S_{min} is the minimum cell size allowed to appear in the Quadtree/Octree algorithm, and S_{tol} is a value between 0 and 1. This value is multiplied by 256 and rounded to the nearest integer to determine the allowable range of color intensity that will be used as a stopping criterion during the Octree decomposition. In other words, the range of each Octree cell is calculated by subtracting the maximum and minimum color values in the cell, and if this range is less than or equal to the permitted range, the decomposition process is terminated. The use of the Quadtree/Octree algorithm allows the mesh to be adapted to the geometry of the structure and ensures that the cells are of an appropriate size for the analysis being performed.

จุฬาลงกรณ์มหาวิทยาลัย
Chulalongkorn University

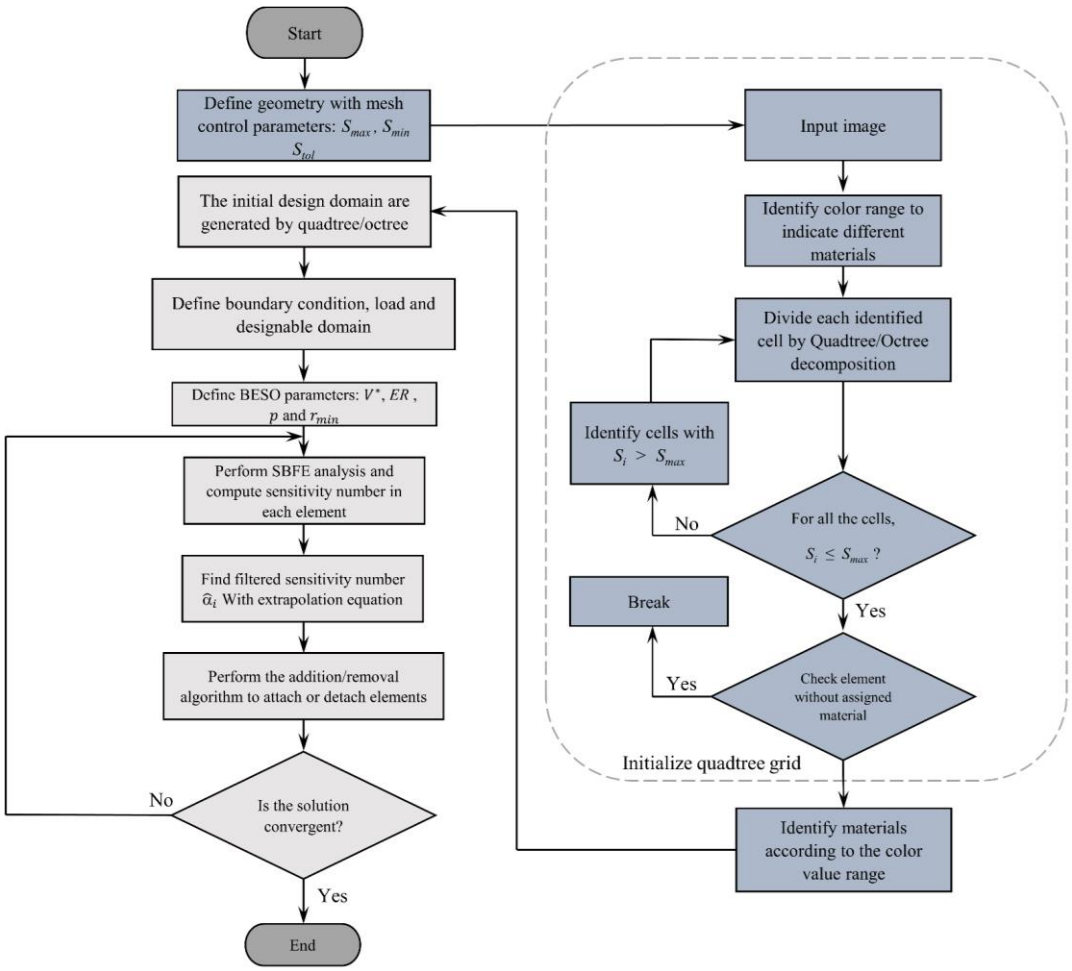

Figure 3.6 Flow chart of the overall process

จุฬาลงกรณ์มหาวิทยาลัย
CHULALONGKORN UNIVERSITY

2.4 Benchmark problems for 2D uniform mesh SMTO with static load structures

2.4.1 SMTO of a short cantilever beam

Problem statement

According to X Huang and Xie (2007b), the design domain for a short cantilever beam is 2L in length, L in height, and 1 mm in thickness (as shown in Figure 3.7). A downward force, P, is applied at the center of the free end, and the modulus of elasticity is set to 1, with a Poisson's ratio of 0.3. The available material (volume fraction, V^*) occupies 40 % of the design domain, and the BESO (boundary element single objective) parameters include an evolutionary rate ratio of 10 %, a maximum aspect ratio of 5 %, a filter radius of 8 mm, and a convergence criterion of 0.01 %.

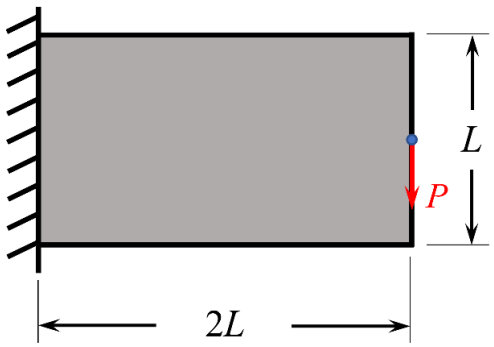

Figure 3.7 Dimensions of the design domain, boundary, and loading conditions for a short cantilever.

จุฬาลงกรณ์มหาวิทยาลัย
CHULALONGKORN UNIVERSITY

SMTO Results using the FEM

As demonstrated in this dissertation, the soft-kill BESO technique was effectively implemented using standard FEM and an optimal solution for the short cantilever benchmark problem was established. The domain is discretized into different mesh sizes: 128 × 64, 256 × 128, and 512 × 256 orthogonal finite element mesh composed of four-node quadrilateral elements. The evolution of the mean compliance for all mesh sizes are plotted in Figure 3.8. Table 3.1 depicts the optimal topology results for a variety of mesh sizes and the evolution of the mean compliance.

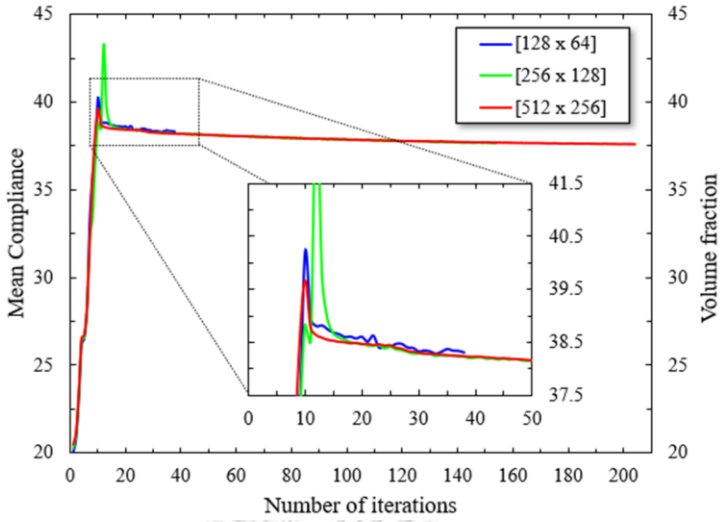

Figure 3.8 Evolution histories of mean compliance for 2D-MBB beam using FEM + BESO.

Mesh size	Iterations	Compliance	Optimal result
128 × 64	38	38.3007	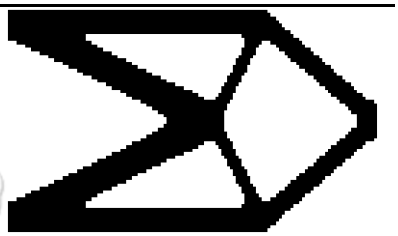
256 × 128	154	37.6805	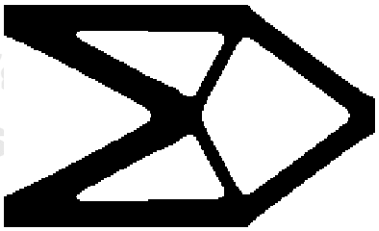
512 × 256	204	37.6298	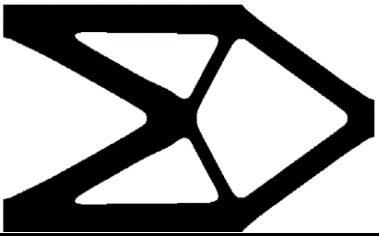

Table 3.1 Topology results of short cantilever beam performed using FEM + SMTO-BESO.

SMTO Results using the SBFEM

As aforementioned on the results from single material TO using FEM, this work is motivated by the adoption of SBFEM for solving TO problems, and with several beneficial features, the SBFEM has proven itself as a remarkably versatile tool in automatic image-based stress analysis. Compared to conventional FEM, the initial design domain is also uniformly discretized into the same grid. The evolution of the mean compliance and the optimal topology results for a variety of mesh sizes are displayed in Figure 3.9 and Table 3.1.

With image-based implementation, remeshing at each iteration is required, and the historical compliance averaging scheme in Eq. (4.14) is not utilized in the processes.

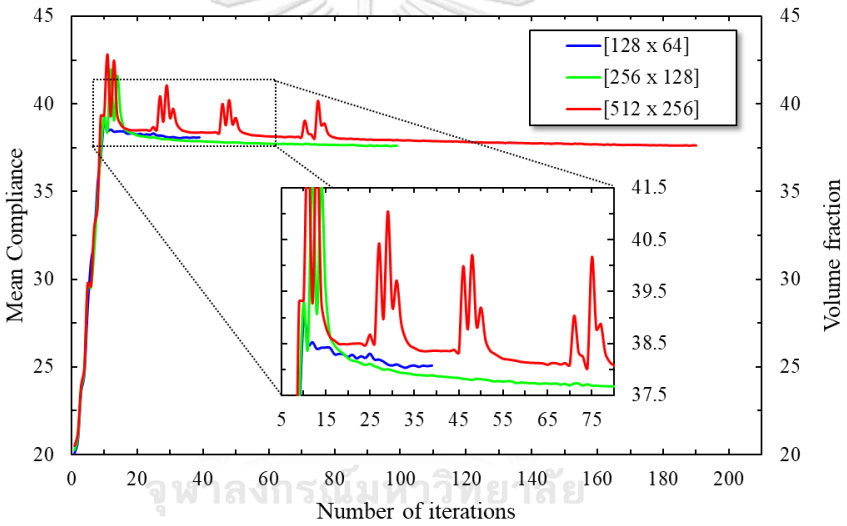

จุฬาลงกรณ์มหาวิทยาลัย
Chulalongkorn University

Figure 3.9 Evolution histories of mean compliance for 2D-MBB beam by using SBFEM + BESO.

Mesh size	Iterations	Compliance	Optimal result
128 × 64	39	38.0819	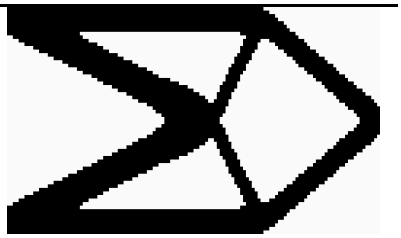
256 × 128	99	37.6288	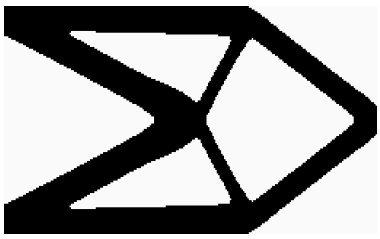
512 × 256	190	37.6232	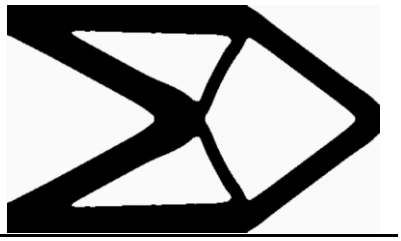

Table 3.2 Topology results of short cantilever beam performed using SBFEM + SMTO-BESO.

จุฬาลงกรณ์มหาวิทยาลัย
CHULALONGKORN UNIVERSITY

2.4.2 SMTO of a Symmetric Beam

Problem statement

In this working example, P loads the beam at its upper center, as seen in Figure 3.10. With a 1-mm thickness, the symmetric right half of the $5L \times L$ domain is discretized using four-node plane stress elements with three different mesh sizes: 320 × 64, 640 × 128, and 1280 × 256. Assume that the final construction can only be built using 50% of the design domain volume and that the material is elastic. When the material has a Young's modulus of E = 1 and a Poisson's ratio of v = 0.3, it initially fills the whole design domain. In this example, the BESO parameters utilized are: ER = 5%, AR_{max} = 5%, r_{min} = 8 pixels, and τ = 0.01%.

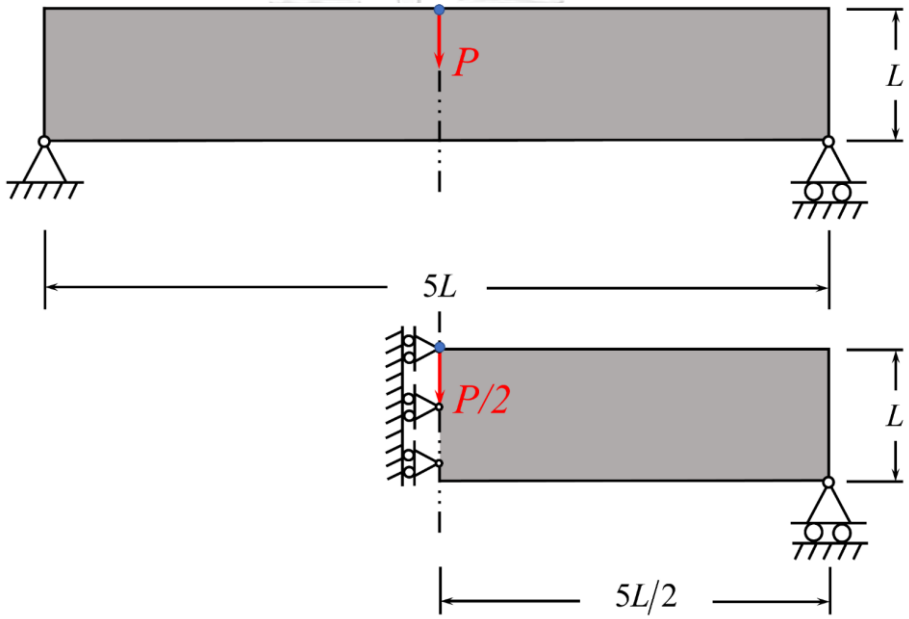

Figure 3.10 The dimensions of the design domain, as well as the boundary and loading conditions of a beam.

SMTO Results using the FEM

Here, the symmetric beam benchmark issue is solved to the best of its ability utilizing the soft-kill BESO approach and conventional FEM. Figure 3.11 Table 3.3 shows the histories of the mean compliance and the best solution for different mesh sizes. The mean compliance occasionally jumps due to a large change in topology brought on by the removal of one or more particular regions in one iteration.

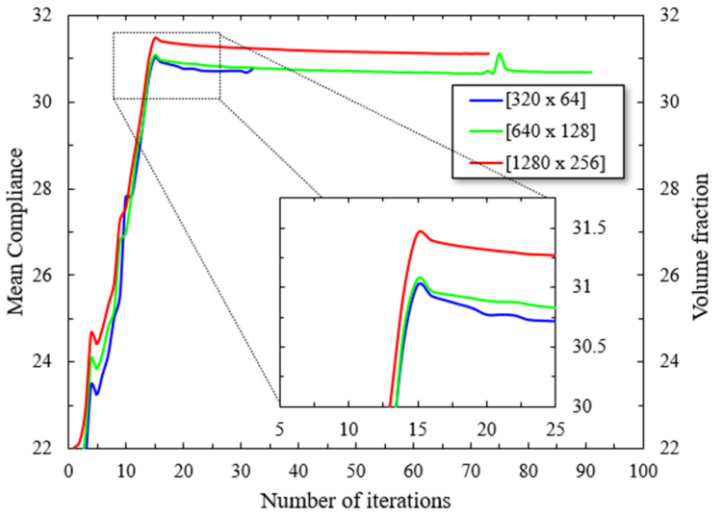

Figure 3.11 Evolution histories of mean compliance for symmetric beam using FEM + BESO.

Mesh size	Iterations	Compliance	Optimal result
320 × 64	32	30.7552	
640 × 128	91	30.6837	
1280 × 256	73	31.1033	

Table 3.3 Topology results of symmetric beam performed by FEM + SMTO-BESO.

จุฬาลงกรณ์มหาวิทยาลัย
Chulalongkorn University

The aforementioned examples show that the BESO approach may determine the best topology from a complete design, and more particularly, the BESO technique's nature is employed to search for an acceptable guess design for usage in later rounds before achieving the desired volume. The model's whole volume must be reduced over numerous phases to reach the appropriate volume. After that, the volume stays constant but the mean compliance steadily declines until convergence is reached.

SMTO Results using the SBFEM

In the same manner as the previous example, the TO of symmetric beam problem can be performed using the SBFEM instead of the conventional method. At this point, the evolution of

mean compliance and the optimal topology results for this example are shown in Figure 3.12 and Table 3.1.

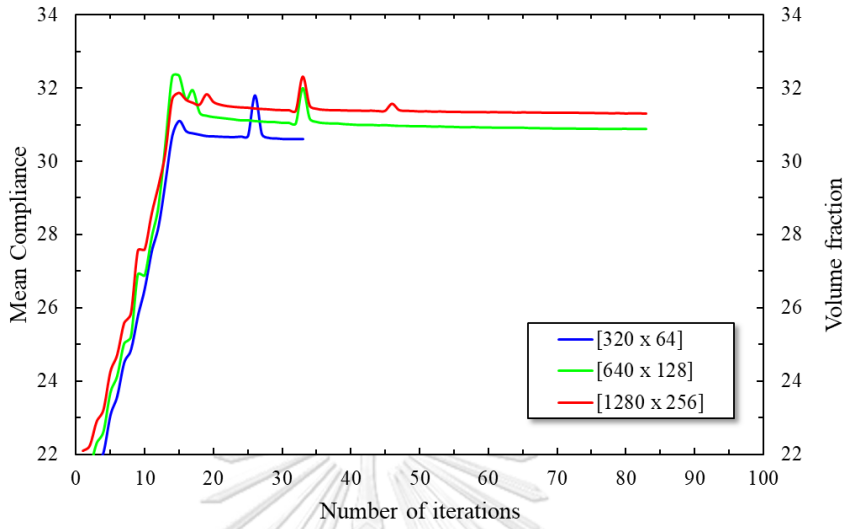

Figure 3.12 Evolution histories of mean compliance for symmetric beam using SBFEM + BESO.

Mesh size	Iterations	Compliance	Optimal result
320 × 64	68	30.4983	
640 × 128	83	30.8927	
1280 × 256	89	31.3030	

Table 3.4 Topology results of symmetric beam performed using SBFEM + SMTO-BESO.

The SBFEM-BESO approach is presented and used to optimize the topology of 2D continuum structures from all of the 2D instances. The SBFEM is discovered to be a promising numerical strategy and a substitute for the FEM in resolving structural optimization issues, according to the findings. Such S-elements are matched and can speed up calculation due to the benefit of distinctive patterns of node configurations that have been computed in advance.

2.5 Benchmark problems for 3D uniform mesh SMTO with static load structures.

2.5.1 SMTO of a 3D-MBB Cantilever Beam

Here, an extended cantilever beam example from a 3D scenario is shown to illustrate the computational effectiveness of the current BESO approach. A 3D cantilever's design domain is seen in Figure 3.13 with a specified load, F = 1 kN, operating at the free end's center. Brick pieces with a size of 64 × 32 × 16 have been used to represent the building. Poisson's ratio v = 0.3 and the elastic Young's modulus E = 1 GPa are presumptive values. 7.5% of the design domain's whole volume is represented by the volume fraction, and BESO begins with the complete design. ER = 3%, AR_{max} = 50%, r_{min} = 3 voxels, and τ = 0.1% are additional BESO parameters. It is seen that a very high AR max is used, thereby removing the cap on the maximum number of components that may be added during each iteration.

The optimal design shown in Figure 3.14(b) is concluded by the SIMP algorithm after 200 iterations. The structural compliance of the final topology is 21.0536 N-mm (Figure 3.14[a]). This final layout and overall compliance are achieved by compact 169 lines MATLAB code ((K. Liu & Tovar, 2014)).

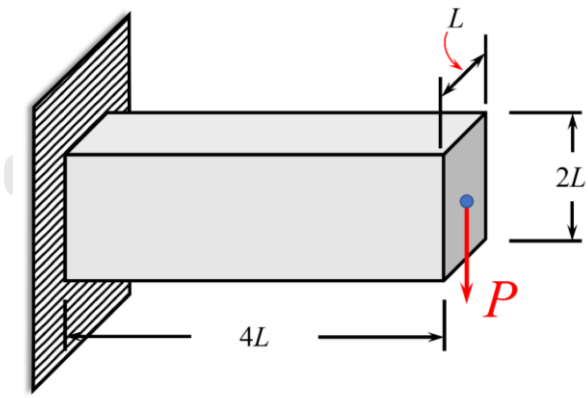

Figure 3.13 Schematic design domain for a 3D MBB cantilever problem.

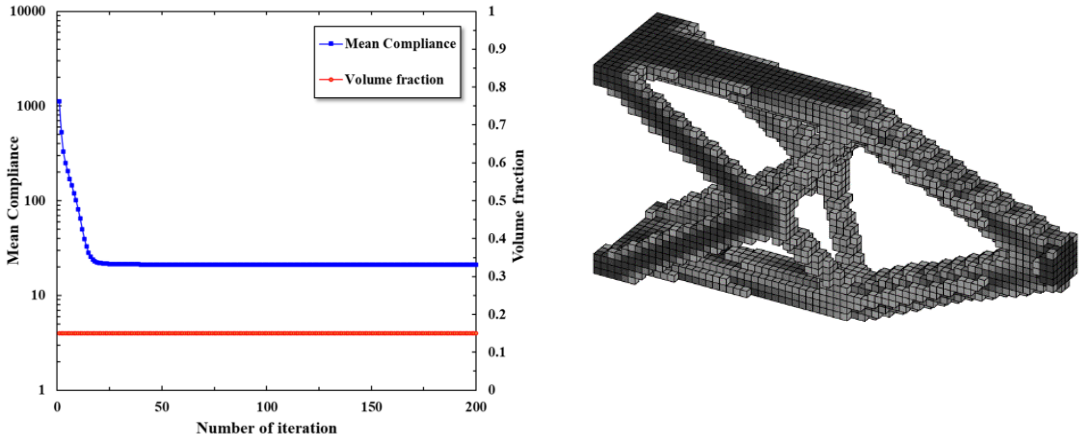

(a) (b)

Figure 3.14 Solving 3D-MBB cantilever beam using the SIMP when p = 3.0 ((K. Liu & Tovar, 2014)): (a) Evolution histories of the mean compliance (C = 21.0536 at iteration 200) and (b) optimal solution for 3D MBB cantilever beam.

Herein, the soft-kill BESO technique is successfully performed in the 3D domain using the SBFEM and an optimal solution to the single-phase material of 3D cantilever beam benchmark problem is obtained. The histories of the mean compliance and optimal solution with various mesh sizes are depicted in Table 3.5

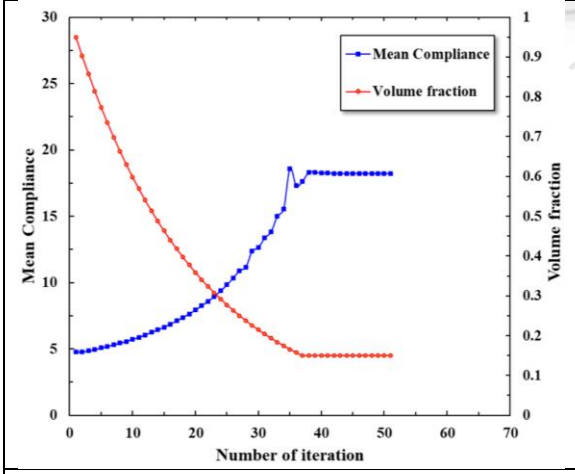	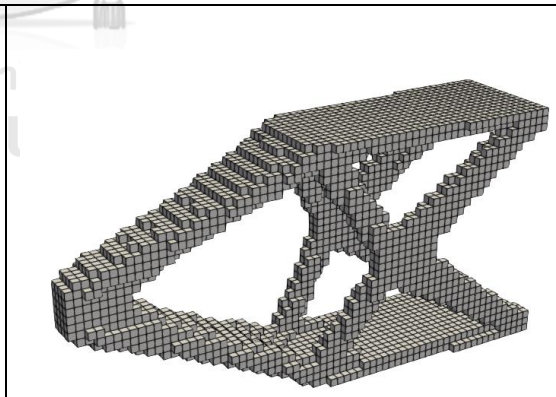
Evolution histories of mean compliance when using FEM + BESO **(C = 18.2157)**	An optimal solution with 64 × 32 × 16 (iteration 51)

Table 3.5 Our solution of 3D MBB cantilever beam using SMTO - BESO + SBFEM.

The solution shows that SBFEM are appropriate numerical techniques for performing TO. However, with the large amount of DOFs in design domain, the analysis for each optimization iteration is performed with high computational effort, and when varying the discretized elements into a smaller size, higher memory is required, resulting in lack of CPU memory.

จุฬาลงกรณ์มหาวิทยาลัย
Chulalongkorn University

3. Adaptive mesh refinement

In applications such as image processing, a convolution-based filtering technique can be applied to mesh generation ((Egger, Saputra, Triantafyllou, & Chatzi, 2019)). Conversely to conventional approaches, remeshing at each iteration is required, a filter utilizing MATLAB's built-in 'conv2' function is implemented with a radius of density r_{den} pixels. This filtering process is a technique for modifying or enhancing an image. This process is known as the density filter technique. Their defining characteristic comprises the inclusion of void material during analysis by severely reducing such an element's stiffness. Input of convolution function is easily constructed by small scripts or obtained from (Andreassen et al., 2011). The example of 2D image convolution filtered is depicted in Figure 3.15.

Figure 3.15 Example of 2D image convolution filtered: the parameter r_{den} = 4 pixels.

จุฬาลงกรณ์มหาวิทยาลัย
Chulalongkorn University

With the benefit of convolution filter, the grid of design variables is fed as a gray-scale image to the decomposition algorithm, which outputs an analysis-ready hierarchical mesh. The process of "conv2" with Quadtree mesh generation is summarized in flowchart as shown in Figure 3.16. Unlike the conventional grid approaches, utilizing image compression techniques facilitates the creation of automated AMs. The suggested drop-in replacement for the forward solver significantly decreases the amount of DOFs present during analysis. This concept is constructed and applied to the TO of linear 2D and 3D problems, and the solutions obtained are compared to those produced using conventional element-based approaches in order to demonstrate its effectiveness.

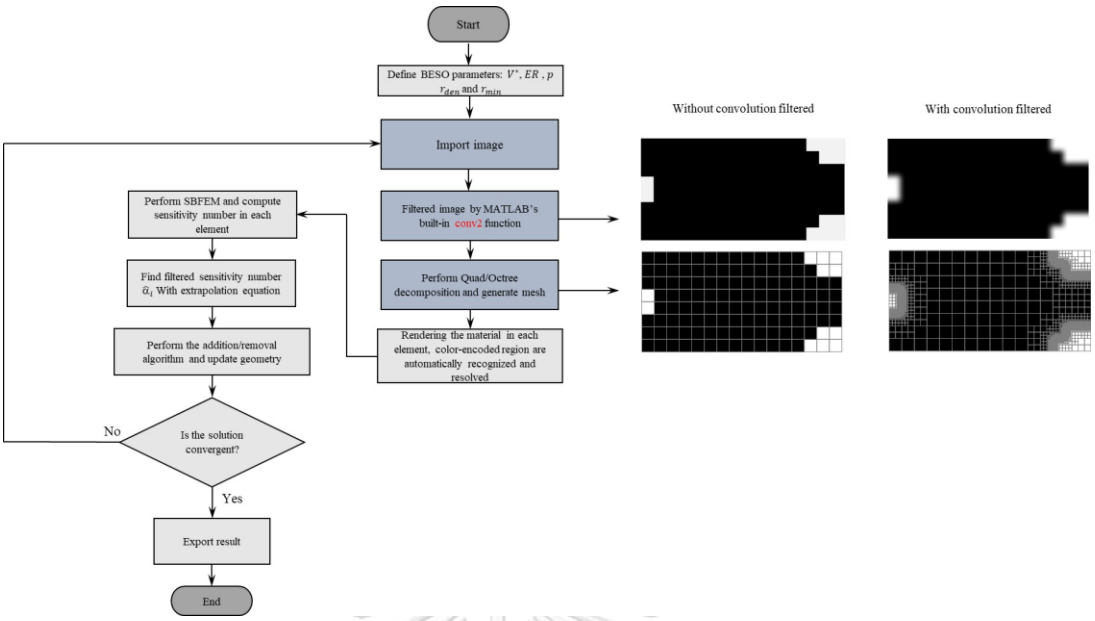

Figure 3.16 Flowchart for BESO+SBFEM with convolution filtered.

จุฬาลงกรณ์มหาวิทยาลัย
Chulalongkorn University

3.1 Benchmark problems for 2D AM-SMTO with static load structures

3.1.1 AM-SMTO of a short cantilever beam

In this example, a short cantilever problem from section 2.4.1 is recalled to perform TO using a convolution-filtered technique. The prescribed volume fraction, V^*, is chosen as 0.4 and a filter with MATLAB's built-in "conv2" function is applied with a radius of 8 pixels. Three cases of elements arising during Quadtree decomposition are limited in size to $\leq$ 64, 32, and 16 pixels, and it should be noted that the subdomains are varied in size and the calculated sensitivities must be normalized per unit volume.

Case	Max. size (Pixels)	Iterations	Compliance	Optimal result
1	64	36	36.9363	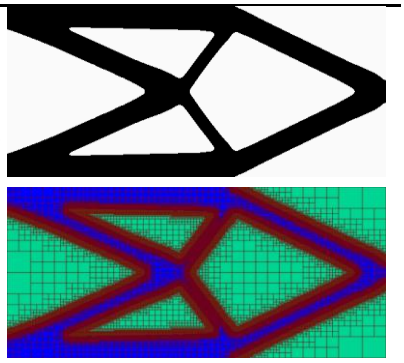
2	32	27	36.9442	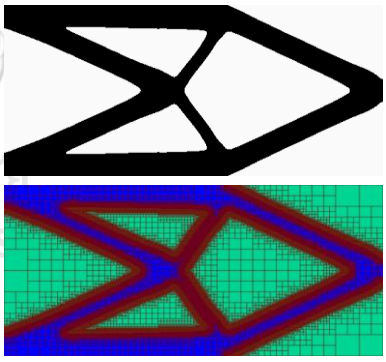
3	16	98	37.5389	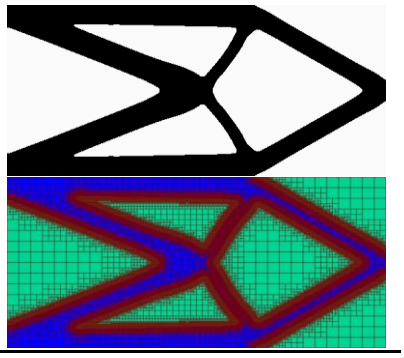

จุฬาลงกรณ์มหาวิทยาลัย
Chulalongkorn University

Table 3.6 Topology results of AM for short cantilever beam performed using SBFEM + SMTO-BESO.

The optimal topology results for AM are shown in Table 3.6, and the evolution of the mean compliance for all cases are plotted in Figure 3.17. Clearly, the results of AM from a convolution-filtered technique are less computationally efforted than are uniform meshes (UM) in previous sections. Moreover, coarse discretization results in a stiffer structure and therefore lower compliance.

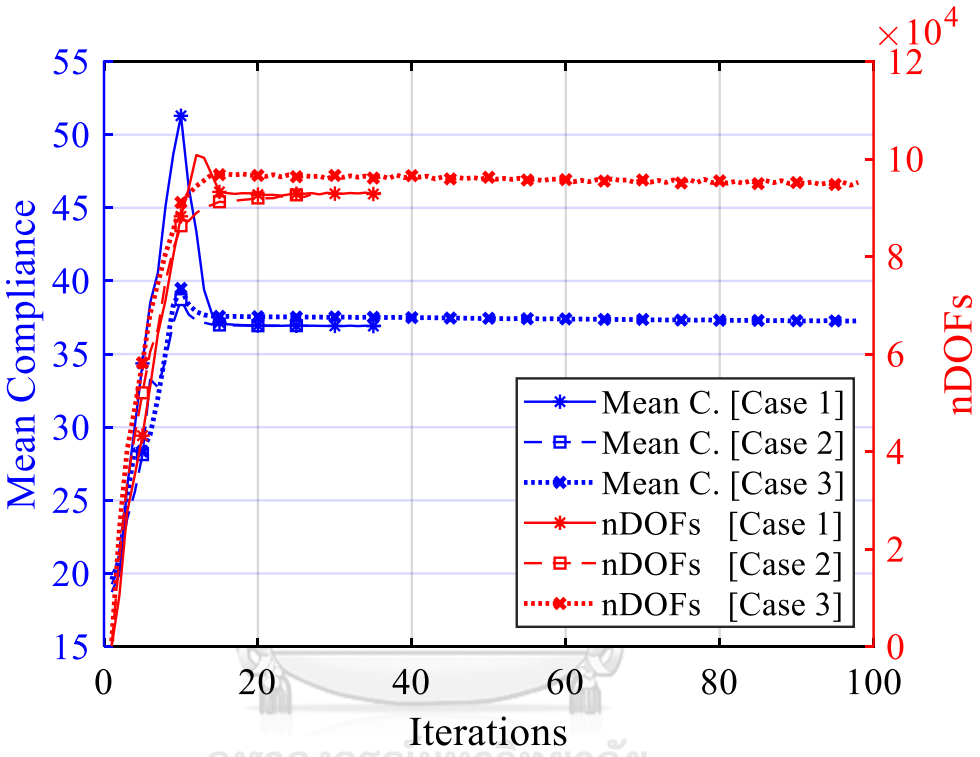

จุฬาลงกรณ์มหาวิทยาลัย
Chulalongkorn University

Figure 3.17 Evolution histories of mean compliance for AM of short cantilever beam using SBFEM + BESO.

3.1.2 AM-SMTO of a symmetric beam

The same concepts are applied to the symmetric beam problem in Section 2.4.2. Applying the convolution-filtered technique with $r_{den} = 8$ pixels and $r_{min} = 8$ pixels, three cases of elements arising during quadtree decomposition are limited in size to $\leq$ 64, 32 and 16 pixels. For the first iteration, the discretization of the conventional grid is adopted and the optimal topology results for all cases of AMs are shown in Table 3.7. The evolution of the mean compliance and total number of degrees of freedom for all cases are plotted in Figure 3.18.

Case	Max. size (Pixels)	Iterations	Mean C.	Optimal result
1	64	40	29.2738	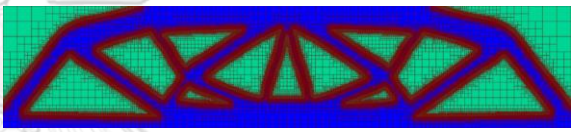
2	32	60	29.3537	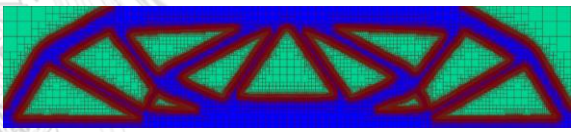
3	16	63	29.3461	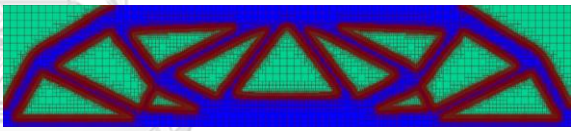

Table 3.7 Topology results of AM for Symmetric beam performed by SBFEM + SMTO-BESO.

จุฬาลงกรณ์มหาวิทยาลัย
Chulalongkorn University

As expected, the results of AM from convolution-filtered technique are introduced to a slightly more flexible structure and therefore smaller compliance. However, the image-based implementation in the previous two examples are not complex in geometry, and the next example considers more complexity of structure.

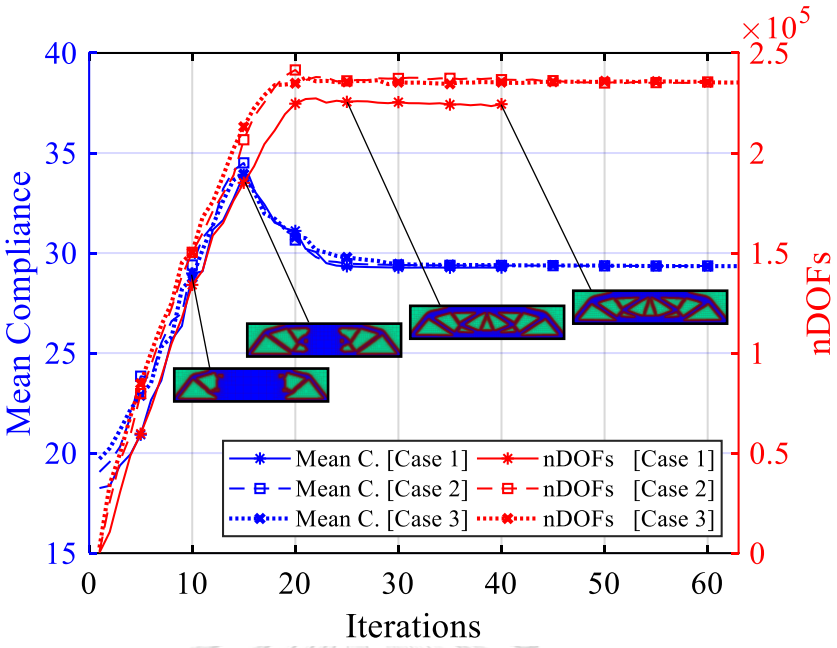

Figure 3.18 Evolution histories of mean compliance for AM of symmetric beam using SBFEM + BESO.

จุฬาลงกรณ์มหาวิทยาลัย
Chulalongkorn University

3.1.3 AM-SMTO of a Rectangular beam with two holes

A modified symmetric beam setup (Figure 3.19) is considered with width and height discretized by 1024 and 256 pixels, respectively, and for this analysis, only a color-encoded input image is provided. During the automated decomposition step, the proposed scheme automatically distinguishes key regions and their associated processes, and the colors, blue, red, green, white, gray, and black, correspond to boundary conditions, vertical static loads, non-designable, void, eliminated, and designable domain pixels, respectively. A volume fraction of 0.4 is specified. The BESO parameters include evolutionary rate ration (ER) = 5%, r_{min}= 5 pixels, and the convergence criterion (τ) = 0.01%.

For AM refinement, the conv2-type filter is employed with radius equal to 5 pixels. The SMTO of rectangular beam with two holes under static load were successfully performed in both the uniform and AM and the results of both cases are illustrated in Table 3.8 and directly compared in Figure 3.20. The total time for the TO processes of uniform mesh (UM) took around 18,522.83 s while the AM took only 1,298.27 s. In this contrived example in which both cases share a common implementation, differing only in the process of solving the forward problem, a glimpse of the computational potential of the proposed scheme is possible: For this specific numerical example, an analysis concludes almost 10x faster when employing the convolution-filtered technique.

จุฬาลงกรณ์มหาวิทยาลัย
Chulalongkorn University

Figure 3.19 Boundary conditions of rectangular beam with two holes via automated image-based analysis.

Case	Max. size (Pixels)	Iterations	Mean C.	Optimal result
Uniform	1	124	5.884×10^7	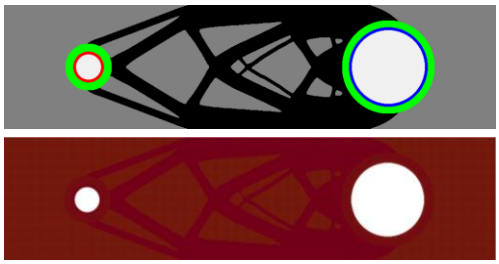
Adaptive	32	112	5.847×10^7	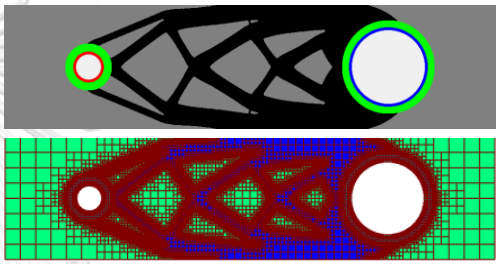

Table 3.8 Topology results of AM for rectangular beam with two holes performed using SBFEM + SMTO-BESO.

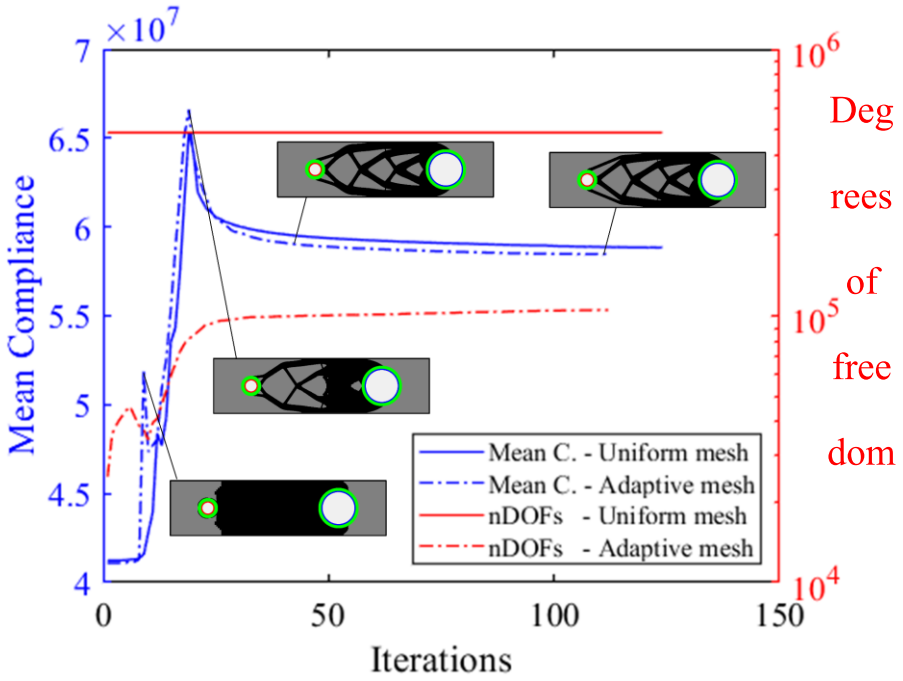

Figure 3.20 Evolution histories of mean compliance for rectangular beam with two holes using SBFEM + BESO.

3.1.4 AM-SMTO of a Circular domain with single hole

In this example, we consider the donut-shaped domain with torsion loaded boundary conditions shown in Figure 3.21(a). To be specific, the colors, black, magenta, white and gray, corresponded to designable domain, displacement boundary condition, void and eliminated elements. With single material design, the volume fraction is set to occupy no more than 40% of initial volume fraction. The BESO parameters include evolutionary rate ration (ER) = 10%, r_{min}= 5 pixels, and the convergence criterion (τ) = 0.01%.

The UM resulting in Figure 3.21(b) has six lines of symmetry and recognizes a flower (perfect symmetry is not achieved due to the rectangle-shaped mesh). For uniformly mesh scenario, their final mean compliances are 198.327 N-mm. The terminated result is obtained in 51 iterations and consumed the computational time for 5154.85 seconds. Once again, Figure 3.22 show the convergent histories of the mean compliance, developed design shape and volume constraint.

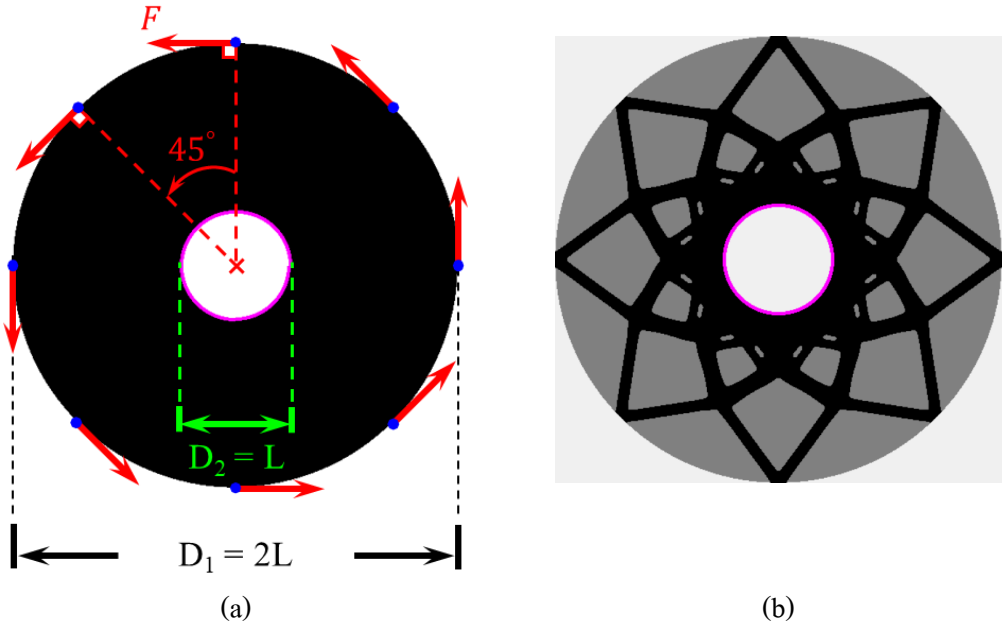

Figure 3.21 (a) Load and displacement boundary conditions for circular with single hole problem and (b) UM single-material designs.

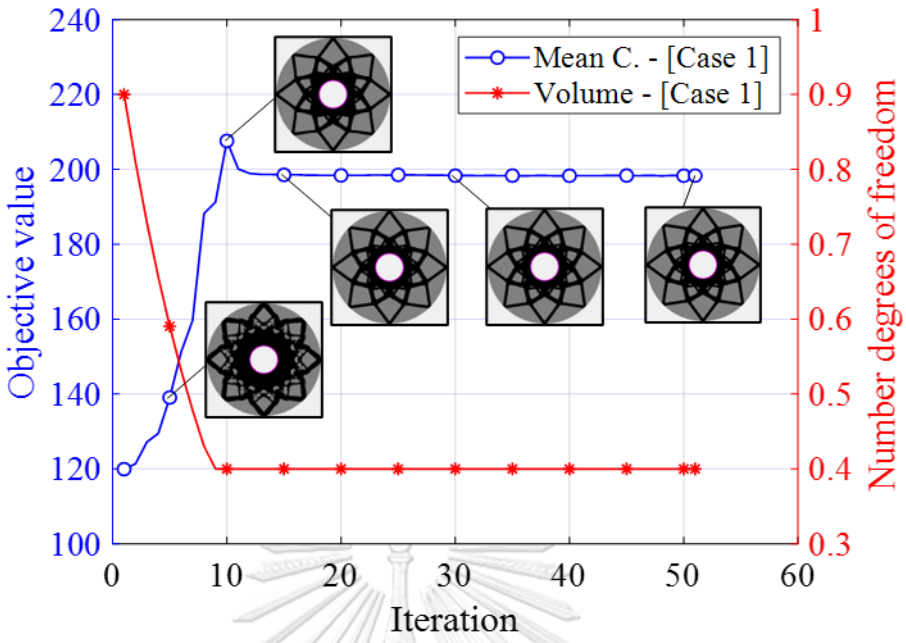

Figure 3.22 Evolution histories of the mean compliance with a volume fraction constraint for uniform SMTO circular domain using SBFEM + BESO.

For AM refinement, the density filter is applied with radius equal to 5 pixels (same as sensitivity filtered). Three cases of elements appearing during Quadtree decomposition are limited in size to $\leq$ 32, 16, and 8 pixels, and calculated sensitivities are normalized per unit volume. The SMTO of circular domain under static load were successfully performed in AM and the results of all cases are illustrated in Table 3.9 and directly compared in Figure 3.23. The total time for the TO processes of AM took only 1,121.93, 1,251.87 and 1,055.42 s. For this specific numerical example, the final results for AM are obtained by perform iterative analysis more than uniform mesh in some cases. The reason is BESO has several tuning parameters that may need extra iterations to converge in objective values in some cases. However, an analysis concludes almost 5x faster when employing the convolution-filtered technique.

Case	Max. size (Pixels)	Iterations (time)	Mean C.	Optimal result
1	8	48	197.667	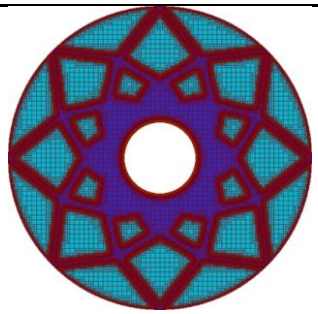
2	16	58	197.431	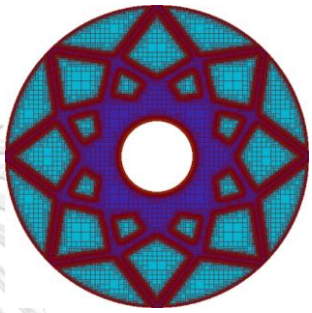
3	32	59	197.443	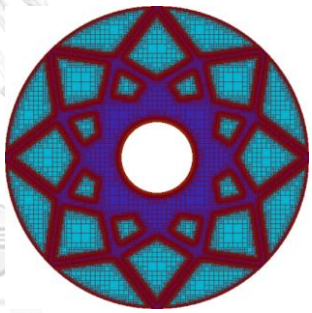

Table 3.9 Topology results of AM for Circular domain performed by SBFEM + SMTO-BESO.

CHULALONGKORN UNIVERSITY

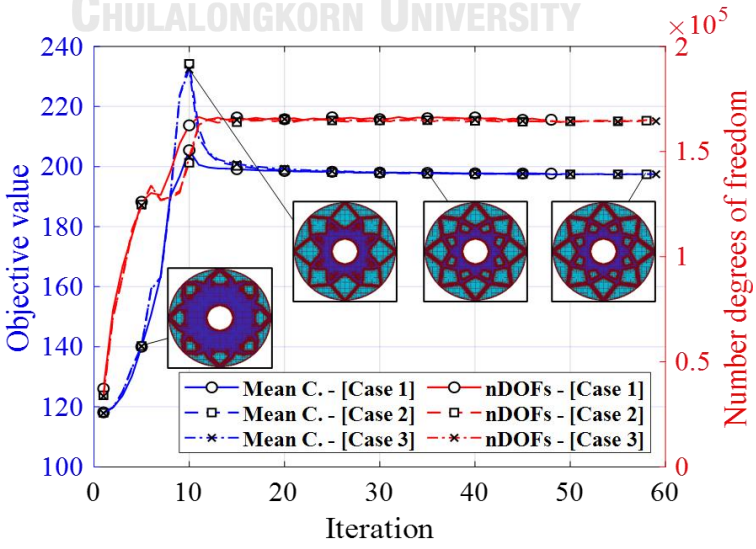

Figure 3.23 Evolution histories for AM of Circular domain using SBFEM + BESO.

3.2 Benchmark problems for 3D AM-SMTO with static load structures

3.2.1 AM-SMTO of a 3D-MBB cantilever beam

The same convolution-filtered processes are extended for 3D problems, and from section 2.5.1, the 3D-MBB cantilever beams performed SMTO by static load. The width, depth, and height are discretized by 64, 32, and 16 voxels, respectively, and a volume fraction of 0.15 is sought. The filter radius is given as 8 pixels in both r_{min} and r_{den}, all Octree elements are $\leq$ 4 voxels in size, and the convergence criterion (τ) = 0.01%.

The initial design domain and final topology are depicted in Figure 3.24 along with a sample of the Octree mesh, and the evolution of compliance and amount of degrees of freedom (DOFs) are plotted in Figure 3.25. It is revealed that the amount of DOFs and number of nonzero entries in the stiffness matrix is significantly reduced and computational effort is lessened by only computing the element stiffness matrices for the unique elements and cloning the remainder. However, the predominant computational cost still resides in solving the forward problem.

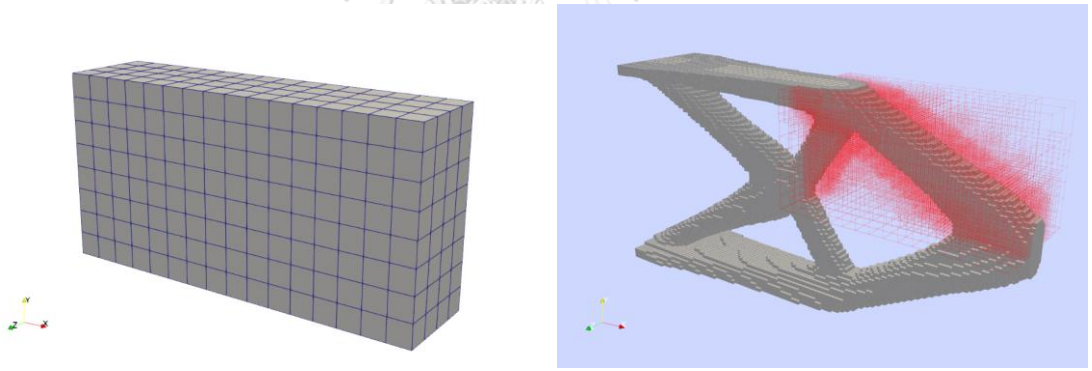

Figure 3.24 The convolution-filtered technique was used to optimize the topology of a 3D MBB cantilever beam. The input image is shown on the left, and the resulting topology is shown on the right.

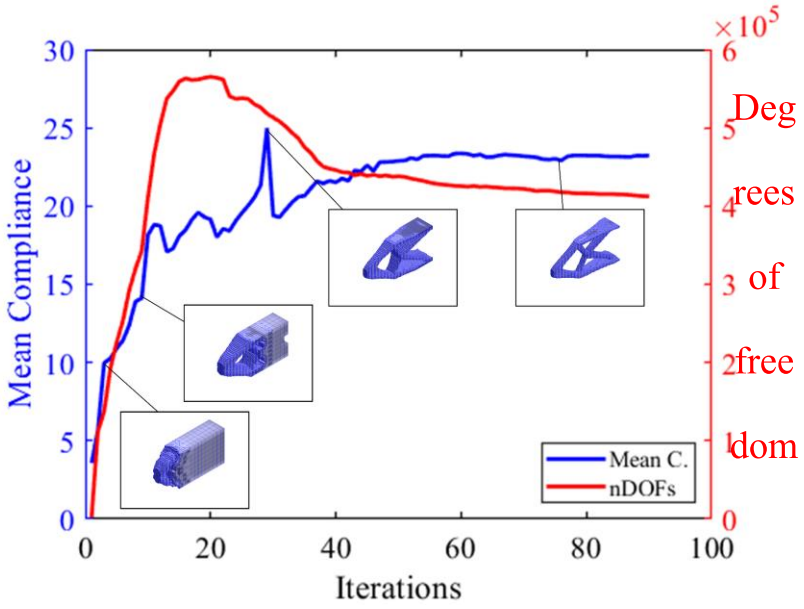

Figure 3.25 Evolution of DOFs and compliance across iterations obtained from AM.

จุฬาลงกรณ์มหาวิทยาลัย
Chulalongkorn University

3.2.2 AM-SMTO of a 3D Cantilever beam with uniform loaded

The structural mean compliance of a 3D cantilever beam under certain load and displacement boundary conditions is minimized in this numerical example. The analytic domain is represented by a prism with dimensions $1 \times 2 \times 1$ in Figure 3.26, with the biggest dimension orientated on the x-axis. On the design domain's left face, displacements are required, and along its bottom-right border, a distributed vertical load is placed. Half of the domain is discretized by $192 \times 96 \times 48$ using 2 unit cubic hexahedral components while maintaining the symmetry to the x-y plane. Poisson's ratio v = 0.3 and the elastic Young's modulus E = 1 GPa are presumptive values. Remaining 15% of the design domain's overall volume is represented by the volume fraction. Other BESO parameters include: ER = 5%, AR_{max} = 50%, r_{min} = 6 voxels, and τ = 0.01%.

The optimal design shown in Figure 3.27 is concluded by uniform mesh after 103 iterations and consumed the computational time for 93,060.76 seconds. The mean compliance of the final topology is 4,818.98 N-mm. The first principal stress plots of the optimal design are plotted in Figure 3.27(b) and (d), where red and blue colors represent the tensile and compressive regions, respectively.

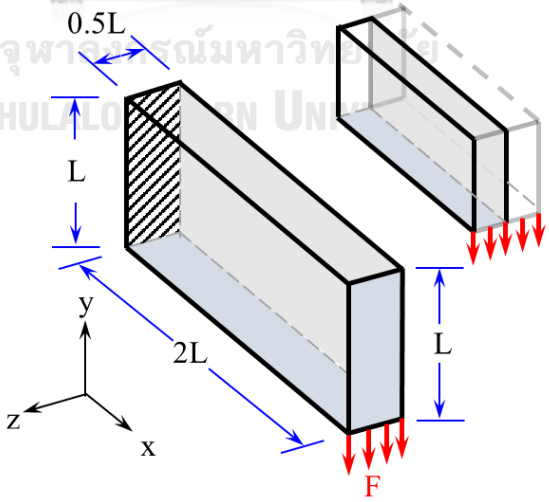

Figure 3.26 Cantilever beam domain with a distributed vertical load is applied on the bottom-right edge while the displacements are prescribed on the left surface of the domain.

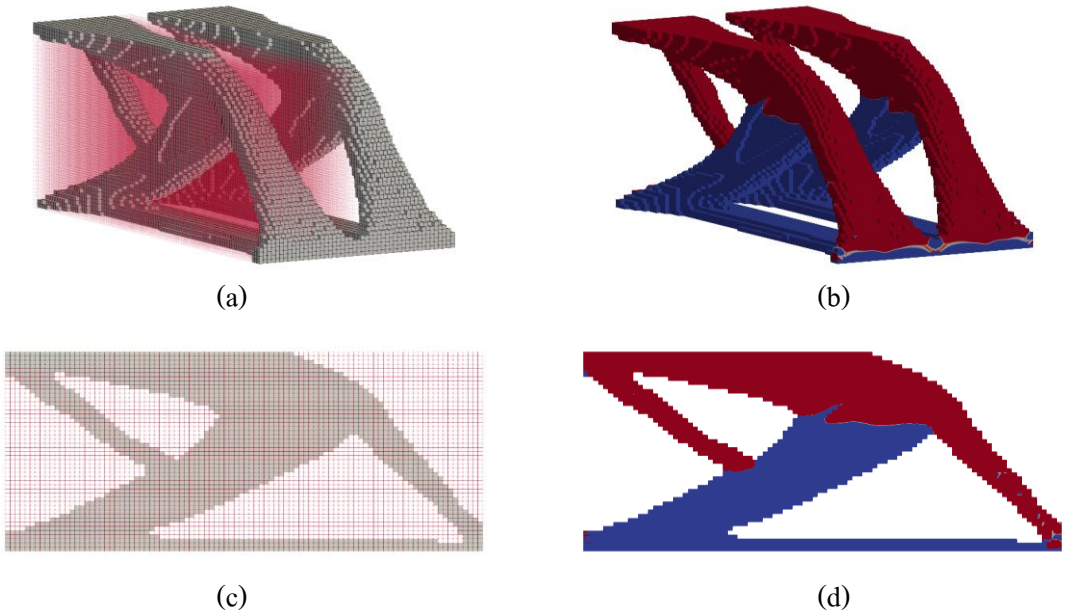

Figure 3.27 Solution of 3D cantilever beam using uniform mesh SMTO - BESO + SBFEM: (a) Optimal shape plotted in 3D view, (b) First principal stress plotted in 3D view, (c) Optimal shape with mesh grid plotted in x–y plane and (d) First principal stress plotted in x–y plane.

For AM refinement in 3D problem, the MATLAB built-in function convn-type filter is employed with r_{den} equal to 6 voxels. The elements appearing during Octree decomposition are limited in size to $\leq$ 16 voxels. The SMTO of 3D Cantilever beam under static load were successfully performed in AM and the results are illustrated in Figure 3.28. The topologies can be compared and found that as the complexity of bars decreases. This solution is made of a small number of thin bars, making it easier to manufacture and less likely to buckle. For this specific numerical example, the final results for AM are obtained after 145 iterations. The structural compliance of the final topology is 4,774.98 N-mm. The total time for the TO processes took only 42,915.93 s. The historical objective values and number degrees of freedom of both cases are directly compared and plotted in Figure 3.29.

To show the powerful in computational time saving in AM, the comparison in time consumed per iterations for both cases are plotted in Figure 3.30. An analysis concludes almost 2x faster when employing the convolution-filtered technique.

จุฬาลงกรณ์มหาวิทยาลัย
CHULALONGKORN UNIVERSITY

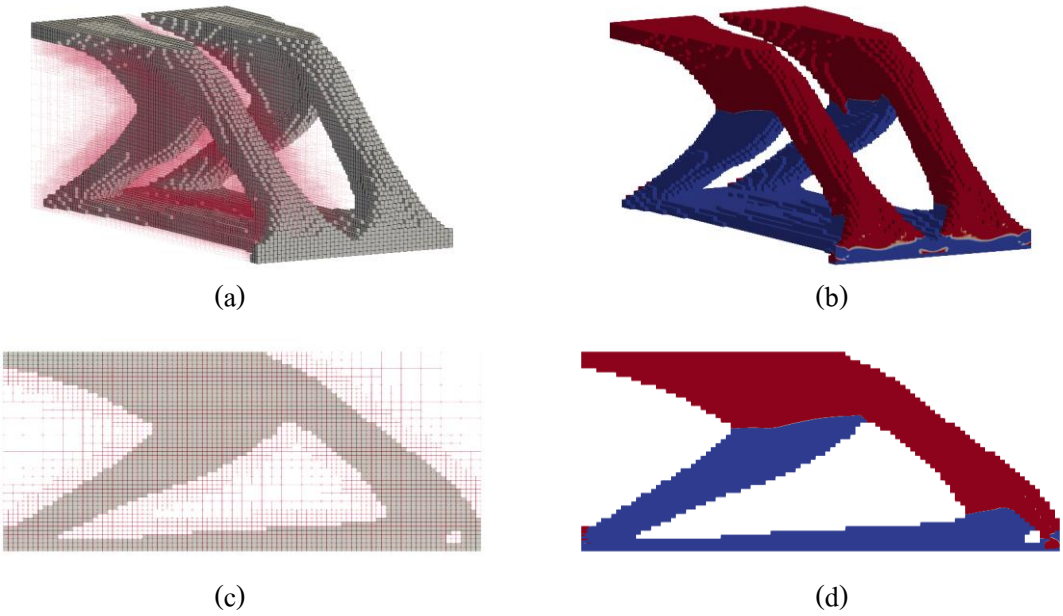

Figure 3.28 Solution of 3D cantilever beam using adaptive mesh SMTO - BESO + SBFEM: (a) Optimal shape plotted in 3D view, (b) First principal stress plotted in 3D view, (c) Optimal shape with mesh grid plotted in x–y plane and (d) First principal stress plotted in x–y plane.

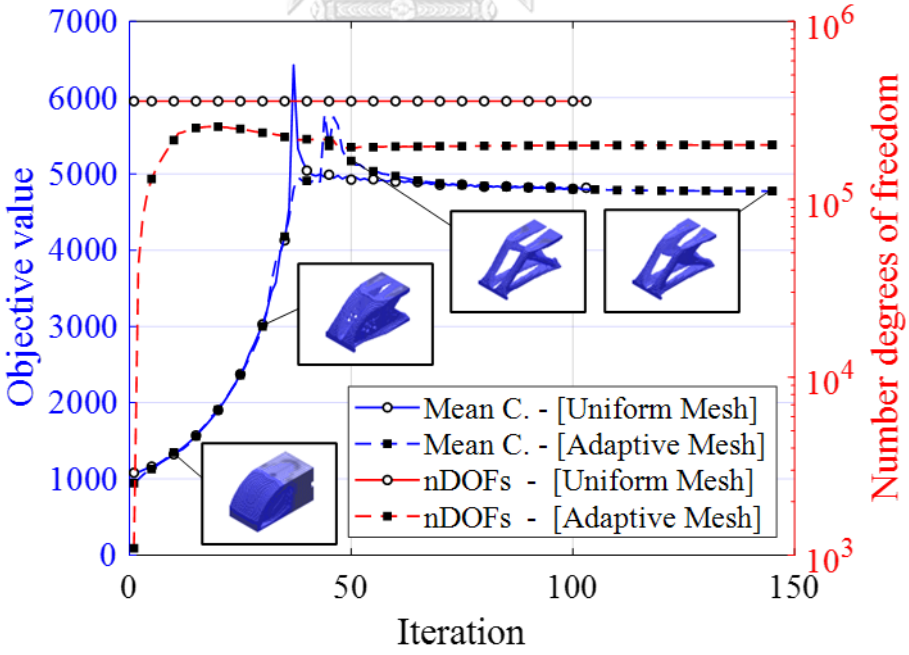

Figure 3.29 Evolution histories of mean compliance and number degrees of freedom for 3D Cantilever beam using SBFEM + BESO.

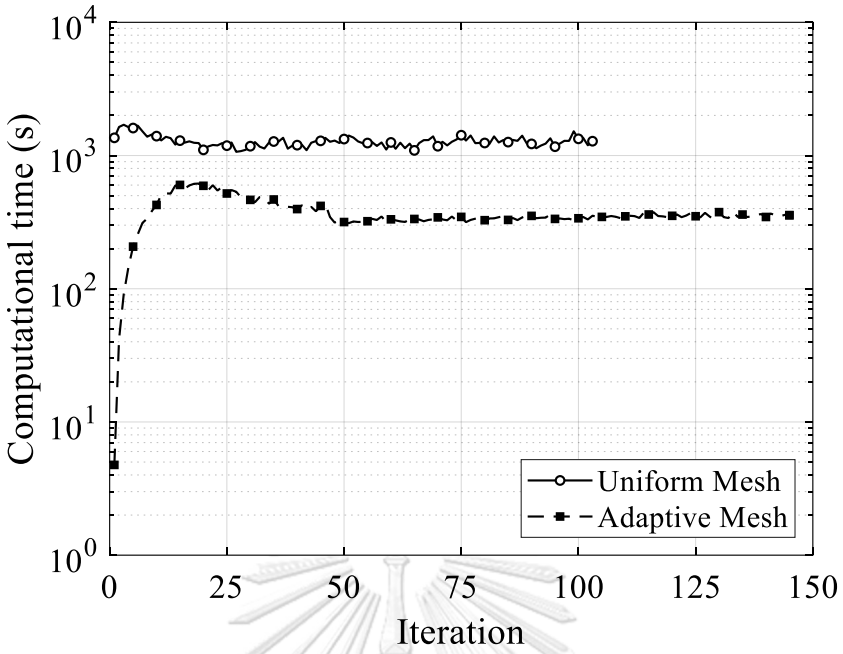

Figure 3.30 Comparison in time consumed per iterations for UM and AM.

จุฬาลงกรณ์มหาวิทยาลัย
Chulalongkorn University

3.2.3 AM-SMTO of a 3D L-shaped structure

In this example, a hook-like structure is optimized. A load is applied at a specific point ($z = 0, x = L$ and $y = \frac{L}{6}$), and the displacement at the top surface near the left edge is prescribed. The design domain is symmetrical with respect to the x–y plane and has $108 \times 108 \times 18$ brick elements in its structural mesh. This simplified version of the hook is shown in Figure 3.31.

This example involves comparing the uniform and adaptive mesh approaches on a more complex design domain to demonstrate how well the proposed method can handle non-rectangular shapes. The volume fraction of the design domain is 15 %. The BESO (boundary element single objective) parameters include an evolutionary ratio of 5 %, a maximum aspect ratio of 50 %, a minimum filter radius of 2 voxels, and a tolerance of 0.01 %. This problem is similar to the previous example, but with a more complex design domain.

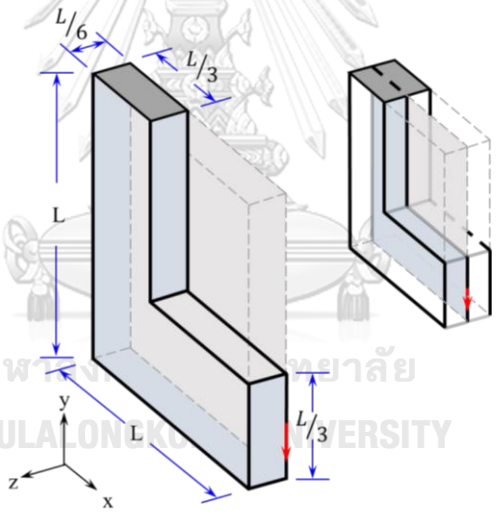

Figure 3.31 An L-shaped domain is subjected to a vertical load on the bottom-right surface, while the displacements are prescribed on the top-left surface.

The obtained results for the L-shaped structure by UM are illustrated in Figure 3.32 is concluded after 73 iterations and consumed the computational time for 73,478.36 seconds. The mean compliance of the final topology is 2.453 N-mm. The first principal stress plots of the optimal design are plotted in Figure 3.32(b) and (d), where red and blue colors represent the tensile and compressive regions, respectively.

Again, the MATLAB built-in function convn-type filter is applied with r_{den} equal to 2 voxels to achieve adaptive mesh design. The elements arising during Octree decomposition are limited in size to $\leq$ 16 voxels. The SMTO of 3D L-shaped under static load were successfully performed in AM and the results are depicted in Figure 3.33. The design of the structure is similar in both cases, but there are some differences in the lower part of the structure, particularly in the topological complexity of the layout. The complexity is lower in the adaptive mesh (AM) case, which consists of a small number of bars that are easier to manufacture and less prone to buckling. In this numerical example, the AM case required 116 iterations and took 24,783.64 s to complete the topology optimization process. The objective values and number of degrees of freedom for both cases are compared and plotted in Figure 3.34.

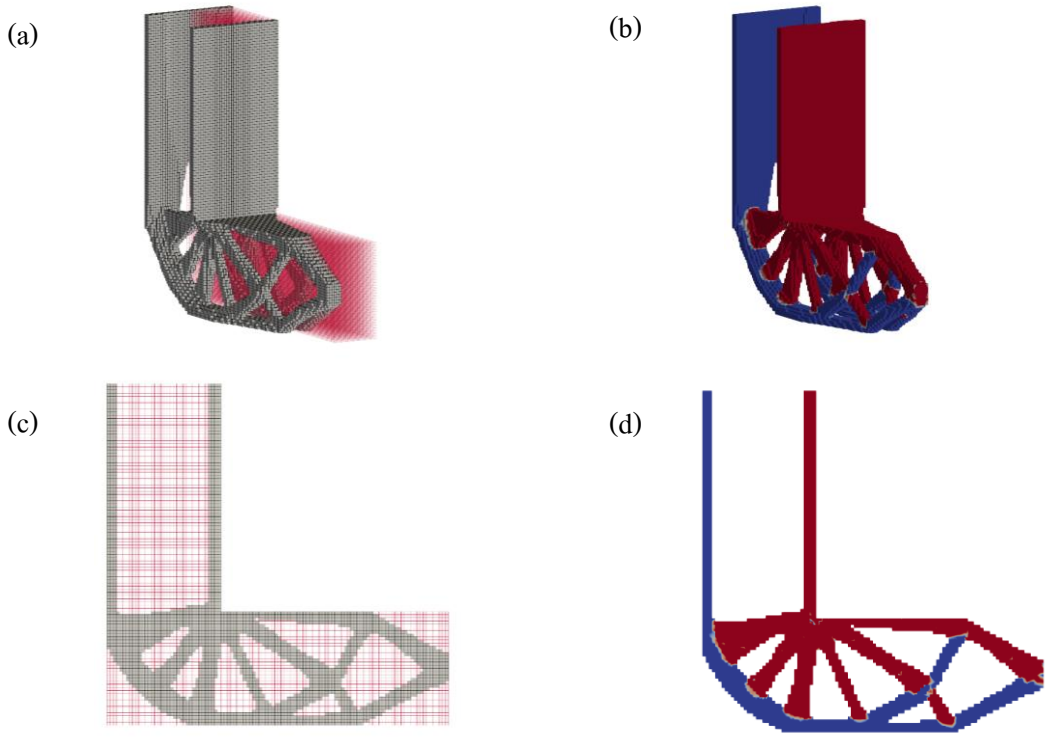

Figure 3.32 Solution of 3D L-shaped domain using uniform mesh SMTO - BESO + SBFEM: (a) Optimal shape plotted in 3D view, (b) First principal stress plotted in 3D view, (c) Optimal shape with mesh grid plotted in x–y plane and (d) First principal stress plotted in x–y plane.

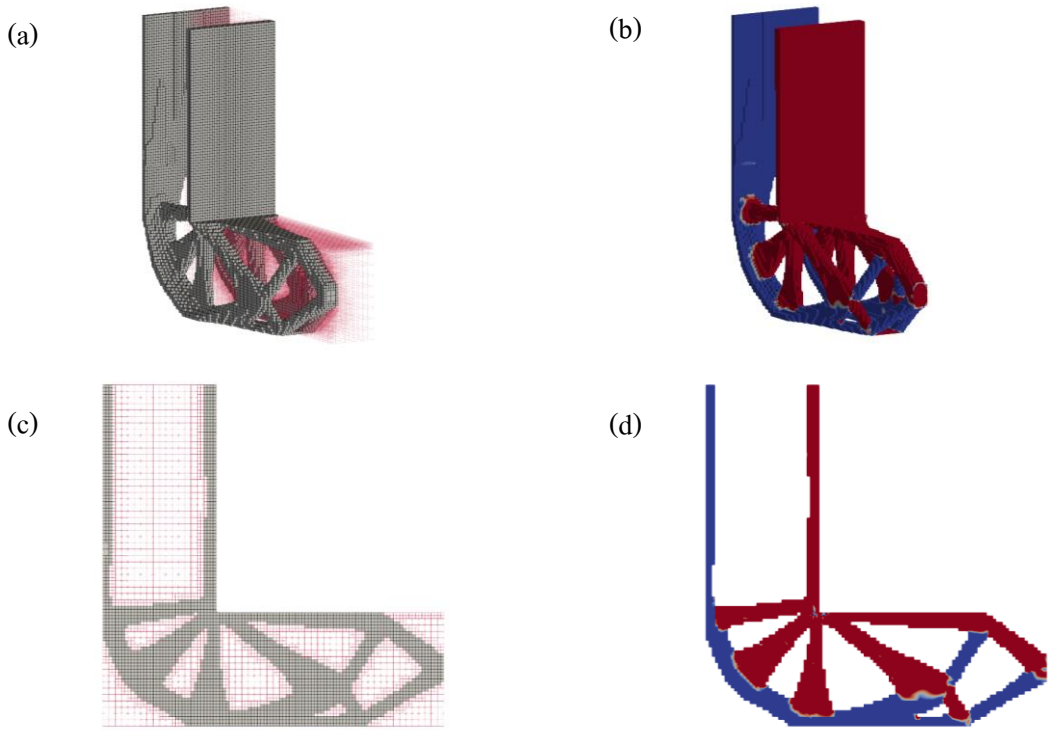

Figure 3.33 Solution of 3D L-shaped domain using adaptive mesh SMTO - BESO + SBFEM: (a) Optimal shape plotted in 3D view, (b) First principal stress plotted in 3D view, (c) Optimal shape with mesh grid plotted in x–y plane and (d) First principal stress plotted in x–y plane.

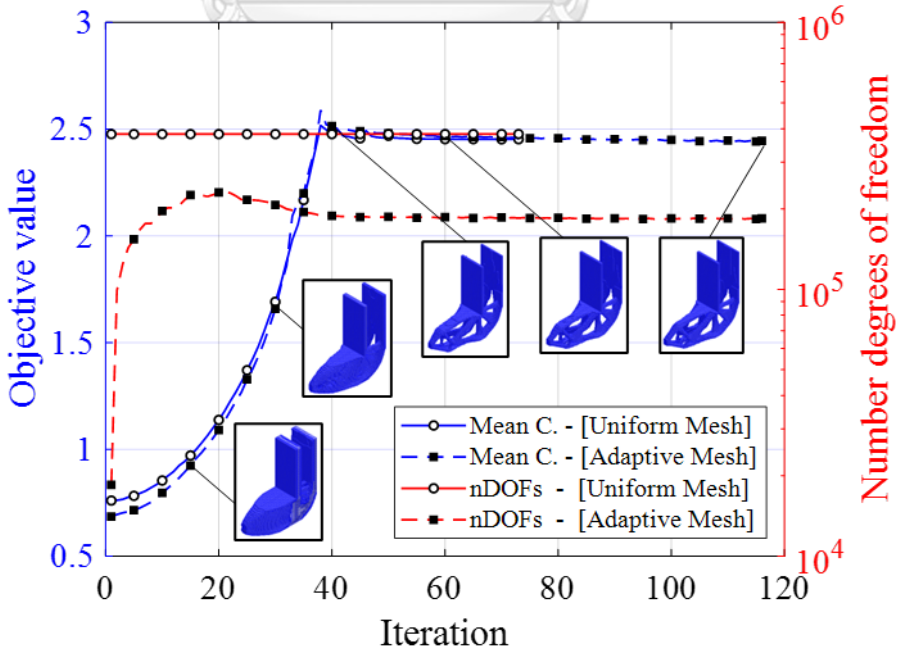

Figure 3.34 Evolution histories of mean compliance and number degrees of freedom for 3D L-shaped using SBFEM + BESO.

3.2.4 AM-SMTO of a 3D Strut and tie structure

This example shows how well the proposed method can handle the strut and tie modeling (STM) of a console structure. The geometry, boundary conditions, and design domain are shown in Figure 3.35. A single vertical load is applied at the end of the corbel, and the displacements at the top and bottom surfaces are prescribed. The volume fraction is 15 %, the filter radius is set to 2 voxels, and the evolutionary ratio is 2 % during the optimization process. The initial uniform mesh (UM) design domain consists of 131,072 eight-node hexahedral elements.

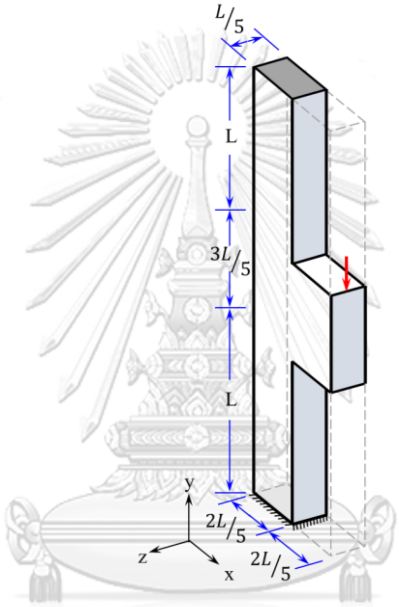

Figure 3.35 Strut and tie structure with a single vertical load is applied on the right end while the displacements are prescribed on the top and bottom surface of the design domain.

จุฬาลงกรณ์มหาวิทยาลัย
CHULALONGKORN UNIVERSITY

Again, this problem will provide a comparison in complex design domain between the UM and AM approaches, thus showing the performance of non-rectangular shaped structures. The obtained results for the STM by UM are illustrated in Figure 3.36(a) is concluded after 129 iterations and consumed the computational time for 174,192.10 s. The final topology for the mean compliance in the adaptive mesh (AM) approach using the convn-type filter with a radius of 2 voxels and limiting element size to 8 voxels or fewer during Octree decomposition is 2.988248606 N-mm. This was achieved after 93 iterations and took 32,947.60 s to complete. The results of the static load strut and tie modeling (STM) in 3D using AM are shown in Figure 3.36(b). In comparison, the mean compliance of the final topology using the uniform mesh (UM)

approach is 2.995680477 N-mm. The continuous formulation consistently leads to smaller compliance values for quadtree AM structures. The objective values and number of degrees of freedom for both cases are compared and plotted in Figure 3.37.

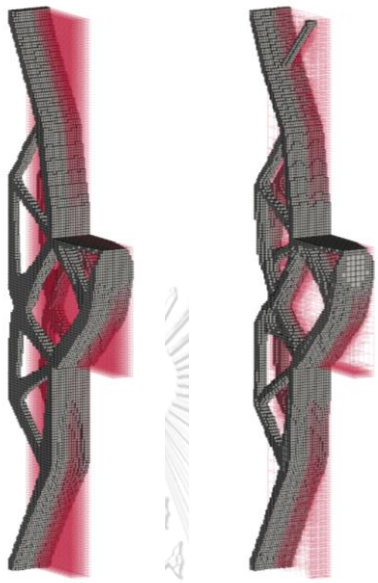

(a) (b)

Figure 3.36 Topological results of: (a) UM and (b) AM for 3D STM

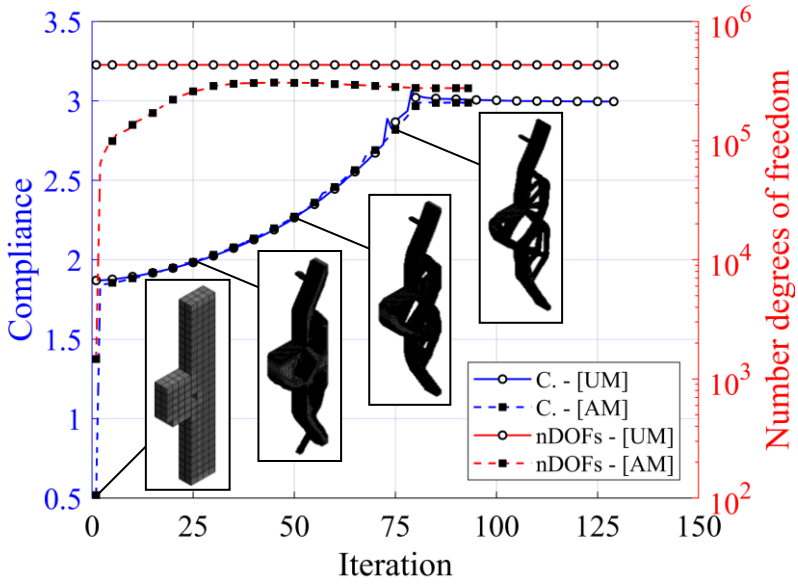

Figure 3.37 Comparison of mean compliance and number degrees of freedom between UM and AM for 3D STM using SBFEM + BESO.

4. MMTO Application and expected results

The application of single-phase material (SMTO) BESO can be further extended for MMTO, and with the merit of image-based application, color-encoding input images are automatically recognized as significant regions during the automated decomposition phase. This concept allows the user to separate the materials in the dissimilar colorized design domain, and in this section, our contribution to perform MMTO with SBFEM is presented. In order to validate the methodologies presented, the same structural optimization problems from previous section are selected to be solved.

4.1 2D MMTO cantilever beam with static load structures

Problem statement

In this case, the design domain is 512 by 256 pixels in width and height, respectively, and a downward force of 1 N is applied at the midpoint of the free end. The elastic modulus of the candidate materials, which are regularly spaced in the range $[0.2, 1]$ and have a Poisson's ratio of 0.3, is shown in Figure 3.38. These materials cover 40% of the design domain. The BESO (boundary element single objective) parameters include an evolutionary rate ratio (ER) = 2 %, a r_{min} = 8 pixels, and a τ = 0.001%. Table 3.10 lists the candidate materials and specified volume constraints for all cases. This information was previously introduced in section 3.1.

จุฬาลงกรณ์มหาวิทยาลัย

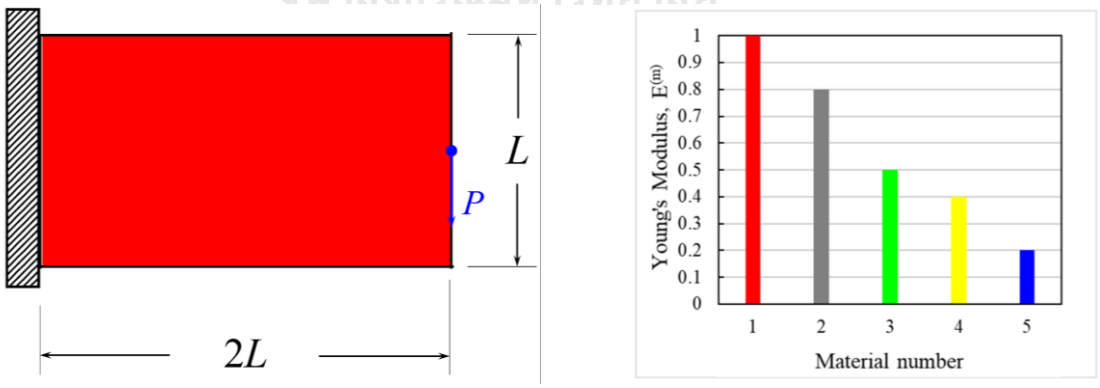

Figure 3.38 Problem statement of MMTO for MBB cantilever beam. Initial design (left) and Young's modulus of 5 materials (right).

Mat.	$E^{(m)}$	2-material		3-material			4-material				5-material				
		g_1	g_2	g_1	g_2	g_3	g_1	g_2	g_3	g_4	g_1	g_2	g_3	g_4	g_5
1	1	✓		✓			✓				✓				
2	0.8							✓				✓			
3	0.5		✓		✓								✓		
4	0.4								✓					✓	
5	0.2					✓				✓					✓
Volume fraction		$\frac{1}{5}$	$\frac{1}{5}$	$\frac{2}{15}$	$\frac{2}{15}$	$\frac{2}{15}$	$\frac{1}{10}$	$\frac{1}{10}$	$\frac{1}{10}$	$\frac{1}{10}$	$\frac{4}{5}$	$\frac{4}{5}$	$\frac{4}{5}$	$\frac{4}{5}$	$\frac{4}{5}$

Table 3.10 The candidate materials and specified volume constraints for short cantilever problem.

MMTO Results using the SBFEM with uniform mesh

The cantilever beam is created with a volume limitation for each of the potential materials 2, 3, 4, and 5, in order to show that the proposed formulation is successful in distributing materials in accordance with fundamental mechanics.

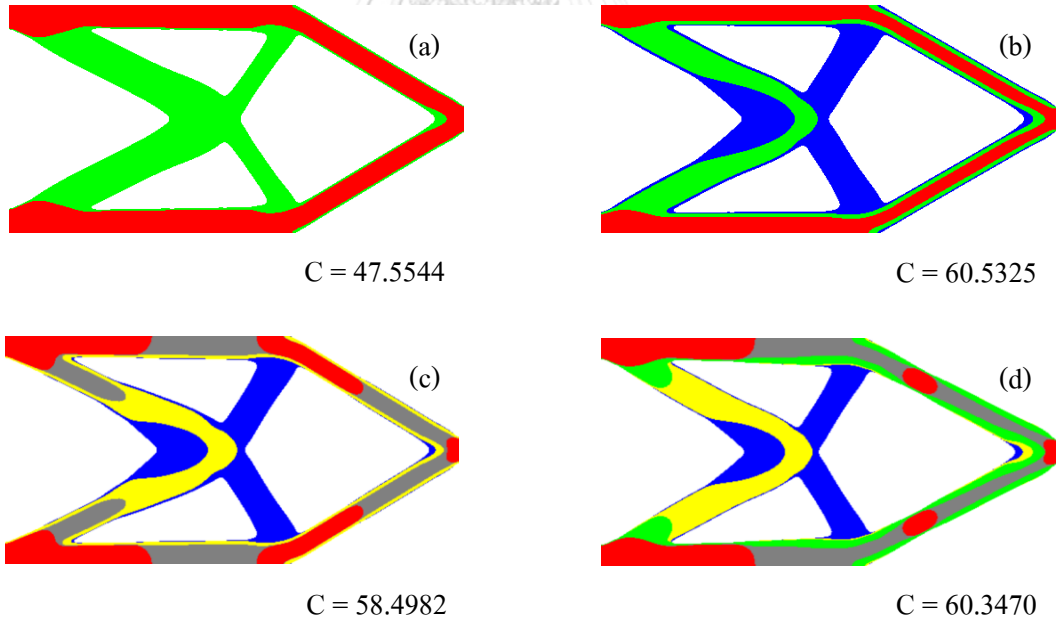

Figure 3.39 Uniform mesh multimaterials cantilever beam designs with individual global volume constraints for each of (a) 2; (b) 3; (c) 4; and (d) 5 candidate materials.

In each case, the stiffest material is distributed to the areas of the beam where stresses are anticipated to be the highest, and the least stiff material is spread toward the neutral axis, where stresses are predicted to be the lowest. This convergence of results is shown in Figure 3.39, demonstrating that from a mechanical perspective, the provided formulation yields results consistent with intuition. Figure 3.39 shows the ultimate objective value for each design, and Figure 3.40 shows the entire convergence plot for each. An analysis of the situations shown in Figure 3.39 in comparison shows that the various multimaterial designs result in various geometrical and topological arrangements.

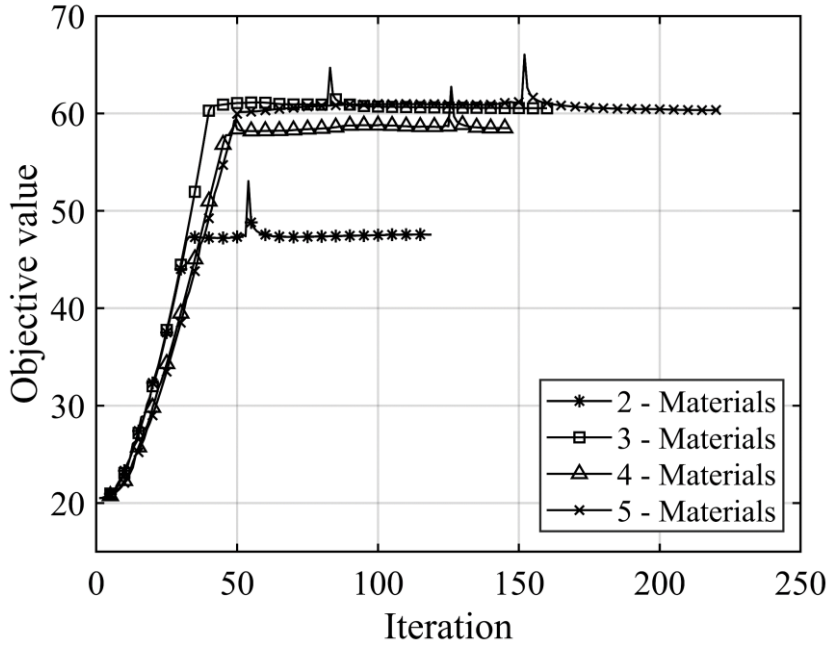

Figure 3.40 Objective value vs iteration for uniform mesh multimaterials short cantilever beams with unique global volume limitations for each of the candidate materials

MMTO Results using the SBFEM with AM

To obtain optimal solutions in AM refinement, the convolution-filtered techniques are directly applied with r_{den} and $r_{min} = 8$ pixels, respectively, and the elements arising during Quadtree decomposition are limited in size to $\leq$ 16 pixels.

The MMTO for AM are successfully performed using the SBFEM and the optimal results in Figure 3.41 show that the least stiff materials are located toward the middle, while the stiffest are toward the top, bottom and the applied load region.

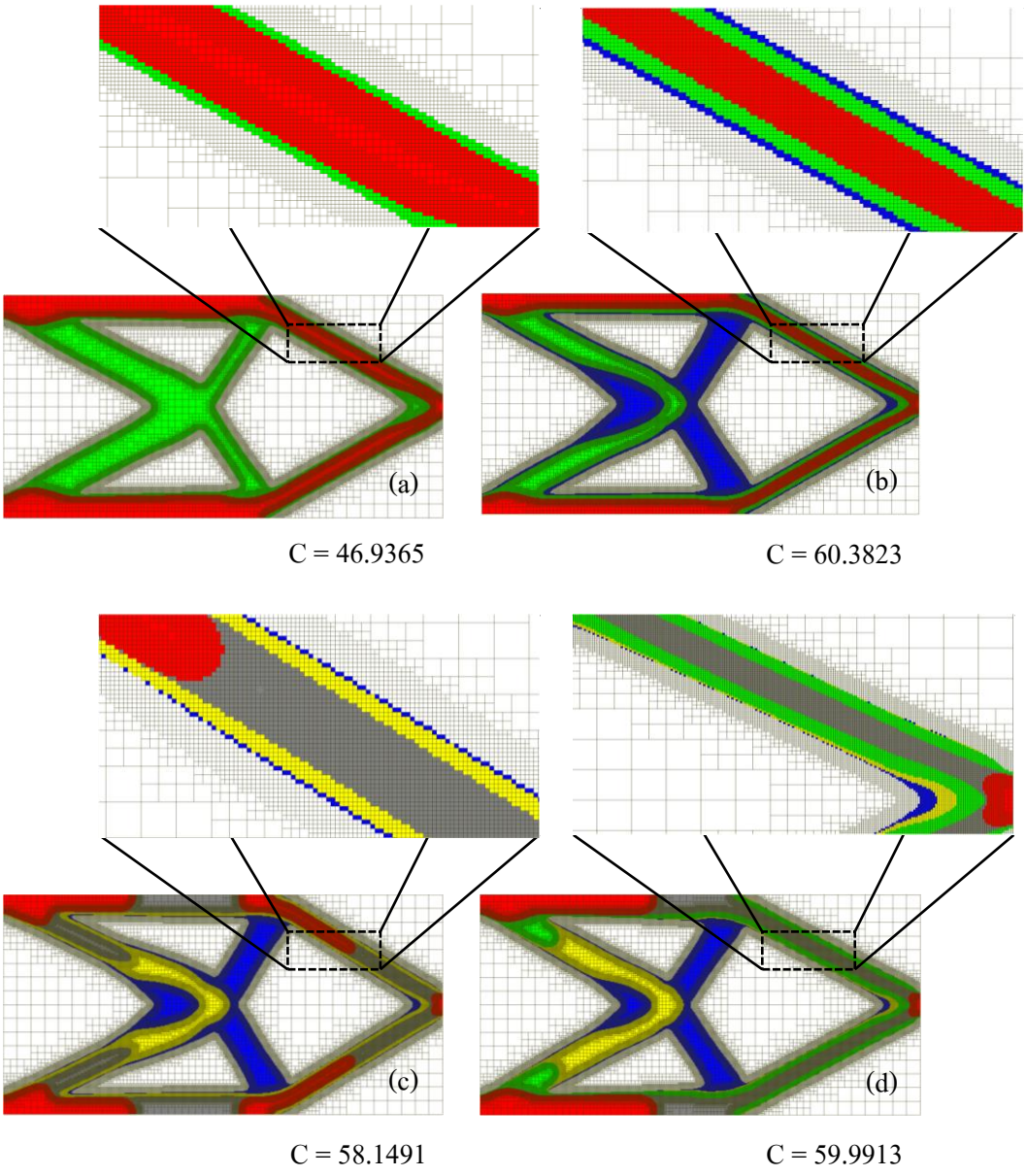

Figure 3.41 AM multimaterials short cantilever beam designs with individual global volume constraints for each of (a) 2; (b) 3; (c) 4; and (d) 5 candidate materials.

The full convergence plot for each of the candidate materials is provided in Figure 3.42. Obviously, the results of AM from a convolution-filtered technique are also less computationally

efforted than are uniform meshes in MMTO. Moreover, coarse discretization results in a stiffer structure and therefore lower compliance.

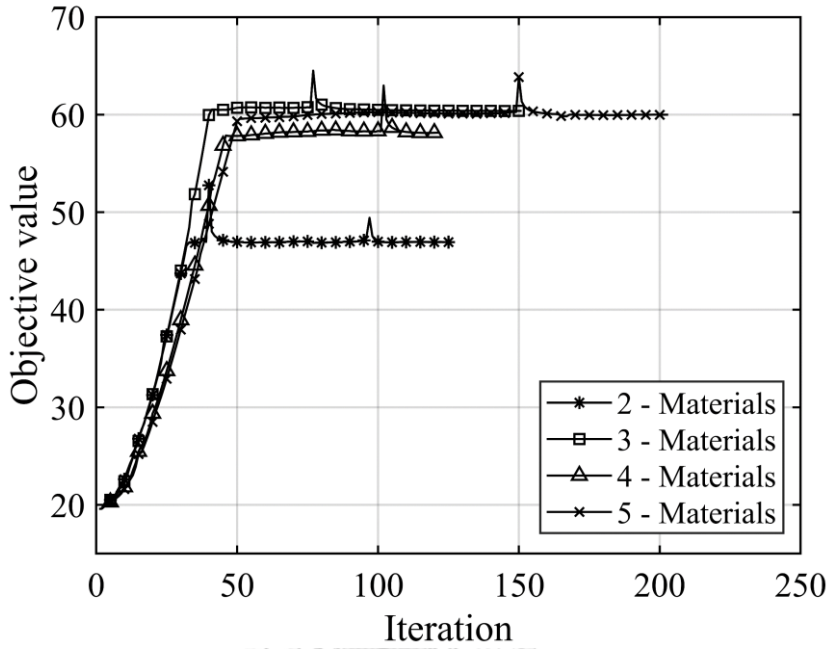

Figure 3.42 Objective value vs. iteration for non-uniform mesh multimaterials short cantilever beams with individual global volume constraints for each of the candidate materials

จุฬาลงกรณ์มหาวิทยาลัย
Chulalongkorn University

4.2 2D MMTO symmetric beam with static load structures

Problem statement

The design domain discretized 1,024 by 256 pixels in width and height with all specified candidate materials are displayed in Figure 3.43. A 1-N downward force is prescribed at the midpoint of the top edge and the remaining material covers 50% of the initial structure. The BESO parameters include evolutionary rate ratio (ER) = 2%, r_{min} = 16 pixels, and τ = 0.001%, and Table 3.11 shows the candidate materials and specified volume constraints for all cases.

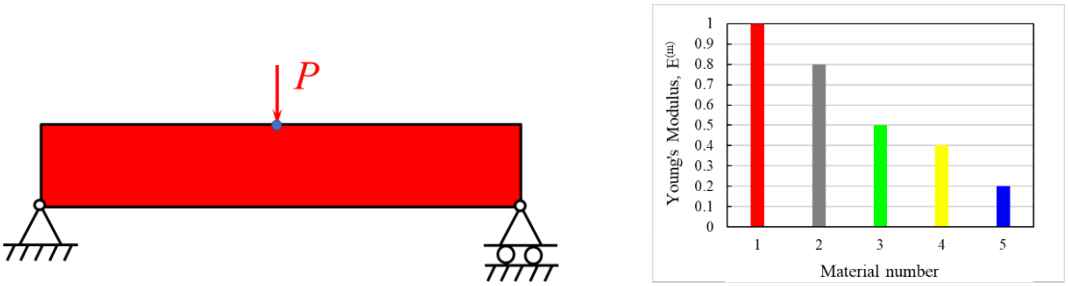

(a) (b)

Figure 3.43 Problem statement of symmetric beam: (a) Boundary condition and (b) elastic modulus of 5 materials.

Mat.	$E^{(m)}$	2-material		3-material			4-material				5-material				
		g_1	g_2	g_1	g_2	g_3	g_1	g_2	g_3	g_4	g_1	g_2	g_3	g_4	g_5
1	1	✓		✓			✓				✓				
2	0.8							✓				✓			
3	0.5		✓		✓								✓		
4	0.4								✓					✓	
5	0.2					✓				✓					✓
Volume fraction		$\frac{1}{4}$	$\frac{1}{4}$	$\frac{1}{6}$	$\frac{1}{6}$	$\frac{1}{6}$	$\frac{1}{8}$	$\frac{1}{8}$	$\frac{1}{8}$	$\frac{1}{8}$	$\frac{1}{10}$	$\frac{1}{10}$	$\frac{1}{10}$	$\frac{1}{10}$	$\frac{1}{10}$

Table 3.11 The candidate materials and volume constraints for symmetric beam problem.

จุฬาลงกรณ์มหาวิทยาลัย
CHULALONGKORN UNIVERSITY

MMTO Results using the SBFEM with uniform mesh

The symmetric beam is designed with volume constraints for four of the candidate materials. The design domain, which is 1024×256, is divided into 262,144 quadrilateral elements with unit edge length to demonstrate that the proposed formulation effectively distributes materials according to fundamental mechanics. This symmetric beam is designed with volume constraints for each of the second, third, fourth, and fifth candidate materials.

To optimize the structural performance of the beam, the stiffest material is used in areas where high stresses are expected, while the least stiff material is used in areas where low stresses are anticipated. This allows for a more efficient distribution of materials and helps to minimize the overall weight of the structure. The areas of the beam where the highest stresses are expected are typically located farther from the neutral axis, while the areas with the lowest stresses are closer to the neutral axis. This convergence of results is shown in Figure 3.44, demonstrating that from a mechanical perspective, the provided formulation yields result consistent with intuition. Figure 3.44 shows the ultimate objective value for each design, and Figure 3.45 shows the entire convergence plot for each. An analysis of the situations shown in Figure 3.44 in comparison shows that the various multimaterial designs result in various geometrical and topological arrangements.

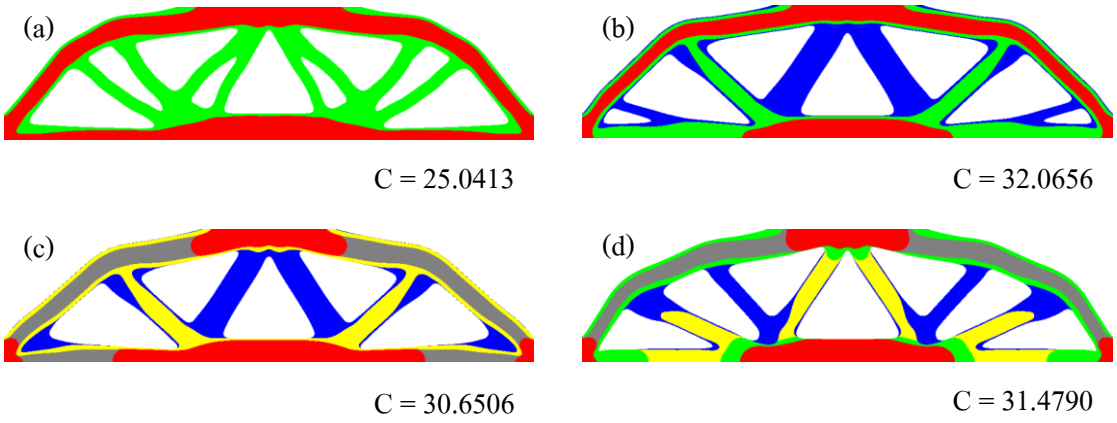

Figure 3.44 Designs for uniform mesh multimaterial symmetric beams that have distinct global volume restrictions for each of the possible materials (a), (b), (c), and (d) are 2, 3, 4, and 5 materials, respectively.

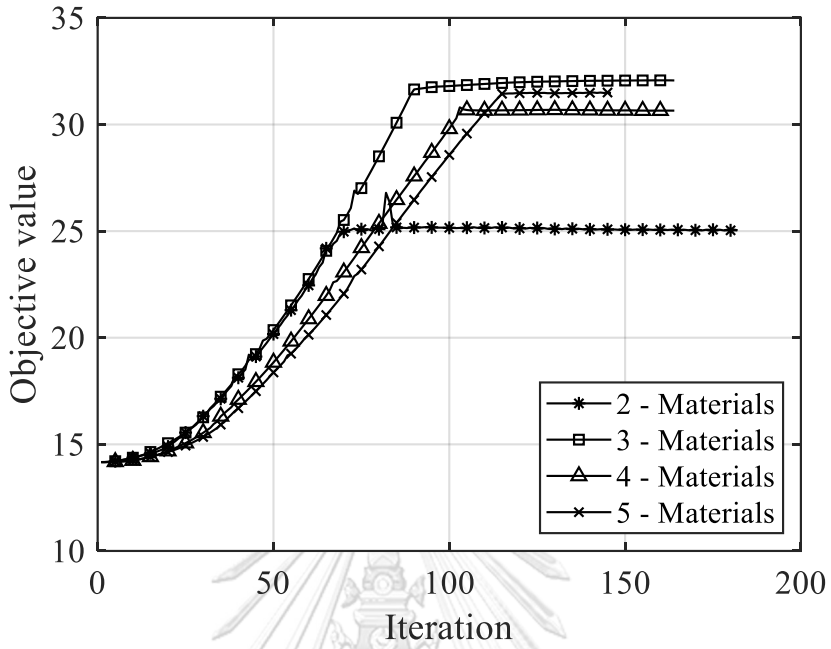

Figure 3.45 Objective value vs. iteration for uniform mesh multimaterials symmetric beams with individual global volume constraints for each of the candidate materials

MMTO Results using the SBFEM with AM

To obtain optimal solutions in AM refinement, the convolution-filtered techniques are directly applied with r_{den} and $r_{min} = 16$ pixels, respectively, and the elements arising during Quadtree decomposition are limited in size to ≤ 16 pixels. The MMTO for AM are successfully performed using the SBFEM and the optimal results in Figure 3.46 show that the least stiff materials are located toward the middle, while the stiffest are toward the top and bottom surfaces. Again, the results of AM from a convolution-filtered technique are less computationally efforted than UM in MMTO. In addition, AM results with non-uniform mesh layout provide stiffer structure and therefore lower compliance. However, the image-based implementations of previous 2 examples are not complex in geometry, the next example considers more complexity of structure.

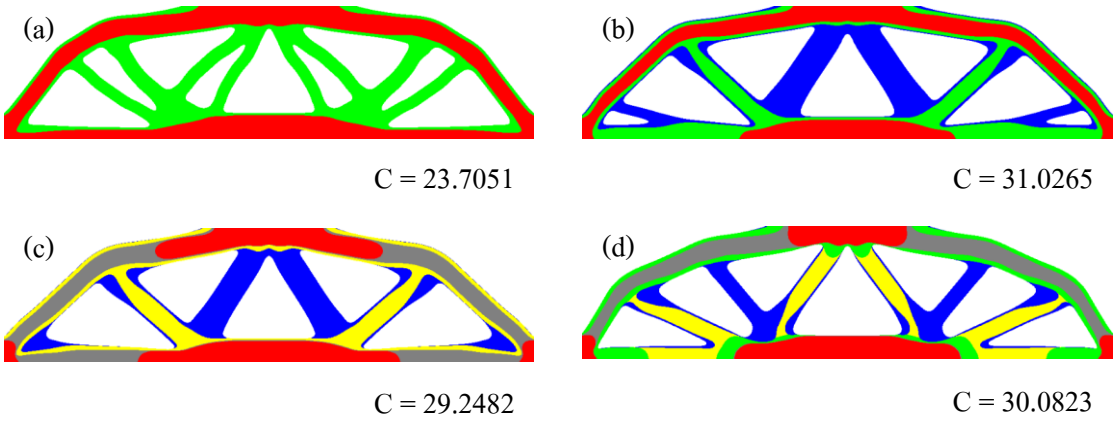

Figure 3.46 AM multimaterials symmetric beam designs with individual global volume constraints for each of (a) 2; (b) 3; (c) 4; and (d) 5 candidate materials.

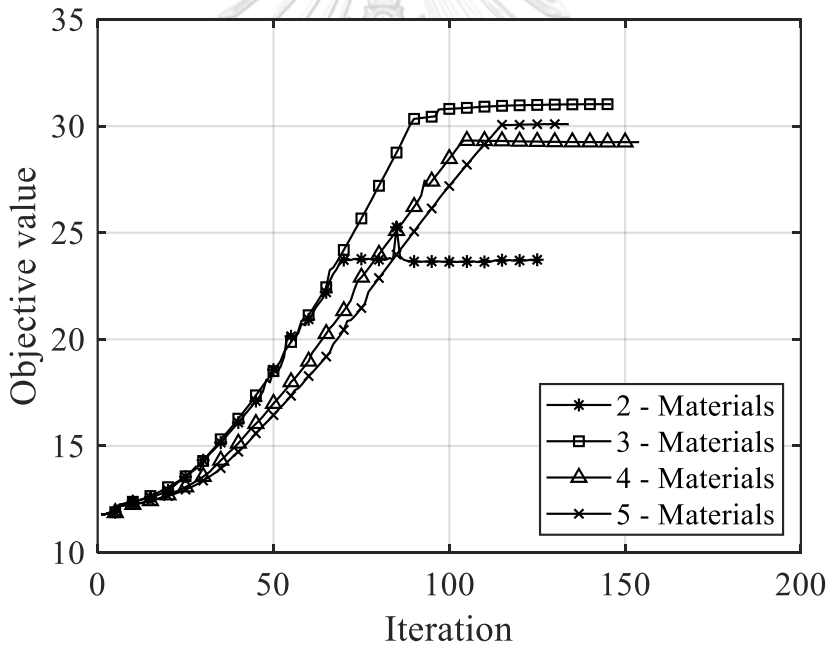

Figure 3.47 Objective value vs. iteration for AM multimaterial symmetric beams with individual global volume constraints for each of the candidate materials

4.3 2D MMTO circular domain with static load structures

From example 3.1.4, we extend the donut-shaped domain with torsion loaded boundary conditions shown in Figure 3.48. The fixed support is applied at the inner circle of the annular domain (i.e., magenta color). With multi-materials design, the global volume constraint is set to appear no more than 50 % of initial volume fraction. The candidate materials and specified volume constraints for all cases are prescribed in Table 3.11. The BESO parameters include evolutionary rate ratio (ER) = 5 %, r_{min}= 8 pixels, and the convergence criterion (τ) = 0.01 %.

Figure 3.49(a)–(d) illustrates the final topology outcomes for all cases for the UM scenario. All candidate materials show up in the final design as expected when each material is governed by a separate global constraint, and they are distributed so that stiffer materials are located where stress is anticipated to be high and more compliant materials are located where stress is anticipated to be low.

For AM scheme, the MATLAB built-in function conv2-type filter is applied with r_{den} equal to 8 pixels. The elements appearing during quadtree decomposition are limited in size to $\leq$ 32 pixels. Figure 3.49(e)–(h) shows the final topology results for 2–5 candidate materials. This optimal AM designs are analogized to the UM design as mentioned earlier. Nevertheless, compared to their heuristically and uniformly optimized counterparts, continuously optimized AM quadtree architectures perform much stiffer (less compliant). Table 3.12 compares the outcomes between UM and AM, including the number of iterations, average time, and compliance. The circular domain problem's total CPU time is presented. Since the addition/elimination procedures must be accessed several times during each iteration, the bi-section technique takes longer as the number of distinct volume restrictions increases. However, because the AM method only makes up a minor portion of the overall duration, an analysis ends almost twice as quickly as UM situations, as shown in Table 3.12. The evolutionary goal value for the circular domain of UM and AM multi-materials with individual global volume restrictions is displayed in Figure 3.50 for each of the candidate materials.

จุฬาลงกรณ์มหาวิทยาลัย
Chulalongkorn University

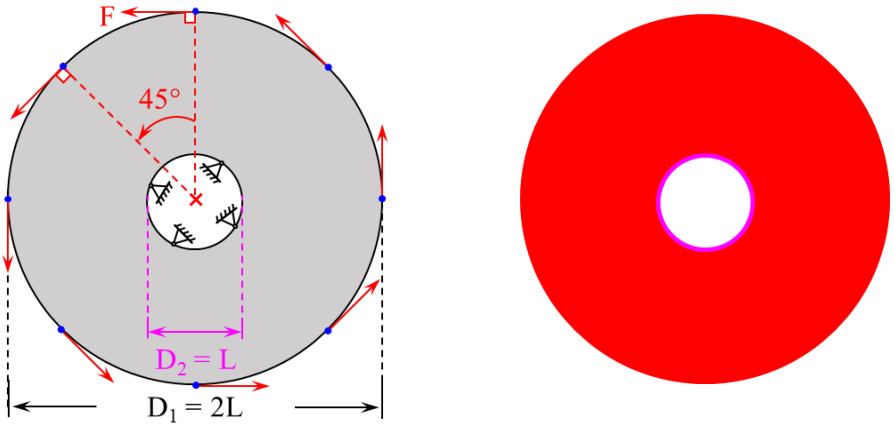

Figure 3.48 Donut shaped structure: (a) loads and boundary conditions and (b) an input image.

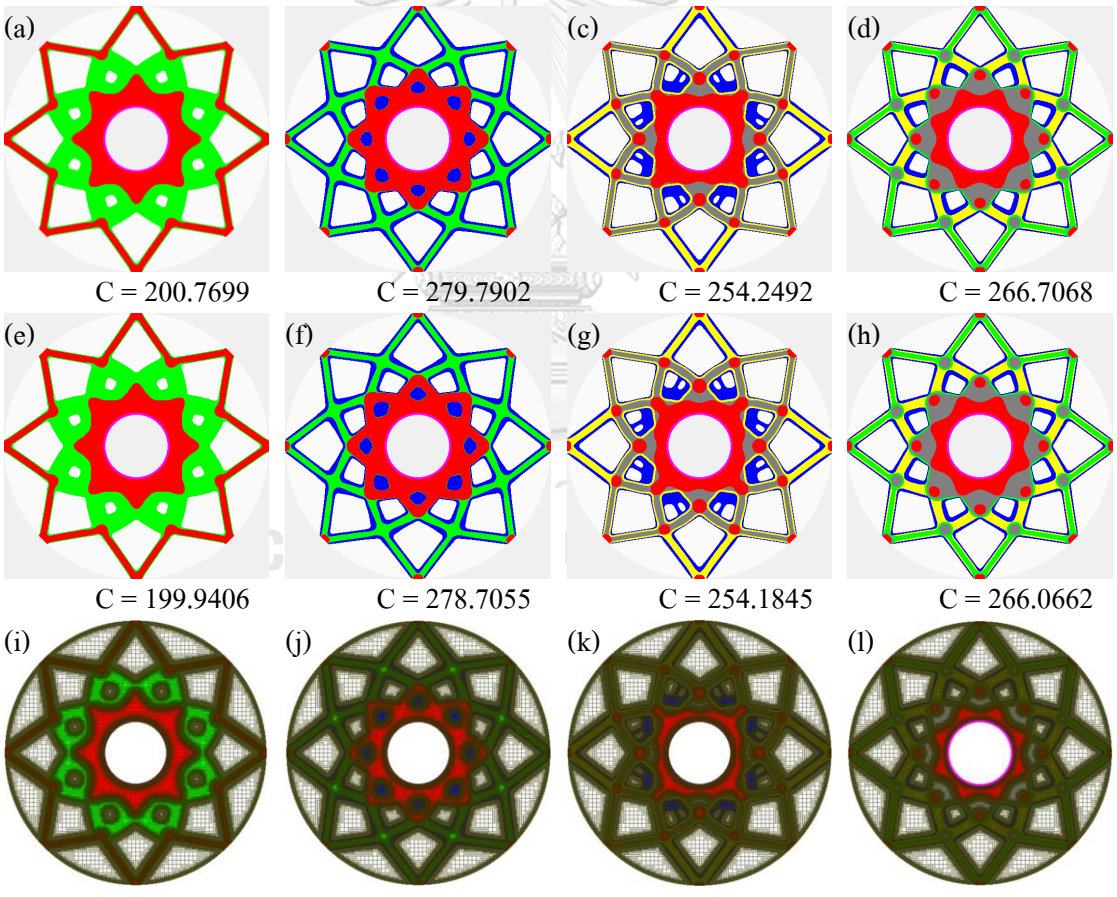

Figure 3.49 Multimaterials circular domain designs with individual global volume constraints for: (a)–(d) are UM with 2–5 candidate materials, (e)–(h) are AM with 2–5 candidate materials and (i)–(l) are final mesh for 2–5 candidate materials design

Case	Design	Iterations	Avg. time (s)	C.
UM 2-Mats	Figure 3.49(a)	96	80.3370	200.7699
UM 3-Mats	Figure 3.49(b)	167	92.7677	279.7902
UM 4-Mats	Figure 3.49(c)	103	111.3124	254.2492
UM 5-Mats	Figure 3.49(d)	105	123.3882	266.7068
AM 2-Mats	Figure 3.49(e)	105	39.5650	199.9406
AM 3-Mats	Figure 3.49(f)	138	43.8096	278.7055
AM 4-Mats	Figure 3.49(g)	89	47.2396	254.1845
AM 5-Mats	Figure 3.49(h)	110	57.3125	266.0662

Table 3.12 Comparative results between UM and AM for MMTO circular domain.

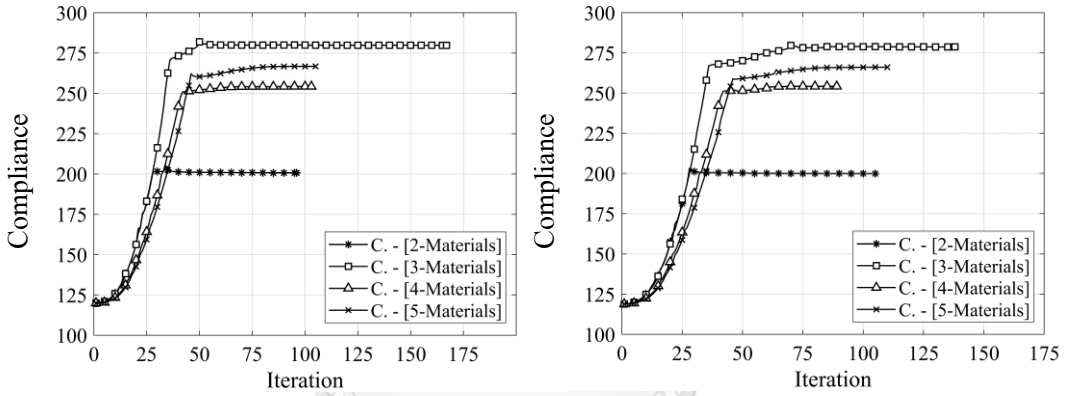

Figure 3.50 Objective value vs. iteration for (a) UM multi-materials and (b) AM multi-materials circular domain.

จุฬาลงกรณ์มหาวิทยาลัย
CHULALONGKORN UNIVERSITY

4.4 3D MMTO MBB cantilever beam with static load structures

Problem statement

A 3D framework is also extended for the MMTO with static load. Again, the arising elements in this specific problem are subdivided by using polyhedral elements. The potential materials and stated volume limitations for each situation are shown in Table 3.13 when designing a 3D cantilever beam with a vertical point load at the tip. Figure 3.51 shows the domain and boundary conditions, where P is a unit load and the length parameter, L, is assumed to be 128.

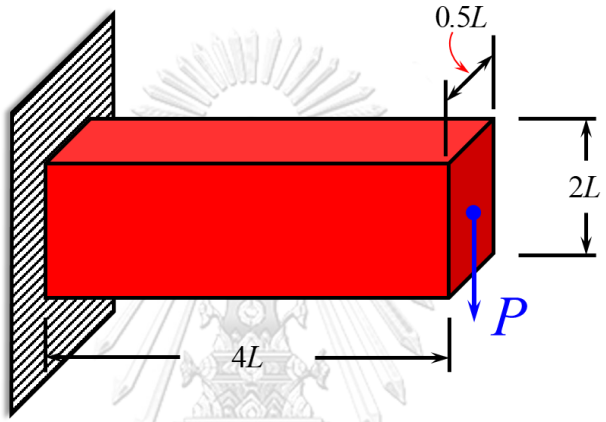

Figure 3.51 Problem domain of the 3D MBB beam cantilever.

Mat.	$E^{(m)}$	2-material		3-material			4-material			
		g_1	g_2	g_1	g_2	g_3	g_1	g_2	g_3	g_4
1	1	✓		✓			✓			
2	0.8							✓		
3	0.5		✓		✓					
4	0.4								✓	
5	0.2					✓				✓
Volume fraction		$\frac{1}{5}$	$\frac{1}{5}$	$\frac{2}{15}$	$\frac{2}{15}$	$\frac{2}{15}$	$\frac{1}{10}$	$\frac{1}{10}$	$\frac{1}{10}$	$\frac{1}{10}$

Table 3.13 The potential materials and volume restrictions for the 3D MBB beam problem.

MMTO Results using the SBFEM with uniform mesh

For MMTO with uniform mesh, the 128 × 64 × 16 domain is separated into 131,072 eight-node polygonal elements with unit edge length, and the BESO parameters used in this example include ER = 5%, r_{min} = 5 voxels, and τ = 0.01%.

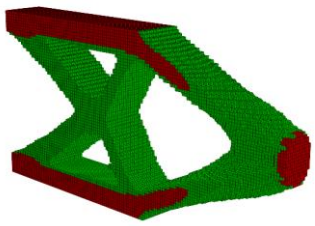

(a) 3D cantilever design based on two volume constraints at final stage (110 iterations).

(b) Separated material with individual global volume constraints

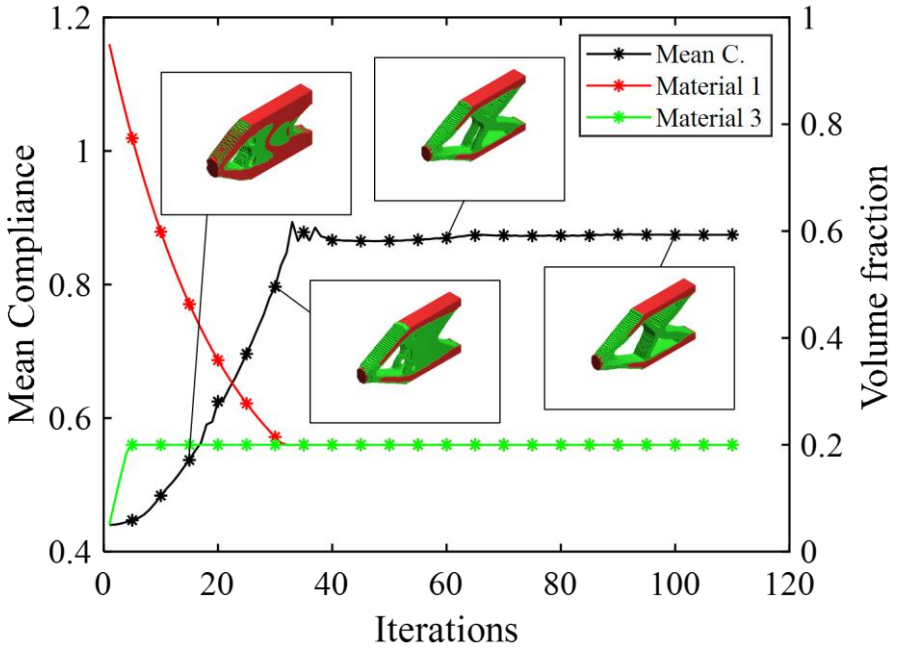

(c) Iteration histories curves of compliance values and volume constraints (C. = 0.8744).

Figure 3.52 Uniform mesh 2–phase materials 3D cantilever beam designs with individual global volume constraints.

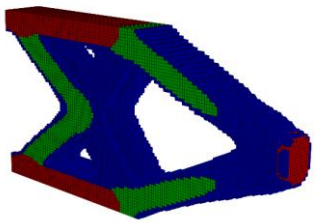

(a) 3D cantilever design based on three volume constraints at final stage (105 iterations).

(b) Separated material with individual global volume constraints

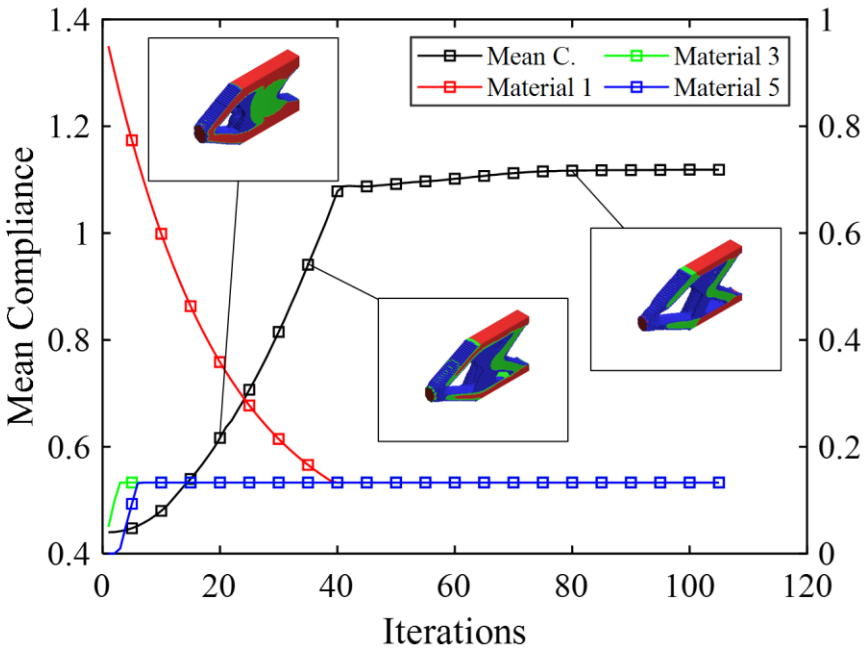

(c) Iteration histories curves of compliance values and volume constraints (C. = 1.1187).

Figure 3.53 Uniform mesh 3–phase materials 3D cantilever beam designs with individual global volume constraints.

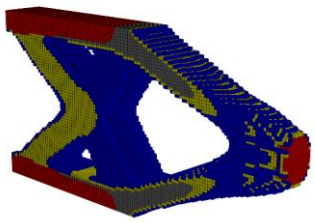

(a) 3D cantilever design based on four volume constraints at final stage (97 iterations).

(b) Separated material with individual global volume constraints

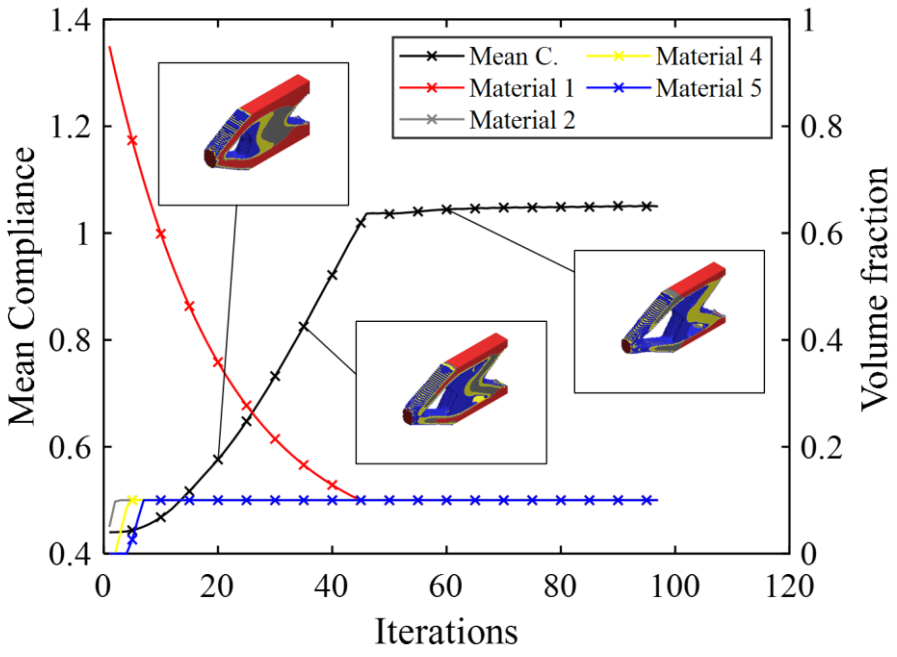

(c) Iteration histories curves of compliance values and volume constraints (C. = 1.051).

Figure 3.54 Uniform mesh 4–phase materials 3D cantilever beam designs with individual global volume constraints.

To get the best topological shape in each situation, the uniform mesh MMTO-BESO techniques were effectively used. The solution specifics (i.e., design shape with individual global volume restrictions and iteration history curves of compliance values) for a 3D cantilever beam were shown in a sequence of Figure 3.52 to Figure 3.54. It is obvious that the BESO method allows for both the addition of required elements as well as their deletion for different intended volume fractions. First material's layout position is mostly constant, but another material's topology rapidly changes as a result of which the structure tends to define volume restrictions. Figure 3.55 shows the mean compliance's history of convergence for 3D short cantilever beams with uniform mesh and multiple materials and individual global volume limitations based on static load.

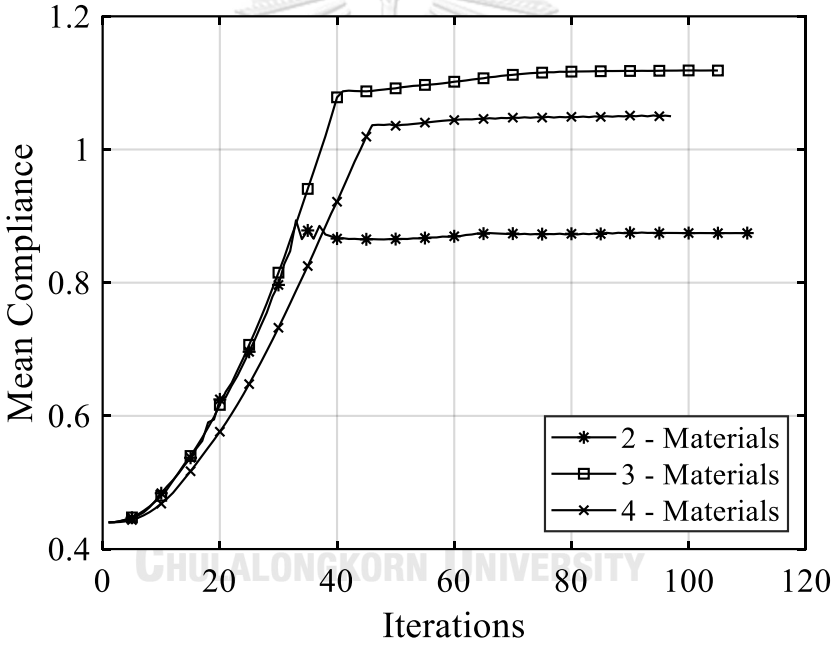

Figure 3.55 Iteration vs. objective value for uniform mesh multi-materials for each of the potential materials, 3D short cantilever beams with unique global volume limitations are set.

MMTO Results using the SBFEM with AM

In the same manner as non-uniform mesh in 2D cases, the convolution-filtered techniques are directly applied with r_{den} and $r_{min} = 5$ voxels, respectively, and the elements arising during octree decomposition are limited in size to ≤ 4 voxels.

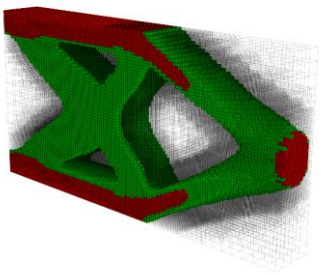

(a) AM 3D cantilever design based on two volume constraints at final stage (66 iterations).

(b) Separated material with individual global volume constraints

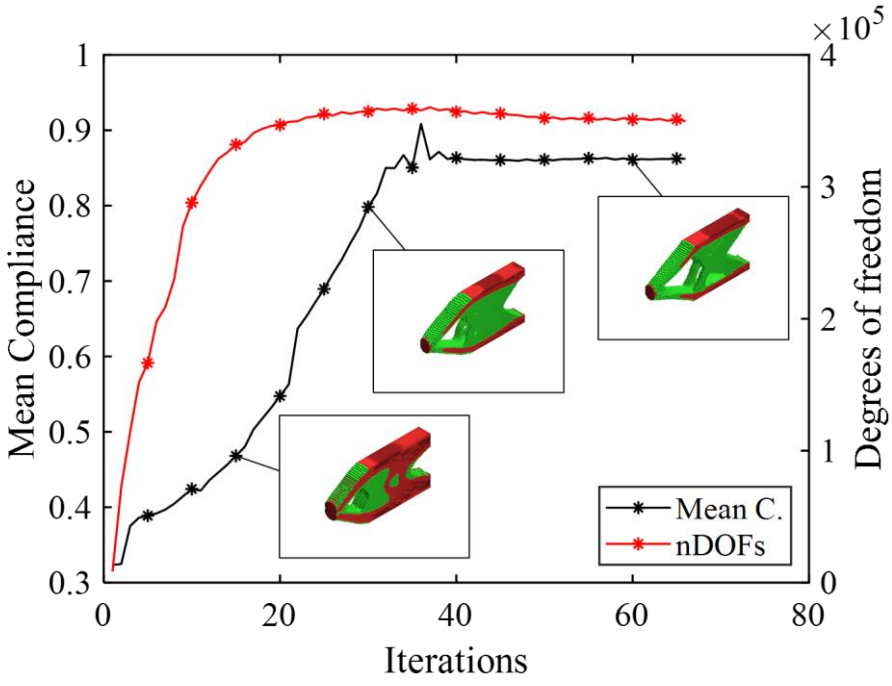

(c) Iteration histories curves of compliance values and number DOFs (C. = 0.8625).

Figure 3.56 AM 2–phase materials 3D cantilever beam designs with individual global volume constraints.

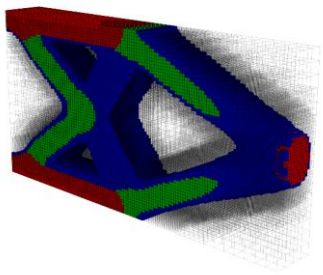

(a) AM 3D cantilever design based on three volume constraints at final stage (91 iterations).

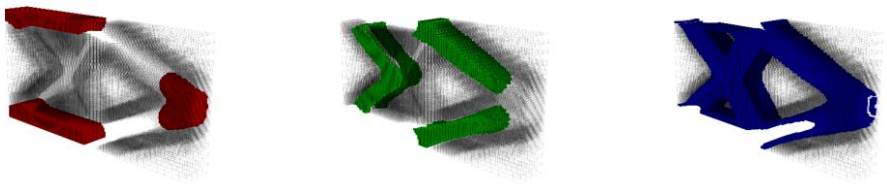

(b) Separated material with individual global volume constraints

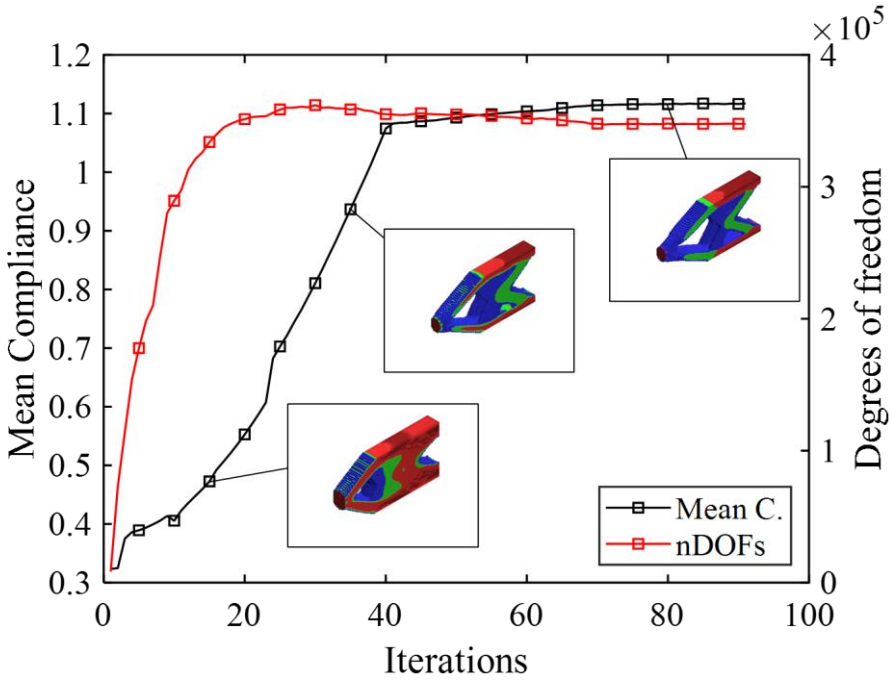

(c) Iteration histories curves of compliance values and number DOFs (C. = 1.1172).

Figure 3.57 AM 3–phase materials 3D cantilever beam designs with individual global volume constraints.

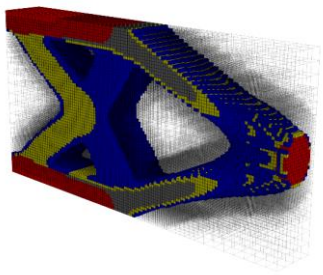

(a) AM 3D cantilever design based on four volume constraints at final stage (106 iterations).

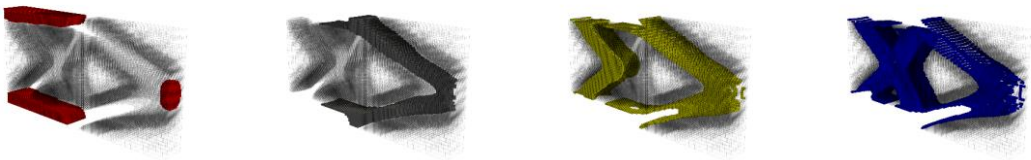

(b) Separated material with individual global volume constraints

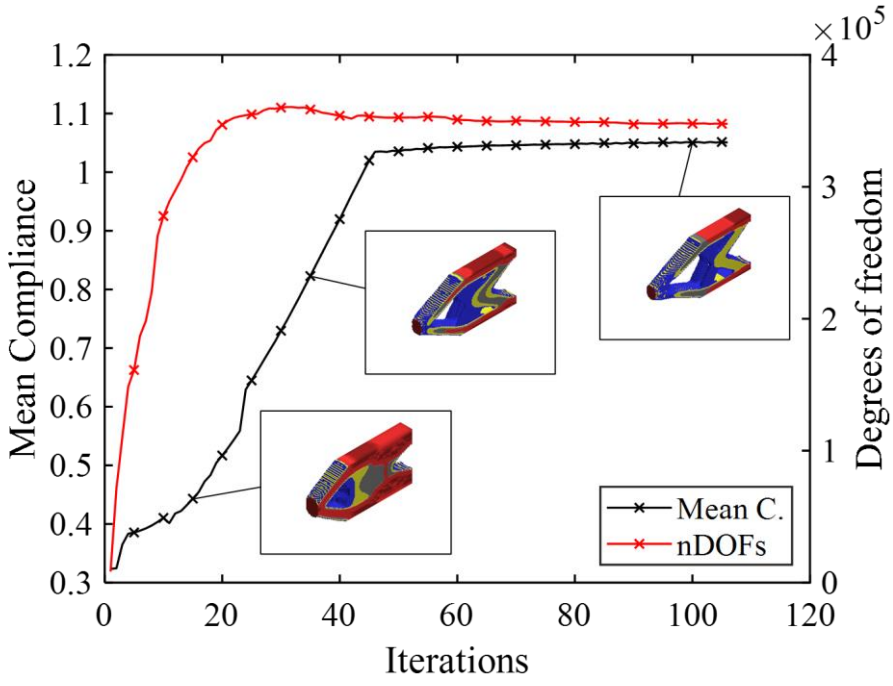

(c) Iteration histories curves of compliance values and number DOFs (C. = 1.0500).

Figure 3.58 AM 4–phase materials 3D cantilever beam designs with individual global volume constraints.

For non-uniform mesh MMTO cases, Figure 3.56 to Figure 3.58 presented the solution details (i.e., non-uniform grid design shape with individual global volume constraints and iteration histories curves of compliance values) for 3D cantilever beam. A comparative investigation of the cases illustrated by previous figures indicate that the different multi-materials designs lead to different geometrical and topological configurations. Obviously, the topological results from AM agreed well with the uniform mesh results. Moreover, for this specific numerical example, an analysis based on convolution filtered technique concludes at least 2x faster, when comparing the uniform mesh results.

The full convergence and number degrees of freedom plot for all cases is provided in Figure 3.59. It is evidenced that the amount of DOFs is also converged by employing the convolution filtered scheme.

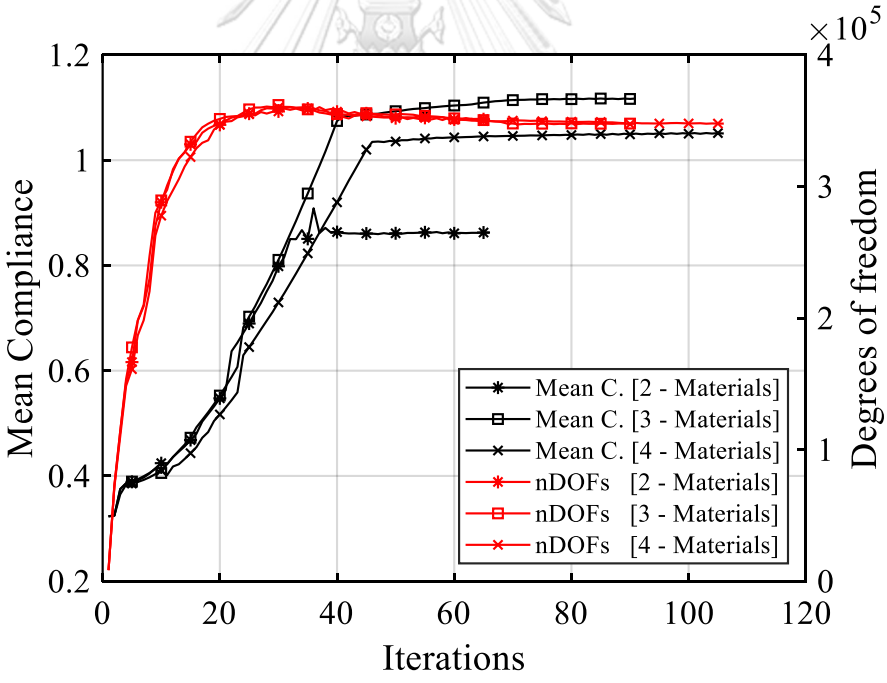

Figure 3.59 Objective value and number degrees of freedom vs. iteration for non-uniform mesh multi-materials 3D short cantilever beams for each of the candidate materials.

4.5 3D MMTO cantilever beam with uniformly static load structures

Problem statement

The SMTO with uniformly distributed loads in example 3.2.2 is also extended in a MMTO. In this specific example, the weights of all materials $W^{(m)}$ are considered in volume fractions. To separate the individual mass of each material for all cases, the final volumes are modified (i.e., $W^{(m)} \times g_i$) to match total weight equally. In this example, a 3D cantilever beam with a vertical distributed load at the bottom-right edge is designed subject to volume constraints. The limited materials and volume fractions for all cases are shown in Table 3.14. The domain and boundary conditions for the beam are depicted in Figure 3.60, where the length parameter, L, is set to 192 and F represents a unit load.

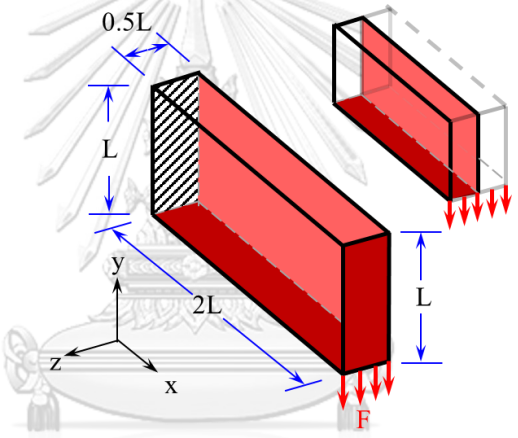

Figure 3.60 Load and boundary conditions for 3D MMTO cantilever under distributed load.

Mat.	$W^{(m)}$	$E^{(m)}$	2-material		3-material			4-material			
			g_1	g_2	g_1	g_2	g_3	g_1	g_2	g_3	g_4
1	1	1	✓		✓			✓			
2	0.8	0.8							✓		
3	0.5	0.5		✓		✓					
4	0.4	0.4								✓	
5	0.2	0.2					✓				✓
Volume fraction			$\frac{3}{40}$	$\frac{3}{20}$	$\frac{1}{20}$	$\frac{1}{10}$	$\frac{1}{4}$	$\frac{3}{80}$	$\frac{3}{64}$	$\frac{3}{32}$	$\frac{3}{16}$
Total mass			$\frac{3}{40}$	$\frac{3}{40}$	$\frac{1}{20}$	$\frac{1}{20}$	$\frac{1}{20}$	$\frac{3}{80}$	$\frac{3}{80}$	$\frac{3}{80}$	$\frac{3}{80}$

Table 3.14 The candidate materials, volume constraints and total mass for 3D cantilever beam.

MMTO Results using the SBFEM with uniform mesh

For MMTO with uniform mesh, thanks to the symmetry with respect to x–y plane, the 192 × 96 × 48 domain is discretized with 2 unit sized into 110,592 eight-node hexahedral elements with unit edge length, and the BESO parameters used in this example include ER = 5%, r_{min} = 6 voxels, and τ = 0.01%. The uniform mesh MMTO-BESO approaches were successfully performed to obtain the optimal topological shape of all cases. A series of Figure 3.61 to Figure 3.63 represented the solution details (i.e., design shape with individual global volume constraints) for 3D cantilever beam under uniformly distributed loads. It can be observed that the "hardest" material (red) is placed to the top and bottom sides, where the tension-compression state's internal forces are at their highest, while the "softer" material components (grey, green, and blue), which are supported by lower internal forces, are added to the center side.

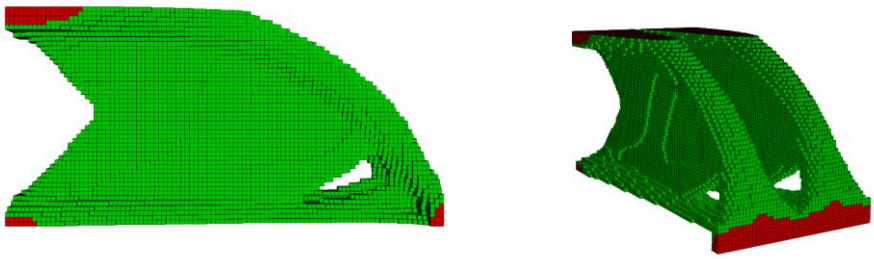

(a)

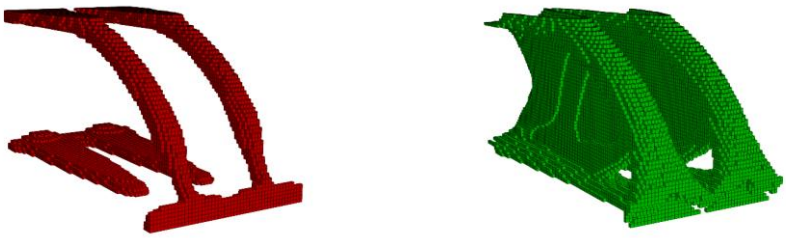

(b)

Figure 3.61 UM 2–phase materials 3D cantilever beam designs with separated global volume constraints.

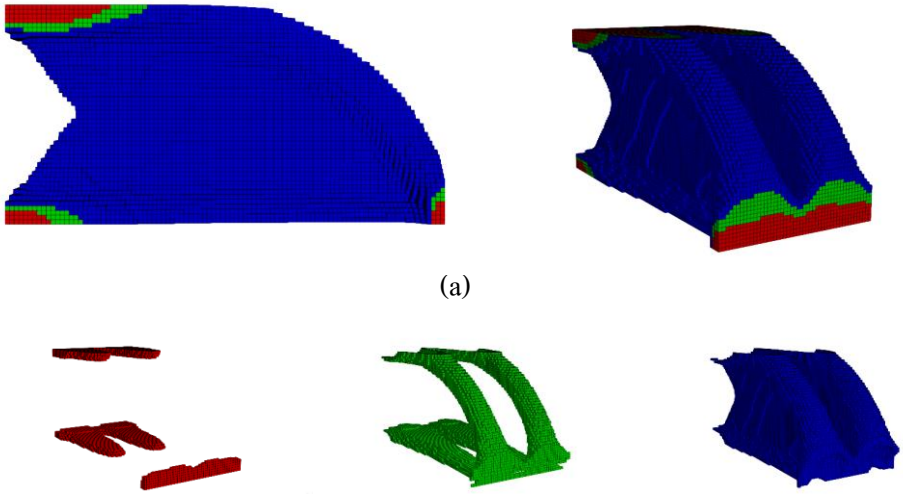

(a)

(b)

Figure 3.62 UM 3–phase materials 3D cantilever beam designs with separated global volume constraints.

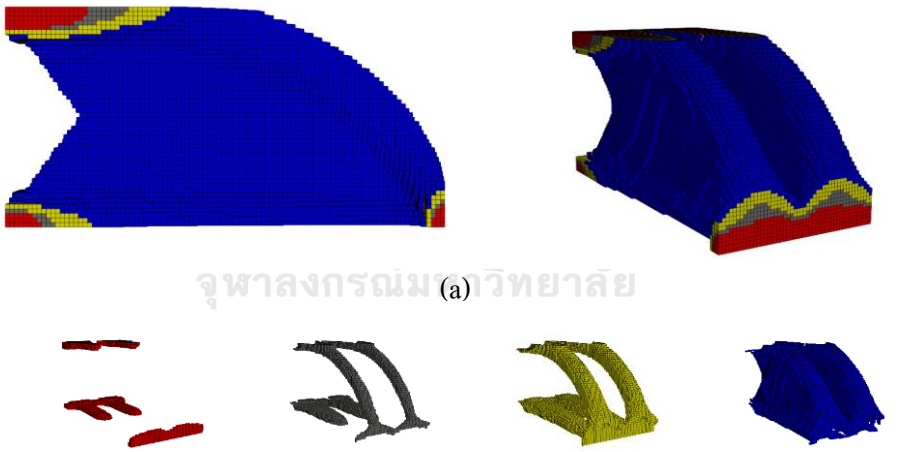

(a)

(b)

Figure 3.63 UM 4–phase materials 3D cantilever beam designs with separated global volume constraints.

MMTO Results using the SBFEM with adaptive mesh

For adaptive mesh MMTO-BESO approaches, the convolution-filtered techniques are employed with r_{den} and r_{min} =6 voxels, respectively, and the elements sizing are limited to ≤ 16 voxels. Note that the minimum element size is set to ≥ 2 voxels to prevent the exceed of CPU memories. A series of Figure 3.64 to Figure 3.66 represented the solution details (i.e., design shape with individual global volume constraints) for 3D cantilever beam under uniformly distributed loads. It should also be noticed that the findings of the 3-phase and 2-phase materials TO for 3D cantilever beams required less initial material in comparison to the single-phase material TO from the example in section 3.2.2. This is the benefit of employing MMTO with a mass fraction limitation since it selects the best candidate material quantity to utilize, and the optimal placement based on the specific load instance. The stiffest design with the predefined mass is created to achieve this. Table 3.15 demonstrates how the adoption of the total mass limitation that is being discussed successfully increases the stiffness of the design. Finally, Figure 3.67 plots the evolutionary objective value for the 3D cantilever made of UM and AM multi-materials.

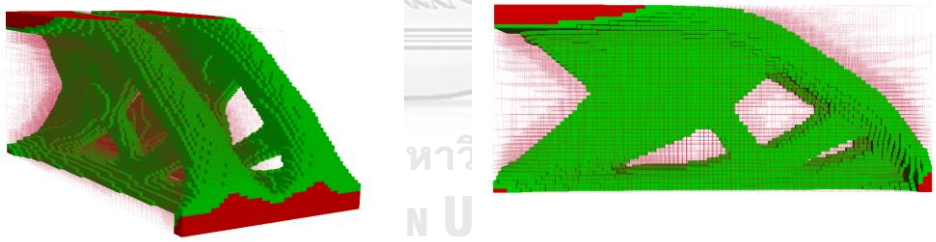

(a)

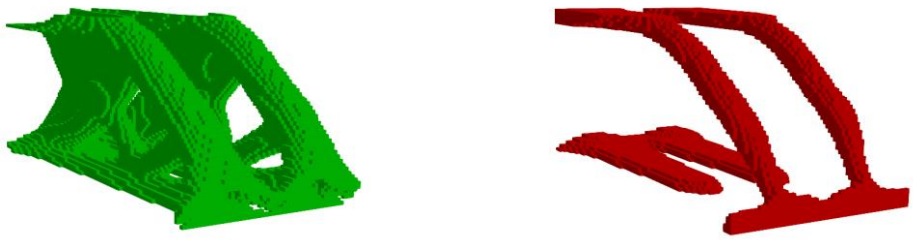

(b)

Figure 3.64 AM 2–phase materials 3D cantilever beam designs with separated global volume constraints.

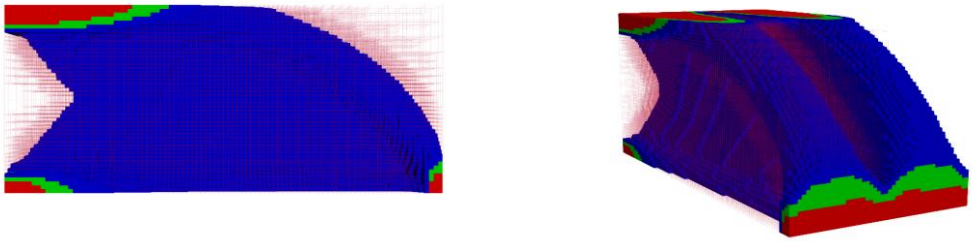

(a)

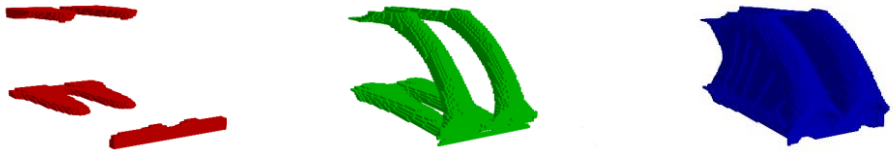

(b)

Figure 3.65 AM 3–phase materials 3D cantilever beam designs with separated global volume constraints.

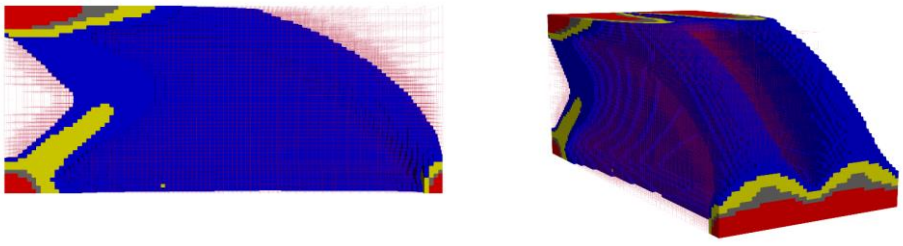

(a)

(b)

Figure 3.66 AM 4–phase materials 3D cantilever beam designs with separated global volume constraints.

Case	Design	Iterations	Avg. time (s)	C.
UM 1-Mats	Figure 3.27	103	403.5025	4818.9841
UM 2-Mats	Figure 3.61	126	454.8891	4391.6349
UM 3-Mats	Figure 3.62	110	515.5694	4345.3345
UM 4-Mats	Figure 3.63	123	554.7559	4343.4650
AM 1-Mats	Figure 3.28	145	195.9720	4774.9827
AM 2-Mats	Figure 3.64	97	218.7025	4346.5284
AM 3-Mats	Figure 3.65	92	232.5519	4342.9160
AM 4-Mats	Figure 3.66	86	240.8014	4341.6252

Table 3.15 Comparative results between UM and AM for 3D MMTO cantilever beam structure.

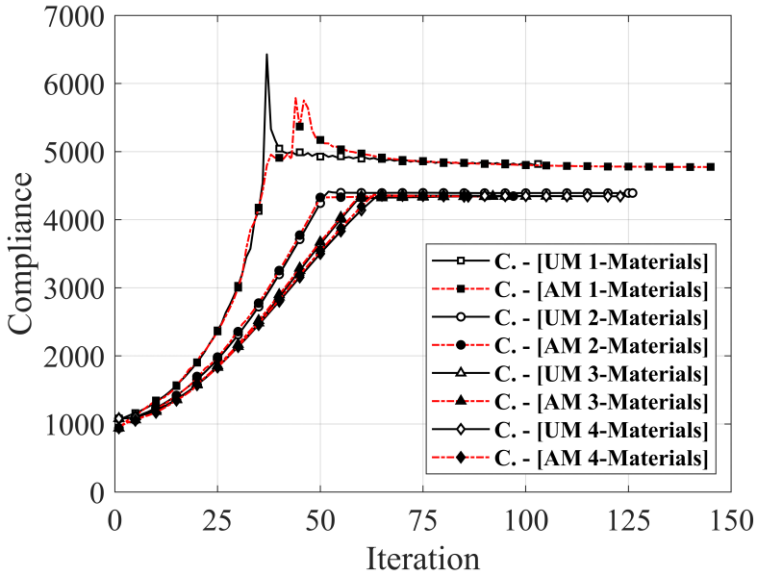

Figure 3.67 Objective value vs. iteration for UM and AM multi-materials cantilever beam structure.

4.6 3D L-shaped with static load structures

Problem statement

The example 3.2.2 is further extended in a MMTO to demonstrate its effectiveness. Similar to the previous example, the weights of all materials $W^{(m)}$ are affected in volume fractions. In essence, the 3D L-shaped construction with a single vertical point load at the middle-right node is prescribed taking into account volume restrictions, and the candidate materials and stated volume constraints for all scenarios are directly shown in Table 3.14. Figure 3.68, where the length parameter, L, is assumed to be 108 and F is a unit load, shows the domain and boundary conditions.

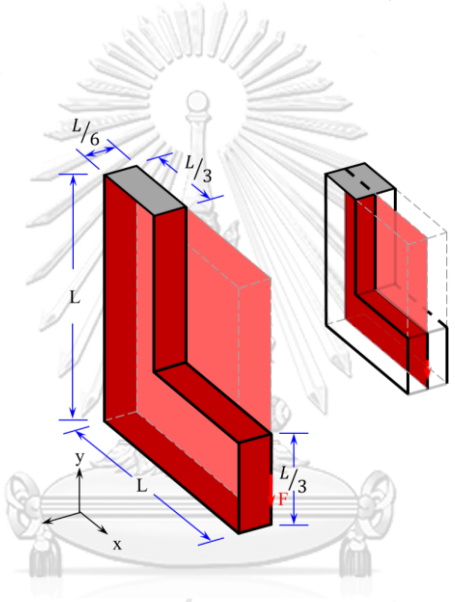

Figure 3.68 Load and boundary conditions for 3D L-shaped structure.

Chulalongkorn University

Mat.	$W^{(m)}$	$E^{(m)}$	2-material		3-material		
			g_1	g_2	g_1	g_2	g_3
1	1	1	✓		✓		
2	0.8	0.8					
3	0.5	0.5		✓		✓	
4	0.4	0.4					
5	0.2	0.2					✓
Volume fraction			$\frac{3}{40}$	$\frac{3}{20}$	$\frac{1}{20}$	$\frac{1}{10}$	$\frac{1}{4}$
Total mass			$\frac{3}{40}$	$\frac{3}{40}$	$\frac{1}{20}$	$\frac{1}{20}$	$\frac{1}{20}$

Table 3.16 The candidate materials, volume constraints and total mass for 3D L-shaped structure.

MMTO Results using the SBFEM with uniform mesh

With the symmetry in x–y plane, the 108 × 108 × 18 domain is discretized with unit sized into 116,640 eight-node hexahedral elements with unit edge length. The BESO parameters used in this example include ER = 5%, r_{min} = 3 voxels, and τ = 0.01%. The uniform mesh MMTO-BESO approaches were successfully performed to obtain the optimal topological shape of all cases. A series of Figure 3.69 to Figure 3.70 represented the solution details (i.e., design shape with individual global volume constraints) for 3D L-shaped structure with vertical loads. The "red" material is distributed along two sides from the fixed support site in the optimal topology, where the local equivalent stress is greater than the others. The softer materials are located where stress is expected to be low. After that, this schematic can be exported to an STL structure for use in additive manufacturing (3D-printing).

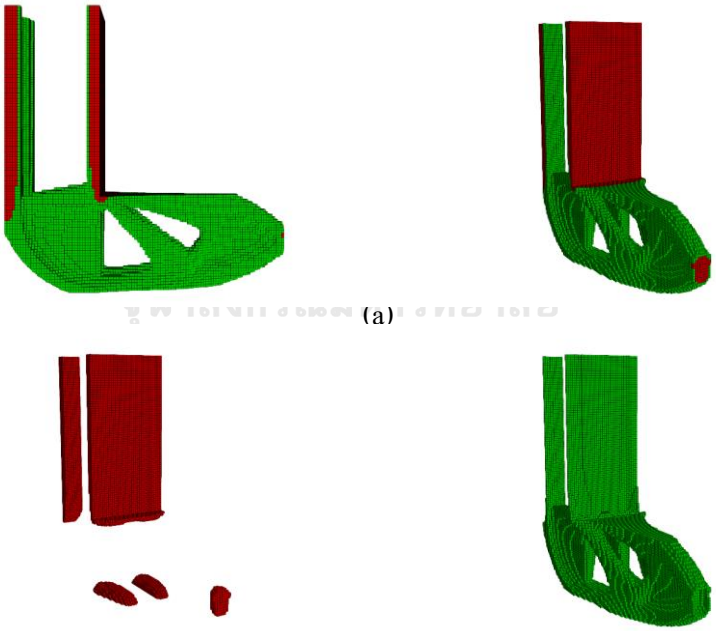

(a)

(b)

Figure 3.69 UM 2–phase materials 3D L-shaped structure designs with individual global volume constraints.

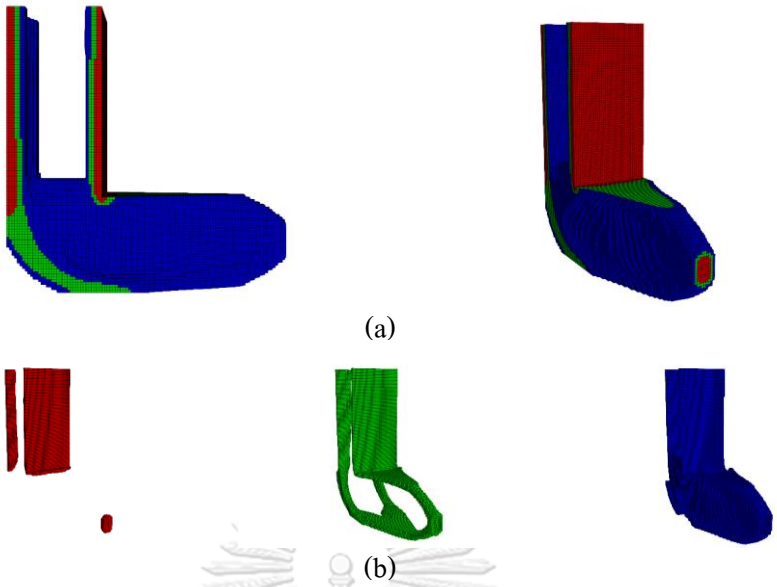

(a)

(b)

Figure 3.70 UM 3–phase materials 3D L-shaped structure designs with individual global volume constraints.

MMTO Results using the SBFEM with adaptive mesh

Similar to the AM in 2D cases, the convolution-filtered techniques are employed with r_{den} and $r_{min} = 3$ voxels, respectively, and the elements arising during octree decomposition are limited in size to ≤ 16 voxels. For this specific example, it should be noted that the domains are uniformly discretized by 4 unit-voxels in the first iteration to prevent the rapid change in shape of a structure. The topological layouts (i.e., non-uniform grid design shape with individual global volume constraints) for 3D L-shaped structure are depicted in Figure 3.71 and Figure 3.72. Comparative analysis of the scenarios depicted in the preceding illustrations reveals that various multi-material designs result in various geometrical and topological arrangements. Evidently, the topological results from AM and the uniform mesh results were in good agreement. The comparative results (e.g., number of iterations, average time, and compliance) between UM and AM are reported in Table 3.17. The overall CPU time for the L-shaped problem is presented; increased cost due to a greater number of individual volume constraints presents itself in extra time for the bi-section technique, because the addition/elimination procedures must be accessed several times in each iteration. However, since the AM method only makes up a minor portion of the overall runtime, an analysis concludes nearly twice as quickly as UM scenarios, as shown in

Table 3.17. Finally, the evolutionary objective value for UM and AM multi-materials L-shaped structure with individual global volume constraints for each of the candidate materials are plotted in Figure 3.73.

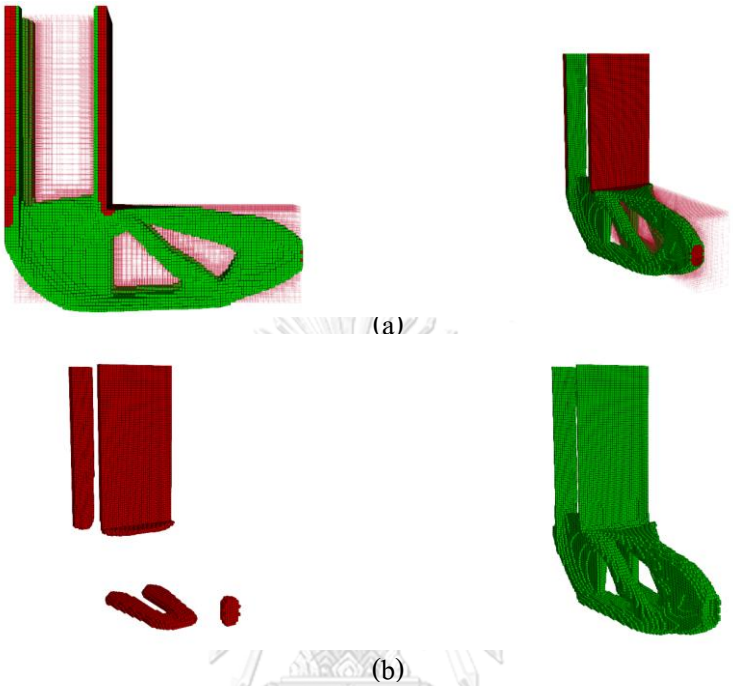

(a)

(b)

Figure 3.71 AM 2–phase materials 3D L-shaped structure designs with individual global volume constraints.

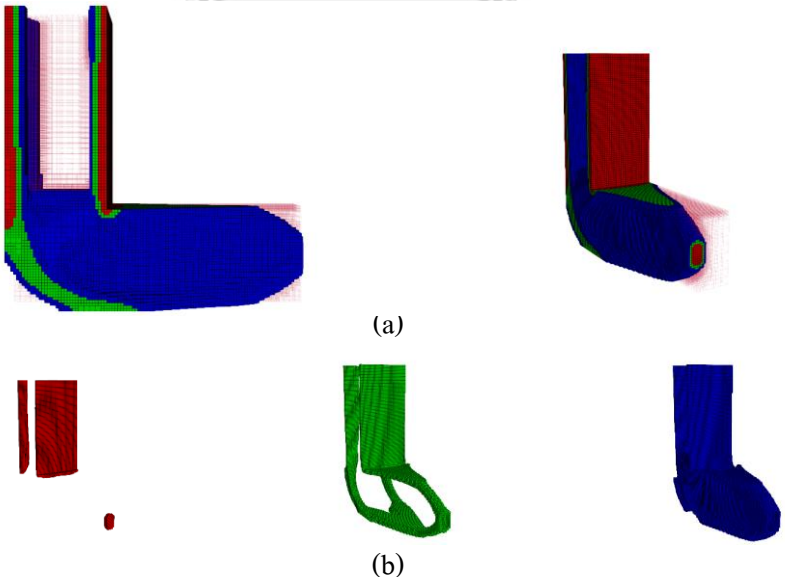

(a)

(b)

Figure 3.72 AM 3–phase materials 3D L-shaped structure designs with individual global volume constraints.

Case	Design	Iterations	Avg. time (s)	C.
UM 1-Mats	Figure 3.*32*	73	1,006.5528	2.45291
UM 2-Mats	Figure 3.69	169	2,964.8140	2.48001
UM 3-Mats	Figure 3.70	96	3,226.9898	2.39537
AM 1-Mats	Figure 3.*33*	116	213.6520	2.44576
AM 2-Mats	Figure 3.71	77	315.5873	2.47314
AM 3-Mats	Figure 3.72	97	439.0134	2.39470

Table 3.17 Comparative results between UM and AM for 3D MMTO L-shaped structure.

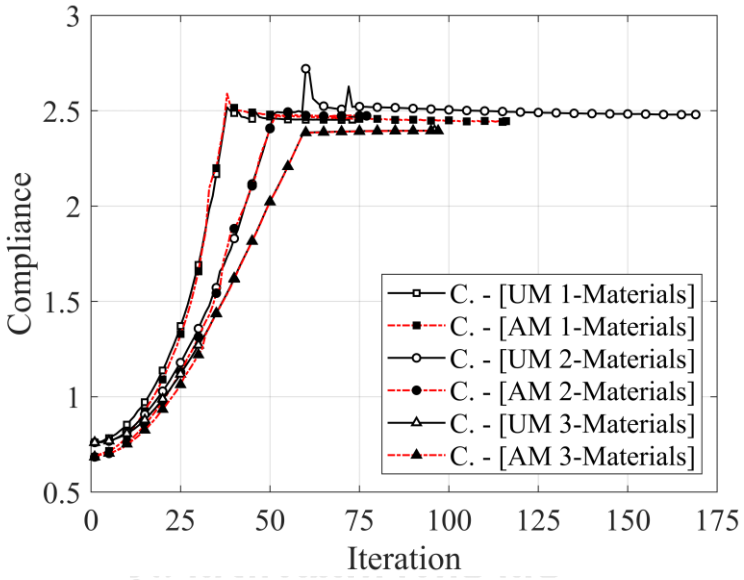

Figure 3.73 Objective value vs. iteration for UM and AM multi-materials L-shaped structure.

CHULALONGKORN UNIVERSITY

In conclusion, multi-material design refers to the use of multiple materials in the design of an object or structure. This approach allows for greater flexibility in the design process, as it allows the designer to select materials that are optimal for different parts of the structure. There are several advantages to using a multi-material design approach in topology optimization:

1. Improved performance: By using multiple materials, it is possible to optimize the design for specific performance criteria, such as strength, stiffness, or weight. For example, a structure that requires high stiffness in certain areas may benefit from using a stiffer material in those areas, while using a lighter material in other areas where weight is a concern.

2. Cost savings: Using multiple materials can also help to reduce the overall cost of the design. By selecting materials that are optimal for specific parts of the structure, it may be possible to use less of the more expensive materials, while still meeting the performance requirements of the design.
3. Manufacturing feasibility: In some cases, it may be easier to manufacture a multi-material design than a single-material design. For example, a design that combines metal and plastic components may be easier to manufacture than a design that is made entirely of metal.

Overall, the use of multi-material design in topology optimization offers a number of benefits, including improved performance, cost savings, improved manufacturing feasibility, and improved durability.

จุฬาลงกรณ์มหาวิทยาลัย
Chulalongkorn University

CHAPTER 4 TOPOLOGY OPTIMIZATION FOR DYNAMIC LOAD

1. Introduction.

As previously mentioned, the SBFEM has been demonstrated to be one of the most appropriate strategies for resolving TO issues. Several TO problems have been completely solved using the BESO algorithm. In the past, most topology optimization methods were developed for static analysis, which is concerned with the behavior of a structure under constant or slowly varying loads. However, there is growing interest in extending topology optimization techniques to consider dynamic responses as well. This is because many real-world structures are subjected to dynamic loads, and it is important to ensure that they are able to withstand these loads without failing (Díaaz & Kikuchi, 1992). In addition, the behavior of a structure under dynamic loads may be very different from its behavior under static loads, so it is important to take this into account in the design process.

There is increasing interest in using dynamic response topology optimization (TO) techniques, which consider the behavior of a structure under dynamic loads, rather than just static imposed loads. This is because dynamic forces often play a significant role in real-life situations, and it is important to design structures that can withstand these forces. In addition, the optimal design for static and dynamic performance of a structure is often carried out separately, and it is up to the designer to make multiple revisions to the design to achieve the desired combination of static and dynamic performance.

จุฬาลงกรณ์มหาวิทยาลัย
CHULALONGKORN UNIVERSITY

This chapter presents a method for performing TO of continuum structures using the SBFEM (strong form boundary element method) with dynamic loads. The proposed method is applied to both 2D and 3D problems, and the results are compared to those obtained using static response techniques to demonstrate the effectiveness and usefulness of the method. The goal is to show that the proposed method can be used to optimize the design of structures for both static and dynamic performance, without the need for multiple revisions by the designer.

2. Dynamic and Vibration Analysis

Dynamic and vibration analysis are important tools in the field of structural engineering for predicting the response of structures to various types of loading. These analyses are used to evaluate the performance of structures under both static and dynamic loads and can be applied to a wide range of structures, including buildings, bridges, and mechanical systems.

Dynamic analysis involves the study of the motion and behavior of structures under the influence of time-varying loads. This type of analysis is used to predict the response of structures to earthquakes, wind, and other types of dynamic loads. Dynamic analysis typically involves the use of advanced mathematical techniques, such as finite element analysis and modal analysis, to determine the natural frequencies, mode shapes, and response of the structure under different loading conditions.

Vibration analysis is a type of dynamic analysis that focuses specifically on the vibrations of structures. Vibration analysis is used to predict the response of structures to periodic loads, such as those caused by machinery or wind. It is also used to evaluate the effect of vibrations on the performance of structures, such as the fatigue life of materials or the comfort of occupants in a building.

Dynamic and vibration analysis are essential tools for ensuring the safety and reliability of structures in the built environment. These analyses help engineers to design structures that can withstand the various types of loads that they may be subjected to over their lifetime, and to identify potential problems before they occur.

2.1 Equation of Motion

In order to treat dynamic response, a brief summary of the SBFEM in elastodynamic is given. For a more elaborate derivation and detailed explanations, see the report by (C. Song & Wolf, 1997). To formulates the equation of motion, an infinitesimal volume of the solid body, Eq. (1.3a), is modified as

$$\frac{\partial \sigma_{xx}}{\partial x} + \frac{\partial \tau_{xy}}{\partial y} + \frac{\partial \tau_{xz}}{\partial z} + V_x = \rho \ddot{u}_x \tag{1}$$

$$\frac{\partial \tau_{xy}}{\partial x} + \frac{\partial \sigma_{yy}}{\partial y} + \frac{\partial \tau_{yz}}{\partial z} + V_y = \rho \ddot{u}_y$$

$$\frac{\partial \tau_{xz}}{\partial x} + \frac{\partial \tau_{yz}}{\partial y} + \frac{\partial \sigma_{zz}}{\partial z} + V_z = \rho \ddot{u}_z,$$

where V_i is the body forces, ρ is the mass density, and $\ddot{u}_i$ is the accelerations (second derivatives of displacements). By using differential operator $[L]$, Eq. (1) can be reduced in matrix notation as

$$[L]^T\{\sigma\} + \{V_i\} = \rho \ddot{u}_i \tag{2}$$

By omitting body forces, Eq. (2) are simplified as

$$[L]^T\{\sigma\} = 0 \tag{3}$$

The principle of virtual work statement in Eq. (2.2b) is augmented to include the inertial forces $\rho\{\ddot{u}\}$

$$\int_V \{\delta\varepsilon\}^T\{\sigma\}dV + \int_V \{\delta u\}^T \rho\{\ddot{u}\}dV = \{\delta u_b\}^T\{F\} \tag{4}$$

Following the derivation of the SBFE equation in Chapter 2, by assembling the contributions of mass matrix from all sectors, the principle of virtual work is expressed as

$$\{\delta u_b\}^T[K]\{u_b\} + \{\delta u_b\}^T[M]\{\ddot{u}\} = \{\delta u_b\}^T\{F\} \tag{5}$$

จุฬาลงกรณ์มหาวิทยาลัย
CHULALONGKORN UNIVERSITY

Since the virtual displacement, δu_b, is arbitrary, the equation of motion can be state as

$$[K]\{u_b\} + [M]\{\ddot{u}\} = \{F\} \tag{6}$$

By assembling the equation of motion of the S-elements, the equation of the global system is constructed in the same manner as the standard FEM

$$[K_G]\{u_G\} + [M_G]\{\ddot{u}_G\} = \{F_G\}, \tag{7}$$

where the mass matrices of the S-elements are combined to create the global mass matrix $[M_G]$. The external force vector $\{F_G\}$ is created by converting the external forces to comparable nodal forces.

The nodal displacement vector is divided into unknown displacements $\{u_1\}$ and required nodal displacements $\{u_2\}$ in order to impose the boundary constraints. The equation of the global system is enlarged as follows when the stiffness matrix, mass matrix, and external force vector are separated out.

$$\begin{bmatrix}[K_{11}] & [K_{12}]\\ [K_{21}] & [K_{22}]\end{bmatrix}\begin{Bmatrix}\{u_1\}\\ \{u_2\}\end{Bmatrix} + \begin{bmatrix}[M_{11}] & [M_{12}]\\ [M_{21}] & [M_{22}]\end{bmatrix}\begin{Bmatrix}\{\ddot{u}_1\}\\ \{\ddot{u}_2\}\end{Bmatrix} = \begin{Bmatrix}\{F_1\}\\ \{F_2\}\end{Bmatrix} \quad (8)$$

By moving the components containing the known displacements, $\{u_2\}$, to the right side, the equations in the first row may be solved to get the unknown displacements, $\{u_1\}$.

$$[K_{11}]\{u_1\} + [M_{11}]\{\ddot{u}_1\} = \{F_1\} - [K_{12}]\{u_2\} - [M_{12}]\{\ddot{u}_2\} \quad (9)$$

which is represented as a system of second order nonhomogeneous ordinary differential equations.

2.2 Time History Analysis Using the Newmark Method

Direct integration of Eq. (9) in time yields a dynamic response time-history of the system. The mass matrix is symmetric and positive definite, whereas the static stiffness matrix generated using the SBFEM is symmetric and semi-positive definite. Time history analysis completely obtains the structural reaction at designated intervals for a specific enduring interaction, which is opposed to other existing analysis techniques that reveal the structure reaction in the form of amplitudes obtained at a single moment.

จุฬาลงกรณ์มหาวิทยาลัย
CHULALONGKORN UNIVERSITY

The Newmark method is used to solve the above-presented task, and it belongs to the group of algorithms that are unconditionally convergent for appropriately defined method parameters. The Newmark time integrator operates predictor–corrector scheme with the parameters, γ and β. Denoting the size of the time step as Δ_t, the system of 2nd order ODE at l^{th} time step $t_l = l\Delta_t$ is expressed as

$$[K_{11}]\{u_1\}_l + [M_{11}]\{\ddot{u}_1\}_l = \{F_1\}_l - [K_{12}]\{u_2\}_l - [M_{12}]\{\ddot{u}_2\}_l \quad (10)$$

At the initial state, the system is assumed to be at rest with: $\{u\}_0 = \{\dot{u}\}_0 = 0$, and the displacements $\{u\}_l$ and velocity $\{\dot{u}\}_l$ are obtained using the correctors as follows.

$$\{u\}_l = \{\tilde{u}\}_l + \beta\Delta_t^2\{\ddot{u}\}_l \tag{11}$$
$$\{\dot{u}\}_l = \{\tilde{\dot{u}}\}_l + \gamma\Delta_t\{\ddot{u}\}_l \tag{12}$$

where $\{\tilde{u}\}_l$ and $\{\tilde{\dot{u}}\}_l$ are the predictors of the displacement and velocities, respectively.

$$\{\tilde{u}\}_l = \{u\}_{l-1} + \Delta_t\{\dot{u}\}_{l-1} + (0.5-\beta)\Delta_t^2\{\ddot{u}\}_{l-1} \tag{13}$$
$$\{\tilde{\dot{u}}\}_l = \{\dot{u}\}_{l-1} + (1-\gamma)\Delta_t\{\ddot{u}\}_{l-1} \tag{14}$$

Predictor information are computed from the responses at the previous time step $(l-1)$ and the parameters, γ and β, control the stability of the step-by-step integration and the amount of numerical damping introduced into the system by the method.

Substituting both Eqs. (11) and (12) into Eq. (10) and transferring the known term at time step, l, to the right-hand side yields a system of algebraic equations

$$\begin{aligned}\left(\beta\Delta_t^2[K_{11}] + [M_{11}]\right)\{\ddot{u}_1\}_l \\ = \{F_1\}_l - [K_{11}]\{\tilde{u}_1\}_l - [K_{12}]\{u_2\}_l - [M_{12}]\{\ddot{u}_2\}_l\end{aligned} \tag{15}$$

The unknown accelerations $\{\ddot{u}_1\}_l$ is directly solved using Eq. (15) and the displacements $\{u\}_l$ and velocities $\{\dot{u}\}_l$ are obtained from both Eqs. (11) and (12)

จุฬาลงกรณ์มหาวิทยาลัย
Chulalongkorn University

At the initial stage (time step $l = 0$), if external forces $\{F_1\}_0$ or prescribed accelerations $\{\ddot{u}_2\}_0$ exist, the initial unknown accelerations $\{\ddot{u}_1\}_0$ are obtained by solving

$$[M_{11}]\{\ddot{u}_1\}_0 = \{F_1\}_0 - [M_{12}]\{\ddot{u}_2\}_0 \tag{16}$$

The processes of Newmark algorithm are illustrated in Figure 4.1 and the outputs consist of the times, displacement responses, velocity responses, and acceleration responses.

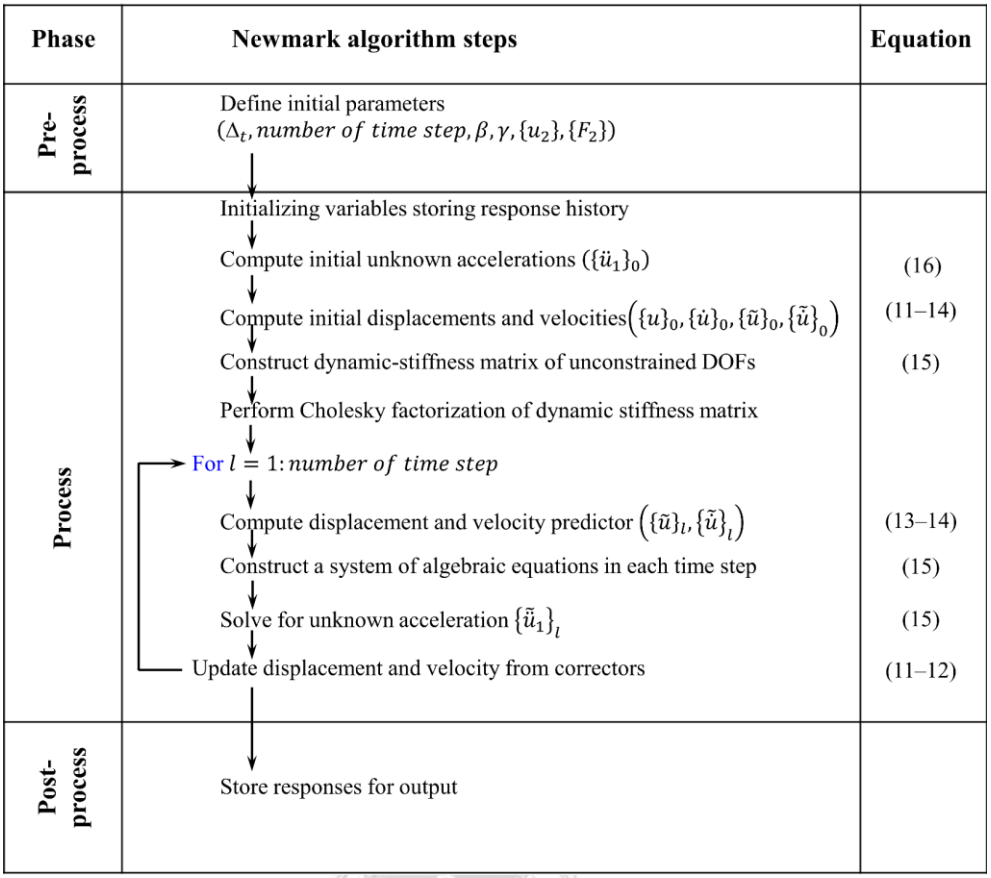

Figure 4.1 Flowchart of predictor/corrector Newmark algorithm.

2.3 High Order implicit time integration Method

A unique time-stepping technique dubbed "High-order Implicit Time Integration Scheme Based on Padé Expansions" has recently been created via dynamic analysis based on time domain. This numerical method was put out by Chongmin Song, Eisenträger, and Zhang (2022) to deal with the matrix exponential solution of a system of first-order ordinary differential equations that were expressed in state space. There is no need for a direct inversion of the mass matrix, which is a key component of the innovative approach. Based on the diagonal Padé expansion of order M, an order $2M$ time-stepping technique is built. Recursively solving one real matrix equation system and $(M-1)/2$ complex matrix equation systems is possible when M is odd. There exist $M/2$ complex matrices-based systems of equations where M is even. These systems are sparse and comparable in complexity to the classical Newmark method since the effective system matrix is a linear combination of the static stiffness, damping, and mass matrices. Analytically speaking, the

resulting second-order technique is equivalent to the Newmark constant average acceleration method.

This section briefly explains the theory required for the high-order time integration scheme's derivation. A Padé series expansion is used as an approximation based on the accurate solution of the motion equations. This produces an extremely precise unconditionally stable implicit system that can be applied to a number of structural dynamics problems.

2.3.1 Development of time integration method

The equation of motion in structural dynamic problems is a semi-discrete system of 2nd-order ODEs which can be expressed in time t as

$$[M]\{\ddot{u}\}_t + [C]\{\dot{u}\}_t + [K]\{u\}_t = \{f\}_t \tag{17}$$

With the initial conditions

$$\{u\}_{t=0} = \mathbf{u}_0 \tag{18a}$$

$$\{\dot{u}\}_{t=0} = \dot{\mathbf{u}}_0 \tag{18b}$$

where $[M]$, $[C]$, $[K]$ denote the mass, damping, and stiffness matrices respectively. $\{f\}$ is the external excitation force vector, and $\{u\}$, $\{\dot{u}\}$, $\{\ddot{u}\}$ represent displacement, velocity, and acceleration vectors, respectively.

จุฬาลงกรณ์มหาวิทยาลัย
Chulalongkorn University

The whole simulation time is split up into a finite number of periods in a numerical time-stepping process, which is conceptually somewhat similar to a one-dimensional spatial discretization. It is assumed, without losing generality, that the time step n covers the range $[t_{n-1}, t_n]$. With $n = 1,2,\cdots n_s$ being the number of time steps, the time step size (increment) is therefore simply stated as $\Delta t = t_n - t_{n-1}$. For each time step, a (local) dimensionless time variable named s is added in the sake of clarity and consistency. At the start of a time step, s is specified as 0, and at the conclusion, it is equal to 1. As a result, the time inside time step n is defined as

$$t_s = t_{n-1} + s\Delta t, \quad 0 \le s \le 1 \tag{19}$$

with $t(s=0)=t_{n-1}$ at the start of a time step and $t(s=1)=t_n$ at the conclusion of a time step. The chain rule is used to translate the vectors of velocity and acceleration inside a time step $(t_{n-1} \le t \le t_n)$ into terms of the dimensionless time s.

$$\{\dot{u}\} = \frac{1}{\Delta t}\frac{d\mathbf{u}}{ds} = \frac{1}{\Delta t}\dot{\mathbf{u}} \tag{20a}$$

$$\{\ddot{u}\} = \frac{1}{\Delta t^2}\frac{d^2\mathbf{u}}{ds^2} = \frac{1}{\Delta t^2}\ddot{\mathbf{u}} \tag{20b}$$

Therefore, the equation of motion can be expressed in the dimensionless time as

$$\mathbf{M}\ddot{\mathbf{u}} + \Delta t\mathbf{C}\dot{\mathbf{u}} + \Delta t^2\mathbf{K}\mathbf{u} = \Delta t^2\mathbf{f} \tag{21}$$

Introducing a state-space vector $\mathbf{z}$ defined as

$$\mathbf{z} = \begin{Bmatrix}\dot{u}\\ u\end{Bmatrix} \tag{22}$$

Eq. (21) can be transformed into a system of first-order ODEs

$$\dot{\mathbf{z}} \equiv \frac{d\mathbf{z}}{ds} = \mathbf{A}\mathbf{z} + \mathbf{F} \tag{23}$$

where $\mathbf{A}$ is the constant coefficient matrix defined as

$$\mathbf{A} = \begin{bmatrix}-\Delta t\mathbf{M}^{-1}\mathbf{C} & -\Delta t^2\mathbf{M}^{-1}\mathbf{K}\\ \mathbf{I} & 0\end{bmatrix} \tag{24}$$

and $\mathbf{F}$ is the non-homogeneous (force) term

$$\mathbf{F} = \begin{Bmatrix}\Delta t^2\mathbf{M}^{-1}\mathbf{f}\\ 0\end{Bmatrix} \tag{25}$$

จุฬาลงกรณ์มหาวิทยาลัย
CHULALONGKORN UNIVERSITY

The general solution of Eq. (23) at time t_n is obtained with the matrix exponential function as

$$\mathbf{z}_n = e^{\mathbf{A}s}\mathbf{z}_{n-1} + e^{\mathbf{A}s}\int_0^s e^{\mathbf{A}\tau}\mathbf{F}(\tau)d\tau \tag{26}$$

The force vector $\mathbf{f}$, and thus $\mathbf{F}$, is expressed as a polynomial expansion at the middle of the time step n

$$\mathbf{F}_n(s) = \sum_{k=0}^{p_f}\tilde{\mathbf{F}}_{mn}^{(k)}(s-0.5)^k = \tilde{\mathbf{F}}_{mn}^{(0)} + \tilde{\mathbf{F}}_{mn}^{(1)}(s-0.5) + \tilde{\mathbf{F}}_{mn}^{(2)}(s-0.5)^2 + \cdots + \tilde{\mathbf{F}}_{mn}^{(p_f)}(s-0.5)^{p_f} \tag{27}$$

The expansion consists of $p_f + 1$ terms, where p_f is the order of the polynomial approximation of the forcing function. The solution in Eq. (26) at the end $(s=1)$ of the time step is simplified to

$$\mathbf{z}_n = e^{\mathbf{A}}\mathbf{z}_{n-1} + \sum_{k=0}^{p_f} \mathbf{B}_k \tilde{\mathbf{F}}_{mn}^{(k)} \tag{28}$$

where $\mathbf{B}_k$ is integrated by parts and can determined recursively

$$\mathbf{B}_k = e^{\mathbf{A}} \int_0^1 (\tau - 0.5)^k e^{-\mathbf{A}\tau} d\tau = \mathbf{A}^{-1}\left(k\mathbf{B}_{k-1} + \left(-\frac{1}{2}\right)^k (e^{\mathbf{A}} - (-1)^k)\mathbf{I}\right) \quad \forall k = 0,1,2,\dots,p_f \tag{29}$$

with the starting value at $k = 0$

$$\mathbf{B}_0 = e^{\mathbf{A}} \int_0^1 e^{-\mathbf{A}\tau} d\tau = \mathbf{A}^{-1}(e^{\mathbf{A}} - \mathbf{I}) \tag{30}$$

2.3.2 Padé expansion of the matrix exponential function

To reduce computing costs, it may be possible to approximate the matrix exponential in Equation (28) with simpler and more computationally efficient functions. One way to do this is to use polynomial approximation techniques such as Taylor expansions, which result in explicit time-stepping systems that are only conditionally stable. This means that there is a critical time increment that must not be exceeded in order for the algorithm to be stable. On the other hand, using approximation techniques based on rational functions, such as Padé expansions, can result in implicit algorithms that are unconditionally stable. In this case, the size of the time step is determined solely by the accuracy requirements in relation to the response history, rather than being limited by stability considerations. It is worth noting that both Taylor expansions and Padé expansions have been proposed as methods for approximating matrix exponentials, but they have different properties and may be more or less suitable for different types of problems (Chongmin Song, Eisenträger, et al., 2022).

จุฬาลงกรณ์มหาวิทยาลัย
Chulalongkorn University

The approximation of the matrix exponential $e^{\mathbf{A}}$ is applied by diagonal Padé expansion (see Eq. B.2). The diagonal Padé approximation of order M is expressed as

$$e^{\mathbf{A}} \approx e_M^{\mathbf{A}} = \mathbf{Q}_M^{-1}(\mathbf{A})\mathbf{P}_M(\mathbf{A}) \tag{31}$$

where the polynomials $\mathbf{P}_M(\mathbf{A})$ and $\mathbf{Q}_M(\mathbf{A})$ can be expressed as

$$\mathbf{P}_M(\mathbf{A}) = \sum_{m=0}^{M} \frac{(2M-m)!}{m!\,(M-m)!}\mathbf{A}^m \tag{32a}$$

$$\mathbf{Q}_M(\mathbf{A}) = \sum_{m=0}^{M} \frac{(2M-m)!}{m!\,(M-m)!}(-\mathbf{A})^m \tag{32b}$$

Unless necessary, the order M and the argument $\mathbf{A}$ will be omitted hereafter for simplicity of notation. Pre-multiplying Eq. (28) with $\mathbf{Q}$ and using Eq. (31) leads to

$$\mathbf{Q}\mathbf{z}_n = \mathbf{P}\mathbf{z}_{n-1} + \sum_{k=0}^{p_f} \mathbf{C}_k \tilde{\mathbf{F}}_{mn}^{(k)} \tag{33}$$

where the matrices $\mathbf{C}_k$ are introduced and expressed as polynomials of $\mathbf{A}$ employing Eqs. (29) and (31). The general formula to determine $\mathbf{C}_k$ is given as

$$\mathbf{C}_k = \mathbf{Q}\mathbf{B}_k = \mathbf{A}^{-1}\left(k\mathbf{C}_{k-1} + \left(-\frac{1}{2}\right)^k \left(\mathbf{P} - (-1)^k\right)\mathbf{Q}\right) \quad \forall k = 0,1,2,\dots,p_f \tag{34}$$

Which can be further simplified to

$$\mathbf{C}_0 = \mathbf{Q}\mathbf{B}_0 = \mathbf{A}^{-1}(\mathbf{P} - \mathbf{Q}) \quad \forall k = 0,1,2,\dots,p_f \tag{35}$$

A computationally efficient implementation process must be developed in order to execute the time-stepping strategy shown in Eq. (33) as it still necessitates the explicit computation of the matrix $\mathbf{A}$. This procedure is covered in depth in the next section.

2.3.3 Time-stepping scheme

Following Chongmin Song, Zhang, Eisenträger, and Ankit (2022) to develop an efficient algorithm, the polynomial $\mathbf{Q}$ is factorized as

$$\mathbf{Q} = (r_1\mathbf{I} - \mathbf{A})(r_2\mathbf{I} - \mathbf{A})\dots(r_M\mathbf{I} - \mathbf{A}) \tag{36}$$

The root r are either real or pairs of complex conjugates. Using Eq. (36), Eq. (33) is rewritten as

$$(r_1\mathbf{I} - \mathbf{A})(r_2\mathbf{I} - \mathbf{A})\dots(r_M\mathbf{I} - \mathbf{A})\mathbf{z}_n = \mathbf{b}_n \tag{37}$$

Where the right-hand side $\mathbf{b}_n$ is expressed as

$$\mathbf{b}_n = \mathbf{P}\mathbf{z}_{n-1} + \sum_{k=0}^{p_f} \mathbf{C}_k \tilde{\mathbf{F}}_{mn}^{(k)} \tag{38}$$

Equation (37) is reformulated as series of equations linear in matrix $\mathbf{A}$ by introducing the auxiliary variables $\mathbf{z}^{(k)}(k\epsilon\{1,2,\dots,M-1\})$

$$\begin{aligned}(r_1\mathbf{I} - \mathbf{A})\mathbf{z}^{(1)} &= \mathbf{b}_n \\ (r_2\mathbf{I} - \mathbf{A})\mathbf{z}^{(2)} &= \mathbf{z}^{(1)}\end{aligned} \tag{39}$$

จุฬาลงกรณ์มหาวิทยาลัย
Chulalongkorn University

...

$$(r_M\mathbf{I}-\mathbf{A})\mathbf{z}_n=\mathbf{z}^{(M-1)}$$

The equations are solved successively by considering one root a time.

When a root is real, the corresponding line in Eq. (39) denoted as

$$(r\mathbf{I}-\mathbf{A})\mathbf{x}=\mathbf{g} \tag{40}$$

where r is the real root. The unknown vector $\mathbf{x}$ is determined in relation to given right-hand side denoted by $\mathbf{g}$. Partitioning $\mathbf{x}$ and $\mathbf{g}$ into sub-vectors of equal size

$$\mathbf{x}=\begin{Bmatrix}\mathrm{x}_1\\ \mathrm{x}_2\end{Bmatrix} \text{ and } \mathbf{g}=\begin{Bmatrix}\mathrm{g}_1\\ \mathrm{g}_2\end{Bmatrix} \tag{41}$$

by using Eq. (24), Eq. (40) is rewritten as

$$(r^2\mathbf{M}+r\Delta t\mathbf{C}+\Delta t^2\mathbf{K})\mathrm{x}_1=r\mathbf{M}\mathrm{g}_1-\Delta t^2\mathbf{K}\mathrm{g}_2 \tag{42}$$

for the solution of x_1 and

$$\mathrm{x}_2=\frac{1}{r}(\mathrm{x}_1+\mathrm{g}_2) \tag{43}$$

for determining x_2.

For a pair of complex conjugate roots r and $\bar{r}$ (the overbar indicates a complex conjugate), the two equations are considered together and expressed for the unknown vector $\mathbf{x}$ as

$$(r\mathbf{I}-\mathbf{A})(\bar{r}\mathbf{I}-\mathbf{A})\mathbf{x}=\mathbf{g} \tag{44}$$

จุฬาลงกรณ์มหาวิทยาลัย
Chulalongkorn University

Another auxiliary vector $\mathbf{y}$ is introduced

$$(r\mathbf{I}-\mathbf{A})\mathbf{y}=\mathbf{g} \tag{45}$$

Partitioning the vector $\mathbf{y}$ in the same way

$$\mathbf{y}=\begin{Bmatrix}\mathrm{y}_1\\ \mathrm{y}_2\end{Bmatrix} \tag{46}$$

the sub-vector y_1 is obtained from

$$(r^2\mathbf{M}+r\Delta t\mathbf{C}+\Delta t^2\mathbf{K})\mathrm{y}_1=r\mathbf{M}\mathrm{g}_1-\Delta t^2\mathbf{K}\mathrm{g}_2 \tag{47}$$

While the second sub-vector y_2 follows as

$$y_2=\frac{1}{r}(y_1+\mathrm{g}_2) \tag{48}$$

The solution of Eq. (44) for the unknown vector $\mathbf{x}$ is expressed as

$$\mathbf{x} = \frac{-1}{2\mathrm{Im}(r)i}(\mathbf{y} - \bar{\mathbf{y}}) = \frac{\mathrm{Im}(\mathbf{y})}{\mathrm{Im}(r)} \tag{49}$$

It should be noted that the system of algebraic equations (42) and (47) are in the same form as that found in the Newmark time-stepping scheme.

2.4 Natural Frequencies and Mode Shapes

The system of second order homogeneous ordinary differential equations (subscripts are omitted for simplicity) associated with the equation of motion (Eq. (9)) is addressed

$$[K]\{u\} + [M]\{\ddot{u}\} = 0 \tag{50}$$

The harmonic vibration is considered

$$\{u\} = \{U\}\sin\omega t \tag{51}$$

$$\{\ddot{u}\} = -\omega^2\{U\}\sin\omega t \tag{52}$$

where $\{U\}$ represents the amplitudes of the nodal displacements. ω is the circular frequency of the vibration. A generalized eigenvalue problem can be constructed by substituting Eqs. (51) and (52) into Eq. (50) as

$$([K] - \lambda[M])\{U\} = 0 \tag{53}$$

where the eigenvalues λ leads to the natural frequencies

จุฬาลงกรณ์มหาวิทยาลัย
CHULALONGKORN UNIVERSITY

$$\omega = \sqrt{\lambda} \tag{54}$$

Only the positive roots are chosen. The processes of harmonic analysis are illustrated in Figure 4.2. The eigenvector $\{U\}$ represents the corresponding mode shapes; the period of free vibration is equal to $T = 2\pi/\omega$; the natural frequencies are sorted in ascending order; and the output arguments consist of the initial number of modes of which natural frequencies are the smallest and the accompanying mode shapes.

Phase	Harmonic analysis steps	Equation
Pre-process	Define initial parameters $(number\ of\ mode, [K], [M], \{u_2\})$	
Process	Initialization of free DOFs with unknown displacements ↓ Remove constrained DOFs ↓ Solve eigenproblem considering unconstrained DOFs only ↓ Compute the lowest number of modes ↓ Compute all modes ↓ Sort eigenfrequencies (ω) in ascending order ↓ Arrange eigenvectors in the same order ↓ Initialize mode shapes to include constrained DOFs ↓ Fill mode shapes in unconstrained DOFs	 (53) (53) (53) (54) (15)
Post-process	Output selected natural frequencies	

Figure 4.2 Flowchart for the calculation of natural frequencies and mode shapes.

จุฬาลงกรณ์มหาวิทยาลัย
CHULALONGKORN UNIVERSITY

3. Dynamic Response Topology Optimization

Structures are actually susceptible to dynamic loads, thus it makes sense to optimize them taking these factors into account. With the representation of the shape of the structure as a material property and the fact that the dynamic TO has primarily been used in the frequency domain based on homogenization (Díaaz & Kikuchi, 1992), a method for determining the shape of the structure and TO that maximizes the natural frequency or eigenfrequency has been developed (J. Du & Olhoff, 2007; Pedersen, 2000). Reducing vibration and noise is the goal of frequency-domain issues (JOG, 2002). A modified structural TO approach based on the level set method was recently used by Shu, Wang, Fang, Ma, and Wei (2011) to minimize frequency response at certain spots or surfaces on the structure. The eigenvalue, the eigenvector, the applied frequency, and the strength of the applied force are significant variables in the frequency domain. The performance of harmonic analysis is analogous to transient analysis across a certain range of time, and it is specifically done for the range of frequency. As a result, in many situations, time-dependent constraints might be converted to frequency-dependent constraints, necessitating the need for sensitivity analysis on functions with frequency dependence.

In the specific time domain, another dynamic structural optimization has been investigated (Choi & Park, 2002; Jang, Lee, & Park, 2009; Min, Kikuchi, Park, Kim, & Chang, 1999). Minimizing a weight or increasing the overall stiffness of a structure are the primary objectives of time-domain issues. The numerical computation range gets uncontrollably vast when the structure is massive, or the duration of the loads is prolonged.

The sum of the dynamic compliances across the whole-time range is typically used to describe the main target function in dynamic response TO. This situation shows that the compliance profile of the optimized model can be quickly improved at a given time, and since only the overall compliance is considered, the compliance value at each time step is not regulated, implying that the optimal structure can experience significant deformation at a particular moment. A novel TO technique for dynamic and nonlinear features has been described (Jang, Lee, Lee, & Park, 2012) using the equivalent static loads for nonlinear static response structure optimization (ESLSO)

จุฬาลงกรณ์มหาวิทยาลัย
Chulalongkorn University

method. In both linear static analysis and nonlinear dynamic analysis, equivalent static loads (ESLs) are loads that result in the identical response field at every time step. Lee and Park (2015) suggested utilizing ESLSO to optimize topology for nonlinear dynamic systems, while Zhao and Wang (2016) suggested employing model reduction techniques to cut down on computing costs as dynamic response TO is often costly. A MATLAB implementation for TO of structures subject to dynamic loads known as "PolyDyna" was recently reported by Giraldo-Londoño and Paulino (2021).

3.1 Topology Optimization in the Time Domain

Topology optimization determines the optimal layout of structures under applied forces. The presence of dynamic load regimes poses major challenges in any standard design techniques, and the problem is known as a dynamic response topology optimization. This section proposes a novel image-based adaptive scaled boundary finite element (SBFE) method for the optimal topology design of continuum (in-plane two-dimensional) structures under time-dependent dynamic responses. In essence, a so-called bi-evolutionary structural optimization (BESO) algorithm is developed within the SBFE framework that advantageously enables automatic adaptive meshes using the simple yet effective image-based procedures. The mechanical compliance is minimized under a series of decreasing volume fractions in the time domain. What is important is the images of stress responses well present the criteria, rather than some specific error functions, for automatic adaptive mesh schemes. Underpinning the digital images, a quadtree/octree mesh refinement overcomes the problems associated with hanging nodes and provides the fast mesh convergence during the optimization process. Moreover, a single-step high-order implicit time integration technique (incorporating an adjustable numerical dissipation at high frequency) provides a close approximation of equivalent static loads presenting dynamic responses of the optimally designed topology structure in the time domain. The calculated equivalent static forces provide the accurate displacement field as one mapped under the actual dynamic responses at each time step. Various numerical examples and benchmarks illustrate the accuracy and robustness of the proposed dynamic response topology optimization method.

3.1.1 Problem statement

Some researchers often use the accumulation of compliance over all time steps when analyzing the dynamic response to a problem. However, in time-dependent topology optimization, maximizing the stiffness of a structure involves minimizing the risk of failure, especially because high strain energy at certain locations can make the structure more prone to failure. The modified objective function, defined by the weighted sum of compliances near the peaks in the time domain (Jang et al., 2012), aims to address this issue. The objective function can be expressed as follows:

$$\begin{aligned} &\min C(\mathbf{u}_v, x_e^m) = \sum_{v=1}^{w} \omega_v \, (\mathbf{F}_v^T \mathbf{u}_v);\ v = 1, \dots, w \\ &s.t. \, h_j(x_e^m) = \frac{\sum_e \left[V_e \prod_{m=1}^{j} (x_e^m) \right]}{\sum_e V_e} \leq V_j^* \ \ j = 1, \dots, M \\ &\mathbf{M}(x_e^m)\ddot{\mathbf{u}}(t) + \mathbf{C}(x_e^m)\dot{\mathbf{u}}(t) + \mathbf{K}(x_e^m)\mathbf{u}(t) = \mathbf{F}(t) \ \ t = 1, \dots, l \\ &x_e^m = x_{min} \ or \ 1, e = 1, \dots, n; \ m = 1, \dots, M \end{aligned} \tag{55}$$

where w is the number of time steps near the peak with l is the total number of time steps in dynamic analysis, ω_v is the weighting factor (usually setting to 1), $\mathbf{F}_v^T$ is dynamic load vector at the v^{th} time step, $\mathbf{u}_v$ displacement vector of the v^{th} time step, $\mathbf{M}(x_e^m)$ is the mass matrix, $\mathbf{C}(x_e^m)$ is the damping matrix, $\mathbf{K}(x_e^m)$ is the stiffness matrix corresponding to the design variable x_e^m, $\ddot{\mathbf{u}}(t)$ is the acceleration vector, $\dot{\mathbf{u}}(t)$ is the velocity vector, $\mathbf{u}(t)$ is the displacement vector, V_e is the volume vector of each element and V_j^* is the specific volume fraction of the structure given by the user, totally M constraints for M materials, x_{min} is the lower bound of the design variable, and n is the total number of elements.

For volume constrained with compliance minimization, the sensitivity for equivalent static loads method for nonlinear static response structural optimization (ESLSO) is described as

$$\frac{\partial C(\mathbf{u}_v, x_e^m)}{\partial x_e^m} = \frac{1}{2}(x_e^m)^{p-1} \sum_{v=1}^{w} \omega_v \, \mathbf{u}_v^T \frac{\mathbf{K}_e}{E_e} \frac{\partial E}{\partial \boldsymbol{\varphi}_e^m} \mathbf{u}_v \tag{56}$$

จุฬาลงกรณ์มหาวิทยาลัย
Chulalongkorn University

3.1.2 The ESLSO Procedure

The loads that generate the same displacement field as dynamic loads at each time step are called ESLs and the governing equation of dynamic analysis is

$$\mathbf{M}(x_e^m)\ddot{\mathbf{u}}(t) + \mathbf{C}(x_e^m)\dot{\mathbf{u}}(t) + \mathbf{K}(x_e^m)\mathbf{u}(t) = \mathbf{F}(t) \;\; t = 1, \dots, l \tag{57}$$

The above equation can be modified to obtain the ESLs vector as

$$\mathbf{F_{eq}}(t) + \mathbf{K}(x_e^m)\mathbf{u}(t) = \mathbf{F}(t) - \mathbf{M}(x_e^m)\ddot{\mathbf{u}}(t) + \mathbf{C}(x_e^m)\dot{\mathbf{u}}(t) \;\; t = 1, \dots, l \tag{58}$$

where $\mathbf{F_{eq}}(t)$ is ESLs vector at the time step, t, and includes the dynamic characteristics of $\mathbf{M}(x_e^m)\ddot{\mathbf{u}}(t) + \mathbf{C}(x_e^m)\dot{\mathbf{u}}(t)$. The ESLs vector can be evaluated by multiplying the linear stiffness matrix and the dynamic displacement at each time step as follows:

$$\mathbf{F_{eq}}(t) = \mathbf{K}(x_e^m)\mathbf{u}(t) \;\; t = 1, \dots, l \tag{59}$$

It is observed that a point force creates ESLs that are imposed on all nodes and ESLs are only artificial loads designed to complement the two displacement fields. As stated previously, ESLSO was first designed for size/shape optimization, and this dissertation expands on the ESLSO for dynamic response TO.

The optimization process using ESLSO for TO is illustrated in Figure 4.3 and the steps are as follows:

จุฬาลงกรณ์มหาวิทยาลัย
Chulalongkorn University

1. Set the initial design variables and parameters (iteration: $k = 0$, design variables $(x_e^m)^{(k)} = (x_e^m)^{(0)}$ and BESO parameter: RR, r_{min}, p and V_j^*.
2. Perform nonlinear dynamic analysis with $(x_e^m)^{(k)}$ in Eq. (57)
3. Check the response profile of the compliance in the nonlinear dynamic system along $v = 1, \dots, w$ by $\sigma_v^T \varepsilon_v$ and find the number of peak points in the profile.
4. Generate ESLs using Eq. (59) at the time steps near the peaks that are obtained from step 3.
5. Solve the linear static response TO problem as described in Eq. (55).
6. Compute elemental sensitivity number as Eq. (56) and filtered sensitivity number.

7. Check the convergence criterion. If the criterion is satisfied, the optimization process terminates; however, if the convergence criterion is not satisfied, go to step 8. The convergence criterion is defined as Eq. (4.15)
8. Update the design variables, set $k = k + 1$, then go to step 2.

จุฬาลงกรณ์มหาวิทยาลัย
CHULALONGKORN UNIVERSITY

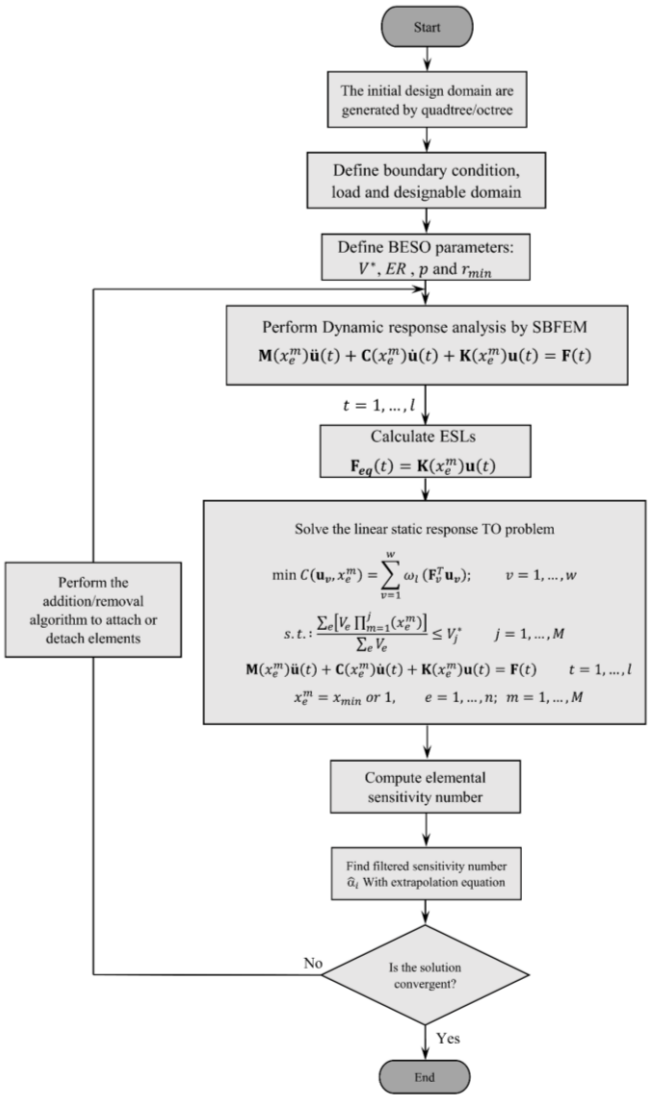

Figure 4.3 Process of linear dynamic response topology optimization using ESLSO.

3.1.3 Numerical examples and expected results

1. Mean compliance design of structure under half-cycle sinusoidal loading

In this example, the design domain is a $2L \times L$ cantilevered rectangular area. A half-cycle sinusoidal load is vertically applied at the centerline of the right end of the structure as shown in Figure 4.4 and the compliance response of the structure during loading phase is taken as the objective function. The prescribed volume fraction of single material design is 0.5; three load cases of t_f = 0.1, 0.01, and 0.001 are considered; the time step used in the time integration is set to Δ_t = 0.0001 for all cases; and the BESO parameters include $ER = 5\%$, radius of the sensitivity filter $r_{min} = 6$ pixels, and convergence criterion, τ = 0.01%

For MMTO design, the candidate materials have elastic modulus, E, regularly spaced in the range $[0.7E11, 2.1E11]$, Poisson's ratio of 0.3 and structural density, ρ_0 = 7800 for fully solid material are assumed. The candidate materials and specified volume constraints for all cases are summarized in Table 4.1.

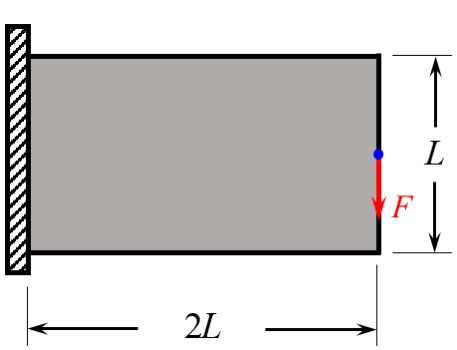

(a) Design domain and boundary conditions

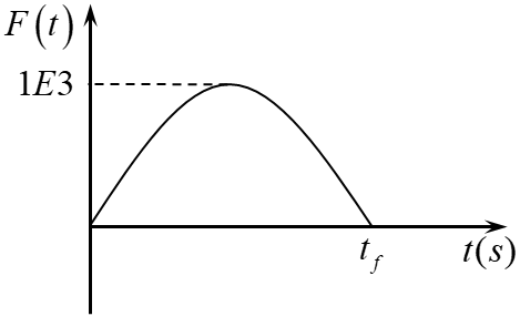

(b) half-cycle sinusoidal load

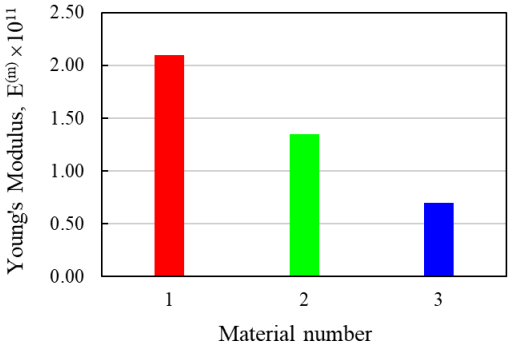

(c) elastic modulus of 3 materials

Figure 4.4 Design of structure under half-cycle sinusoidal loading.

Mat.	$E^{(m)}$	$\rho^{(m)}$	1-material	2-material		3-material		
			g_1	g_1	g_2	g_1	g_2	g_3
1	$2.1E11$	7800	✓	✓		✓		
2	$1.35E11$	4500			✓		✓	
3	$0.7E11$	2700						✓
Volume fraction			$\frac{1}{2}$	$\frac{1}{4}$	$\frac{1}{4}$	$\frac{1}{6}$	$\frac{1}{6}$	$\frac{1}{6}$

Table 4.1 The candidate materials and specified volume constraints for structure under half-cycle sinusoidal loading.

SMTO and MMTO for static load designs

For the static load designs, the first example is solved to numerically validate the proposed method. Figure 4.5 (a) and (b) demonstrates the UM and AM results of static topology optimization. It can be observed that the AM scheme provides less computational time effort and complexity layout than UM approach. Figure 4.5 (c) and (d) demonstrates the AM results of static multi-phase materials topology optimization (MMTO).

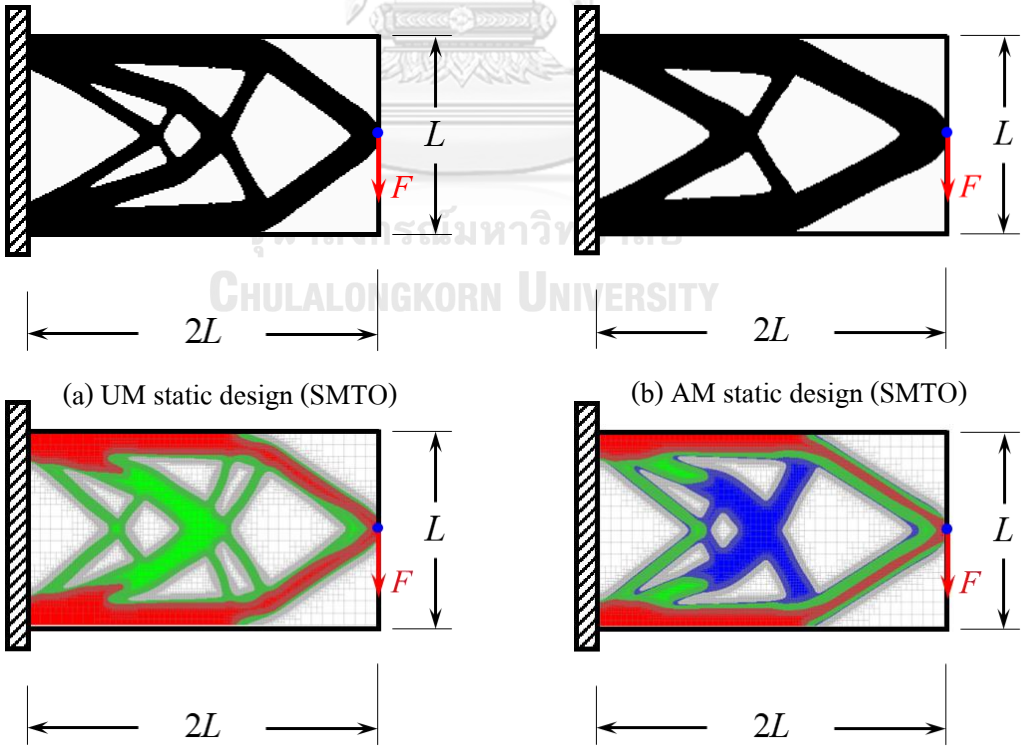

(a) UM static design (SMTO)

(b) AM static design (SMTO)

(c) AM 2–phase materials static design

(d) AM 3–phase materials static design

Figure 4.5 Topological layouts of short–cantilevered structure under static forces.

จุฬาลงกรณ์มหาวิทยาลัย
Chulalongkorn University

SMTO and MMTO for sinusoidal loading designs

For dynamic topology optimization, the first example is solved to numerically validate the proposed method. For SMTO, the International System of Units (SI) is adopted and Young's modulus $E_0 = 2.0E11$, Poisson's ratio $\nu = 0.3$ and structural density $\rho_0 = 7800$ for fully solid material are assumed. Figure 4.6 shows the results of dynamic topology optimization using ESLSO. The single-phase material designs shown in Figure 4.6 (a)–(f) also demonstrate that, for mean dynamic compliance design of structures under a half-cycle sinusoidal loading, when the loading time is long, the dynamic design will be similar with the static design; when the loading time becomes short, the dynamic design will be different from the static one. This is because that, although a sinusoidal load keeps its magnitude constant during the loading phase, it has essential difference from a static load. A static load only contains static component, while a sinusoidal load not only contains a static component, but also contains dynamic components with various frequencies. When the loading time is long, the characteristics of the sinusoidal load is dominated by its static component; when the loading time is short, the characteristic of the sinusoidal load is dominated by those components with higher frequencies. Since we concluded that the long loading time is similar to the static design, the multi-phase materials design using ESLSO are performed by setting $t_f = 0.1$ s. The topological results for UM and AM multi-phase materials using ESLSO are depicted in Figure 4.*6* (g)–(j). As anticipated, in the ideal topology, the stiffer material ("red") is spread along two sides from the fixed support site, where the local equivalent stress is greater than the others. The softer materials ("green and blue") are located where stress is expected to be low.

It is noted that the dynamic designs for the load case of $t_f = 0.001$ s in Figure 4.6 (c) and (f) are statically weak, and its dynamic performance is worse than that of the static design. This shows that the dynamic response design problems may have many local optimums and some of which may be not practical. The structural compliance of the single material and multi-phase materials for both UM and AM are evaluated, as shown in Table 4.2 and Table 4.3. For both optimized models in Figure 4.5 (a) and Figure 4.6 (a), the structural compliance from static analysis are

similar and the maximum compliance from dynamic analysis are similar as well. This means that dynamic response topology optimization can be replaced by static topology optimization which costs lower. This matches with the conclusion of (Jang et al., 2012) that the results of dynamic response optimization with a single dynamic load are the same as those of static topology optimization.

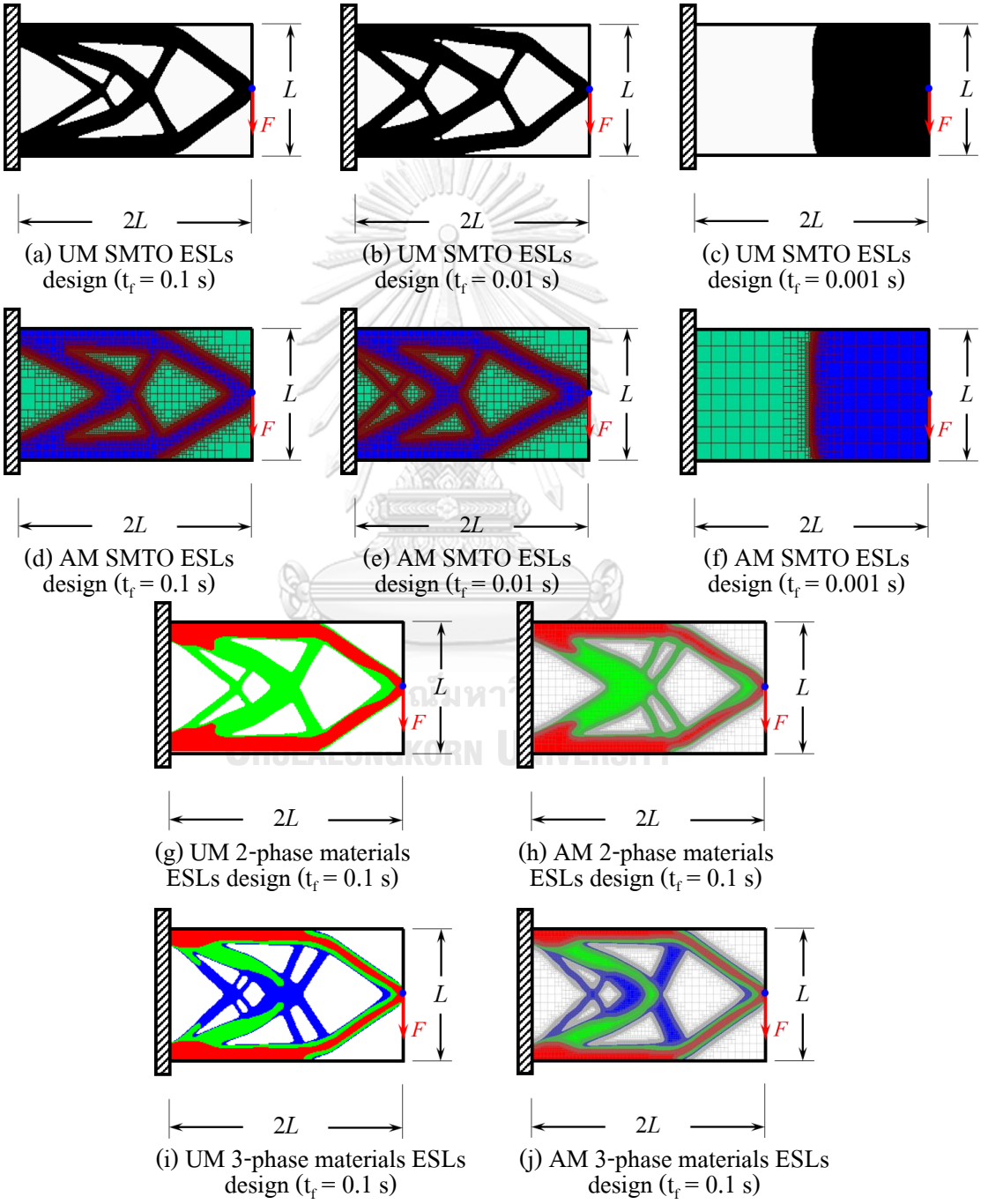

Figure 4.6 Topological layouts of short–cantilevered structure under sinusoidal loading.

จุฬาลงกรณ์มหาวิทยาลัย
Chulalongkorn University

Load cases	SMTO			
	C. from static analysis		C. at peak points from dynamic analysis	
	UM	AM	UM	AM
Static load design	0.0001549	0.0001530	0.0029760	0.0029293
	Figure 4.5 (a)	Figure 4.5 (b)	Figure 4.5 (a)	Figure 4.5 (b)
ESLs design ($t_f = 0.1$)	0.0001639	0.0001616	0.0029899	0.0029447
	Figure 4.6 (a)	Figure 4.6 (d)	Figure 4.6 (a)	Figure 4.6 (d)
ESLs design ($t_f = 0.01$)	0.0003127	0.0003064	0.0009362	0.0009181
	Figure 4.6 (b)	Figure 4.6 (e)	Figure 4.6 (b)	Figure 4.6 (e)
ESLs design ($t_f = 0.001$)	0.0000090	0.0000047	0.0000257	0.0000087
	Figure 4.6 (c)	Figure 4.6 (f)	Figure 4.6 (c)	Figure 4.6 (f)

Table 4.2 Compliance of single-material for short-cantilever beam under different loadings.

Load cases	MMTO			
	C. from static analysis		C. at peak points from dynamic analysis	
	AM-2 mats	AM-3 mats	AM-2 mats	AM-3mats
Static load design	0.0001683	0.0002037	0.002192	0.002902
	Figure 4.5 (c)	Figure 4.5 (d)	Figure 4.5 (c)	Figure 4.5 (d)
ESLs design ($t_f = 0.1$)	0.0001824	0.0002173	0.002213	0.002881
	Figure 4.6 (h)	Figure 4.6 (j)	Figure 4.6 (h)	Figure 4.6 (j)

Table 4.3 Compliance of AM single-material for short-cantilever beam under different loadings.

จุฬาลงกรณ์มหาวิทยาลัย
CHULALONGKORN UNIVERSITY

2. Design of short cantilever beam with two loads

The design domain of the structure is displayed in Figure 4.7(a) and the optimal solution based on static responses is depicted in Figure 4.7(b). In this example, the structure has two dynamic loads, as shown in Figure 4.7(c) and (d).

The prescribed volume fraction of material is 0.5; a single value of the loading time, t_f = 0.2 are considered; the time step used in the time integration is set to Δ_t = 0.001 for all cases; and the BESO parameters include $ER = 2\%$, radius of the sensitivity filter $r_{min} = 8$ pixels, and convergence criterion τ = 0.01%. For the MMTO design, the candidate materials and specified volume constraints for all cases are shown in previous example.

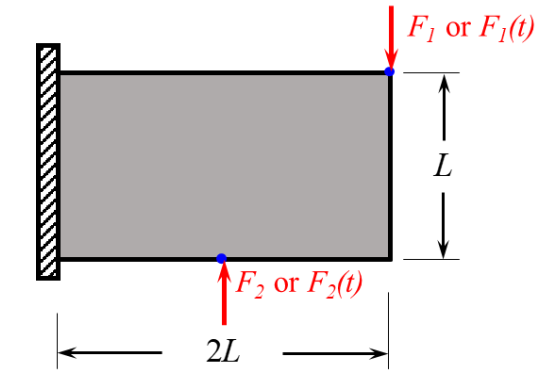

(a) Design domain and boundary conditions

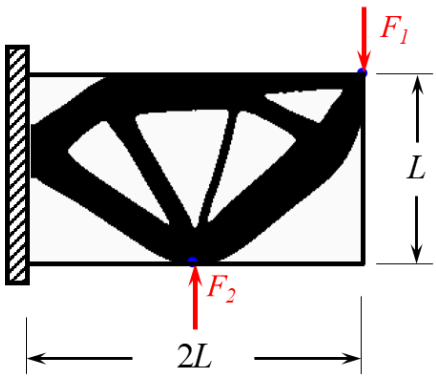

(b) UM Static design (SMTO)

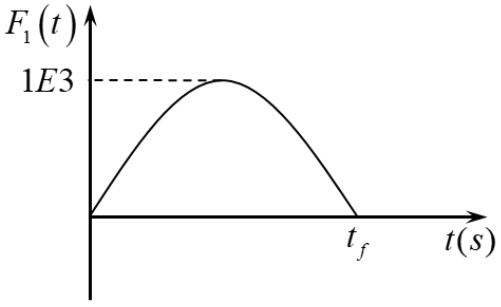

(c) half-cycle sinusoidal load

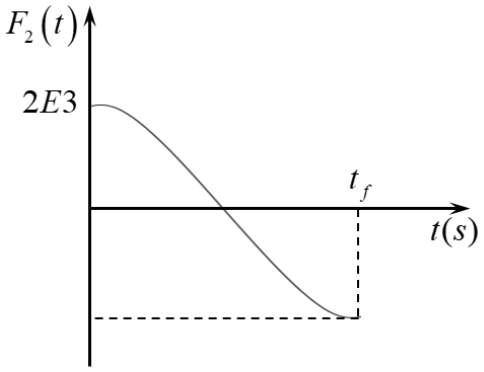

(d) half-cycle cosine load

Figure 4.7 Design of structure under half-cycle sinusoidal and cosine loadings.

SMTO and MMTO for static load designs

As previously demonstrated, the AM (adaptive mesh) scheme greatly reduces the computational time and complexity of the topological layout. This example focuses on the results obtained using the AM scheme for both static and dynamic design. The static design results, obtained using the

AM scheme, are shown in Figure 4.8, while the results for dynamic topology optimization using ESLs with the AM scheme are displayed in Figure 4.9. These results differ significantly from those of previous examples. The validity of these results was confirmed through static and dynamic analyses, as shown in Table 4.4 and Table 4.5. When the model optimized for dynamic response is tested using static analysis, the strain energy is found to be greater than that of the model optimized for static conditions. Similarly, when the model optimized for static conditions is tested using dynamic analysis, the strain energy is greater than that of the model optimized for dynamic response. This can be understood by considering that, for linear elastic problems under the assumption of a single static load and small deformation, the magnitude of the load does not affect the optimal design, but for structures under two static loads, the ratio of their magnitudes can greatly influence the optimal design results. The ratio of the magnitudes of these two dynamic loads changes over time, resulting in different designs under dynamic and static load conditions.

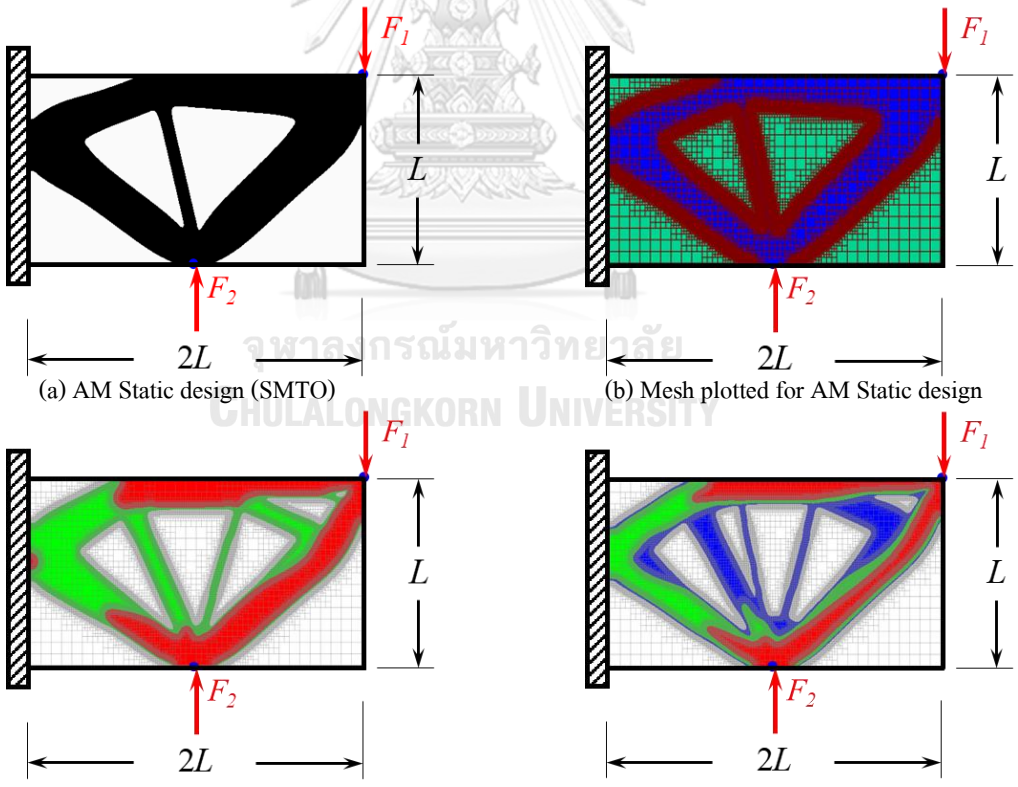

(a) AM Static design (SMTO)

(b) Mesh plotted for AM Static design

(c) AM 2–phase materials static design

(d) AM 3–phase materials static design

Figure 4.8 Results of two static loads topology optimization.

จุฬาลงกรณ์มหาวิทยาลัย
Chulalongkorn University

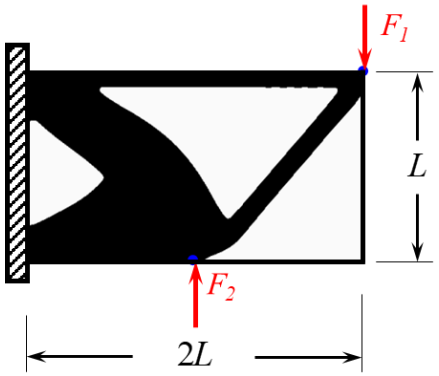

(a) AM ESLSO design (SMTO)

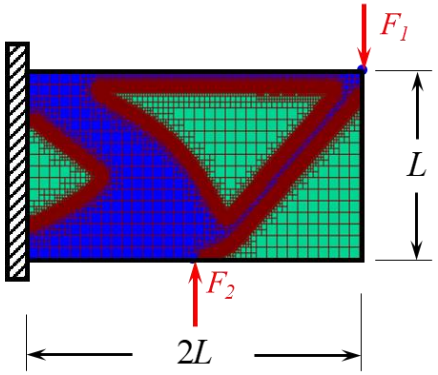

(b) Mesh plotted for AM ESLSO design

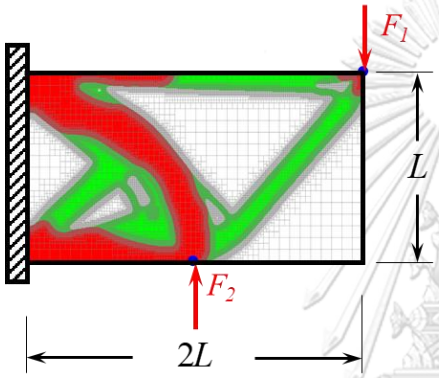

(c) AM 2–phase materials ESLSO design

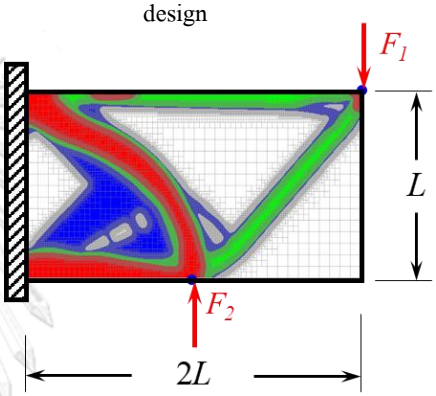

(d) AM 3–phase materials ESLSO design

Figure 4.9 Results of structure under half-cycle sinusoidal and cosine loadings.

จุฬาลงกรณ์มหาวิทยาลัย
CHULALONGKORN UNIVERSITY

Load cases	SMTO	
	C. from static analysis	C. at peak points from dynamic analysis
Static load design	0.000099 Figure 4.8 (a) and (b)	0.508018 Figure 4.9 (a) and (b)
ESLs design ($t_f = 0.2$)	0.000641 Figure 4.8 (a) and (b)	0.063961 Figure 4.9 (a) and (b)

Table 4.4 Compliance of AM single-material for short-cantilever beam with two loads under different loadings.

Load cases	MMTO			
	C. from static analysis		C. at peak points from dynamic analysis	
	AM-2 mats	AM-3 mats	AM-2 mats	AM-3mats
Static load design	0.000114	0.000137	0.564871	0.901163
	Figure 4.8 (c)	Figure 4.8 (d)	Figure 4.8 (c)	Figure 4.8 (d)
ESLs design	0.000737	0.000891	0.074955	0.088975
($t_f = 0.2$)	Figure 4.9 (c)	Figure 4.9 (d)	Figure 4.9 (c)	Figure 4.9 (d)

Table 4.5 Compliance of AM multi-material for short-cantilever beam with two loads under different loadings.

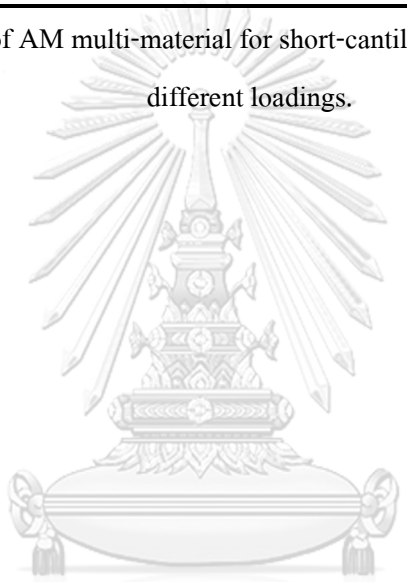

จุฬาลงกรณ์มหาวิทยาลัย
CHULALONGKORN UNIVERSITY

3. Design of 3D MBB simple support beam with uniform dynamic load

An example of 3D solid structure displayed in Figure is optimized. The uniform dynamic loading is acted on the top surface of the beam, as depicted in Figure 4.10. The objective function is the summation of strain energy at the all-time steps. The candidate materials and specified volume constraints for all cases are shown in example 2. The BESO parameters include $ER = 5\%$, radius of the sensitivity filter $r_{min} = 4$ voxels, and convergence criterion τ = 0.01%. The specific value of the loading time, t_f = 0.1, is considered; the time step used in the time integration is set to Δ_t = 0.001 for all cases.

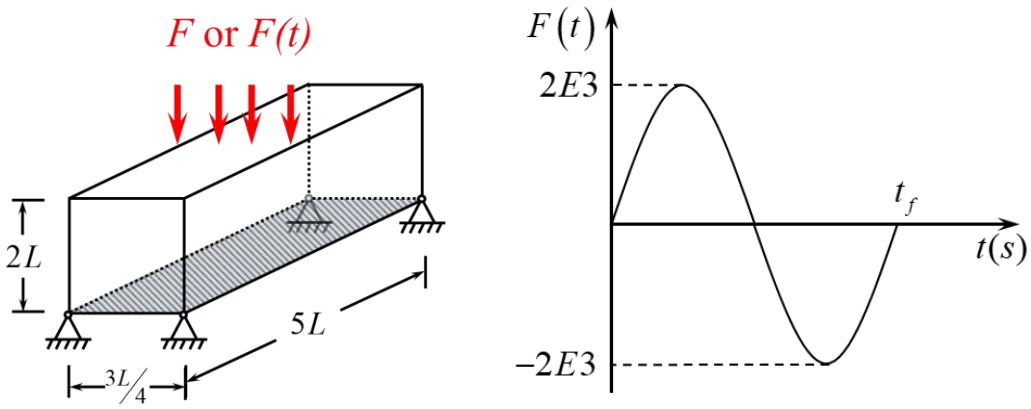

(a) Design domain and boundary conditions (b) Dynamic loading condition

Figure 4.10 Design of 3D solid structure with uniform dynamic loadings.

Mat.	$E^{(m)}$	$\rho^{(m)}$	1-material	2-material		3-material		
			g_1	g_1	g_2	g_1	g_2	g_3
1	$2.1E11$	7800	✓	✓		✓		
2	$1.35E11$	4500			✓		✓	
3	$0.7E11$	2700						✓
Volume fraction			$\frac{3}{10}$	$\frac{3}{20}$	$\frac{3}{20}$	$\frac{1}{10}$	$\frac{1}{10}$	$\frac{1}{10}$

Table 4.6 The candidate materials and specified volume constraints for 3D solid structure under dynamic loading.

SMTO and MMTO for static and dynamic load designs

The BESO algorithm was able to effectively find the optimal solutions for a 3D MBB simple support beam under both static and dynamic load conditions. The results for these cases, including the number of iterations, topological layouts, and structural compliance, are presented in Table 4.7. These results follow the same pattern as previous examples. Using the traditional method of sensitivity analysis to solve this problem, which has a large number of finite elements, would take a significant amount of time. However, the proposed method is able to solve the problem with significantly less cost and time. As a result, high-order time integration method is based on approximating the derivative of a function using a polynomial expression, which can be evaluated more efficiently than the original function. By using the Pade expansion, it is possible to achieve high accuracy in the results of the dynamic analysis with a relatively small number of calculations.

Cases	Iterations	C. from static analysis	C. at peak points from dynamic analysis	Optimal shape
Static load design	57	5.06E-07	1.43E-04	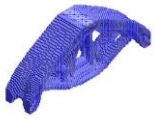
1 MAT ESLs ($t_f = 0.1$)	119	5.19E-07	2.77E-06	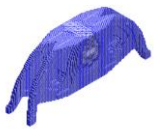
2 MATs ESLs ($t_f = 0.1$)	78	6.08E-07	3.00E-06	
3 MATs ESLs ($t_f = 0.1$)	77	6.81E-07	3.49E-06	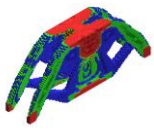

Table 4.7 Optimal results of 3D MBB imply supported beam under static and dynamic loading.

จุฬาลงกรณ์มหาวิทยาลัย
CHULALONGKORN UNIVERSITY

3.2 Topology Optimization in the Frequency Domain

For dynamic behavior of continuum structure, the linear frequency response can be represented by the following general eigenvalue problem

$$(\mathbf{K} - \omega_d^2 \mathbf{M}) U_d = 0, \tag{60}$$

where $\mathbf{K}$ and $\mathbf{M}$ represent the global structural stiffness and mass matrices of structure and ω_d represents the d^{th} natural frequency response and the corresponding eigenvector U_d. The relationship between ω_d and U_d can be expressed by the Rayleigh quotient

$$\omega_d^2 = \lambda_d = \frac{U_d^T \mathbf{K} U_d}{U_d^T \mathbf{M} U_d} \tag{61}$$

Our contribution considers the maximization of the natural frequency of vibrating continuum structure for both SMTO and MMTO with respect to the volume fraction constraint.

3.2.1 Problem statement

In this problem, the dynamic and static characteristics of the structure based on natural frequency TO will be considered. The objective function of optimizing the topology of a continuum structure without damping for minimum value of the integral dynamic compliance can be written as follows:

$$\begin{aligned} &\min C(\lambda_d, x_e^m) = U^{\boldsymbol{T}} \mathbf{K}(\lambda, x_e^m) U = F^{\boldsymbol{T}} U \\ &s.t. h_j(x_e^m) = \frac{\sum_e \left[V_e \prod_{m=1}^{j} (x_e^m) \right]}{\sum_e V_e} \leq V_j^* \quad j = 1, \dots, M \\ &(\mathbf{K} - \lambda_d \mathbf{M}) U_d = 0 \\ &x_e^m = x_{min} \; or \; 1, e = 1, \dots, n; \; m = 1, \dots, M \end{aligned} \tag{62}$$

where $C(\lambda, x_e^m)$ stands for the dynamic compliance corresponding to design variable, x_e^m, and λ_d is eigenvalue that represents the natural frequency response $\left(\omega_d = \sqrt{\lambda_d}\right)$ of the structure. $\mathbf{K}$ and $\mathbf{M}$ represent global structural stiffness and mass matrices of structure, V_e is the volume vector of each element, and V_j^* is the specific volume fraction of the structure given by the user, totally M constraints for M materials, x_{min} is the lower bound of the design variable and n is the total number of elements.

จุฬาลงกรณ์มหาวิทยาลัย
CHULALONGKORN UNIVERSITY

3.2.2 MMTO and Compliance sensitivities

From section 5.2 in Chapter 2, the MMTO problem statement shown in Eq. (5.8) is applied in the current approach. Therefore, the sensitivity calculations of compliance based on natural frequency responses can be expressed in the same manner of traditional compliance sensitivities as

$$\frac{\partial C(x)}{\partial x_e^m} = \frac{\partial C(x)}{\partial \varphi_e^m}\frac{\partial \varphi_e^m}{\partial x_e^m} \tag{63}$$

where $\frac{\partial C(x)}{\partial \varphi_e^m}$ is harmonic compliance responses vector expressed via the chain rule in an identical manner as single material. However, these harmonic compliance responses are included the mass of individual materials. For volume constrained structure, the modified compliance $\frac{\partial C(x)}{\partial \varphi_e^m}$ based on natural frequency $\left(\omega_d = \sqrt{\lambda_d}\right)$ derivatives are

$$\begin{aligned}\frac{\partial C(x)}{\partial \varphi_e^m} &= \frac{\partial \omega_d^2}{\partial \varphi_e^m} \\ &= \frac{1}{2\omega_d U_d^T \mathbf{M} U_d}\left[2\frac{\partial U_d^T}{\partial \varphi_e^m}(\mathbf{K} - \omega_d^2\mathbf{M})U_d + U_d^T\left(\frac{\partial \mathbf{K}}{\partial \varphi_e^m} - \omega_d^2\frac{\partial \mathbf{M}}{\partial \varphi_e^m}\right)U_d\right]\end{aligned} \tag{64}$$

From Eq. (62), it can be further simplified to

$$\frac{\partial C(x)}{\partial \varphi_e^m} = \frac{1}{2\omega_d U_d^T \mathbf{M} U_d}\left[U_d^T\left(\frac{\partial \mathbf{K}}{\partial \varphi_e^m} - \omega_d^2\frac{\partial \mathbf{M}}{\partial \varphi_e^m}\right)U_d\right] \tag{65}$$

Finally, normalizing the vector $U_d^T \mathbf{M} U_d = 1$ leads to the elemental sensitivity based on natural frequency as

$$\frac{\partial C(x)}{\partial \varphi_e^m} = \frac{1}{2\omega_d}\left[U_d^T\left(\frac{\partial \mathbf{K}}{\partial \varphi_e^m} - \omega_d^2\frac{\partial \mathbf{M}}{\partial \varphi_e^m}\right)U_d\right] \tag{66}$$

The partial derivative of the element stiffness matrix to topological design variables can be expressed explicitly by

$$\frac{\partial \mathbf{K}}{\partial \varphi_e^m} = \frac{\mathbf{K_e}}{E_e}\frac{\partial E}{\partial \varphi_e^m} \tag{67}$$

Term of $\frac{\partial E}{\partial \varphi_e^m}$ represent the equivalent elastic modulus interpolation function, express as

$$\frac{\partial E^{(1,\ldots,M)}}{\partial \varphi_e^m} = \frac{\partial\left(\sum_{m=1}^{M} w_m E^{(M-m+1)}\right)}{\partial \varphi_e^m} = \sum_{m=1}^{M}\frac{\partial w_m}{\partial \varphi_e^m}E^{(M-m+1)} \tag{68}$$

จุฬาลงกรณ์มหาวิทยาลัย
Chulalongkorn University

where

$$w_m = [1 - (\varphi^m - \varphi^m \delta_{mM})^p] \prod_{j=1}^{m-1} (\varphi^j)^p \tag{69}$$

$$\delta_{mM} = \begin{cases} 1, m = M \\ 0, m \neq M \end{cases} \tag{70}$$

The partial derivative of the element mass matrix to topological design variables can be expressed explicitly by

$$\frac{\partial \mathbf{M}}{\partial \varphi_e^m} = \frac{\mathbf{M_e}}{W_e} \frac{\partial W}{\partial \varphi_e^m} \tag{71}$$

Term of $\frac{\partial W}{\partial \varphi_e^m}$ represent relative density interpolation function, express as

$$\frac{\partial W^{(1,\ldots,M)}}{\partial \varphi_e^m} = \frac{\partial \left(\sum_{m=1}^{M} \kappa_m W^{(M-m+1)} \right)}{\partial \varphi_e^m} = \sum_{m=1}^{M} \frac{\partial \kappa_m}{\partial \varphi_e^m} W^{(M-m+1)} \tag{72}$$

where

$$\kappa_m = [1 - (\varphi^m - \varphi^m \delta_{mM})^q] \prod_{j=1}^{m-1} (\varphi^j)^q \tag{73}$$

$$\delta_{mM} = \begin{cases} 1, m = M \\ 0, m \neq M \end{cases} \tag{74}$$

where q is the penalty factor like p. In this dissertation, $q = 1$ is used for all examples.

The separated sensitivity number for each design variable is simply expressed as

$$\frac{\partial \varphi_e^m}{\partial x_e^m} = (x_e^m)^{p-1} \tag{75}$$

Finally, by substituting Eqs. (64), (68), (72) and (75) into Eq. (63), the sensitivity number based on natural frequency responses can be represented as

$$\begin{aligned} \frac{\partial C(x)}{\partial x_e^m} &= \frac{1}{2\omega_d} \left[U_d^T \left(\frac{\partial \mathbf{K}(\lambda, x_e^m)}{\partial \varphi_e^m} - \omega_d^2 \frac{\partial \mathbf{M}(\lambda, x_e^m)}{\partial \varphi_e^m} \right) U_d \right] \\ &= \frac{1}{2\omega_d} (x_e^m)^{p-1} U_e^T \left(\frac{\mathbf{K_e}}{E_e} \frac{\partial E}{\partial \varphi_e^m} - \omega_d^2 \frac{\mathbf{M_e}}{W_e} \frac{\partial W}{\partial \varphi_e^m} \right) U_e = \alpha_e^m \end{aligned} \tag{76}$$

where the component-wise of α_e^m is the elemental sensitivity number for multimaterial elements

$$\alpha_e^m = \frac{1}{2\omega_d} (x_e^m)^{p-1} U_e^T \left(\frac{\mathbf{K_e}}{E_e} \frac{\partial E}{\partial \varphi_e^m} - \omega_d^2 \frac{\mathbf{M_e}}{W_e} \frac{\partial W}{\partial \varphi_e^m} \right) U_e \tag{77}$$

จุฬาลงกรณ์มหาวิทยาลัย
Chulalongkorn University

3.2.3 Computational procedure

The proposed evolutionary topology optimization (TO) approach involves an iterative process, which is illustrated in a flow chart in Figure 4.11. The process of multi-material TO using Bi-directional Evolutionary Structural Optimization (MMTO-BESO) begins by starting with a full design and gradually decreasing the volume of material 1. As the volume of material 1 decreases, the volume of base material 2 increases until the required volume of material 2 is reached. At this point, the volume of base material 3 (void element) begins to increase as the volume of material 2 remains unchanged and the volume of material 1 continues to decrease.

In summary, the MMTO-BESO approach involves adjusting the volumes of multiple materials in an iterative manner to achieve the desired material distribution. The process starts with a full design and involves decreasing the volume of one material while increasing the volume of another, resulting in a rise in the volume of the void element. This allows for the optimization of the material distribution based on the specific design requirements and objectives.

จุฬาลงกรณ์มหาวิทยาลัย
Chulalongkorn University

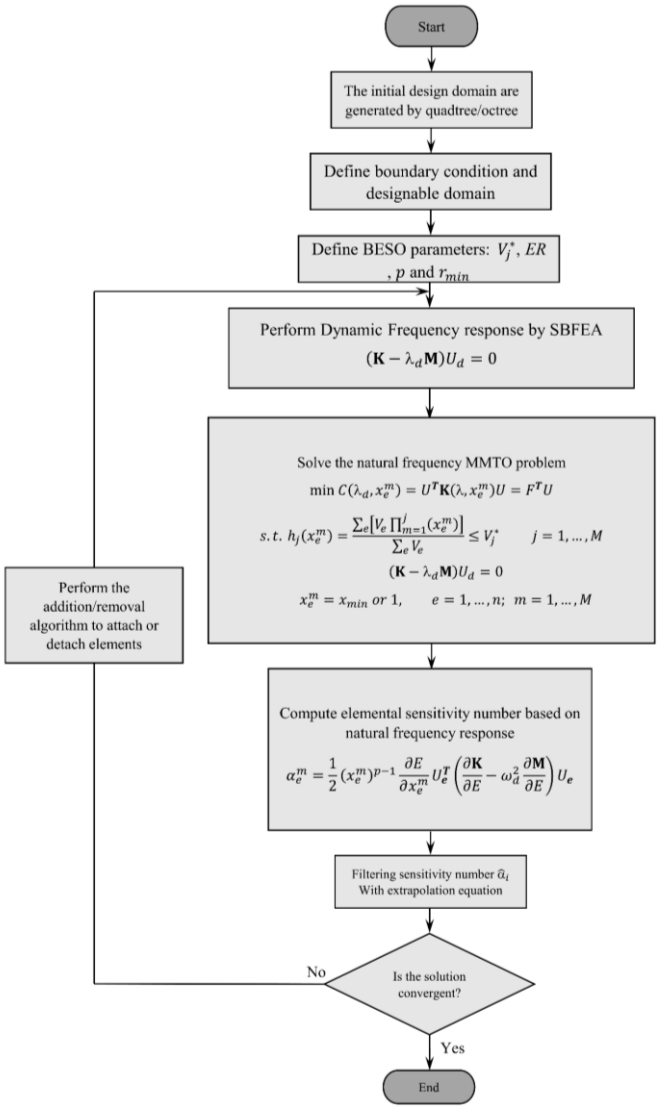

Figure 4.11 Flow chart of the dynamic compliance minimization based on natural frequency procedure.

3.2.4 Numerical example and expected results

1. Beam with simply supported ends

For this example, maximize the fundamental frequency responses of a beam-like 2D structure is shown in Figure 4.12. The beam with dimensions $8L \times L$ is simply supported at both ends with the prescribed volume fraction, $V^* = 0.5$ for a single material design.

For the MMTO design, it is assumed that all potential materials have a modulus of elasticity, E, evenly distributed between $[0.7E11, 2.1E11]$, a Poisson's ratio of 0.30, and a structural density of ρ_0 = 7800 for fully solid material are assumed. Table 4.8 provides a summary of the potential materials and specified volume restrictions for all scenarios.

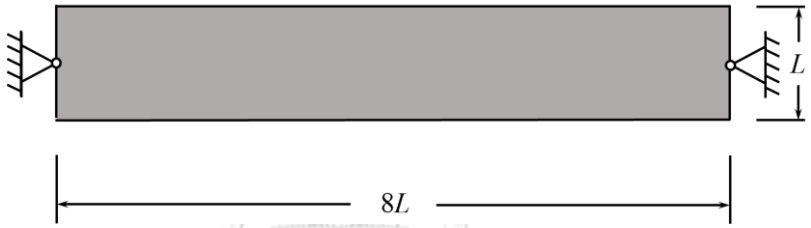

Figure 4.12 Design domain and boundary conditions for beam with simply supported ends problem.

Mat.	$E^{(m)}$	$\rho^{(m)}$	1-material	2-material		3-material		
			g_1	g_1	g_2	g_1	g_2	g_3
1	$2.1E11$	7800	✓	✓		✓		
2	$1.35E11$	4500			✓		✓	
3	$0.7E11$	2700						✓
Volume fraction			$\frac{1}{2}$	$\frac{1}{4}$	$\frac{1}{4}$	$\frac{1}{6}$	$\frac{1}{6}$	$\frac{1}{6}$

Table 4.8 The candidate materials and specified volume constraints for beam with simply supported ends.

Single-phase material design

For natural frequency-based topology optimization, the first example is solved and compared with J. Du and Olhoff (2007) and X Huang et al. (2010) to numerically validate the proposed method.

An image resolution of 128 × 1024 pixels with a uniform element size of 2 pixels is used. The Young's modulus E_0 = 10 MPa, Poisson's ratio ν = 0.3, and structural density ρ_0 = 1 kg/m^3 for a fully solid material are assumed as the necessary parameters. An evolutionary ratio ER = 2 % with r_{min} = 6 pixels is utilized. Figure 4.13 shows the optimal design with a specific volume fraction. The first two eigenmodes of the optimal design are shown in Figure 4.13 (a) and (b). In general, as the volume fraction decreases, the first natural frequency increases while the second and third natural frequencies decrease. A multimodal example is one in which the first and second frequencies become similar in later stages. However, the sensitivity of multiple frequencies is not unique due to the lack of usual differentiability properties of the subspace spanned by the eigenvectors associated with multiple frequencies.

(a) UM design for maximizing the first natural frequency (SMTO)

(b) The first eigenmodes of the optimal design

(c) The second eigenmodes of the optimal design

Figure 4.13 Optimal topology for maximizing the first natural frequency for beam with simply supported ends.

For adaptive mesh design, the convolution-filtered techniques are applied with $r_{den} = 6$ voxels. and the elements arising during quadtree decomposition are limited in size to ≤ 16 pixels. The AM results for maximizing the first natural frequency for beam with simply supported ends are depicted in Figure 4.14. As expected, both of UM and AM results are significantly related. In addition, the results are compared with the references (J. Du & Olhoff, 2007; X Huang et al.,

2010) and reported in Table 4.9. It is noted that the above optimal topology and its natural frequencies and eigenmodes agree well with the results in references that previously mentioned.

(a) AM design for maximizing the first natural frequency (SMTO)

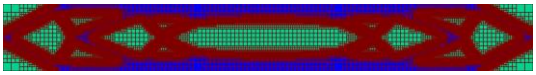

(b) Mesh plotted for AM design for maximizing the first natural frequency (SMTO)

Figure 4.14 AM design for maximizing the first natural frequency for beam with simply supported ends.

	Our work		references	
	UM	AM	(J. Du & Olhoff, 2007)	(X Huang et al., 2010)
ω_1 (rad/s)	171.4	172.3	174.7	171.5
Iterations	65	53	80	53
Design	Figure 4.13	Figure 4.14		

Table 4.9 Comparison results of first natural frequency for single-material beam with simply supported ends with references.

Multi-phase material design

For MMTO design, the results of all materials cases and specified volume restrictions for all scenarios in Table 4.8 are reported in Table 4.10. It should be noted that the AM results are limited in element size to $\leq$ 16 pixels and $\geq$ 1 pixel. As expected, both of UM and AM results are almost the same. This example shows that the presented natural frequency constraint implementation is effectively able to increase the fundamental frequency of the design.

Case	Iterations	Avg. time (s)	ω_1 (rad/s)	Topological layout
UM 2-Mats	108	6.4925	212.9229	
UM 3-Mats	116	6.8497	219.3107	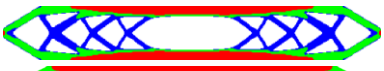
AM 2-Mats	105	13.9584	214.7164	
AM 3-Mats	129	15.6429	219.5395	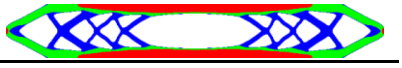

Table 4.10 Results of first natural frequency for multi material beam with simply supported ends.

2. Beam with clamped ends

In this example, the beam of dimensions $7L \times L$ is clamped on both sides as shown in Figure 4.15 (a). For SMTO, the Young's modulus E_0 = 100 N/cm^2, Poisson's ratio ν = 0.3 and structural density $\rho_0 = 10^{-6}$ kg/m^3 for fully solid material are assumed. For UM procedure, an image resolution 128 × 896 pixels is discretized with uniformly discretized by square elements of size 2 pixels. The BESO parameters are ER = 2 %, r_{min} = 6 pixels and $V^* = 0.5$ for a single material design.

For the MMTO design, Table 4.8 provides a summary of the potential materials and specified volume restrictions for all scenarios.

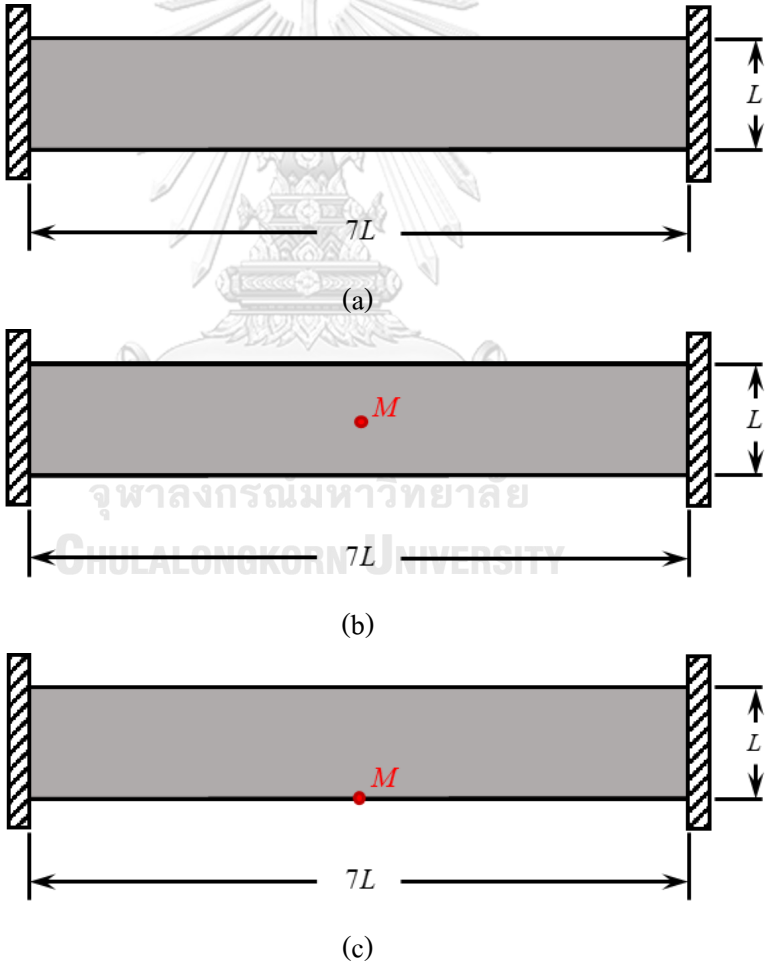

Figure 4.15 Boundary conditions for beam with clamped ends: (a) without concentrated nonstructural mass, (b) concentrated mass applied at center and (c) concentrated mass attached at the midpoint of the lower edge.

Single-phase material design

For dynamic SMTO based on natural frequency responses, this example is successfully solved in both UM and AM cases. Notice that we consider the topology optimization problems for maximization of the first natural frequency of vibrating continuum structures. The topological layouts for both schemes are displayed in. Figure 4.16 and Figure 4.17. As expected, the AM topological layouts provide slightly less complexity shapes than UM layouts. Additionally, the first natural frequency of Figure 4.16 (b) and Figure 4.17 (b) are agreed well with the reference (X Huang et al., 2010).

(a) $\omega_1 = 121.8$ and $\omega_2 = 128.6$ rad/s

(b) $\omega_1 = 36.5$ and $\omega_2 = 175.1$ rad/s

(c) $\omega_1 = 36.4$ and $\omega_2 = 169.2$ rad/s

Figure 4.16 Optimal topology for maximizing the first natural frequency for beam with clamped ends.

จุฬาลงกรณ์มหาวิทยาลัย
Chulalongkorn University

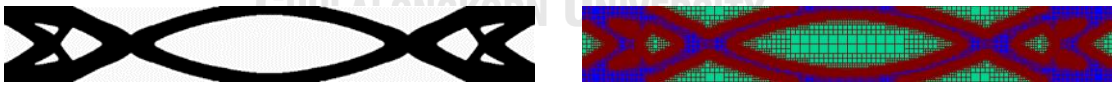

(a) $\omega_1 = 123.6$ and $\omega_2 = 128.6$ rad/s

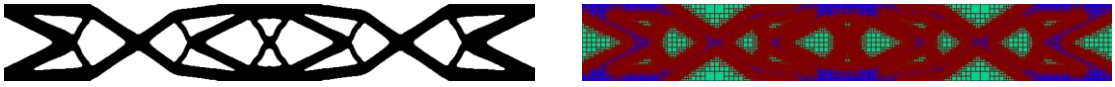

(b) $\omega_1 = 36.6$ and $\omega_2 = 171.5$ rad/s

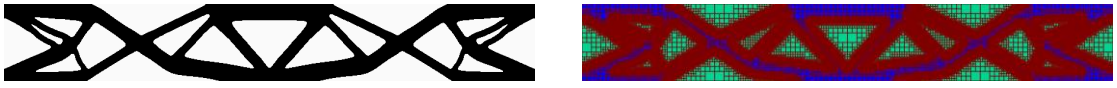

(c) $\omega_1 = 36.6$ and $\omega_2 = 165.0$ rad/s

Figure 4.17 AM design for maximizing the first natural frequency for beam with clamped ends.

Multi-phase material design

For MMTO design, the individual volume constraints with corresponding to material properties are followed by Table 4.8. The TO results obtained using AM with different materials are displayed in Figure 4.18. Using different materials in the topology optimization process leads to significant changes in the design. From Figure 4.16 to Figure 4.18, it can be seen that single-material topology optimization (SMTO), two-material MMTO (2MMTO), and three-material MMTO (3MMTO) all result in different material layouts when different materials are used. One primary advantage of using multi-material topology optimization (MMTO) for continuum structures under frequency responses is the ability to tailor the material distribution to optimize the structure's performance for a specific frequency range. By using multiple materials in the design, it is possible to select materials with different mechanical properties and optimize their distribution in the structure to achieve the desired frequency response.

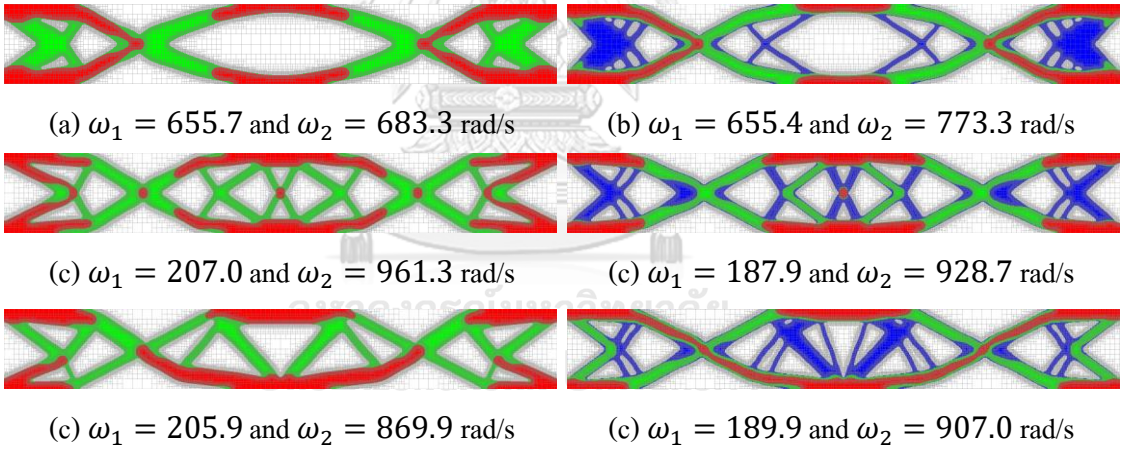

(a) $\omega_1 = 655.7$ and $\omega_2 = 683.3$ rad/s (b) $\omega_1 = 655.4$ and $\omega_2 = 773.3$ rad/s

(c) $\omega_1 = 207.0$ and $\omega_2 = 961.3$ rad/s (c) $\omega_1 = 187.9$ and $\omega_2 = 928.7$ rad/s

(c) $\omega_1 = 205.9$ and $\omega_2 = 869.9$ rad/s (c) $\omega_1 = 189.9$ and $\omega_2 = 907.0$ rad/s

Figure 4.18 AM multi-materials design for maximizing the first natural frequency for beam with clamped ends.

In conclusion, the advantage of MMTO is the ability to optimize the structure's performance under dynamic loading conditions. By considering the frequency response of the structure, it is possible to optimize the material distribution to minimize the risk of failure or other detrimental effects of dynamic loading.

Overall, the use of MMTO for continuum structures under frequency responses allows for the optimization of the material distribution to achieve the desired performance and can be an effective tool for improving the performance of structures subjected to dynamic loading.

จุฬาลงกรณ์มหาวิทยาลัย
Chulalongkorn University

CHAPTER 5 CONCLUSIONS

Previous research has demonstrated that Bi-directional Evolutionary Structural Optimization (BESO) is an effective method for topology optimization using the traditional finite element method (FEM). It has been shown to be efficient, produce high-quality results, and be easy to implement. The main aim of this study was to investigate the potential use of BESO with the novel image-based adaptive scaled boundary finite element (SBFE) approach. Upon achieving this objective, the methodology was extended to consider different material design scenarios.

A review of various structural topology optimization algorithms that have been applied to material design is presented, along with a brief overview of some of these techniques. Material design often involves designing continuum structures for a range of applications, such as adaptive mesh refinement, structures with multiple materials, and dynamic response topology optimization.

In the first stage, the topology optimization of static loads structures using BESO for image-based SBFE method has been sought for topological layouts with adaptive mesh refinement that increases the mesh resolution in the boundary region. Our contributions found that the quadtree/octree mesh refinement overcomes the problems associated with hanging nodes and provides the fast mesh convergence during the optimization process. In addition, the adaptive structure outperforms the uniform patterns and provides highly optimal stiffness for specified mechanical loads. Meanwhile the adaptive structure covers the inside of the mechanical portion with gradually variable void sizes that can be controlled, making it stable for modest, unknown disturbance forces. The BESO method is then extended in this dissertation to topology optimization problems for structures made of multi-phase materials using material interpolation systems with penalization. A novel convolution filter in association with a polytope-based adaptive mesh strategy for multi-material topology optimization problems was presented. In comparison to the regularly fine mesh, this technique provides smooth boundaries for ideal designs while spending less computational effort.

Next, An algorithm has been developed for designing structures based on their dynamic responses. However, it is generally recognized that dynamic response optimization is computationally expensive and that dynamic response topology optimization for large-scale (3D) structures is almost impractical. This work addresses this issue by using quadtree/octree meshes and pattern-based pre-computation approaches, which reduce memory requirements and computational time during simulations. The dynamic analysis is performed using a high-order implicit time-stepping approach based on Padé series expansions of the matrix exponential function, and the equivalent static loads method for non-linear static response structural optimization (ESLSO) is used to optimize the dynamic response topology in the time domain. The objective function is defined as the weighted summation of compliances near the peaks, which is minimized to maximize the stiffness of the whole design region. The results show that, while dynamic response topology optimization does not offer any advantages over static topology optimization when dealing with a single load, it can significantly reduce structural compliance compared to static topology optimization when multiple dynamic loads are present.

Thereafter, the BESO model was significantly adjusted by maintaining the same mass/stiffness ratio for solid and void elements in order to eliminate artificial localized modes during frequency optimization. Several numerical examples and benchmarks involving the plane-stress 2D structures are used to prove the validity and efficiency of the proposed method for the frequency optimization problems. Then, continuum structures made of multiple materials are included in the mathematical framework for performing topology optimization while taking dynamic eigenfrequencies into account. The proposed methodology enables designers to select the most efficient multi-material design within the intended frequency range from the very beginning of the design process.

Furthermore, the extend SBFEM-powered topology optimization to 3D problems and demonstrate an effective means for exporting results to STL format for subsequent additive manufacturing (3D printing). The final designs after post-processing generated by Fusion 360

จุฬาลงกรณ์มหาวิทยาลัย
Chulalongkorn University

software are provided in Figure 5.1. The optimal structural boundaries are automatically smoothed and can be exported to manufacturing.

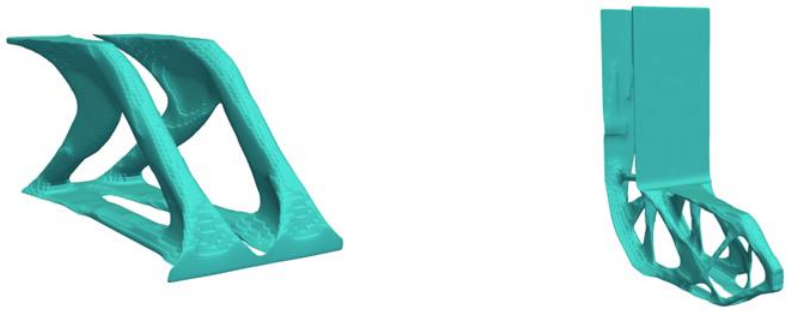

(a) (b)

Figure 5.1 3D postprocessing design provided by Fusion 360 software: (a) 3D cantilever beam and (b) 3D L-shaped structure.

Finally, The topology optimization problems addressed in this dissertation are somewhat simplified. However, the design scenarios presented in this thesis demonstrate that the BESO method can be applied to more complex and advanced applications. In engineering, material systems may need to meet a variety of functional or performance requirements, and these applications can be expanded upon based on the work presented in this dissertation.

จุฬาลงกรณ์มหาวิทยาลัย
Chulalongkorn University

Appendix A

4-nodes iso-parametric Formulation

In two-dimensional problem, the standard FEM formulation for continuum solid element is generally written and solved for the displacement vector $\mathbf{u}$ in the domain Ω. To obtain all information values from a discrete number of points in the domain, FEM are approximated the continuous $\mathbf{u}$ into a piecewise defined field $\hat{\mathbf{u}}$ by numerical interpolation technique. All displacements in the domain are assembled together as a column vector $\{\phi_i\}$. The displacement inside each element can be expressed equivalently in terms of the shape functions as

$$\mathbf{u} \approx \hat{\mathbf{u}} = \sum_{i=1}^{M} N_i \phi_i \text{ and } \sum_{i=1}^{M} N_i = 1 \tag{A.1}$$

where M is the number of element degrees of freedom, N_e are known as the interpolation or shape functions. This shape functions are most often polynomial forms of the independent variables, derived to satisfy certain required conditions at the nodes.

By using Eq. (A.1) using the shape function in term of natural coordinates system (ξ, η), the approximated displacement function inside each element can be expanded as

$$\hat{\mathbf{u}}(\xi,\eta) = N_1(\xi,\eta)\phi_1 + N_2(\xi,\eta)\phi_2 + N_3(\xi,\eta)\phi_3 + N_4(\xi,\eta)\phi_4 \tag{A.2}$$

For the iso-parametric 4 nodes element, the individual shape function are

$$\begin{aligned} N_1(\xi,\eta) &= \frac{1}{4}(1-\xi)(1-\eta) \\ N_2(\xi,\eta) &= \frac{1}{4}(1+\xi)(1-\eta) \\ N_3(\xi,\eta) &= \frac{1}{4}(1+\xi)(1+\eta) \\ N_4(\xi,\eta) &= \frac{1}{4}(1-\xi)(1+\eta) \end{aligned} \tag{A.3}$$

Now we need to convert from the cartesian coordinate system (x, y) into a natural coordinate system (ξ, η). By the usual rules of partial differentiation and chain rule, the derivative of a shape function in terms of the natural element coordinates system (ξ, η) are

จุฬาลงกรณ์มหาวิทยาลัย
Chulalongkorn University

$$\frac{\partial N_i}{\partial \xi} = \frac{\partial N_i}{\partial x}\frac{\partial x}{\partial \xi} + \frac{\partial N_i}{\partial y}\frac{\partial y}{\partial \xi}$$
$$\frac{\partial N_i}{\partial \eta} = \frac{\partial N_i}{\partial x}\frac{\partial x}{\partial \eta} + \frac{\partial N_i}{\partial y}\frac{\partial y}{\partial \eta} \quad \text{(A.3)}$$

By written in the matrix form, we obtain

$$\begin{Bmatrix} \frac{\partial N_i}{\partial \xi} \\ \frac{\partial N_i}{\partial \eta} \end{Bmatrix} = \begin{bmatrix} \frac{\partial x}{\partial \xi} & \frac{\partial y}{\partial \xi} \\ \frac{\partial x}{\partial \eta} & \frac{\partial y}{\partial \eta} \end{bmatrix} \begin{Bmatrix} \frac{\partial N_i}{\partial x} \\ \frac{\partial N_i}{\partial y} \end{Bmatrix} \quad \text{(A.4)}$$

where Jacobian matrix $[J]$ arises because the change of coordinates.

$$[J] = \begin{bmatrix} \frac{\partial x}{\partial \xi} & \frac{\partial y}{\partial \xi} \\ \frac{\partial x}{\partial \eta} & \frac{\partial y}{\partial \eta} \end{bmatrix} \quad \text{(A.5)}$$

Equation (A.4) can also be written as

$$\begin{Bmatrix} \frac{\partial N_i}{\partial x} \\ \frac{\partial N_i}{\partial y} \end{Bmatrix} = [J]^{-1} \begin{Bmatrix} \frac{\partial N_i}{\partial \xi} \\ \frac{\partial N_i}{\partial \eta} \end{Bmatrix} \quad \text{(A.6)}$$

The transformation of local to global coordinates requires determinant of Jacobian matrix, which can be expressed in term integration from as

$$\int\int dxdy = \int_{-1}^{1}\int_{-1}^{1} \det|J| \, d\xi d\eta \quad \text{(A.7)}$$

Since the approximated displacement field $\hat{\mathbf{u}}$ has two directions known u and v. Using the shape function to interpolate within the element as follows

$$\hat{\mathbf{u}} = \begin{Bmatrix} u \\ v \end{Bmatrix} = \begin{bmatrix} N_1 & 0 & N_2 & 0 & N_3 & 0 & N_4 & 0 \\ 0 & N_1 & 0 & N_2 & 0 & N_3 & 0 & N_4 \end{bmatrix} \begin{Bmatrix} u_1 \\ v_1 \\ u_2 \\ v_2 \\ u_3 \\ v_3 \\ u_4 \\ v_4 \end{Bmatrix} \quad \text{(A.8)}$$

จุฬาลงกรณ์มหาวิทยาลัย
Chulalongkorn University

where u and v are horizontal and vertical displacement corresponding at each node in element. With the defined displacement field, we can apply differential operator $[B] = \partial[N]$. From this point, the strain field are obtained as

$$\begin{Bmatrix} \varepsilon_x \\ \varepsilon_y \\ \gamma_{xy} \end{Bmatrix} = \begin{bmatrix} \frac{\partial}{\partial x} & 0 \\ 0 & \frac{\partial}{\partial y} \\ \frac{\partial}{\partial y} & \frac{\partial}{\partial x} \end{bmatrix} \hat{\mathbf{u}} \tag{A.9}$$

Now, the strain field can be expressed in term of (ξ, η) by

$$\begin{Bmatrix} \varepsilon_x \\ \varepsilon_y \\ \gamma_{xy} \end{Bmatrix} = \frac{1}{|J|} \begin{bmatrix} \frac{\partial y}{\partial \eta}\frac{\partial}{\partial \xi} - \frac{\partial y}{\partial \xi}\frac{\partial}{\partial \eta} & 0 \\ 0 & \frac{\partial x}{\partial \xi}\frac{\partial}{\partial \eta} - \frac{\partial x}{\partial \eta}\frac{\partial}{\partial \xi} \\ \frac{\partial x}{\partial \xi}\frac{\partial}{\partial \eta} - \frac{\partial x}{\partial \eta}\frac{\partial}{\partial \xi} & \frac{\partial y}{\partial \eta}\frac{\partial}{\partial \xi} - \frac{\partial y}{\partial \xi}\frac{\partial}{\partial \eta} \end{bmatrix} \begin{Bmatrix} u \\ v \end{Bmatrix} \tag{A.10}$$

Or written in matrix form as

$$\{\varepsilon\} = [D][N]\{\phi\} \tag{A.11}$$

where $[D]$ is an operator matrix by

$$[D] = \frac{1}{|J|} \begin{bmatrix} \frac{\partial y}{\partial \eta}\frac{\partial}{\partial \xi} - \frac{\partial y}{\partial \xi}\frac{\partial}{\partial \eta} & 0 \\ 0 & \frac{\partial x}{\partial \xi}\frac{\partial}{\partial \eta} - \frac{\partial x}{\partial \eta}\frac{\partial}{\partial \xi} \\ \frac{\partial x}{\partial \xi}\frac{\partial}{\partial \eta} - \frac{\partial x}{\partial \eta}\frac{\partial}{\partial \xi} & \frac{\partial y}{\partial \eta}\frac{\partial}{\partial \xi} - \frac{\partial y}{\partial \xi}\frac{\partial}{\partial \eta} \end{bmatrix} \tag{A.12}$$

จุฬาลงกรณ์มหาวิทยาลัย
CHULALONGKORN UNIVERSITY

Introducing $[B]$ matrix as

$$\underset{(3\times8)}{[B]} = \underset{(3\times2)}{[D]}\underset{(2\times8)}{[N]} \tag{A.13}$$

Now we have matrix $[B]$ expressed in term of ξ and η with strain field in term of ξ and η, respectively. The explicit form of $[B]$ can be obtained by substituting $[D]$ and the shape functions $[N]$ into Equation (2.5b). The matrix multiplications yield

$$\left[B(\xi,\eta)\right]=\frac{1}{|J|}\begin{bmatrix}B_1 & B_2 & B_3 & B_4\end{bmatrix} \tag{A.14}$$

With the submatrices of B are given by

$$B_i=\begin{bmatrix}a\left(N_{i,\xi}\right)-b\left(N_{i,\eta}\right) & 0\\ 0 & c\left(N_{i,\eta}\right)-d\left(N_{i,\xi}\right)\\ c\left(N_{i,\eta}\right)-d\left(N_{i,\xi}\right) & a\left(N_{i,\xi}\right)-b\left(N_{i,\eta}\right)\end{bmatrix} \tag{A.15}$$

where the dummy index, i equal to 1, 2, 3, and 4. The constant a, b, c and d are expanded as

$$\begin{aligned}
a&=\frac{1}{4}\left[y_1(\xi-1)+y_2(-1-\xi)+y_3(1+\xi)+y_4(1-\xi)\right]\\
b&=\frac{1}{4}\left[y_1(\eta-1)+y_2(1-\eta)+y_3(1+\eta)+y_4(-1-\eta)\right]\\
c&=\frac{1}{4}\left[x_1(\eta-1)+x_2(1-\eta)+x_3(1+\eta)+x_4(-1-\eta)\right]\\
d&=\frac{1}{4}\left[x_1(\xi-1)+x_2(-1-\xi)+x_3(1+\xi)+x_4(1-\xi)\right]
\end{aligned} \tag{A.16}$$

The determinant $|J|$ is a polynomial in term of ξ, η and can be expressed as

$$|J|=\frac{1}{8}\{X_c\}^T\begin{bmatrix}0 & 1-\eta & \eta-\xi & \xi-1\\ \eta-1 & 0 & \xi+1 & -\xi-\eta\\ \xi-\eta & -\xi-1 & 0 & \xi+1\\ 1-\xi & \xi+\eta & -\eta-1 & 0\end{bmatrix}\{Y_c\} \tag{A.17}$$

where

$$\{X_c\}^T=\begin{Bmatrix}x_1 & x_2 & x_3 & x_4\end{Bmatrix} \text{ and } \{Y_c\}=\begin{Bmatrix}y_1\\ y_2\\ y_3\\ y_4\end{Bmatrix} \tag{A.18}$$

จุฬาลงกรณ์มหาวิทยาลัย
Chulalongkorn University

Appendix B

Padé expansion of the exponential function

To derive an efficient time-stepping scheme, the direct computation of the matrix exponential is avoided by employing a rational approximation, i.e., a ratio of two polyomials $\mathbf{P}(\mathbf{A})$ and $\mathbf{Q}(\mathbf{A})$. The Padé approximation of a function $y(x)$ of order $\mathcal{O}(L,M)$ is written as

$$y_{L/M}(x) = \frac{\mathbf{P}_L(x)}{\mathbf{Q}_M(x)} = \frac{p_0 + p_1 x + \cdots + p_L x^L}{q_0 + qx + \cdots + q_M x^M} \tag{B.1}$$

where L and M are the degrees of polynomials in the numerator and denominator, respectively. The constants $p_k(k = 0,1, \dots, L)$ and $p_k(k = 0,1, \dots, M)$ can be determined by equating the Padé series with a Taylor expansion. In the present study, only the diagonal Padé approximations of the exponential function ex is of interest. Hence, the order of the approximation is $\mathcal{O}(L,M)$ or in short M, which is expressed as

$$e_M^x = \frac{\mathbf{P}_M(x)}{\mathbf{Q}_M(x)} \tag{B.2}$$

where the polynomials in the numerator and denominator are given by

$$\mathbf{P}_M(x) = \sum_{m=0}^{M} \frac{(2M-m)!}{m!\,(M-m)!} x^m \tag{B.3a}$$

$$\mathbf{Q}_M(x) = \mathbf{P}_M(-x) = \sum_{m=0}^{M} \frac{(2M-m)!}{m!\,(M-m)!} (-x)^m \tag{B.3b}$$

From Eqs. (B.3), it is obvious that $\mathbf{Q}_M(x) = \mathbf{P}_M(-x)$ holds. The accuracy of the approximation is of the order of $2M$. The denominator polynomial $\mathbf{Q}_M(x)$ of degree M can be factorized as

$$\mathbf{Q}_M(x) = \prod_{i=1}^{M} (r_i - x) = (r_1 - x)(r_2 - x) \dots (r_M - x) \tag{B.4}$$

where r_i denote the roots of the polynomial, which are either real or pairs of complex conjugates numbers. Note that a fraction can be decomposed into partial fractions if the denominator is a factorized polynomial, e.g.,

จุฬาลงกรณ์มหาวิทยาลัย
Chulalongkorn University

$$\frac{1}{(r_1 - x)(r_2 - x)} = \frac{1}{r_2 - r_1}\left(\frac{1}{r_1 - x} - \frac{1}{r_2 - x}\right) \tag{B.5}$$

with the condition that $r_1 \neq r_2$ holds.

จุฬาลงกรณ์มหาวิทยาลัย
CHULALONGKORN UNIVERSITY

REFERENCES

Abdi, M. (2015). *Evolutionary topology optimization of continuum structures using X-FEM and isovalues of structural performance.* University of Nottingham,

Allaire, G. (1997). The homogenization method for topology and shape optimization. In *Topology optimization in structural mechanics* (pp. 101-133): Springer.

Ananthasuresh, G. K. (1994). *A new design paradigm for micro-electro-mechanical systems and investigations on the compliant mechanisms synthesis.* (Doctoral dissertation), University of Michigan,

Andreassen, E., Clausen, A., Schevenels, M., Lazarov, B. S., & Sigmund, O. (2011). Efficient topology optimization in MATLAB using 88 lines of code. *Structural and multidisciplinary optimization, 43*(1), 1-16.

Aremu, A. (2013). *Topology optimization for additive manufacture.* (Doctoral Dissertation), Loughborough University,

Bazyar, M. H., & Song, C. (2008). A continued‐fraction‐based high‐order transmitting boundary for wave propagation in unbounded domains of arbitrary geometry. *International Journal for Numerical Methods in Engineering, 74*(2), 209-237.

Bendsøe, M. P. (1989). Optimal shape design as a material distribution problem. *Structural optimization, 1*(4), 193-202.

Bendsøe, M. P., & Kikuchi, N. (1988). Generating optimal topologies in structural design using a homogenization method. *Computer Methods in Applied Mechanics and Engineering, 71*(2), 197-224.

Bendsoe, M. P., & Sigmund, O. (2003). *Topology optimization: theory, methods, and applications*: Springer Science & Business Media.

Bendsøe, M. P., & Sigmund, O. (1999). Material interpolation schemes in topology optimization. *Archive of applied mechanics, 69*(9), 635-654.

Burry, J., Felicetti, P., Tang, J., Burry, M., & Xie, M. (2005). Dynamical structural modeling: a collaborative design exploration. *International Journal of Architectural Computing, 3*(1), 27-42.

Chen, X., Birk, C., & Song, C. (2015). Transient analysis of wave propagation in layered soil by

จุฬาลงกรณ์มหาวิทยาลัย
CHULALONGKORN UNIVERSITY

using the scaled boundary finite element method. *Computers and Geotechnics, 63*, 1-12.

Cheng, K.-T., & Olhoff, N. (1981). An investigation concerning optimal design of solid elastic plates. *International Journal of Solids and Structures, 17*(3), 305-323.

Choi, W.-S., & Park, G.-J. (2002). Structural optimization using equivalent static loads at all time intervals. *Computer Methods in Applied Mechanics and Engineering, 191*(19-20), 2105-2122.

Chu, D. N., Xie, Y., Hira, A., & Steven, G. (1996). Evolutionary structural optimization for problems with stiffness constraints. *Finite Elements in Analysis and Design, 21*(4), 239-251.

Deeks, A. J., & Wolf, J. P. (2002a). Semi-analytical elastostatic analysis of unbounded two-dimensional domains. *International Journal for Numerical and Analytical Methods in Geomechanics, 26*(11), 1031-1057. doi:10.1002/nag.232

Deeks, A. J., & Wolf, J. P. (2002b). A virtual work derivation of the scaled boundary finite-element method for elastostatics. *Computational Mechanics, 28*(6), 489-504. doi:10.1007/s00466-002-0314-2

Deng, H., Vulimiri, P. S., & To, A. C. (2021). An efficient 146-line 3D sensitivity analysis code of stress-based topology optimization written in MATLAB. *arXiv preprint arXiv:2104.01210*.

Díaaz, A. R., & Kikuchi, N. (1992). Solutions to shape and topology eigenvalue optimization problems using a homogenization method. *International Journal for Numerical Methods in Engineering, 35*(7), 1487-1502.

Du, J., & Olhoff, N. (2007). Topological design of freely vibrating continuum structures for maximum values of simple and multiple eigenfrequencies and frequency gaps. *Structural and multidisciplinary optimization, 34*(2), 91-110.

Du, Y., Chen, L., & Luo, Z. (2008). Topology synthesis of geometrically nonlinear compliant mechanisms using meshless methods. *Acta Mechanica Solida Sinica, 21*(1), 51-61.

Egger, A. W. (2019). *A Scaled Boundary Approach to Forward and Inverse Problems with Applications in Computational Fracture Mechanics, Damage Localization and Topology Optimization.* ETH Zurich,

Egger, A. W., Saputra, A., Triantafyllou, S. P., & Chatzi, E. (2019). *Exploring Topology Optimization on Hierarchical Meshes by Scaled Boundary Finite Element Method.* Paper

จุฬาลงกรณ์มหาวิทยาลัย
Chulalongkorn University

presented at the Proceedings of the International Conference on Computational Methods.

Ferrari, F., & Sigmund, O. (2020). A new generation 99 line Matlab code for compliance topology optimization and its extension to 3D. *Structural and multidisciplinary optimization, 62*(4), 2211-2228.

Frey, P. J., & George, P.-L. (2007). *Mesh generation: application to finite elements*: Iste.

Gan, N., & Wang, Q. (2021). Topology optimization of multiphase materials with dynamic and static characteristics by BESO method. *Advances in Engineering software, 151*, 102928.

Gantmacher, F. R. (1960). *The Theory of Matrices. Volume one*. USA: Chelsea Publishing Company.

George, P., & Hermeline, F. (1992). Delaunay's mesh of a convex polyhedron in dimension d. Application to arbitrary polyhedra. *International Journal for Numerical Methods in Engineering, 33*(5), 975-995.

Ghabraie, K. (2015). An improved soft-kill BESO algorithm for optimal distribution of single or multiple material phases. *Structural and Multidisciplinary Optimization, 52*(4), 773-790.

Giraldi, L., Nouy, A., Legrain, G., & Cartraud, P. (2013). Tensor-based methods for numerical homogenization from high-resolution images. *Computer Methods in Applied Mechanics and Engineering, 254*, 154-169.

Giraldo-Londoño, O., & Paulino, G. H. (2021). PolyDyna: a Matlab implementation for topology optimization of structures subjected to dynamic loads. *Structural and multidisciplinary optimization, 64*(2), 957-990.

Greaves, D. M., & Borthwick, A. G. L. (1999). Hierarchical tree-based finite element mesh generation. *International Journal for Numerical Methods in Engineering, 45*(4), 447-471. doi:Doi 10.1002/(Sici)1097-0207(19990610)45:4<447::Aid-Nme592>3.0.Co;2-#

Guo, H., Ooi, E. T., Saputra, A. A., Yang, Z., Natarajan, S., Ooi, E. H., & Song, C. (2019). A quadtree-polygon-based scaled boundary finite element method for image-based mesoscale fracture modelling in concrete. *Engineering Fracture Mechanics, 211*, 420-441. doi:10.1016/j.engfracmech.2019.02.021

Han, Y., Xu, B., & Liu, Y. (2021). An efficient 137-line MATLAB code for geometrically nonlinear topology optimization using bi-directional evolutionary structural optimization method. *Structural and multidisciplinary optimization, 63*(5), 2571-2588.

จุฬาลงกรณ์มหาวิทยาลัย
Chulalongkorn University

Hinton, E., & Sienz, J. (1995). Fully stressed topological design of structures using an evolutionary procedure. *Engineering computations, 12*(3), 229-244.

Hirshikesh, Pramod, A. L. N., Annabattula, R. K., Ooi, E. T., Song, C., & Natarajan, S. (2019). Adaptive phase-field modeling of brittle fracture using the scaled boundary finite element method. *Computer Methods in Applied Mechanics and Engineering, 355*, 284-307. doi:10.1016/j.cma.2019.06.002

Hjaltason, G. R., & Samet, H. (2002). Speeding up construction of PMR quadtree-based spatial indexes. *The VLDB Journal, 11*(2), 109-137.

Huang, X., & Xie, M. (2010). *Evolutionary topology optimization of continuum structures: methods and applications*: John Wiley & Sons.

Huang, X., & Xie, Y.-M. (2010). A further review of ESO type methods for topology optimization. *Structural and multidisciplinary optimization, 41*(5), 671-683.

Huang, X., & Xie, Y. (2007a). Bidirectional evolutionary topology optimization for structures with geometrical and material nonlinearities. *AIAA journal, 45*(1), 308-313.

Huang, X., & Xie, Y. (2007b). Convergent and mesh-independent solutions for the bi-directional evolutionary structural optimization method. *Finite Elements in Analysis and Design, 43*(14), 1039-1049.

Huang, X., & Xie, Y. (2008). Topology optimization of nonlinear structures under displacement loading. *Engineering Structures, 30*(7), 2057-2068.

Huang, X., & Xie, Y. (2010). Evolutionary topology optimization of continuum structures with an additional displacement constraint. *Structural and multidisciplinary optimization, 40*(1-6), 409.

Huang, X., & Xie, Y. M. (2009). Bi-directional evolutionary topology optimization of continuum structures with one or multiple materials. *Computational Mechanics, 43*(3), 393-401.

Huang, X., Zuo, Z., & Xie, Y. (2010). Evolutionary topological optimization of vibrating continuum structures for natural frequencies. *Computers & structures, 88*(5-6), 357-364.

Jang, H.-H., Lee, H.-A., & Park, G.-J. (2009). Preliminary study on linear dynamic response topology optimization using equivalent static loads. *Transactions of the Korean Society of Mechanical Engineers A, 33*(12), 1401-1409.

Jang, H.-H., Lee, H., Lee, J., & Park, G. (2012). Dynamic response topology optimization in the

จุฬาลงกรณ์มหาวิทยาลัย
CHULALONGKORN UNIVERSITY

time domain using equivalent static loads. *AIAA journal, 50*(1), 226-234.

JOG, C. S. (2002). Topology design of structures subjected to periodic loading. *Journal of Sound and Vibration, 253*(3), 687-709.

Jung, Y. H., & Lee, K. (1993). Tetrahedron-Based Octree Encoding for Automatic Mesh Generation. *Computer-Aided Design, 25*(3), 141-153. doi:Doi 10.1016/0010-4485(93)90039-Q

Kohn, R. V., & Strang, G. (1986a). Optimal design and relaxation of variational problems, I. *Communications on Pure and Applied Mathematics, 39*(1), 113-137. doi:https://doi.org/10.1002/cpa.3160390107

Kohn, R. V., & Strang, G. (1986b). Optimal design and relaxation of variational problems, II. *Communications on Pure and Applied Mathematics, 39*(2), 139-182. doi:https://doi.org/10.1002/cpa.3160390202

Kohn, R. V., & Strang, G. (1986c). Optimal design and relaxation of variational problems, III. *Communications on Pure and Applied Mathematics, 39*(3), 353-377. doi:https://doi.org/10.1002/cpa.3160390305

Laub, A. (1978). *A Schur method for solving algebraic Riccati equations*. Paper presented at the IEEE Conference on Decision and Control including the 17th Symposium on Adaptive Processes, San Diego, CA, USA.

Le, C., Norato, J., Bruns, T., Ha, C., & Tortorelli, D. (2010). Stress-based topology optimization for continua. *Structural and multidisciplinary optimization, 41*(4), 605-620.

Lee, H.-A., & Park, G.-J. (2015). Nonlinear dynamic response topology optimization using the equivalent static loads method. *Computer Methods in Applied Mechanics and Engineering, 283*, 956-970.

Legrain, G., Cartraud, P., Perreard, I., & Moës, N. (2011). An X‐FEM and level set computational approach for image‐based modelling: application to homogenization. *International Journal for Numerical Methods in Engineering, 86*(7), 915-934.

Li, C., Man, H., Song, C., & Gao, W. (2013). Analysis of cracks and notches in piezoelectric composites using scaled boundary finite element method. *Composite Structures, 101*, 191-203.

Li, D., & Kim, I. Y. (2018). Multi-material topology optimization for practical lightweight design.

จุฬาลงกรณ์มหาวิทยาลัย
Chulalongkorn University

Structural and multidisciplinary optimization, 58(3), 1081-1094.

Li, Y. (2014). *Topology Optimization of Compliant Mechanisms Based on the BESO Method.* RMIT University,

Liu, K., & Tovar, A. (2014). An efficient 3D topology optimization code written in Matlab. *Structural and Multidisciplinary Optimization, 50*(6), 1175-1196.

Liu, Y., Saputra, A. A., Wang, J. C., Tin-Loi, F., & Song, C. M. (2017). Automatic polyhedral mesh generation and scaled boundary finite element analysis of STL models. *Computer Methods in Applied Mechanics and Engineering, 313*, 106-132. doi:10.1016/j.cma.2016.09.038

Lo, D. S. (2014). *Finite element mesh generation*: CRC Press.

Lo, S. (1991). Automatic mesh generation and adaptation by using contours. *International Journal for Numerical Methods in Engineering, 31*(4), 689-707.

Lo, S., & Lee, C. (1992). On using meshes of mixed element types in adaptive finite element analysis. *Finite Elements in Analysis and Design, 11*(4), 307-336.

Man, H., Song, C., Natarajan, S., Ooi, E. T., & Birk, C. (2014). Towards automatic stress analysis using scaled boundary finite element method with quadtree mesh of high-order elements. *arXiv preprint arXiv:1402.5186*.

Meagher, D. (1982). Geometric modeling using octree encoding. *Computer graphics and image processing, 19*(2), 129-147.

Michell, A. G. M. (1904). LVIII. The limits of economy of material in frame-structures. *The London, Edinburgh, and Dublin Philosophical Magazine and Journal of Science, 8*(47), 589-597.

Min, S., Kikuchi, N., Park, Y., Kim, S., & Chang, S. (1999). Optimal topology design of structures under dynamic loads. *Structural optimization, 17*(2), 208-218.

Montes, M. O., Ivvan, S., Pe, V., & Rionda, S. (2016). *Topology optimization algorithms for the solution of compliance and volume problems in 2D.* (Doctoral Dissertation), Guanajuato, Mexico.

Ooi, E. T., Shi, M., Song, C., Tin-Loi, F., & Yang, Z. J. (2013). Dynamic crack propagation simulation with scaled boundary polygon elements and automatic remeshing technique. *Engineering Fracture Mechanics, 106*, 1-21. doi:10.1016/j.engfracmech.2013.02.002

Ooi, E. T., Song, C. M., Tin-Loi, F., & Yang, Z. J. (2012). Polygon scaled boundary finite elements

จุฬาลงกรณ์มหาวิทยาลัย
Chulalongkorn University

for crack propagation modelling. *International Journal for Numerical Methods in Engineering, 91*(3), 319-342. doi:10.1002/nme.4284

Pedersen, N. L. (2000). Maximization of eigenvalues using topology optimization. *Structural and multidisciplinary optimization, 20*(1), 2-11.

Phai, N. V. (1982). Automatic mesh generation with tetrahedron elements. *International Journal for Numerical Methods in Engineering, 18*(2), 273-289.

Prager, W. (1968). Optimality criteria in structural design. *Proceedings of the National Academy of Sciences of the United States of America, 61*(3), 794.

Prager, W., & Rozvany, G. (1977). Optimal layout of grillages. *Journal of Structural Mechanics, 5*(1), 1-18.

Querin, O., Steven, G., & Xie, Y. (1998). Evolutionary structural optimisation (ESO) using a bidirectional algorithm. *Engineering computations, 15*(8), 1031-1048.

Querin, O., Steven, G., & Xie, Y. (2000). Evolutionary structural optimisation using an additive algorithm. *Finite Elements in Analysis and Design, 34*(3-4), 291-308.

Querin, O., Young, V., Steven, G., & Xie, Y. (2000). Computational efficiency and validation of bi-directional evolutionary structural optimisation. *Computer Methods in Applied Mechanics and Engineering, 189*(2), 559-573.

Radman, A. (2013). *Bi-directional Evolutionary Structural Optimization (BESO) for Topology Optimization of Material's Microstructure.* (Doctoral dissertation), RMIT University,

Rietz, A. (2001). Sufficiency of a finite exponent in SIMP (power law) methods. *Structural and multidisciplinary optimization, 21*(2), 159-163.

Rivara, M. C. (1997). New longest‐edge algorithms for the refinement and/or improvement of unstructured triangulations. *International Journal for Numerical Methods in Engineering, 40*(18), 3313-3324.

Rozvany, G. (1972a). Grillages of maximum strength and maximum stiffness. *International Journal of Mechanical Sciences, 14*(10), 651-666.

Rozvany, G. (1972b). Optimal load transmission by flexure. *Computer Methods in Applied Mechanics and Engineering, 1*(3), 253-263.

Rozvany, G., & Zhou, M. (1991). The COC algorithm, part I: cross-section optimization or sizing. *Computer Methods in Applied Mechanics and Engineering, 89*(1-3), 281-308.

จุฬาลงกรณ์มหาวิทยาลัย
Chulalongkorn University

Rozvany, G. I., & Querin, O. M. (2002). Combining ESO with rigorous optimality criteria. *International journal of vehicle design, 28*(4), 294-299.

Sanders, E. D., Aguiló, M. A., & Paulino, G. H. (2018). Multi-material continuum topology optimization with arbitrary volume and mass constraints. *Computer Methods in Applied Mechanics and Engineering, 340*, 798-823.

Saputra, A., Talebi, H., Tran, D., Birk, C., & Song, C. M. (2017). Automatic image-based stress analysis by the scaled boundary finite element method. *International Journal for Numerical Methods in Engineering, 109*(5), 697-738. doi:10.1002/nme.5304

Shu, L., Wang, M. Y., Fang, Z., Ma, Z., & Wei, P. (2011). Level set based structural topology optimization for minimizing frequency response. *Journal of Sound and Vibration, 330*(24), 5820-5834.

Sigmund, O. (1997). On the design of compliant mechanisms using topology optimization. *Journal of Structural Mechanics, 25*(4), 493-524.

Sigmund, O. (2001). A 99 line topology optimization code written in Matlab. *Structural and multidisciplinary optimization, 21*(2), 120-127.

Sigmund, O., & Bondsgc, M. (2003). Topology optimization. *State-of-the-Art and Future Perspectives, Copenhagen: Technical University of Denmark (DTU)*.

Sluiter, M. (1982). A general purpose automatic mesh generator for shell and solid finite elements. *Computers in engineering*.

Song, C. (2018). *The Scaled Boundary Finite Element Method : Introduction to Theory and Implementation / by Chongmin Song*: Hoboken, New Jersey : John Wiley & Sons.

Song, C., Eisenträger, S., & Zhang, X. (2022). High-order implicit time integration scheme based on Padé expansions. *Computer Methods in Applied Mechanics and Engineering, 390*, 114436.

Song, C., & Wolf, J. P. (1997). The scaled boundary finite-element method - Alias consistent infinitesimal finite-element cell method - For elastodynamics. *Computer Methods in Applied Mechanics and Engineering, 147*(3-4), 329-355. doi:Doi 10.1016/S0045-7825(97)00021-2

Song, C., Zhang, X., Eisenträger, S., & Ankit, A. (2022). High-order implicit time integration scheme with controllable numerical dissipation based on mixed-order Pad\'e expansions. *arXiv preprint arXiv:2206.04183*.

จุฬาลงกรณ์มหาวิทยาลัย
Chulalongkorn University

Song, C. M., Tin-Loi, F., & Gao, W. (2010). A definition and evaluation procedure of generalized stress intensity factors at cracks and multi-material wedges. *Engineering Fracture Mechanics, 77*(12), 2316-2336. doi:10.1016/j.engfracmech.2010.04.032

Song, C. M., & Wolf, J. P. (1999). Body loads in scaled boundary finite-element method. *Computer Methods in Applied Mechanics and Engineering, 180*(1-2), 117-135. doi:Doi 10.1016/S0045-7825(99)00052-3

Song, C. M., & Wolf, J. P. (2000). The scaled boundary finite-element method - a primer: solution procedures. *Computers & structures, 78*(1-3), 211-225. doi:Doi 10.1016/S0045-7949(00)00100-0

Su, R., Van, T. H., & Tangaramvong[1], S. (2021). *BESO Approach for the Optimal Retrofitting Design of Steel Hollow-Section Columns Supporting Industry Cranes*. Paper presented at the The 12th International Conference on Computational Methods, 4th-8th July 2021 online.

Sundar, H., Sampath, R. S., & Biros, G. (2008). Bottom-up construction and 2: 1 balance refinement of linear octrees in parallel. *SIAM Journal on Scientific Computing, 30*(5), 2675-2708.

Suzuki, K., & Kikuchi, N. (1991). A homogenization method for shape and topology optimization. *Computer Methods in Applied Mechanics and Engineering, 93*(3), 291-318.

Talebi, H., Saputra, A., & Song, C. (2016). Stress analysis of 3D complex geometries using the scaled boundary polyhedral finite elements. *Computational Mechanics, 58*(4), 697-715. doi:10.1007/s00466-016-1312-0

Terada, K., Miura, T., & Kikuchi, N. (1997). Digital image-based modeling applied to the homogenization analysis of composite materials. *Computational Mechanics, 20*(4), 331-346.

Tikenoğulları, O. Z. (2015). *Bi-directional evolutionary algorithm for volume constrained topology optimization of axisymmetric solids.* (Doctoral Dissertation),

Timoshenko, S., & Goodier, J. (1971). Theory of Elasticity, McGraw-Hill, New York, 1970. *Fok-Ching Chong received the BS degree from the Department of Electrical Engineering, National Taiwan University, Taipei, Taiwan, in*.

Weiler, F., Schindler, R., & Schneiders, R. (1996). *Automatic geometry-adaptive generation of quadrilateral and hexahedral element meshes for the FEM*. Retrieved from

จุฬาลงกรณ์มหาวิทยาลัย
Chulalongkorn University

Wille, S. (1992). A structured tri-tree search method for generation of optimal unstructured finite element grids in two and three dimensions. *International Journal for Numerical Methods in Fluids, 14*(7), 861-881.

Wolf, J. P., & Song, C. M. (2000). The scaled boundary finite-element method - a primer: derivations. *Computers & structures, 78*(1-3), 191-210. doi:Doi 10.1016/S0045-7949(00)00099-7

Xia, L. (2016). *Multiscale structural topology optimization*: Elsevier.

Xia, L., & Breitkopf, P. (2017). Recent advances on topology optimization of multiscale nonlinear structures. *Archives of Computational Methods in Engineering, 24*(2), 227-249.

Xia, L., Zhang, L., Xia, Q., & Shi, T. (2018). Stress-based topology optimization using bi-directional evolutionary structural optimization method. *Computer Methods in Applied Mechanics and Engineering, 333*, 356-370.

Xie, Y. M., & Steven, G. P. (1993). A simple evolutionary procedure for structural optimization. *Computers & structures, 49*(5), 885-896.

Xie, Y. M., & Steven, G. P. (1997). Basic evolutionary structural optimization. In *Evolutionary structural optimization* (pp. 12-29): Springer.

Xing, W. W., Zhang, J. Q., Song, C. M., & Tin-Loi, F. (2019). A node-to-node scheme for three-dimensional contact problems using the scaled boundary finite element method. *Computer Methods in Applied Mechanics and Engineering, 347*, 928-956. doi:10.1016/j.cma.2019.01.015

จุฬาลงกรณ์มหาวิทยาลัย
Chulalongkorn University

Xu, B., Han, Y., & Zhao, L. (2021). Bi-directional evolutionary stress-based topology optimization of material nonlinear structures. *Structural and multidisciplinary optimization, 63*(3), 1287-1305.

Xuan, J. (2012). Topology optimization for continuum structure with numerical methods.

Yang, X., Xie, Y., Liu, J., Parks, G., & Clarkson, P. (2002). Perimeter control in the bidirectional evolutionary optimization method. *Structural and multidisciplinary optimization, 24*(6), 430-440.

Yerry, M. A., & Shephard, M. S. (1983). A modified quadtree approach to finite element mesh generation. *IEEE Computer Graphics and Applications, 3*(1), 39-46.

Yerry, M. A., & Shephard, M. S. (1984). Automatic three-dimensional mesh generation by the

modified-octree technique. *International Journal for Numerical Methods in Engineering, 20*(11), 1965-1990.

Yoon, G. H., & Kim, Y. Y. (2005). Element connectivity parameterization for topology optimization of geometrically nonlinear structures. *International Journal of Solids and Structures, 42*(7), 1983-2009.

Yuge, K., Iwai, N., & Kikuchi, N. (1999). Optimization of 2-D structures subjected to nonlinear deformations using the homogenization method. *Structural optimization, 17*(4), 286-299.

Zhao, J., & Wang, C. (2016). Dynamic response topology optimization in the time domain using model reduction method. *Structural and multidisciplinary optimization, 53*(1), 101-114.

Zhou, M., & Rozvany, G. (1991). The COC algorithm, Part II: Topological, geometrical and generalized shape optimization. *Computer Methods in Applied Mechanics and Engineering, 89*(1-3), 309-336.

Zhou, M., & Rozvany, G. (2001). On the validity of ESO type methods in topology optimization. *Structural and multidisciplinary optimization, 21*(1), 80-83.

Zhu, J., Zienkiewicz, O., Hinton, E., & Wu, J. (1991). A new approach to the development of automatic quadrilateral mesh generation. *International Journal for Numerical Methods in Engineering, 32*(4), 849-866.

จุฬาลงกรณ์มหาวิทยาลัย
CHULALONGKORN UNIVERSITY

จุฬาลงกรณ์มหาวิทยาลัย
Chulalongkorn University

VITA

NAME	Rut Su
DATE OF BIRTH	16 Dec 1994
PLACE OF BIRTH	Neihu, Taiwan
INSTITUTIONS ATTENDED	B.Eng. (Survey Engineering) GPA: 3.24 M.Eng. (Civil Engineering) GPA: 3.81 Ph.D. (Civil Engineering) GPA: 4.00
HOME ADDRESS	Sathorn premier place condominium, Phrachaotaksin Road, Bukkalo, Thonburi, Bangkok, Thailand.
PUBLICATION	Su, R., Van, T. H., & Tangaramvong, S. (2021). BESO Approach for the Optimal Retrofitting Design of Steel Hollow-Section Columns Supporting Industry Cranes. In The 12th International Conference on Computational Methods (ICCM2021).

จุฬาลงกรณ์มหาวิทยาลัย
Chulalongkorn University